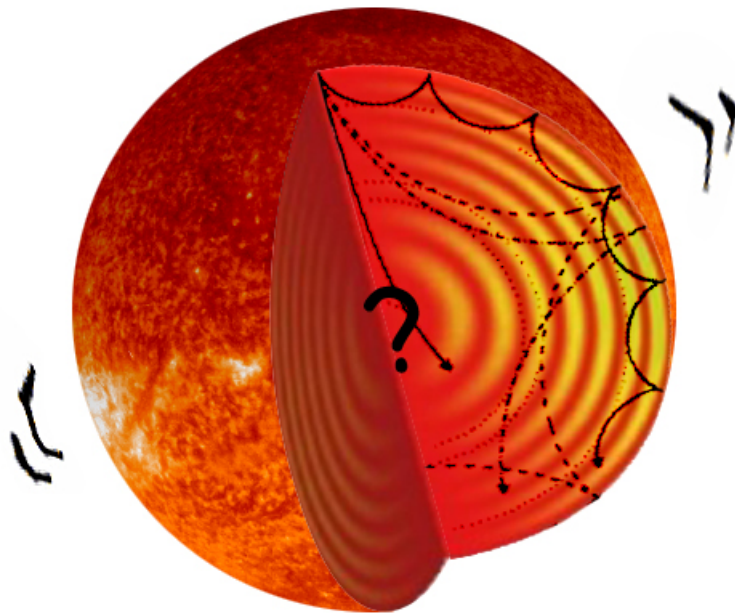


Asteroseismic Modelling of Solar-like Stars

Dissertation for the degree of Doctor of Philosophy



Gülnur Doğan

September 2010



Department of Physics and Astronomy
Aarhus University
Denmark

Cover graphic: Collage by Thomas Holst
Images from: <http://astro.phys.au.dk/KASC/seismology/intro.html>,
<http://science.nasa.gov/>, and <http://www.phys.au.dk/jcd/oscilnotes/>

Asteroseismic Modelling of Solar-like Stars: Interpreting the Data

A Dissertation
Presented to the Faculty of Science
at Aarhus University
in Partial Fulfilment of the Requirements for the
PhD Degree

by
Gülnur Doğan
September 2010

Supervisor: Professor Jørgen Christensen-Dalsgaard,
IFA, Aarhus University

To my parents, F. Hatice Dođan and Prof. Nadir Dođan...

Acknowledgments

It wasn't the easiest period in my life, and I wouldn't have completed the PhD programme if it weren't for the wonderful people in my life.

First of all, I would like to express my deep gratitude to my supervisor, Prof. Jørgen Christensen-Dalsgaard, who has also been a very good friend during my stay in Aarhus, for his constant support and patience towards me. Jørgen has inspired me with his unlimited scientific enthusiasm and has made the long and dark days enjoyable with his unique sense of humour. He has always been warm and his door has always been open to me. I am one of the lucky ones who had the opportunity to get one-to-one lectures from him, and yet it is entirely my responsibility not having received every piece of knowledge he had to offer, with the hope to catch up in the many years of collaboration to come. It has been a great pleasure and an invaluable experience working with him. *Tusind tak for alt, Jørgen!*

Part of my project has been carried out in cooperation with the Kepler Asteroseismic Science Consortium, which is coordinated from the Aarhus University. I am indebted to my numerous collaborators from all around the world for fruitful discussions, especially to Isa Brandão, Travis Metcalfe, Alfio Bonanno, Tim Bedding, Margarida Cunha, Bill Chaplin, Vichi Antoci and Victor Silva Aguirre. Many thanks to Travis and Alfio also for inviting me and supporting my visits over the summer of 2009; both were productive and very enjoyable experiences. I thank Travis also for his extra coaching efforts. I gratefully acknowledge Aarhus University and Danish Science Research Council for not only funding my research but also covering my expenses for numerous international conferences, which gave me the opportunity to start international collaborations.

I enjoyed the working atmosphere in Aarhus University, particularly within the Astrophysics and Cosmology Group, very much – thanks to my friends and colleagues, who were there when I needed help or just to relax over a coffee. I specially thank Tiago Campante, Pierre-Olivier Quirion, Jyoti Rajput, Aasa Feragen, Philip Jarnhus, Lutz Lammich, Tina Lund, Rasmus Handberg, Frank Grundahl, Christoffer Karoff, and Hans Kjeldsen. I also thank Anette Skovgaard and Marianne Sodemann for their warmth and kind help with the practical issues. Thanks again to Jørgen and Tiago for providing comments on an earlier draft of this dissertation.

I would like to thank all my friends who made life easier and more fun over the last three years, especially to Canan Doğanlı, Joan Marler, Aasa Feragen, Joanna Kauczor, Tiago Campante, Isabel Nawroth, Christina Kirkegaard Pedersen, Fabia Febbraro, Muwan Chen, and many more from Vennelyst Kollegiet and IFA, and also those dear friends back at home that I have been missing, for the moral support I received. One can never complain as much as it is possible in the mother tongue, therefore I thank Canan once again for

putting up with me all these years, and I thank Muwan also for her enjoyable company during thesis-writing sessions in the late hours, which made it possible for me to finish in time. I also acknowledge the hospitality of Løve's Bog- og Vincafé in Aarhus C, which was a savior when I felt like writing away from my office during the working hours. I thank my officemates and everyone around me, for tolerating my aggression during this period. I am deeply grateful to Holsts for giving me a very warm place in their lives and for all the joyful time we spent together; special thanks to Thomas Holst for colouring my life, cheering me up, encouraging and supporting me extraordinarily, in good and bad times – and bad times are often there along the harsh road toward a PhD degree. I thank Jorge Cham (www.phdcomics.com) for letting me know -in an hilarious way- that I am not the only one feeling this way.

I would like to take this opportunity to thank some of the most affectionate teachers I have had in my life; my primary school teacher Günaydın Diker for teaching me the fundamentals in such a tender and enthusiastic manner; my father for somewhat-forced-on-me private maths lessons which helped me a great deal afterwards; my prep-class English teacher Neşe Ünlü for setting an ideal example as a strong and caring teacher and teaching me the language; and my master's degree supervisor Prof. Halil Kırbıyık for teaching me the basics of our field and for encouraging and convincing me to stay in it.

Last but not least, I am most grateful to my loving and beloved family and relatives for supporting me by all means over the years, respecting my decisions, always believing in me, and being there for me. I especially thank the oldest member of my family, my dad, for inspiring me as an astronomer, and the youngest one – my newborn nephew, Ali Ege – for reminding me that life is a miracle and that I should not waste my time worrying.
Sevgili aileme sonsuz teşekkürler...

Gülnur Doğan
Århus, September 2010

Abstract

Asteroseismology, the science that deals with the oscillations in the stars with the goal of understanding the stellar structure and evolution better, has been in rapid development since 1980s. Many ground-based observation campaigns and quite a few space missions have been fully or partly dedicated to asteroseismology. There are still aspects of stellar structure that are relatively poorly understood. Since the observed oscillation parameters are highly determined by the global stellar properties and the inner structure of the stars, asteroseismology is a perfect tool to test our current understanding of stars. With the acquisition of high quality oscillation data, the theories of stellar structure and evolution and theories of stellar pulsation are challenged – at least there is strong need for revision of some simplifications that have been widely used.

This thesis includes brief theoretical and observational overviews regarding asteroseismology of solar-like stars and focuses on the stellar modelling aspects. The main results obtained through studying individual solar-like stars are presented. The results emphasize that asteroseismology helps us to put strong constraints on the global and internal properties of the observed stars and we can reach much higher precision than before in determining these properties using the currently available data and methods. The possibilities to uncover more are being explored by the entire community of asteroseismology, and partly discussed in this dissertation.

Contents

I	Overview	1
1	Introduction	3
2	Solar-like Oscillations	5
2.1	Theoretical overview	5
2.1.1	Stellar oscillations in general	5
2.1.2	Excitation mechanisms	6
2.1.3	Oscillation modes	7
2.1.4	Characteristics of solar-like oscillations	11
2.2	Observational overview	12
2.2.1	Oscillations in the Sun	12
2.2.2	Solar-like oscillations in solar-like stars	14
2.2.3	Solar-like oscillations in other stars	15
3	Modelling Solar-like Oscillators	16
3.1	Observational constraints	16
3.2	Input physics	17
3.3	Implications of initial parameters on the resulting models	19
3.4	The Methods Used for Modelling	21
3.5	Modifications in relation to frequency calculations	24
3.5.1	A new identification scheme for the dipolar mode stellar oscillations	25
3.5.2	Near-surface effects on the frequencies	28
4	Results on Individual Solar-like Stars	32
4.1	β Hydri	32
4.1.1	β Hydri with grid-computing approach	32
4.1.2	β Hydri with AMP	34
4.2	Procyon	40
4.3	<i>Kepler</i> stars	43
4.3.1	KIC 11026764	44
4.3.2	A special group of solar-like stars	55
5	Summary and Outlook	57

II Relevant publications and related work	63
List of Publications	65
A Dipole modes of stellar oscillations	69
B Near-surface effects and solar-age determination	73
C Asteroseismic modelling of the solar-like star β Hydri	79
D Asteroseismic modelling of the solar-type subgiant star β Hydri	85
E Asteroseismic modelling of Procyon A: Preliminary results	95
F The asteroseismic potential of <i>Kepler</i> : First results for solar-type stars	101
G Asteroseismology of Solar-type stars with Kepler II: Stellar Modeling	111
H A precise asteroseismic age and radius for the evolved sun-like star KIC 11026764	117
I NOT "Fast Track" proposal for five <i>Kepler</i> stars	135

Part I

Overview

Chapter 1

Introduction

Astrophysics is the scientific study that deals with understanding the physical and chemical phenomena related to stars, planets, etc. Stars have always attracted interest, due to their mysterious and fascinating appearance in the night-time sky. We know that they are hot, gaseous spheres that are held together by self-gravity. They generate energy in their cores through nuclear fusion and emit it in the form of light. Furthermore, most of the elements that the Earth and all the living things are made up of have been produced in the stars.

Scientists are in particular interested in understanding what is beyond apparent. However, all the information we have about the stars are obtained through the observation of the light emitted from the stellar surfaces, opaqueness of which prevents us from directly seeing their interiors. Nevertheless, the desire to do so has motivated the efforts to discover scientific methods to use the observations in a way to help us predict what the physical picture inside a star is. Therefore, the theories and observations have driven one another as is the case in many other scientific fields. Our laboratory, however, is the sky, and universe has always more to offer.

Asteroseismology is the field of astrophysics that allows us to study the stellar oscillation data to probe stellar interiors and it remains a unique tool to do so. Stellar oscillation data are mainly the resonant frequencies of standing sound waves inside a star, and by "listening" to these we can determine the properties like the size, the chemical composition, etc. of the stars. It is analogous to guessing what an instrument is like by only hearing it. The development of this field owes to the achievements of helioseismology, which studies the solar interior through the observed oscillations in the Sun, the nearest star to Earth. Observations of these oscillations made it possible to predict the inner structure of our Sun in more detail than before. Although there are still some aspects to be understood better, helioseismology led substantial improvements in the field (see Christensen-Dalsgaard (2002) for a review on helioseismology). The quality of the solar data is better than we can ever achieve for the other stars, hence our knowledge of other stars is highly dependent on what we know about the Sun.

The success of helioseismology naturally brought the idea of applying similar methods to the stars other than the Sun. This started by searching for a solar-like power excess in the oscillation data of the nearby solar-like stars through ground-based observations,

with the first detection almost two decades ago. The field has been in rapid development since, and currently we are receiving excellent quality data on more distant stars thanks to the space telescopes, such as COROT (Baglin et al. 2002) and *Kepler* (Koch et al. 2010). Asteroseismic investigations are of course not limited to solar-like stars. Most of the stars are believed to pulsate at some stage in their lives; therefore, asteroseismology has application for different types of oscillations in different types of stars. The high-quality data in hand serve not only asteroseismology but also exoplanet science, which is the search for planets orbiting stars other than our Sun with the motivation of finding habitable Earth-like planets. Asteroseismology provides support for this research field by characterizing the stars potentially hosting planets. As a result, in addition to bringing the opportunity to test our understanding of the structure and evolution of the stars, asteroseismology will eventually help us to improve our general understanding of the universe.

This thesis addresses the interpretation of asteroseismic data on solar-like stars, in terms of stellar modelling, which involves finding the set of parameters that would best represent the observed properties of the star. This is carried out by matching the frequencies, and other observed properties of the stars, to the corresponding model properties. A model refers to a set of parameters calculated theoretically to simulate a star by using the existing knowledge related to stellar structure and evolution. The goal is not only to determine the global properties of the stars, but also to pinpoint the potential problems in stellar modelling and investigate how the models can be improved, on the basis of the observed oscillation frequencies. The higher the accuracy and the precision of the data, the more detailed our analysis can get.

In the next chapter, I give a brief background of the theory and observations of solar-like oscillations. This is followed by Chapter 3, which focuses on the modelling aspect including the tools and methods employed for the purpose of modelling. In Chapter 4, I present the results regarding individual stars, and Chapter 5 provides a brief summary and outlook.

The manuscripts that are published, in press, or in the reviewing process are given as appendices of the dissertation. Two papers on a side project related to slowly pulsating B stars (given in the list of publications) are not included in this thesis as I have made only minor contribution, and they lie outside the main scope of my project.

Chapter 2

Solar-like Oscillations

Stellar variability is known to be first observed in late 1500s in Mira due to the large amplitude of variation. Since then stellar variations have been observed in eclipsing binary systems and in different types of intrinsic variable stars. A summary of the development of stellar pulsation theory is given by, e.g., Gautschy (1997). In this chapter I give a brief overview of solar-like variability. The basic properties of solar-like oscillations are discussed, and the background of the theory and observations is presented.

2.1 Theoretical overview

2.1.1 Stellar oscillations in general

Stellar oscillations are governed mainly by the basic hydrodynamical equations; namely, continuity equation (conservation of mass), equation of motion (conservation of momentum), and energy equation; together with the Poisson's equation (see, e.g., Unno et al. (1989)). Since the amplitudes of the stellar oscillations are small, we regard the variables in these equations as being perturbed around an equilibrium state, by the oscillations. After separation of variables, the perturbed variables can be expressed as shown in the example for the radial displacement, ξ_r , and pressure perturbation below (similarly for the perturbations to the density, ρ , and the gravitational potential, Φ), and the equations of adiabatic oscillations are then represented by a fourth order system of ordinary differential equations.

$$\xi_r(r, \theta, \phi, t) = \sqrt{4\pi} \tilde{\xi}_r(r) Y_l^m(\theta, \phi) \exp(-i\omega t), \quad (2.1)$$

$$p'(r, \theta, \phi, t) = \sqrt{4\pi} \tilde{p}'(r) Y_l^m(\theta, \phi) \exp(-i\omega t), \quad (2.2)$$

where, $\tilde{\xi}_r(r)$, and $\tilde{p}'(r)$ are the amplitude functions, $Y_l^m(\theta, \phi)$ represents the spherical harmonics, with θ and ϕ being the longitude and co-latitude, and ω is the angular frequency of oscillations (For a detailed discussion, I refer the reader to the textbook by Aerts et al. (2010), which I mainly follow here). Three quantum numbers are used to characterize the

oscillations: l , the spherical degree; m , the azimuthal order, and n , the radial order. Here, l represents the number of lines dividing the stellar surface, $|m|$ is the number of those that are longitudinal lines. The third quantum number, n , defines the number of nodes from centre to the surface of the star for each mode. This is referred to as the radial order of the mode, and is useful in the conventional mode identification, which cannot be determined by the observations, but becomes meaningful within the concept of comparing different stellar models. In the following, the discussion is carried out under spherical symmetry, and the rotational effects that are assumed to be negligibly small in the case of slow rotation are not taken into account; hence $m = 0$.

Most of the stars are believed to oscillate at some stage during their evolution. The mechanism driving the oscillations, however, varies from star to star. In stars like δ Scutis and β Cepheids, the oscillations are due to the so-called kappa mechanism, while in the Sun and other solar-like stars, the oscillations are excited stochastically due to turbulent convection in the outer layers. In this dissertation, I focus on the solar-like oscillations.

2.1.2 Excitation mechanisms

In the outer layers of the Sun and the solar-like stars, energy is transported by convection. Turbulence in these layers generates random acoustic noise and the resonating sound waves form the solar acoustic spectrum, which reveals the existence of p-mode oscillations (as standing sound waves) with a period of around 5 minutes. In the Sun, millions of acoustic modes of oscillation are excited simultaneously within a broad range of frequencies. These oscillations are believed to be intrinsically damped and stochastically excited by the turbulent convection in the very near-surface layers (see, e.g., Houdek 2006 for a review). The balance between the excitation and damping determines the amplitudes of the oscillations. It is discussed in detail by Houdek et al. (1999) that the damping of these modes are due to the processes related to turbulence and nonadiabaticity affecting the momentum balance and the thermal energy balance. In the standard stellar models, however, both the turbulence and the nonadiabaticity are ignored due to their complexity, and the offset between the observed and model frequencies at high-frequency range is attributed to this improper modelling. With increasing quality of stellar oscillation data, a complete modelling of these layers, which takes into account the interaction of convection and pulsations, is needed in order to achieve high accuracy in the frequency calculations.

By solar-like oscillations, we refer to the oscillations excited in the same way as they are in the Sun, although the other properties of the stars might be different from those of the Sun.

Other Types of Oscillations

Apart from stochastically excited oscillations there are two major driving mechanisms. One of them is the κ -mechanism, which is currently considered as the driving mechanism for many stars in the Cepheid instability strip as well as some others out of the strip, such as beta Cephei (β Cep) stars. The principle of this mechanism is similar to that of a

heat engine. The heat that is stored in a radial layer in the compression phase can drive the pulsations. In such a layer, radiative luminosity is blocked due to opacity and the gas heats (see, e.g., Saio 1993). The layers causing the opacity to block radiation are the ionization layers of H and He in the case of the stars in the Cepheid instability strip, while the κ -mechanism in the β Cep stars works due to the iron enhanced opacity. It should be noted that there is also evidence that convection contributes to the driving of long-period g-mode pulsations; as in γ Dor stars through "convective blocking" (Pesnell 1987) at the base of the convection zone (BCZ), which contributes to heating in the compression phase, and in DB and DA white dwarfs via redistribution of energy at the BCZ throughout the thin convection zone, which results in heating of the convection zone (Brickhill 1991). For a brief overview including the recent results, see Aerts et al. (2010).

The other mechanism is the ϵ -mechanism, where ϵ refers to the nuclear energy generation rate. It is thought that the variations in ϵ could drive oscillations, but such oscillations have not been observed yet (Aerts et al. 2010).

2.1.3 Oscillation modes

Stellar oscillation modes are investigated, in a broad sense, under two categories: the acoustic modes (p modes), and the gravity modes (g modes), with the restoring force being pressure and buoyancy, respectively. In most cases, but not for dipolar oscillations, there is also an intermediate fundamental mode, the so-called f mode, which has no radial node in the vertical displacement (for a detailed discussion; see Christensen-Dalsgaard & Gough 2001). In the case of p modes, most of the energy is contained in a region close to the surface, whereas for g modes most of the energy is confined to the central regions. Thus, g-mode frequencies carry information about the deep interior. But, unfortunately the g modes are not likely to be observed in many cases, due to the fact that their amplitude becomes extremely small when they reach the stellar surface. Low-order g modes are observed in δ Scuti and β Cephei stars, while high-order g modes are observed in γ Doradus and SPB stars. In the case of the Sun and other solar-like oscillators, however, we mostly observe the p-mode spectra. For evolved stars there are also "mixed modes" that show a mixed character as behaving like a g mode in the core and like a p mode in the outer layers.

The frequencies of the modes are determined by the characteristic frequencies: acoustic (Lamb) frequency, S_l , and the buoyancy (Brunt-Väisälä) frequency, N , which are given below.

$$N^2 = g \left(\frac{1}{\Gamma_1} \frac{d \ln p}{dr} - \frac{d \ln \rho}{dr} \right), \quad (2.3)$$

where p is the pressure, ρ is the density, r is the distance from the stellar centre, and Γ_1 the first adiabatic exponent given as:

$$\Gamma_1 = \left(\frac{\partial \ln p}{\partial \ln \rho} \right)_{\text{ad}}. \quad (2.4)$$

$$S_l^2 = \frac{l(l+1)c^2}{r^2}, \quad (2.5)$$

where c is the adiabatic sound speed given as:

$$c^2 = \frac{\Gamma_1 p}{\rho}, \quad (2.6)$$

which, under the approximation for an ideal gas, is written as:

$$c^2 = \frac{k_B T}{\mu m_u}, \quad (2.7)$$

where k_B is the Boltzmann constant, T , the temperature, μ the mean molecular weight and m_u is the atomic mass unit.

S_l determines the position of the inner turning point of the waves, while the upper reflection (due to the sudden decrease in density) is determined by the so-called *acoustical cut-off frequency* (equation 2.8), below which the wave will be reflected back to oscillate in the stellar envelope, and above which it will propagate through the atmosphere.

$$\omega_{ac} = \frac{c_s}{2H} = \frac{\Gamma_1 g_s}{c_s}, \quad (2.8)$$

where c_s and g_s are the atmospheric sound speed and gravity.

According to the asymptotic analysis of the oscillations, for the motion to be oscillatory, either of the following two conditions must be satisfied: $|\omega| > |N|, S_l$ or $|\omega| < |N|, S_l$. The former condition corresponds to p-mode oscillations, while the latter one to g-mode oscillations. In a star both conditions might be satisfied in different regions, but the dominant nature of the mode is determined by the region where most of the energy is contained, which is referred to as the *trapping region*.

As the star evolves, the p- and g- mode cavities approach each other, mainly as a result of the g mode region extending outward. This is due to the increase in buoyancy frequency, N , in the core. N^2 is approximated for the stellar interiors as

$$N^2 \simeq \left(\frac{g^2 \rho}{p} \right) (\nabla_{ad} - \nabla + \nabla_\mu), \quad (2.9)$$

where $\nabla = \frac{d \ln T}{d \ln p}$, $\nabla_{ad} = \left(\frac{\partial \ln T}{\partial \ln p} \right)_{ad}$, and $\nabla_\mu = \frac{d \ln \mu}{d \ln p}$ are the temperature gradient, adiabatic temperature gradient and μ gradient, respectively. The μ gradient indicates that an increase in the mean molecular weight, μ , with increasing pressure, p , will increase the buoyancy frequency. As a result of nuclear burning, μ increases with increasing depth (and hence with increasing pressure), thus contributing to the increase in buoyancy frequency. Another contribution comes from the increasing g as a result of core contraction along the evolution when the hydrogen is exhausted in the core. On the other hand, the p-mode frequencies decrease with evolution mainly due to the increase in stellar radius.

Consequently, the cavity between these regions gets smaller (see Fig. 2.1), therefore, coupling between the p and g waves causes the p modes to be perturbed. This phenomenon is called avoided crossing (or, mode bumping) due to the fact that the frequencies of p and g modes approach one another but do not cross (see Fig 4.8). The modes that are affected by the avoided crossings are referred to as mixed modes due to having a mixed character caused by the interaction between p and g modes. These mixed modes can be observed in the p-mode solar-like spectra of evolved stars like subgiants. When observed, they constrain the age of the star (see Section 4.3.1).

Timescales of avoided crossings are very small, i.e., the disturbance in the p mode frequency lasts very short for one particular radial order and jumps to the next radial order, while the frequency that was previously "bumped" continues its usual evolution (as having a decreasing frequency) for a long while until it is bumped again by the next g-mode, the frequency of which had been increasing. Therefore, the mixed modes are strong clues for the evolutionary status of the star. This will be illustrated in Chapter 4 for the specific case of the star KIC 11026764.

The theoretical discussion about the avoided crossings (mode bumping) dates back to 1970s (see, e.g., Aizenman et al. 1977). However, observing these mixed modes is relatively new and exciting. They reveal themselves in the power spectrum as narrow and high peaks. Mixed modes have been detected in the spectra of η Bootis (Kjeldsen et al. 1995), β Hydri (Bedding et al. 2007), and now in quite a few more subgiants observed by COROT (Deheuvels & Michel 2010) and *Kepler* (Chaplin et al. 2010). It is very important to have observations covering a large sample of stars so that we can understand the additional features through comparative methods.

Mode energy

The displacement, $\delta\mathbf{r}$, in terms of radial and horizontal components is given as $\delta\mathbf{r} = \xi_r\mathbf{a}_r + \boldsymbol{\xi}_h$, where ξ_r is defined in equation 2.1, \mathbf{a}_r is the unit vector in the radial direction, and $\boldsymbol{\xi}_h$, the horizontal displacement, is given as:

$$\boldsymbol{\xi}_h = \sqrt{4\pi}\tilde{\xi}_h(r) \left(\frac{\partial Y_l^m}{\partial\theta} \mathbf{a}_\theta + \frac{1}{\sin\theta} \frac{\partial Y_l^m}{\partial\phi} \mathbf{a}_\phi \right) \exp(-i\omega t), \quad (2.10)$$

where \mathbf{a}_θ and \mathbf{a}_ϕ are the unit vectors in θ and ϕ directions, and $\tilde{\xi}_h(r)$ is the amplitude function given as:

$$\tilde{\xi}_h(r) = \frac{1}{r\omega^2} \left(\frac{1}{\rho_0} \tilde{p}' + \Phi' \right). \quad (2.11)$$

The time averaged energy of the pulsation is $1/4\omega^2\mathcal{E}$, where the mode inertia, \mathcal{E} is given in terms of displacement amplitudes as:

$$\mathcal{E} = 4\pi \int_0^R [|\tilde{\xi}_r(r)|^2 + l(l+1)|\tilde{\xi}_h(r)|^2] \rho_0 r^2 dr \quad (2.12)$$

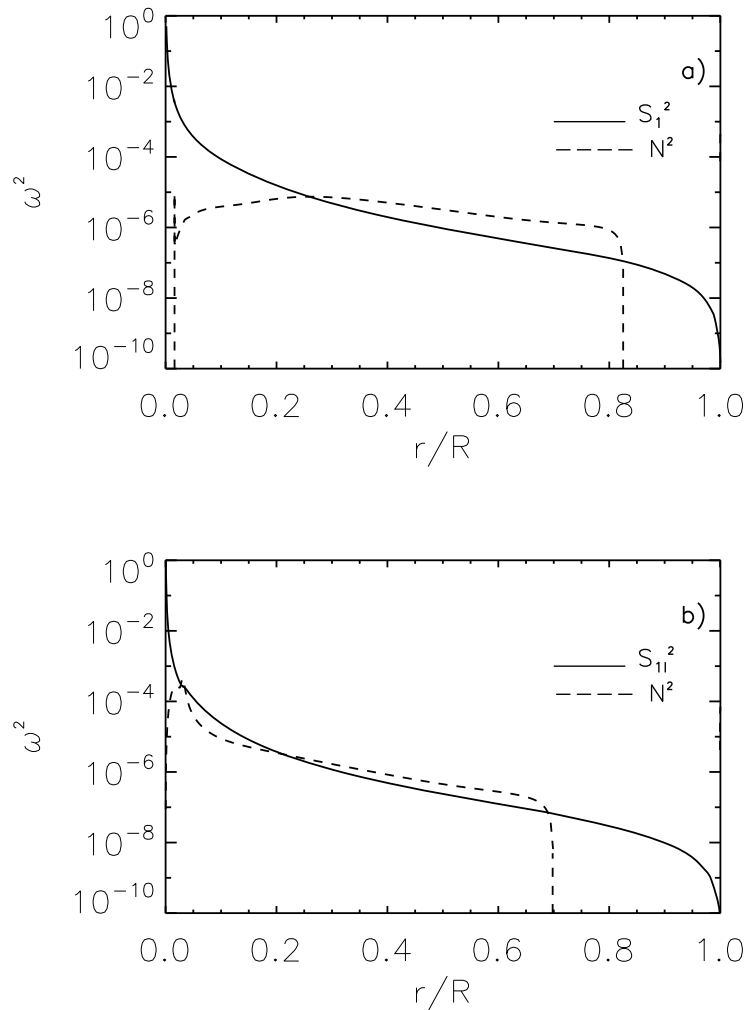


Figure 2.1: N^2 and S_l^2 ($l = 1$) for two models from the same evolutionary track with $M = 1.13 M_\odot$, $Z = 0.019$, and $X = 0.69$. a) $\tau = 1.38$ Gyr (MS), b) $\tau = 5.90$ Gyr (post-MS).

A useful measure of a mode is the dimensionless inertia, E , where the inertia is normalised to the surface displacement:

$$E = \frac{4\pi \int_0^R [|\tilde{\xi}_r(r)|^2 + l(l+1)|\tilde{\xi}_h(r)|^2] \rho_0 r^2 dr}{[|\tilde{\xi}_r(R)|^2 + l(l+1)|\tilde{\xi}_h(R)|^2]} = \frac{M_{\text{mode}}}{M}, \quad (2.13)$$

where M_{mode} is defined as the modal mass. The normalized mode inertia, E , will be used in the discussion in Chapter 4. According to this definition, if a mode has most of its energy at the surface, the normalised inertia will be small. This is the general case for p

modes. On the other hand, when most of the energy is confined to the central regions in the star, as for the g modes, the displacement amplitude at the surface will be small, and hence the normalised inertia will be large. This definition helps us determine which modes have a mixed character, as for the mixed modes normalised inertia is larger than that of pure p modes (see Fig. 4.10) due to the fact that the mixed modes have g-mode character in the centre, hence large amplitudes in the central regions.

2.1.4 Characteristics of solar-like oscillations

Solar-like oscillations observed in the solar-like stars are mostly of low degree and high order (hence high frequency), and they are almost regularly spaced, so they can be studied under some simplifications. The parameters defined in this subsection reflect the characteristics of these observed modes, which satisfy the following asymptotic relation (for a detailed discussion, see, e.g, Tassoul (1980)).

$$\nu_{nl} \sim \Delta\nu \left(n + \frac{l}{2} + \alpha \right), \quad (2.14)$$

where ν_{nl} is the cyclic frequency of a mode with spherical degree, l , and radial order, n , related to the angular frequency ω as $\nu = \omega/2\pi$; α is a phase depending on the near-surface structure; and

$$\Delta\nu \simeq \left(2 \int_0^R \frac{dr}{c} \right)^{-1}, \quad (2.15)$$

which is the inverse of the time it takes sound to travel across the stellar diameter.

This spacing, with which the high-order frequencies are ordered, is called the large frequency separation, and is a function of the individual frequencies of a given l as

$$\Delta\nu_{nl} = \nu_{nl} - \nu_{n-1l}. \quad (2.16)$$

The sound travel time across the star roughly corresponds to the dynamical time scale given as:

$$t_{dyn} \simeq \left(\frac{R^3}{GM} \right)^{1/2} \simeq (G\bar{\rho})^{-1/2}; \quad (2.17)$$

hence, the observed large frequency separation directly gives us a measure of stellar density in terms of solar mean density (equation 2.18), which is a widely-used scaling relation (see, e.g., Kjeldsen & Bedding (1995)).

$$\frac{\Delta\nu_{\text{star}}}{\Delta\nu_{\odot}} \simeq \sqrt{\frac{\bar{\rho}_{\text{star}}}{\bar{\rho}_{\odot}}} \quad (2.18)$$

Another useful measure extracted from solar-like spectra is the so-called small frequency separation, given as:

$$\delta\nu_{nl} = \nu_{nl} - \nu_{n-1,l+2}. \quad (2.19)$$

According to the asymptotic theory, equation 2.19 can be written as

$$\delta\nu_{nl} \simeq -(4l + 6) \frac{\Delta\nu}{4\pi^2\nu_{nl}} \int_0^R \frac{dc}{dr} \frac{dr}{r}. \quad (2.20)$$

What equation 2.20 corresponds to is that when the sound speed is increasing with r , it contributes as a decrease in $\delta\nu_{nl}$. As the star evolves, the helium mass fraction increases inside the core due to nuclear fusion, thus the sound speed decreases close to the center, implying that there exists a positive sound speed gradient with increasing r . Hence, the small frequency separation decreases with increasing age.

2.2 Observational overview

Solar-like oscillations are observed through either high-precision space photometry, which measures changes in brightness at the stellar surface, or ground-based spectroscopy, which measures the radial velocity of the stellar surface through Doppler-shifted spectral lines. Both types of data can be converted into a frequency spectrum from which the resonant frequencies of the oscillations may be extracted.

2.2.1 Oscillations in the Sun

Oscillations with ~ 5 minutes period were first detected in 1961 by Leighton (Leighton et al. 1962), and their global nature was confirmed in 1979 by the Birmingham group (Claverie et al. 1979). It is now known that the Sun oscillates globally with many simultaneous modes. The period of oscillations vary between 3 and 15 minutes with an average of 5 minutes. The amplitudes are relatively small, the largest being $\sim 20 \text{ cm s}^{-1}$ for radial velocity measurements, and a few parts per million (ppm) for intensity measurements. Since the first detection of these oscillations, there have been dedicated ground-based networks, like BISON (Birmingham Solar Observations Network, Elsworth et al. 1995) and GONG (Global Oscillation Network Group, Harvey et al. 1996), and space missions, like the SOHO (Solar and Heliospheric Observatory, Domingo et al. 1995) spacecraft.

Fig. 2.2 provides an example for the amplitude spectrum of the full-disk solar oscillations corresponding to 30-day observations by VIRGO instrument on SOHO. Oscillation modes appear as strong peaks with the frequency of the maximum power corresponding to 3 mHz. The average mode parameters like $\Delta\nu$ and $\delta\nu$ as defined in Section 2.1.4 are very useful in interpreting the solar-like oscillations. Fig. 2.3 is a close-up of the solar amplitude spectrum illustrating these parameters.

As will be shown with examples of individual stars in Chapter 4, for the purpose of comparing the observed and calculated frequencies, we make use of the so-called échelle diagram (see, e.g. Grec et al. (1983)), which is formed by cutting the frequency spectrum into pieces of size $\Delta\nu$ and stacking them on top of each other (by plotting frequency versus frequency modulo $\Delta\nu$). This roughly aligns the frequencies with the same spherical degree, l . Fig. 2.4 is an example of an échelle diagram for a zero age main sequence (ZAMS) model

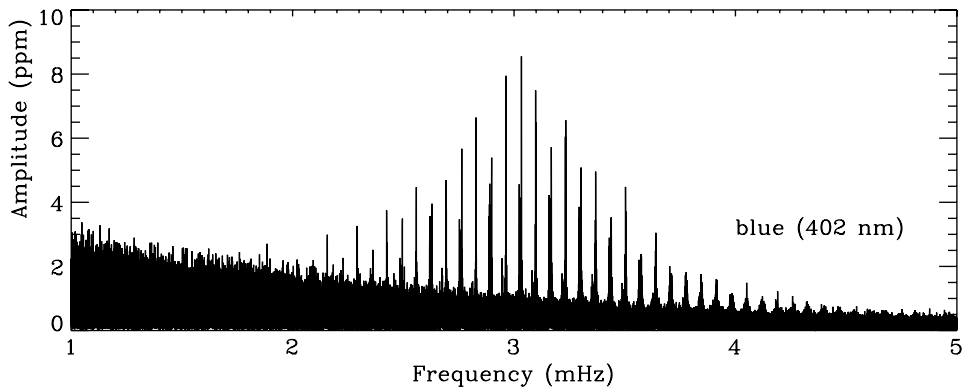


Figure 2.2: Amplitude spectrum of the full-disk solar oscillations corresponding to 30-day observations by VIRGO instrument on SOHO. Figure from Bedding & Kjeldsen (2003).

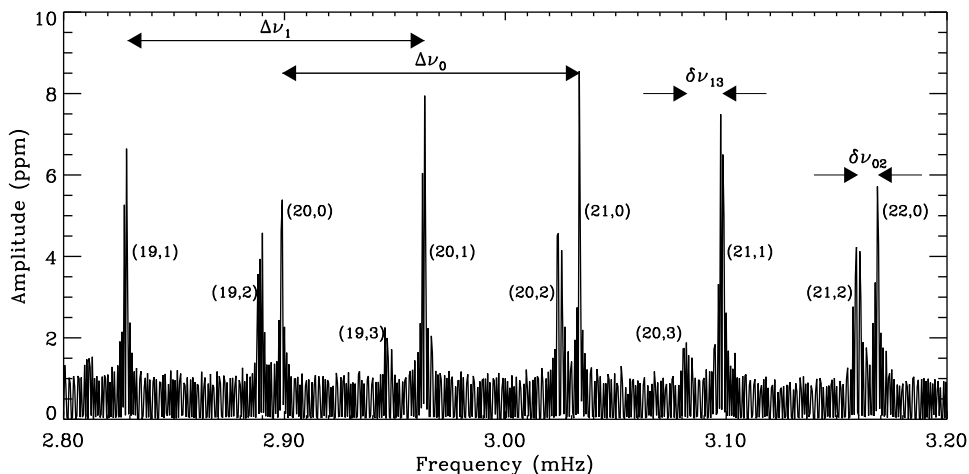


Figure 2.3: Close-up of the solar spectrum given in Fig. 2.2, with the mode labels (n, l) . The large and small frequency separations are indicated with the arrows. Figure from Bedding & Kjeldsen (2003).

with 1.08 solar mass. The large and small frequency separations are indicated with arrows. The regularity of the pattern seen in Fig. 2.4 will turn into being rather complicated for evolved stars due to the mixed modes as will be seen in Chapter 4 for specific cases – β Hydri and KIC 11026764.

Helioseismology has brought substantial new insight on the solar interior. The huge success in the field was followed by the application of the helioseismic methods to the other solar-like stars. Hence asteroseismology, the field that probes the stellar interiors through the observed stellar oscillations, was developed. The progress in asteroseismology is very

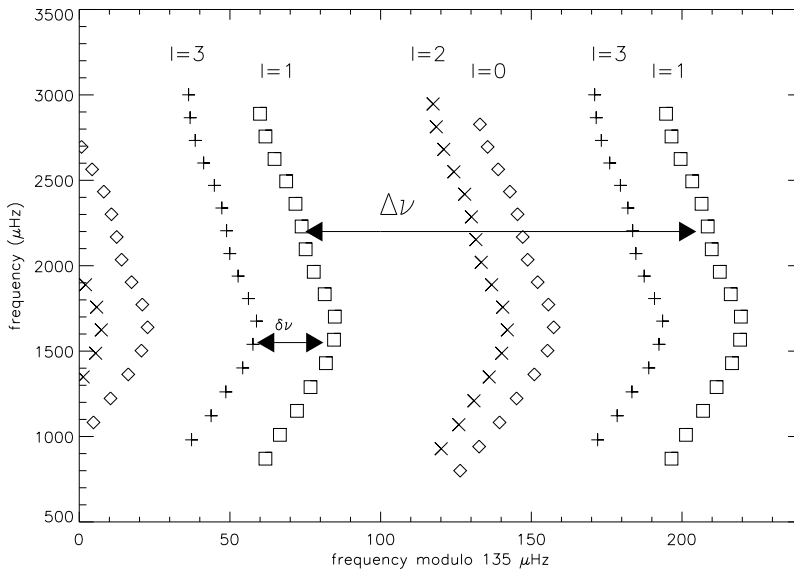


Figure 2.4: Échelle diagram for a 1.08 solar mass ZAMS star

fast due to the applicability of already developed helioseismic tools to asteroseismology. The data we currently obtain is higher quality than ever, especially thanks to the recent space missions like COROT (Baglin et al. 2002) and *Kepler* (Koch et al. 2010), thus we are in a very fruitful era of asteroseismology. In the next subsections, the observations of solar-like oscillations in other stars than the Sun are briefly discussed.

2.2.2 Solar-like oscillations in solar-like stars

An indication of the existence of solar-like oscillations in another star was first seen in α CMi (Procyon) by Brown et al. (1991). On the other hand, individual oscillation frequencies were first detected in η Bootis by Kjeldsen et al. (1995). These detections were later confirmed together with solar-like oscillations in some other stars including α Cen A&B, β Hydri, etc. (See Bedding & Kjeldsen 2003 for a summary). Fig. 2.5 shows the spectra of a sample of these solar-like oscillators. It should be noted that for all the solar-like stars other than the Sun, the disability to resolve the stellar disk results in the geometric cancellation of the amplitudes of the modes with $l > 3$.

In order to detect the solar-like oscillations firmly, observers put much effort into increasing the quality mainly through the multi-site campaigns. They developed techniques to combine and analyse these data obtained through several telescopes located in different continents. An upcoming project which is partly dedicated to these kind of multi-site observations is SONG (Stellar Observations Network Group, Grundahl et al. (2008)), which is a network that is planned to be composed of several telescopes placed in both hemispheres for a continuous sky coverage. The first of these will start to operate in 2011. To date

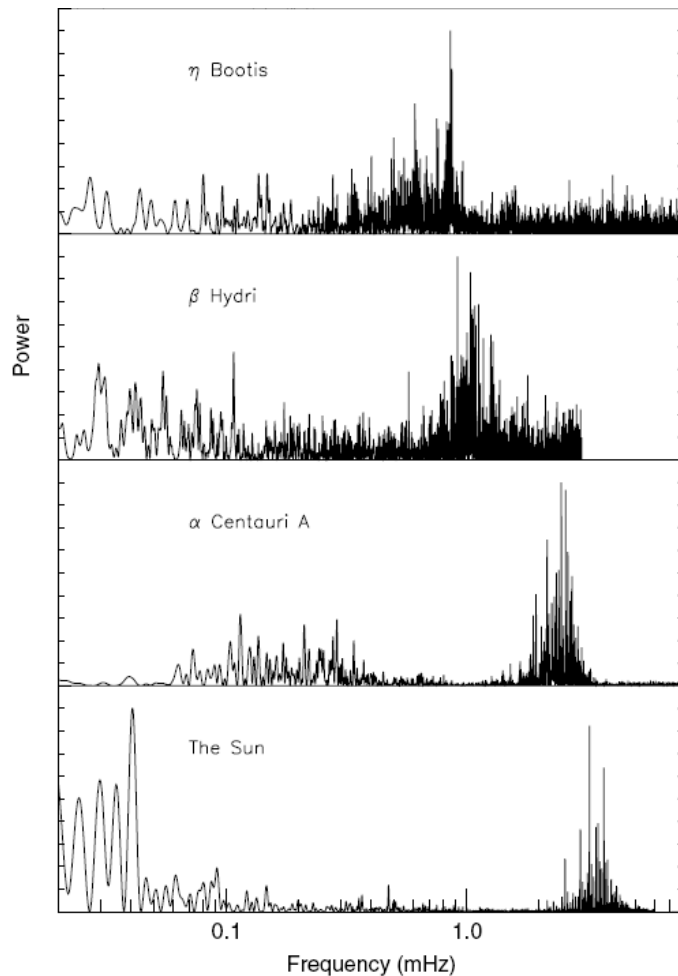


Figure 2.5: Power spectra showing solar-like oscillations in some solar-like stars. Figure from Bedding & Kjeldsen (2003).

there is a large sample of solar-like stars in which solar-like oscillations have been detected, thanks to the space missions like *COROT* and *Kepler*.

2.2.3 Solar-like oscillations in other stars

The only other type of stars in which the solar-like oscillations have so far been detected are the red giants (see De Ridder et al. (2009) for an overview). There are other candidates that are searched for solar-like oscillations in addition to their detected classical oscillations, such as δ Scuti stars (see, e.g., Samadi et al. (2002)). The first true detection of these will be very exciting, if accomplished.

Chapter 3

Modelling Solar-like Oscillators

A stellar model consists of a set of parameters – such as the density, mass, temperature, pressure, chemical composition, etc. – as a function of distance, r , from the stellar centre. There are of course many ingredients to simulate the structure and evolution of a star such as the nuclear energy generation rates, transportation of the energy from centre to the surface, equilibrium conditions, boundary conditions, etc. There are many simplifications, and some of the poorly understood mechanisms – such as convection – are often represented with a parametrization. The models for the solar-like stars are based on the solar models, which are calibrated such that a model with one solar mass will have the solar radius and luminosity at approximately the solar age obtained through meteoritic determinations. This calibration yields reasonable models for other stars as the mentioned properties are known to high precision for the Sun. For the interpretation of the solar-like stars, we often make use of the homology relations implying that some certain properties of the stars within a reasonably localised region around the Sun in a parameter space consisting of temperature, luminosity, etc. can be estimated using scaling relations with respect to the Sun (see, e.g., Kjeldsen & Bedding 1995). These relations, however, should be tested for a large sample of stars. Some specific ingredients of the models and some of the simplifications will be discussed in the following sections.

3.1 Observational constraints

To compute a stellar model, we first need to have some observational constraints to locate the star with respect to the Sun in the parameter space. These constraints can be grouped under two categories: asteroseismic and non-asteroseismic observational constraints, which are discussed in the following.

Non-asteroseismic constraints

The non-asteroseismic constraints available for a star depend mainly on the distance of the star. For many distant stars these constraints include the classical atmospheric parameters of the star; i.e, the surface values of temperature, gravity, and the chemical composition.

These can be determined through the observations of spectral lines or photometric observations. In certain cases when the star in question is relatively close, the size of the star can also be determined through the observed parallax and the angular diameter, then we can also calculate the stellar luminosity. A more direct measure of luminosity comes from the bolometric flux and the parallax. If the star is known to be in a binary system, the mass of the star can additionally be determined through astrometry. See Bruntt et al. (2010) for a recent determination of fundamental parameters for several bright stars.

The classical understanding of stellar modelling would then be to compute models that have parameters within the uncertainty limits of the observed parameters. This is often referred to as the HRD analysis, where HRD stands for the Hertzsprung-Russel Diagram, which shows the luminosity versus effective temperature of the stars, which is a good way to group different types of stars. However, from the point of view of modelling, there is some degeneracy involved when we are dependent only on the position in the HRD, i.e.; a certain point in the HRD can be maintained by using different combinations of stellar parameters (see Section 3.3).

Asteroseismic constraints

The asteroseismic constraints are specific parameters of the oscillation modes. These include at least the average parameters such as the large and small frequency separations defined in Section 2.1.4, and, with the increasing quality of the data, the individual frequencies, mode amplitudes and linewidths, etc. The sensitivity of the average large and small separations to the various characteristics of the star was discussed in the previous chapter. In the context of modelling, these can be used to plot the asteroseismic H-R Diagram (also known as the C-D Diagram; see, e.g., Christensen-Dalsgaard (1988, 1993)) from which the mass and the age of the star can, in principle, be determined – although with large uncertainties due to other parameters like element abundances. If, in addition we have the individual frequencies, we can place additional and stronger constraints on the stellar models. Each mode with frequency ν_{nl} penetrates to a different depth and hence involves a different region inside the star. Therefore, individual frequencies carry invaluable information as will be further discussed in Chapter 4.

3.2 Input physics

The stellar models for the solar-like oscillators are based on the solar models as mentioned above. Some of the models, which neglect complicated processes as diffusion, core overshooting, etc. are conventionally referred to as "standard" models. The current codes that are widely used usually allow the computation of non-standard models as well, but usually starting with a search involving standard models is reasonable in order to gain computation time. Further refinement of the model parameters should test the effects of the remaining complications.

In what follows I briefly discuss the ingredients of the stellar evolution code. The discus-

sion is based on my experience with ASTEC (Aarhus STellar Evolution Code, Christensen-Dalsgaard (2008a)). The numerical aspects and other details of ASTEC and ADIPLS (Aarhus Adiabatic Pulsation Package) are given by Christensen-Dalsgaard (2008a) and Christensen-Dalsgaard (2008b)

Equation of state

Stellar models are computed under the assumptions of hydrostatic and thermal equilibrium. It is the equation of state (in the form of $\rho(p, T)$) that completes the relations between the fundamental variables in a stellar model – density, temperature, and pressure. The temperature gradient is given by the equation of energy transport, and the relation between p and ρ is given by the hydrostatic equilibrium as:

$$\frac{dp}{dr} = -\frac{Gm\rho}{r^2}. \quad (3.1)$$

EOS is essential for the solution of equation 3.1. Hence it is one of the crucial ingredients of microphysics used to determine the stellar structure. In addition, oscillation frequencies depend on the density profile in the star. Effects of using different equation of state tables on the resulting oscillation frequencies are investigated for the case of the Sun by Christensen-Dalsgaard & Däppen (1992). I have mostly made use of the most up-to-date OPAL 2005 EOS tables Rogers & Nayfonov (2002).

Opacity

Opacities are strongly related to the temperature profile, hence also affect the sound speed and consequently the frequencies. Effects of opacity on the solar structure were investigated by Tripathy & Christensen-Dalsgaard (1998). Opacities are calculated for particular choice of the chemical element abundances. Our estimates of chemical composition depend on the solar composition we adopt. There has been significant disagreement in different determinations of the solar composition (see, e.g., Grevesse & Noels (1993); Asplund et al. (2005, 2009)). It was shown, e.g., by Christensen-Dalsgaard & Houdek (2010), that the latter abundances, which support a lower metallicity (Z/X), do not agree with the helioseismic determinations of the sound speed as well as does the former one, unless there is a substantial increase in the opacities (Christensen-Dalsgaard et al. 2009).

Convection

Convection in the stars is most commonly treated according to the mixing length theory (MLT) (Böhm-Vitense 1958). This theory involves parametrization of the average length that an amount of fluid can move without mixing with the surrounding. This mixing length is taken to be proportional to the pressure scale height as $l_{\text{MLT}} = \alpha_{\text{MLT}} H_p$. The proportionality constant, α_{MLT} , referred to as the mixing length parameter, is chosen prior to the computation.

Although this is a widely used treatment, it is far from representing the real physical picture. There are ongoing efforts, however, to develop more realistic 3D hydrodynamical simulations of the surface layers. Recently Trampedach (2010) has provided a comparison of the existing 1D and 3D formalisms.

Diffusion and gravitational settling

These mechanisms are usually neglected in the simplified standard models. However, it is crucial in the correct determination of the surface chemical composition. When included, gravitational settling refers to settling of heavier elements towards deeper regions in the star and rising of light elements like hydrogen to the surface. Diffusion acts roughly in the opposite direction resulting in smoother gradients in chemical composition. In ASTEC, diffusion is treated largely according to Michaud & Proffitt (1993).

For the case of the Sun, the inferred sound speed using the observed frequencies is shown to be in better agreement with the sound speed in the calculated models when diffusive processes are included (see, e.g. Christensen-Dalsgaard et al. 1993). This suggests that we should include these processes in the model calculations for the solar-like stars. They are, however, usually ignored due to the fact that the uncertainties in the observed frequencies are larger than those for the observed solar frequencies; however, the effects should be investigated when using high precision data. On the other hand, in the stars with very thin envelopes, the surface metallicity decreases very fast when settling is included, leaving nothing but hydrogen on the surface at early stages of evolution. Hence one needs to consider other mechanisms in these stars, such that an additional circulation of elements will result in a surface metallicity compatible with the observations.

Nuclear reactions

The nuclear parameters in ASTEC have been largely based on Parker (1986). However, it is possible to switch between several other nuclear reaction rates (e.g., Adelberger et al. 1998; Angulo et al. 1999). The choice mainly affects the time of main sequence evolution depending on the of p-p (or CNO) rates.

3.3 Implications of initial parameters on the resulting models

As mentioned above, many stellar models that are evolved with different initial parameters can be at exactly the same location in HRD. This degeneracy in the parameter space is partly illustrated in Fig. 3.1. Over the last two decades, asteroseismic modelling efforts have brought new insight on the problem. When, in addition to the non-seismic observables, we have seismic observables, we can place additional constraints on the stellar models. This is due to the fact that the oscillation frequencies of the models within a range of given parameters in HRD are expected to be different depending on the structure of the

star. Thus the degeneracy is partly lifted by using the seismic constraints. Effects of changing the initial parameters on the resulting evolutionary tracks are discussed briefly in the following subsections.

Asteroseismic modelling hence involves not only searching for a model that has the same global properties as the observed star, but also a model that would oscillate with the same frequencies as those of the observed star, and thus the precision of the results increase. This is done through the comparison of the computed oscillation frequencies of a stellar model with the observed stellar oscillation frequencies.

Mass and initial chemical composition

Increasing the mass of a given model increases the luminosity of the model, thus the entire evolutionary track will be shifted upwards to higher luminosity if the mass is increased, and vice versa.

The most important uncertainty in the optimization of parameters involves the mass and chemical composition, mainly the helium abundance (see Fernandes & Monteiro 2003 for a discussion in the context of modelling β Hydri). Luminosity of a given model can be reproduced by a less massive model having a higher helium mass fraction Y . Similarly, keeping the mass fraction of heavy elements, Z , constant and decreasing hydrogen mass fraction, X , or keeping X constant and decreasing Z has the same effect. The measure of metallicity that can be obtained through observations is the ratio of heavy elements to hydrogen. Therefore, to maintain a specific position on HRD, one can adjust Y keeping the Z/X fixed. Nevertheless, it is not trivial to select the best model in a case where the calculated frequencies of two models with different Y are very similar (see the discussion for the star KIC 11026764 in Chapter 4).

Fig. 3.1 shows only few of the possible tracks that lay inside a given observational error box (corresponding to the observational uncertainties of Procyon, see Appendix E); there are many more combinations of initial parameters to place the evolutionary track in the desired location. This shows that we definitely need the asteroseismic constraints to determine the evolutionary status of the star, as, for instance, in the right panel there exist eligible models both in main sequence (MS) and post-MS stages. However, when we have the observed frequencies, we have additional constraint on the mean density of the star, hence on the radius, as discussed earlier.

Mixing length parameter

The effect of an increase in this parameter in the HR diagram is seen as a shift of the track to higher temperature, i.e. a given luminosity is reached at a smaller radius (higher temperature). This is seen as a horizontal shift in the right panel of Fig. 3.1. For stellar case, it is not really possible to determine an accurate value of this parameter. In the solar case, however, the calibration of the mixing length parameter is done such that the solar model has the desired radius at the desired age.

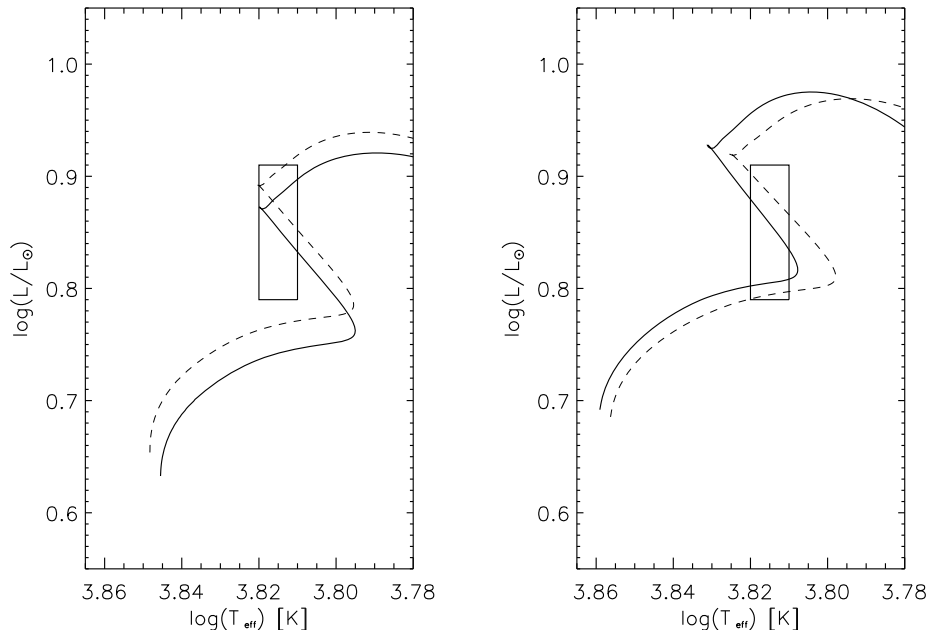


Figure 3.1: HR Diagram for several models evolved with different initial parameters. The rectangular box demonstrates a set of observational uncertainties. Only four of the various tracks are shown, which have both MS and post-MS models lying in the observational error box. In the left panel solid line shows the evolutionary track of a model with $M = 1.430 M_{\odot}$, $Z = 0.018$, $X = 0.70$, $Y = 0.282$, and $\alpha = 1.75$, whereas the dashed line shows a model with $M = 1.470 M_{\odot}$, $Z = 0.017$, $X = 0.72$, $Y = 0.263$, and $\alpha = 1.75$. In the right panel the solid line shows a model with $M = 1.475 M_{\odot}$, $Z = 0.018$, $X = 0.70$, and $\alpha = 2.15$, while the dashed line shows a model with $M = 1.470 M_{\odot}$, $Z = 0.018$, $X = 0.70$, and $\alpha = 1.75$.

Convective overshooting parameter

Convective overshooting takes place when the convective movements in the core (or envelope) cause extra mixing beyond the border of the convection zone. Similar to the mixing-length treatment of the convection, overshooting distance is taken to be proportional to the pressure scale height, with the proportionality constant α_{ov} .

The core overshooting process changes the structure of the central region by mainly bringing more hydrogen to the core and hence prolonging the H-burning phase, which consequently affects the age of the model. It also has an impact on the position of the peak in the buoyancy frequency, which implies a potential effect on the frequencies.

3.4 The Methods Used for Modelling

There are several methods of asteroseismic modelling. These differ with respect to the input observational constraints to be used, computational time that is required, level of precision that is provided, etc. The choice of the suitable method should be based on the

specific goals.

As mentioned before, the C-D diagram can be used to get estimates of the mass and age of the star. This diagram consists of intersecting lines of mass and central hydrogen abundance for fixed chemical composition (Fig. 3.2). The observables used as input are the large and small frequency separations. Although the uncertainty of the result is large when only one set of element abundances is used, one can investigate the effects of changing the chemical composition, the input stellar physics, etc. This is a good method when comparing a large sample of stars.

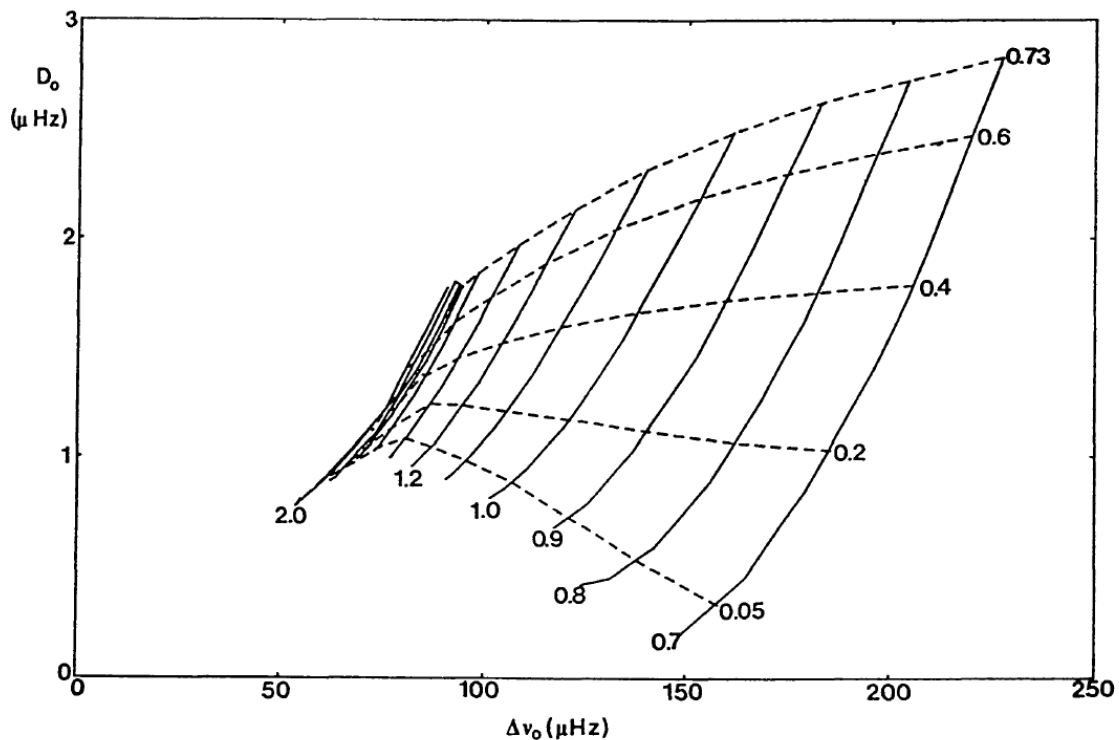


Figure 3.2: Evolution tracks (solid lines), and curves of equal central hydrogen abundance for $Z = 0.02$. Masses are indicated in solar units, and the values of central hydrogen abundance are given as the mass fraction. $\Delta\nu_0$ and D_0 represent the large frequency separation for $l = 0$, and a measure for small frequency separation for $l = 0$ & 2, respectively. Figure from (Christensen-Dalsgaard 1988).

Another approach involves pipeline analyses which are mostly based on pre-computed large grids of stellar models (Stello et al. 2009). Using the non-seismic observational constraints and the average seismic parameters, one can obtain the mass, radius, age, etc. of the star with increased precision when compared to the results of the C-D diagram, provided the pre-computed grids take into account a large enough number of combinations of mass, chemical composition, etc.

There are also other pipeline analyses which do not depend on pre-computed grids, but instead do compute models along the way, and decide which way to proceed in the parameter space, making use of some statistical judgement (see Bazot et al. 2008; Metcalfe et al. 2009). These are expected to reach a global solution in a longer time than that required for the pipeline analysis based on the ready grids (excluding the grid computing time, as the same grid will be used for many stars in question). Nevertheless, the precision of the result is expected to be higher and the freedom of altering the input parameters and input stellar physics is an advantage.

The last method I will mention is computing specific small grids for each star of interest. The advantages are the ability to increase the resolution of the grid as desired, and the freedom of altering the input physics and parameters. On the other hand, it may become a little too time consuming when we do not have reasonable constraints, so, it is more convenient to use this method when there is some constraining information, for instance, obtained through fast pipelines. Nonetheless, such a method, based on the comparison between the individual observed and model frequencies, results in the best matches, though only for a small number of stars. I have mainly used this method in my modelling work, and will continue the discussion on this basis.

Using the available non-seismic observations together with their uncertainty limits, the position of the star is determined in the relevant parameter space. To increase the reliability of the solution, we compute grids of evolutionary tracks that would include models having parameter values that are within $3\text{-}\sigma$ around the determined position of the star, where σ is the uncertainty in the observations. We then need to determine the parameters to be varied in the grid; the basic ones are the mass, Z/X , Y , and α_{MLT} . Diffusion & settling, and convective overshoot can optionally be included.

If an estimate for the stellar mass is not available, first a low-resolution grid is computed covering a large range in mass, to determine a reasonable range likely to host the representative models for the star in question. This determination is based on the comparison with the model frequencies and the observed frequencies. The oscillation frequencies are calculated for those models located within the $3\text{-}\sigma$ uncertainty limit of the observations. We apply some corrections to the model frequencies before comparing to the observed ones; these will be discussed in the following section. Making use of our knowledge on the correlations between the parameters and their effects on the resulting models, as discussed above, further grids are computed. The resolution (inverse of the size of the steps between the grid points in terms of the input parameters, such as the mass M) is increased in the following grids that are computed varying mass, metallicity, etc., while the total range for each parameter is constrained further as we approach the global minimum.

To evaluate the goodness of the fit at each stage, χ^2 -minimization is used in the form given in equation 3.2. The choice of this method is based on the fact that it allows individual frequencies to have an impact on the result and also takes into account the uncertainties.

$$\chi^2 = \frac{1}{N} \sum_{n,l} \left(\frac{\nu_{\text{model}}(n,l) - \nu_{\text{obs}}(n,l)}{\sigma(\nu_{\text{obs}}(n,l))} \right)^2, \quad (3.2)$$

where, N is the number of frequencies included as constraints, $\nu_{\text{model}}(n, l)$, and $\nu_{\text{obs}}(n, l)$ are the model frequencies (including the corrections), and the observed frequencies, while $\sigma(\nu_{\text{obs}}(n, l))$ represents the uncertainty in the observed frequencies. The set (n, l) represents the modes with radial order n and degree l , however, n is only used to emphasize that *individual* frequencies of all available orders are included. The value of n , whenever given together with the observed frequencies, is not used as a constraint, as information on n is model-dependent and cannot be extracted from the observations alone. The spherical degree, l , however can be extracted from the data – often objectively with the exception of some complicated cases as will be discussed in the frame of Procyon in Chapter 4. So, for every set of calculated frequencies, my fitting algorithm finds the group of frequencies that are closest to the observed set with the given l . The χ^2 is then calculated as given in equation 3.2. I include only the individual frequencies in the χ^2 , not the average parameters, since the information on average large and small separations are already included in the frequencies. I also leave the non-seismic observables like temperature, $\log g$, etc. out of the χ^2 as the choice of the models for which the frequencies are calculated, have already been constrained by atmospheric parameters. Therefore, I prefer not to impose further constraints on these; I instead want to leave it to the frequencies to determine the best representative models. One can alternatively define a χ^2 including all the available observables, and assigning different weights to seismic and non-seismic constraints. However, it was shown by Metcalfe et al. (2010) that once we are in a region of somewhat accurately determined atmospheric parameters, the determination of the best representative model depends much more on the frequencies. In Chapter 4, in the frame of KIC 11026764, further constraints that are placed by the use of specific individual frequencies, such as "mixed modes", are discussed.

For the purpose of visualization of the result, we use the so-called échelle diagrams (see Section 2.2.1) as this is a way to illustrate clearly how well the fit is for large and small frequency separations, and for the individual frequencies, hence, it is very practical for seeing the match to the overall structure of the spectrum. Once we have a rough model with an échelle diagram which is more or less in agreement with the observed features, we focus on the detailed pattern of the frequencies, and try to fine-tune the model in a way to have a better agreement.

3.5 Modifications in relation to frequency calculations

Since asteroseismic modelling is performed through comparing the observed and calculated frequencies, and since the quality of the data has become much higher with the recent developments, it is now of priority to increase the accuracy of the calculated frequencies. In some cases this is difficult due to the shortcomings of stellar structure models. In this section two of the possible modifications in order to ease the comparison between frequencies of different models, as well as that between observed and model frequencies, are discussed.

3.5.1 A new identification scheme for the dipolar mode stellar oscillations

Dipolar modes of oscillation ($l = 1$) are of interest due to the fact that they are easily detectable and they are subject to some complications in terms of identification of the modes.

For the purpose of mode identification, we are interested in detecting the nodes of the radial displacement between the centre and the surface. Two variables of specific interest are then given as

$$y_1 = \frac{\xi_r}{R}, \quad (3.3)$$

where, ξ_r is the amplitude of the radial displacement, and

$$y_2 = x \left(\frac{p'}{\rho} + \Phi' \right) \frac{l(l+1)}{\omega^2 r^2} = \frac{l(l+1)}{R} \xi_h, \quad (3.4)$$

where primes are used to indicate the perturbed quantities, ω is the angular frequency of the oscillations, and ξ_h is the amplitude of the horizontal displacement. Following the definitions developed by Scuflaire (1974) and Osaki (1975), the radial order is determined as the difference of the number of p and g nodes. The nodes are assigned p (or g) label at each node as r increases, on the basis whether the phase point (y_1, y_2) crosses $y_1 = 0$ moving counter-clockwise (or clockwise). In this way p modes are assigned positive orders while g modes have negative orders. A so-called phase diagram is illustrated in Fig. 3.3.

However, it was shown by, e.g., Lee (1985) that this is not an efficient classification when the dipolar modes of an evolved star are concerned. Recently, Takata (2005) derived a relation (equation 3.5) specific to dipolar modes, using the conservation of momentum, and including the perturbation to the gravitational field:

$$p' + \frac{g}{4\pi G} \left(\frac{d\Phi'}{dr} + \frac{2}{r}\Phi' \right) = \omega^2 r \left[\rho \xi_r + \frac{1}{4\pi G} \left(\frac{d\Phi'}{dr} - \frac{\Phi'}{r} \right) \right], \quad (3.5)$$

where the primes indicate the Eulerian perturbation, p is the pressure, Φ the gravitational potential, ξ_r the radial displacement, ω the angular frequency of oscillations, and G the gravitational constant. The left hand side comes from the rate of change of momentum of a concentric sphere (M_r) in the star, dP_r/dt , while the right-hand side comes from the displacement of the centre of mass of the sphere, $\delta r_{\text{CM},r}$ (see Takata 2005 for exact expressions). The reason why this is specific only to dipolar oscillations is that in all the other oscillation modes, the surface integrals of spherical harmonics, Y_l^m , present in the expressions for dP_r/dt and $\delta r_{\text{CM},r}$ vanish, implying the centre of mass of each concentric mass, and hence of the star, is stationary. However, in dipole mode oscillations the centre of mass of concentric spheres at each radius is displaced, while the centre of mass of the star is stationary (for the derivation, see Christensen-Dalsgaard 1976).

Using the relation 3.5, Takata (2005, 2006) showed that an invariant mode labelling can be based on the pair of variables, y_1^a and y_2^a , given by equations 3.6 and 3.7.

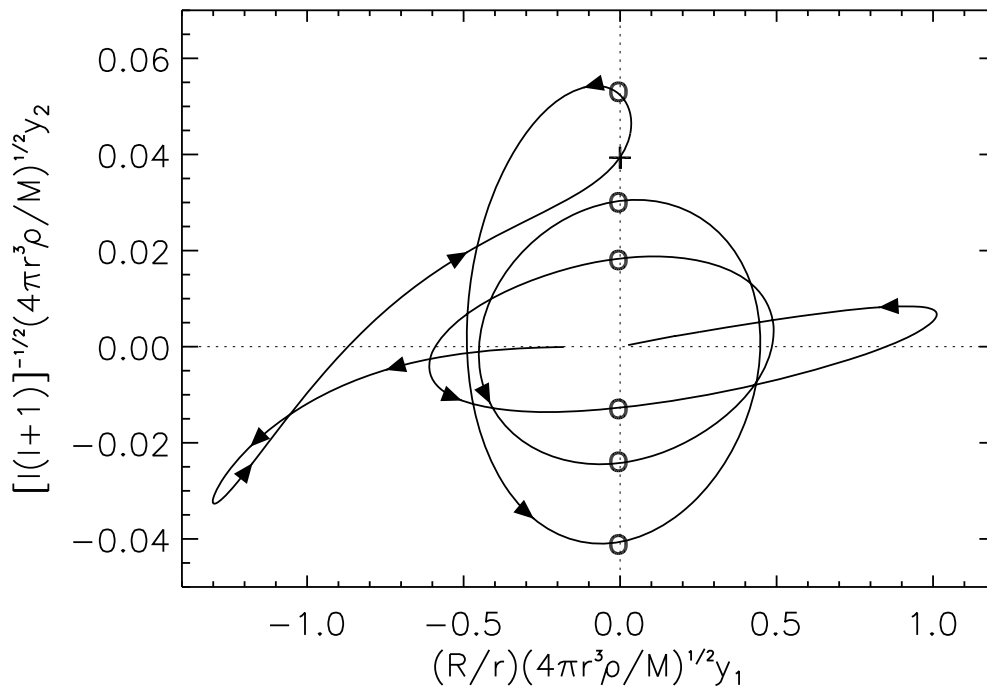


Figure 3.3: Phase diagram for a p mode with $l = 1$ & $n = 6$ of a post-MS model with $M = 1.08 M_{\odot}$, $Z/X = 0.018$, and $Y = 0.28$. p nodes are marked with circles, while the g node is marked with a cross. x-axis and y-axis represent the scaled vertical and horizontal displacements. The arrows indicate the direction of the movement of the phase point.

$$y_1^a = \frac{J\xi_r}{r} + \frac{1}{3g}\left(\frac{\Phi'}{r} - \frac{d\Phi'}{dr}\right), \text{ and} \quad (3.6)$$

$$y_2^a = \frac{Jp'}{\rho gr} + \frac{1}{3g}\left(\frac{\Phi'}{r} - \frac{d\Phi'}{dr}\right), \quad (3.7)$$

$$\text{with } J = 1 - \frac{\rho}{\rho_{r,\text{av}}} = 1 - \frac{4\pi\rho r^3}{3M_r}, \quad (3.8)$$

where $\rho_{r,\text{av}}$ is the mean density of the concentric mass, M_r , at radius r . The mode identification is then performed assigning p and g labels to the nodes as described before but this time for a phase point (y_1^a, y_2^a) . Using these new variables; $n = n_p - n_g$ if $n_p < n_g$, while $n = n_p - n_g + 1$ if $n_p \geq n_g$.

I have tested the applicability of this new mode identification scheme for stellar models, without going into much detail, so far. I have implemented this as an option in ADIPLS (Christensen-Dalsgaard 2008b). The scheme seems to work for stellar models with mass 1-5 M_{\odot} from main sequence through subgiant branch, though a more thorough analysis is

needed. Fig. 3.4 shows the phase diagrams plotted using the old (left panel) and the new variables (right panel) for the evolution of a stellar model with $1M_{\odot}$.

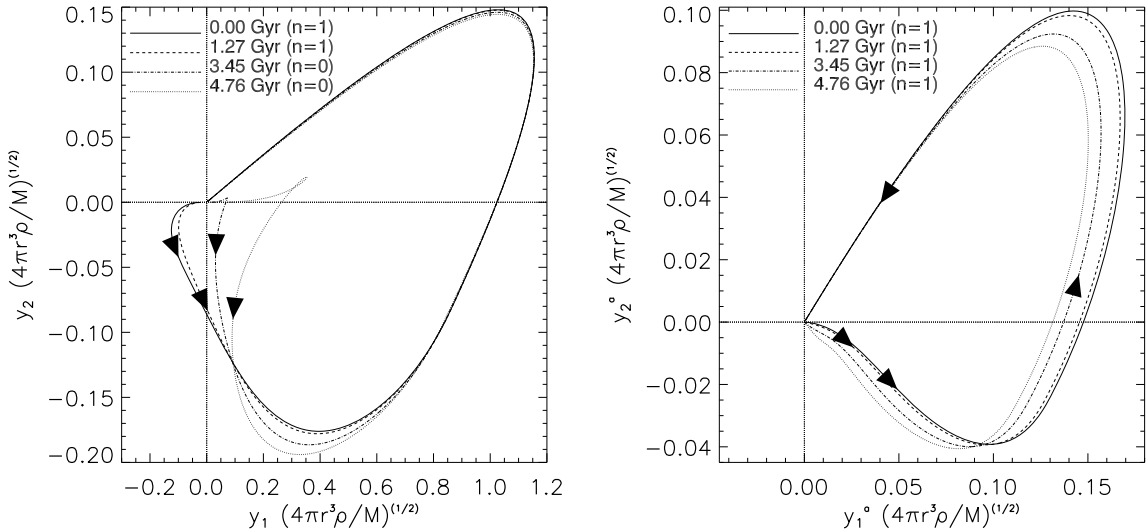


Figure 3.4: Evolution of an $l = 1$ mode for a model with $M = 1.0 M_{\odot}$, and metallicity $Z = 0.02$. The variables, y_1^a and y_1^b , are scaled for a more clear visualization. Starting from the origin, phase points move in the direction of the arrows. In the left panel, which is plotted using the conventional mode identification scheme, the modes do not preserve their label throughout the evolution, while in the right panel, which is plotted using the new mode identification scheme, an invariant mode classification is established. Figure from Doğan et al. (2008) (Appendix A).

It is seen in the left panel that using the conventional mode identification method, some modes that are p modes at the beginning of the evolution are shifted to be f modes as the star evolves. Having a dipolar f mode without a radial node ($n = 0$) in the vertical displacement, does not make sense physically since it corresponds to the shift of the centre of mass of the star (Christensen-Dalsgaard & Gough 2001). With the new classification scheme, however, the dipolar modes preserve their identifications along the evolution, without having a label with $n = 0$.

Using the new definition, the characteristic frequencies are modified as :

$$\tilde{S}_l^2 = S_l^2 J^2, \text{ and} \quad (3.9)$$

$$\tilde{N}^2 = \frac{N^2}{J^2}. \quad (3.10)$$

These corrected frequencies are plotted in Fig. 3.5. With this scheme, it is the corrected buoyancy frequency, \tilde{N}^2 , that determines the turning points of p modes, and corrected Lamb frequency, \tilde{S}_l^2 , determines the turning points of g modes.

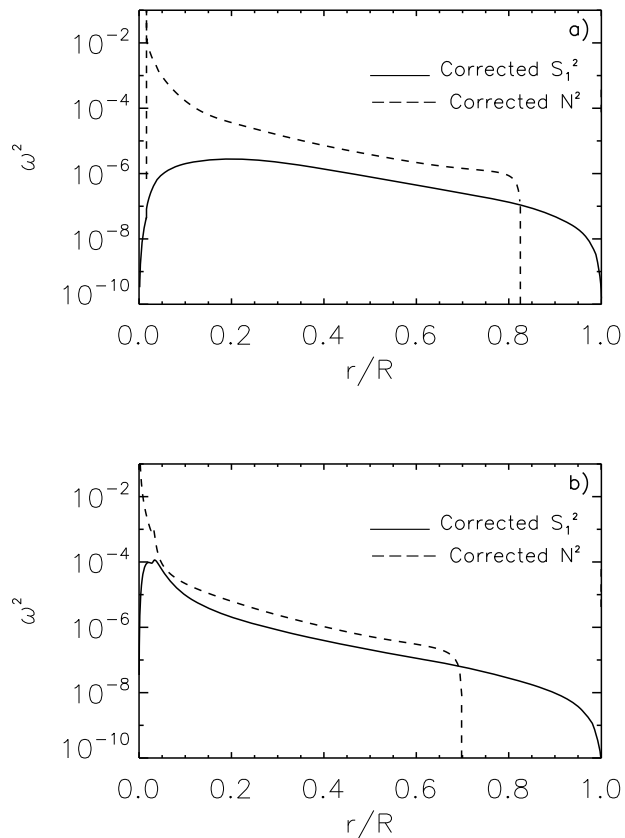


Figure 3.5: Corrected N^2 and S_l^2 for two models from the same evolutionary track with $M = 1.13 M_\odot$, $Z = 0.019$, and $X = 0.69$; a) $\tau = 1.38$ Gyr (MS), and b) $\tau = 5.90$ Gyr (post-MS). The models are the same as those used in Fig. 2.1

3.5.2 Near-surface effects on the frequencies

The turbulent convection in the outer layers of the solar-like stars is the source of stochastic excitation of the solar-like oscillations as discussed in the previous chapter. Nevertheless, we are far from completely understanding the physical picture. We simplify the convection treatment since turbulent convection is not trivial to model. Even the most widely used solar models suffer from improper modelling of the outer stellar layers. Hence there is an offset between the observed solar frequencies and the frequencies of the reference solar models. This offset is a systematic difference that increases with increasing frequency. This is due to the fact that upper turning points of the modes get closer to the surface as the frequency of the mode increases. As a result, the structure of the near-surface layers affects mostly the modes with high frequency.

Kjeldsen et al. (2008) showed that this systematic difference between observed and calculated frequencies for solar radial modes ($l=0$) (see Fig. 3.6) is well approximated by a power law given as

$$\nu_{\text{obs}}(n) - \nu_{\text{best}}(n) = a \left[\frac{\nu_{\text{obs}}(n)}{\nu_0} \right]^b, \quad (3.11)$$

where $\nu_{\text{best}}(n)$, and $\nu_{\text{obs}}(n)$ are the frequencies of the best model, and observations, respectively, a and b are parameters to be determined (see below), and ν_0 is a reference frequency chosen to be the frequency of the peak power, which is $3100 \mu\text{Hz}$ for the Sun.

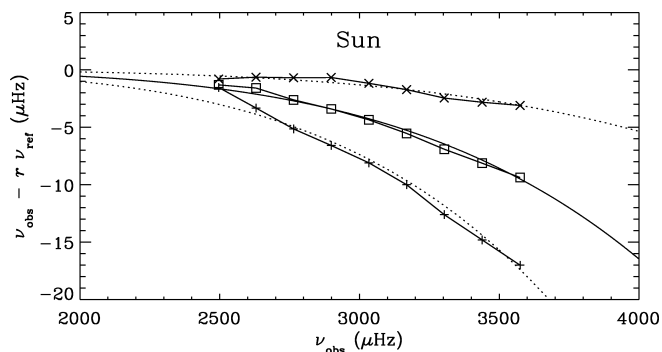


Figure 3.6: Difference between calculated and observed solar frequencies for radial modes with $n = 17 - 25$ (figure from Kjeldsen et al. 2008). Squares denote the frequencies of model S (Christensen-Dalsgaard et al. (1996)), crosses correspond to a younger model ($\tau = 2.25$ Gyr) in the same evolutionary track with model S, and pluses to a more evolved model in the same track ($\tau = 7.44$ Gyr). The solid and dotted curves correspond to the corrections calculated by the equation 3.14

Supposing we have a best model chosen to represent a star and a reference model having frequencies, $\nu_{\text{ref}}(n)$, close to those of the best model, $\nu_{\text{best}}(n)$, a scaling can be introduced as in equation 3.12, with the scaling factor, r , relating the mean densities of the models as in equation 3.13 (Kjeldsen et al. 2008).

$$\nu_{\text{best}}(n) = r\nu_{\text{ref}}(n) \quad (3.12)$$

$$\bar{\rho}_{\text{best}} = r^2\bar{\rho}_{\text{ref}} \quad (3.13)$$

Equations 3.12 and 3.13 suggest that in order to get the mean density of the star correctly, we need r to be as close to unity as possible. Kjeldsen et al. (2008) determined the value of the exponent b as 4.90 for the Sun, using the modes with $n = 17 - 25$ for model S (with $r = 1$). If we insert equation 3.12 into equation 3.11, we get

$$\nu_{\text{obs}}(n) - r\nu_{\text{ref}}(n) = a \left[\frac{\nu_{\text{obs}}(n)}{\nu_0} \right]^b. \quad (3.14)$$

Differentiating equation 3.14 with respect to n , and then combining the result with equation 3.14 we get an expression for r . Having b and calculating r , a can also be calculated using equation 3.14.

Kjeldsen et al. (2008) also showed that a similar offset is present in the differences between the observed frequencies of some other solar-like stars (α Cen A, α Cen B, and β Hydri) and the frequencies of their representative models. Hence, they suggested that the empirical power law derived to represent the high-frequency offset could be used to correct the model frequencies of other solar-like stars adopting the solar value of b . Following Kjeldsen et al. (2008), we use $b = 4.90$ in our calculations. Once we have r and a , we can correct the model frequencies using equation 3.14 (or 3.11 with $r = 1$). In our modelling of β Hydri and KIC 11026764, we followed similar approaches. The results after correcting the frequencies are shown in the next chapter, with illustrations on specific stellar models. Here we continue with the discussion of near-surface corrections using some solar models.

The Sun: Solar age and the near-surface effects

As discussed in the previous chapter, the change in the chemical composition in the stellar core along the evolution is reflected in the small frequency separation, $\delta\nu$. Therefore, $\delta\nu$ is often used for helioseismic solar age determinations through minimization of the difference between observed $\delta\nu$ and the $\delta\nu$ of the solar models (e.g., Dziembowski et al. (1999), Bonanno et al. (2002), Christensen-Dalsgaard (2009)). The age of the solar models selected as a result of this process is expected to be in agreement with the meteoritic solar age, determined by Wasserburg in Bahcall et al. (1995). It is usually the case except when the revised low metallicities (Asplund et al. 2005) are used (see, e.g., Christensen-Dalsgaard 2009). Another tool for age determination is the ratio of small to large separation. The separation ratios, defined as $r_{ll+2}(n) = (\nu_{nl} - \nu_{n-1l+2})/(\nu_{nl} - \nu_{n-1l})$, were introduced by Roxburgh & Vorontsov (2003) and were shown to be insensitive to the near-surface layers.

In order to test the reliability of the application of the near-surface correction, we checked whether we can reproduce the meteoritic solar age using the small separations after applying surface correction to the frequencies (Appendix B, Doğan et al. (2010b)). We computed a series of solar models (some modified versions of Model S (Christensen-Dalsgaard et al. 1996)) with different ages, but fixed values of radius, luminosity and Z/X at the surface, and adjusting the initial chemical composition and the mixing length parameter, α_{MLT} , in order to reproduce the fixed surface values at the given age. Our purpose was to determine the age of the model that would minimize the difference between the observed $\delta\nu$ and the $\delta\nu$ of the model, which was calculated after correcting the frequencies for the near-surface effects. We did this calculation for two different radii, and also using different nuclear reaction rates. We repeated the analysis with two different stellar evolution codes, one of them having the option of pre-main-sequence (pre-MS) calculation (GARSTEC, Weiss & Schlattl (2008)). We show that the results obtained using $\delta\nu$ after correcting the frequencies for the surface effects, and those obtained using the separation ratios are very similar. A more detailed and extended analysis may allow us to find out which reaction rates should be preferred, how one should determine the end point of pre-MS evolution,

3.5. MODIFICATIONS IN RELATION TO FREQUENCY CALCULATIONS

and what the time-scale is in the solar case.

Chapter 4

Results on Individual Solar-like Stars

This chapter gathers the results regarding the modelling of individual stars. My main interest has been mostly towards solar-like stars that are more evolved than the Sun. In the following sections I discuss how specific features of the data from these evolved stars can be used. The related manuscripts are attached as appendices. A list of collaborators for each project can also be seen in the corresponding appendix.

4.1 β Hydri

β Hydri is a subgiant star of spectral type G2, and is referred to as the future of the Sun, as its mass is very close to the solar mass and it is more evolved than the Sun. It shows solar-like oscillations (Bedding et al. 2001, 2007), therefore it has been subject to many seismic investigations (e.g. Di Mauro et al. (2003); Fernandes & Monteiro (2003); Doğan et al. (2010c, Appendix C); Brandão et al. (2010, Appendix D)). It is among the few stars in which solar-like oscillations have been observed from the ground (others include, e.g., η Bootis, α Cen A & B, and Procyon A). Here I present results of modelling efforts in which I was heavily involved. In Section 4.1.1, I summarize the work done through grid-computing approach, while there are two appendices (C and D) including more details on this. I continue with discussing the modelling results from another approach – a more automated analysis – in Section 4.1.2 (Doğan et al., in preparation).

4.1.1 β Hydri with grid-computing approach

β Hydri has guided us through developing the methods for modelling as discussed in Chapter 3. This is the first modelling work where the parametrized correction for the near-surface effects has been applied to the model frequencies, and we show this yielded a very good match. Thanks to the dual-site observations, the data have allowed us for one-to-one comparison between the observed and the model frequencies.

The reason for the inclusion of the surface effects in the form of a parametrization is that the difference between the observed and model frequencies can be expressed by a

power law for the Sun and potentially for the other solar-like stars as proposed by Kjeldsen et al. (2008) and discussed in Section 3.5.2. Fig. 4.1 shows the case for a representative model of β Hydri, which follows well the power law fit. If we correct the model frequencies for this effect, then it gets more reasonable to compare with the overall observed frequency pattern.

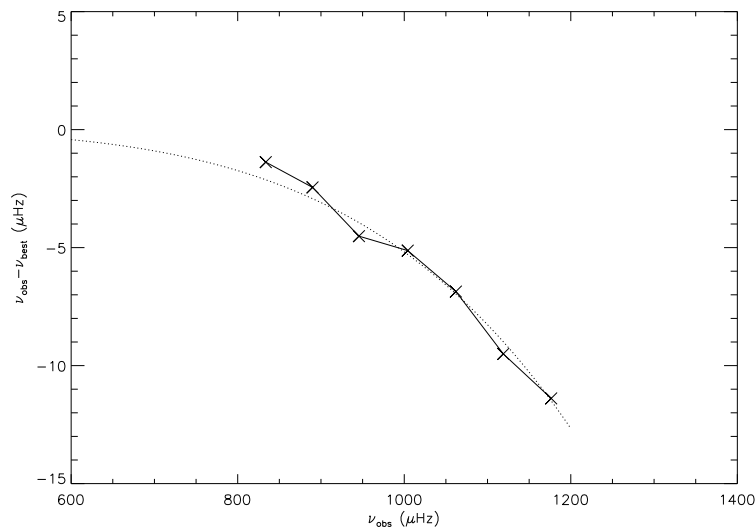


Figure 4.1: Frequency difference between the observed and model frequencies for a selected post-MS model of β Hydri with $M = 1.08 M_{\odot}$, $Z/X = 0.018$, $Y = 0.28$. The dotted curve represents the power-law fit parametrized by Kjeldsen et al. (2008)

This empirical solution to the problem of improper modelling of the surface layers should be regarded as temporary. Nevertheless, working on a proper turbulent convection model is outside the scope of this thesis. Due to the nature of the power law, the low frequency modes are not altered much after the correction, which is good because they are more sensitive to the inner structure of the star. We also took care of the mixed modes, treating them differently than the pure p modes (Brandão et al. 2010). For this purpose, we scaled the correction with the inverse of the normalized mode inertia ratio (Q_{nl}) of a nonradial mode to that of a radial mode with the same frequency. This is a reasonable measure as Q_{nl} is high for the mixed modes, i.e. the expected amplitude at the stellar surface is lower than that of a pure p mode, so they should be less affected by the near-surface layers and hence the correction should accordingly be small (see Section 4.3.1 for details demonstrated on the *Kepler* star KIC 11026764). However, the mixed modes should still be subject to some correction when they are observed at the surface, where they take on p-mode character.

We have used the observationally determined position of β Hydri in the Hertzsprung-Russell Diagram (HRD), together with the seismic observations given in Table 4.1, and later on also with the values given in Table 2 of Appendix D. Making use of the parameters

given in Table 1 of Appendix D, we have computed several stellar evolutionary tracks. Following the method described before, we have calculated oscillation frequencies for the models positioned in the observational error box in the HRD, and applied the near surface correction to the frequencies. We then minimized the differences between the observed and corrected model frequencies in the form of a χ^2 -minimization. The best models properties from initial, and later, stages of our work can be seen in Table 3 of Appendix C, and in Table 5 of Appendix D, respectively, together with the échelle diagrams showing the quality of the fits (Figs 1 & 2 in Appendix C and Figs 2 & 3 in Appendix D. Fig. 4.2 shows the échelle diagrams of two models, one from an early work by Di Mauro et al. (2003), and another from our analysis presented in Brandão et al. (2010). The main reason I show these two is to emphasize the improvement in the data in less than a decade.

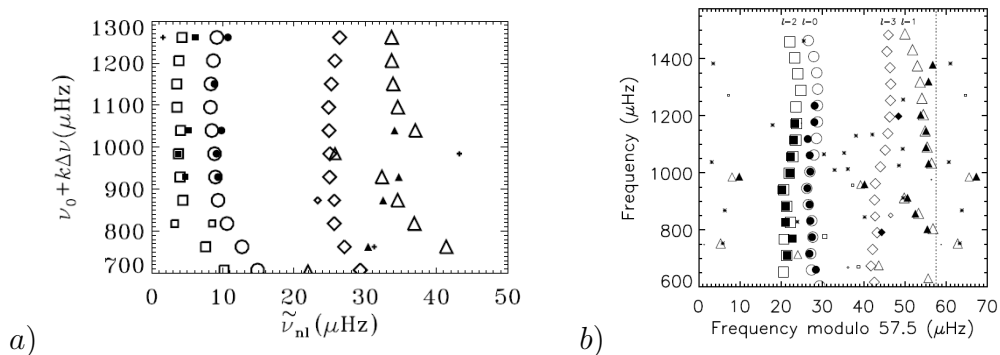


Figure 4.2: Échelle diagrams for the models with a) $M = 1.14 M_{\odot}$, $Z = 0.015$ (Di Mauro et al. 2003) and b) $M = 1.04 M_{\odot}$, $Z = 0.0124$, $Y = 0.30$ (Brandão et al. 2010). The filled symbols represent the observed frequencies, while the open symbols represent the model frequencies. Circles, triangles, squares, and diamonds are used for the modes with $l = 0$, $l = 1$, $l = 2$, and $l = 3$, respectively.

Moreover, the model in Panel (b) shows a remarkable match to the mixed modes in the observations. As discussed before, these modes have g-mode character in the centre, and hence are believed to carry signatures from the stellar core. Since the core is the region of nuclear reactions that drive the stellar evolution, the fundamental information we receive from the mixed modes is related to the evolutionary status of the star. Therefore, it is particularly important to find the models that reproduce the mixed modes together with all the other modes. In the next subsection I discuss the model-fitting results using another method.

4.1.2 β Hydri with AMP

Asteroseismic Modeling Portal (AMP) is a model-fitting pipeline that spans a very large parameter space in a time-saving manner. It makes use of a genetic algorithm, which is a good method for finding the global minimum in a large parameter space. The algorithm keeps the solutions (breeds) that provide a good match to the observations and then decides on which way to go depending on these. This is done through four simultaneous and

independent runs, which in the end cover a large range of initial parameters. The surviving solution globally minimizes the difference between the observables and the model properties (see Metcalfe et al. 2009 for details). After finding the global minimum, the local analysis is treated like a χ^2 -minimization problem, where models are evaluated with a higher resolution around the global minimum. The parameters optimized at the end of the whole search are mass (M), initial mass fraction of heavy elements and helium, Z and Y , and the mixing length parameter, α . The age of the model is optimized along each track by matching the observed large separation $\Delta\nu$. The parameter optimization with AMP takes around 1-2 weeks, and its advantage over the faster pipelines is that it includes all the individual frequencies in the comparison between the observations and models. This becomes very important, especially when the observed spectrum includes mixed modes as is the case for β Hydri. AMP was optimized using the solar data, and the motivation was to use it when a vast amount of Kepler data is available, which now is the case. We ran β Hydri through AMP several times to make the necessary modifications needed for a star other than the Sun given the uncertainties in the frequencies will be larger in the stellar case and what is known about a distant star is hardly close to the existing information about the Sun. Also, a subgiant would introduce different challenges – such as mixed modes – so we checked AMP for all these additional issues, using β Hydri, for which we already had matching models found through a grid-computing approach as discussed above.

The code has been optimized for the Sun, and it automatically applies the near-surface correction to the model frequencies as in equation 4.1, the right-hand side of which is the correction term to be added to the model frequencies before being compared to the observed frequencies,

$$\nu_{\text{obs}}(n, 0) - \nu_{\text{best}}(n, 0) = a \left(\frac{\nu_{\text{obs}}(n, 0)}{\nu_0} \right)^b, \quad (4.1)$$

where $\nu_{\text{obs}}(n, 0)$ and $\nu_{\text{best}}(n, 0)$ are the observed and best model frequencies with $l = 0$ and radial order n , ν_0 is a constant frequency – usually selected to be the frequency corresponding to the maximum power, a is a parameter to be determined for each model, and b is fixed to the value 4.82 (discussed later in the text).

However, for evolved stars that have mixed modes, one should apply a correction which is scaled in a way to be small for mixed modes, and larger for pure p modes. To achieve this, we scaled the correction with the inverse of the normalized mode inertia ratio (Q_{nl} , see Section 4.3.1) as:

$$\nu_{\text{best,corr}}(n, 0) = \nu_{\text{best}}(n, 0) + a \left(\frac{1}{Q_{nl}} \right) \left(\frac{\nu_{\text{obs}}(n, 0)}{\nu_0} \right)^b, \quad (4.2)$$

where $\nu_{\text{best,corr}}$ are the corrected best model frequencies.

The initial frequency list we used includes the frequencies given by Bedding et al. (2007) as in Table 4.1. We ran AMP several times, mostly changing one input at a time to check the effects of the corresponding aspects of the code. The different input that was fed into

Table 4.1: Oscillation frequencies in β Hydri as given in Bedding et al. 2007. The lower part of the table shows the extracted modes without identification.

ν (μHz)	$\nu \bmod \Delta\nu$ (μHz)	S/N	MODE ID
711.03 (1.49)	21.0	4.3	$l = 2, n = 10$
769.62 (1.59)	22.1	4.1	$l = 2, n = 11$
791.19 (1.06)	43.7	6.0	mixed
827.70 (1.19)	22.7	5.2	$l = 2, n = 12$
833.72 (1.10)	28.7	5.7	$l = 0, n = 13$
857.54 (0.86)	52.5	13.0	$l = 1, n = 13$
883.38 (0.94)	20.9	7.5	$l = 2, n = 13$
889.87 (1.45)	27.4	4.4	$l = 0, n = 14$
913.11 (0.89)	50.6	9.3	$l = 1, n = 14$
940.33 (0.95)	20.3	7.2	$l = 2, n = 14$
945.64 (1.13)	25.6	5.5	$l = 0, n = 15$
960.39 (0.87)	40.4	10.9	mixed
998.95 (0.90)	21.5	8.8	$l = 2, n = 15$
1004.21 (0.85)	26.7	18.8	$l = 0, n = 16$
1033.52 (0.86)	56.0	13.3	$l = 1, n = 16$
1056.74 (0.87)	21.7	10.7	$l = 2, n = 16$
1062.06 (1.27)	27.1	4.9	$l = 0, n = 17$
1086.45 (0.93)	51.4	7.6	$l = 1, n = 17$
1114.77 (1.49)	22.3	4.3	$l = 2, n = 17$
1118.93 (0.87)	26.4	11.3	$l = 0, n = 18$
1146.69 (0.95)	54.2	7.2	$l = 1, n = 18$
1171.61 (0.97)	21.6	7.0	$l = 2, n = 18$
1176.48 (0.87)	26.5	11.6	$l = 0, n = 19$
1198.26 (0.90)	48.3	8.5	mixed
1203.52 (1.04)	53.5	6.1	$l = 1, n = 19$
1262.20 (2.66)	54.7	3.0	$l = 1, n = 20$
1320.68 (1.40)	55.7	4.5	$l = 1, n = 21$
1378.92 (1.33)	56.4	4.7	$l = 1, n = 22$
541.36 (1.33)	23.9	4.7	
688.43 (1.59)	55.9	4.1	
753.22 (1.33)	5.7	4.7	
782.04 (1.37)	34.5	4.6	
804.21 (1.02)	56.7	6.3	
851.51 (1.27)	46.5	4.9	
868.49 (1.03)	6.0	6.2	
921.12 (1.04)	1.1	6.1	
986.27 (1.04)	8.8	6.1	
990.19 (1.59)	12.7	4.1	
1016.26 (1.59)	38.8	4.1	
1025.39 (1.02)	47.9	6.3	
1044.24 (1.54)	9.2	4.2	
1048.21 (1.03)	13.2	6.2	
1065.10 (1.11)	30.1	5.6	
1069.44 (1.07)	34.4	5.9	
1074.03 (1.02)	39.0	6.3	
1080.44 (1.17)	45.4	5.3	
1090.78 (1.45)	55.8	4.4	
1136.06 (1.65)	43.6	4.0	
1167.44 (0.95)	17.4	7.2	
1194.14 (1.59)	44.1	4.1	
1237.82 (1.27)	30.3	4.9	
1250.90 (1.02)	43.4	6.3	
1258.87 (1.49)	51.4	4.3	
1267.51 (1.22)	2.5	5.1	
1283.70 (0.99)	18.7	6.7	
1343.97 (1.54)	21.5	4.2	
1383.34 (1.27)	3.3	4.9	

AMP includes excluding mixed modes as constraints, including core overshooting, treating the mixed modes differently in the application of near-surface correction, using a different value of the exponent b in the near-surface correction term, replacing one of the observed frequencies with a neighbouring one that has a higher signal-to-noise ratio, and changing the weighting of the combination of statistical (observational) and systematic uncertainties, where the systematic uncertainties are taken to be half of the applied near-surface corrections (this was to reduce the weight of the high frequencies with large corrections). The input for the selected runs is given in Table 4.2 together with the optimized model parameters. $\chi_{\text{seis.}}^2$ values given in the table are calculated as in equation 3.2. The échelle diagrams corresponding to the resulting models for each run are shown in Fig. 4.3 and can be used to follow the improvement in the fit.

Results

The main results of our AMP runs can be summarized as follows. The use of the mixed modes are crucial in finding the best model, however, they must be treated different than the pure p modes regarding near-surface correction. It is better not to apply any correction on the mixed modes than treating them as if they are pure acoustic modes. However, a stable correction method that is applicable to all the modes as presented is more favourable.

As discussed in Section 3.5.2 Kjeldsen et al. (2008) suggested that as the exponent b in the near-surface correction term, the solar value, $b = 4.90$, shall be used for other solar-like stars, which they calculated using the GOLF data (Lazrek et al. 1997). AMP uses $b = 4.82$, which is calculated using the BISON data (Chaplin et al. 1999). Since our first runs seemed to be suffering from over-correction, we tried a smaller b value in the run (c), which was recalculated for the Sun using a range of radial orders that would correspond to the observed modes of β Hydri regarding the number of radial modes observed around the frequency of the peak power. Nevertheless, this did not solve the problem. We conclude that using the solar value for the exponent b is a good approximation, but the correction works efficiently only for the frequencies that are within the frequency range of radial modes used to calculate the correction term. The less good agreement in the high frequency region (observed high-frequency modes with $l = 1$) can be improved through the detection of $l = 0$ modes with higher frequencies. It will result in the adjustment of the correction term, and maybe of the functional form of the correction.

Inclusion of convective core overshooting can be tested once the analysis converge to a good model as the optimized parameters did not change substantially when core overshooting was included (run (h)). This statement would not be valid for the stars that are more massive and/or less evolved.

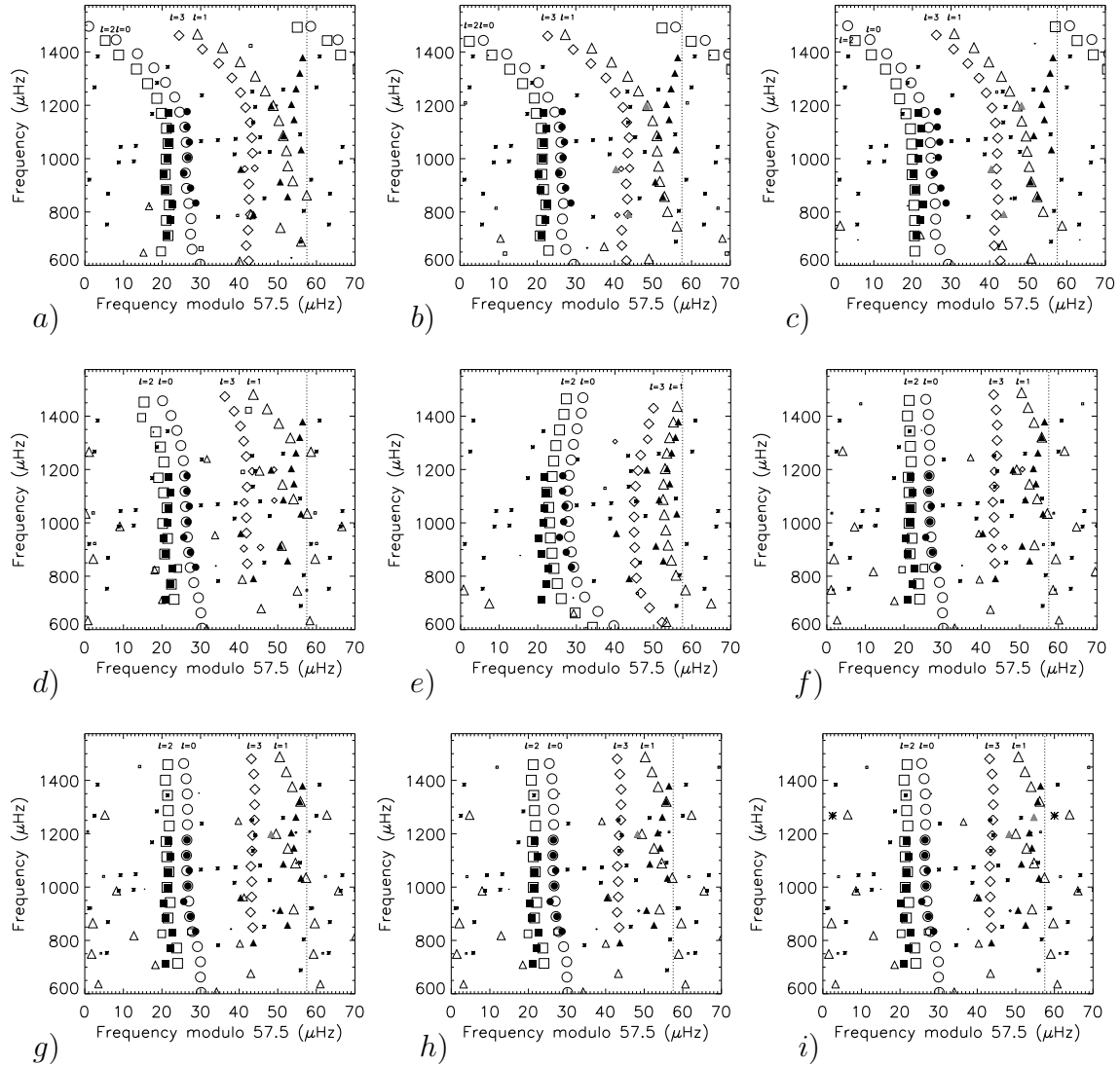


Figure 4.3: Échelle diagrams of the β Hydri models resulting from 9 different AMP runs (see the text for details). Vertical dotted lines are used to mark the large frequency separation ($\Delta\nu$); the gray color is used for symbols representing the frequencies in Table 4.1 which were not used as constraints; the asterisks represent the unidentified modes in Table 4.1; the size of the symbols scales with the expected surface amplitudes of the modes; the large asterisk in panel (i) is used to indicate the mode replacement.

Table 4.2: Properties of the resulting models of the AMP runs (see the text for details) and differences regarding the input and the selection process in each optimization run

M/M_{\odot}	Z	Y	α	τ (Gyr)	$\Delta\nu$ (μHz) before / after	T_{eff} (K)	L/L_{\odot}	R/R_{\odot}	$\chi^2_{\text{seis.}}$	Departure from the the observed list	Other notes
a	1.04	0.00748	0.257	1.64	6.27 / 59.36 / 57.23	5913	3.442	1.771	19.28	none	WS1, (1)
b	1.11	0.00938	0.248	1.50	5.47 / 59.53 / 57.21	5889	3.499	1.800	21.39	3 mixed modes excluded	WS1
c	1.10	0.00773	0.232	1.50	5.90 / 59.59 / 57.10	5899	3.499	1.794	24.08	3 mixed modes excluded	WS1, b=4.09
d	0.97	0.00447	0.223	2.74	9.13 / 58.30 / 57.26	5925	3.404	1.754	9.90	none	WS1,(2)
e	1.01	0.00679	0.299	1.08	4.66 / 56.90 / 57.29	5859	3.389	1.790	16.85	3 mixed modes excluded	WS2, (2)
f	1.10	0.01294	0.258	2.90	6.86 / 57.87 / 57.28	5848	3.521	1.832	5.49	none	WS2,(2)
g	1.09	0.01294	0.266	2.94	6.72 / 57.87 / 57.27	5868	3.554	1.827	5.66	the mode at 1198.26 μHz excluded	WS2,(2)
h	1.10	0.01253	0.251	2.86	7.08 / 57.88 / 57.27	5823	3.464	1.833	5.63	the mode at 1198.26 μHz excluded	WS2, (2), $a_{\text{ov}} = 0.30$
i	1.11	0.01294	0.246	2.82	7.19 / 57.88 / 57.28	5792	3.416	1.839	5.75	the mode at 1198.26 μHz excluded, mode replacement: 1262.20 μHz by 1267.51 μHz	WS2, (3)

(WS1) Weighting scheme 1 is used, where both statistical and systematic uncertainties are included in the model-fitting.

(WS2) Weighting scheme 2 is used, where only the statistical uncertainties are included in the model-fitting.

(1) Convective core overshooting is not included and the exponent in the correction term $b=4.82$ in this and the following models, unless otherwise stated.

(2) No near-surface correction is applied on the model frequencies closest to frequencies of the observed mixed modes.

(3) Near-surface correction is scaled with the inverse of the normalized mode inertia ratio,
and then applied to all model frequencies including those of the mixed modes.

The choice of weighting scheme for the errors has a large effect on the resulting fit, and should be different than that used for the Sun. From the run (f) on, the fits improved substantially.

Other modifications such as replacing one of the observed frequencies with a neighbouring one did not result in substantial improvement, as the model frequency matched to the altered frequency remained the same. Excluding the highest "identified-as-a-mixed mode" did not lead to a significant improvement either, and that is because none of the best models reproduced that frequency as a mixed mode. We suspected that it might be an $l = 3$ mode. Now that an updated analysis of data is available in Brandão et al. (2010, Appendix D), where the mode in question is presented as an $l = 3$ mode, our next step is to submit an AMP run with the updated frequency constraints.

Our model-fitting experiments have improved the efficiency of AMP, and therefore were useful in relation to getting ready to be used for *Kepler* stars.

4.2 Procyon

Procyon is a binary star with a primary component of spectral type F5, Procyon A, and a white dwarf companion, Procyon B. Here, we refer to the solar-like component Procyon A as Procyon. The detection of the solar-like oscillations in this star was subject to ambiguity for around two decades (see Arentoft et al. (2008) for a summary). We adopted the most recent frequency lists from Bedding et al. 2010 as seismic constraints. They showed that the data analysis of Procyon was particularly interesting, because the spectrum obtained from the multi-site observations that involved more than 11 telescopes did not result in unambiguous mode degree identification. Two scenarios have been proposed (Bedding et al. 2010), the difference of which was that the odd and even degrees of l were assigned to the opposite frequency ridges. By the help of modelling, we tried to analyse both scenarios. The methods and the results are summarized in Appendix E (Doğan et al. 2010a). We ran several grids with different initial values of Z/X using a mass range constrained by astrometry. Table 4.3 shows the properties of some of the models resulting from our preliminary analysis, corresponding evolutionary tracks are given in Fig. 4.4, and échelle diagrams for two of the selected models are given in Fig. 4.5.

Procyon is expected to have a different inner structure than the Sun, as its mass $M \sim 1.5 M_{\odot}$ and it has a higher surface temperature $T_{\text{eff}} = 6530 \pm 90$ K. As a different approach in modelling this star, we did not apply the near-surface corrections to the frequencies, as we wanted to see the form of the differences between the observed and the calculated frequencies in both scenarios. Modelling regarding one of the scenarios (scenario A) suggests that very little near-surface correction is needed, if any.

However, convection is expected to affect the high-frequency modes. For a selected model, we plotted the upper turning point of the waves in Fig. 4.6 to find out if there is any possibility that the convection in a very thin layer excites the modes but then the upper turning point of the waves are not within the thin convective layer. Upper turning point is indicated with the frequency where the frequencies are smaller than the acoustical cut-off

Table 4.3: Properties of the selected models of Procyon resulting from different runs

Grid no.	scenario A										
	M/M_{\odot}	Z/X	Y	R/R_{\odot}	$\bar{\rho}/\bar{\rho}_{\odot}$	Age(Gyr)	X_c	T_{eff} (K)	L/L_{\odot}	α	χ^2
1	1.47	0.0243	0.283	2.039	0.173	1.756	0.159	6465	6.521	1.75	4.24
2	1.52	0.0245	0.270	2.066	0.172	1.721	0.170	6515	6.904	1.90	3.87
3	1.48	0.0204	0.260	2.049	0.172	1.923	0.138	6454	6.538	1.80	3.77
4	1.50	0.0235	0.266	2.058	0.172	1.830	0.158	6446	6.565	1.80	3.79
Grid no.	scenario B										
	M/M_{\odot}	Z/X	Y	R/R_{\odot}	$\bar{\rho}/\bar{\rho}_{\odot}$	Age(Gyr)	X_c	T_{eff} (K)	L/L_{\odot}	α	χ^2
1	1.43	0.0236	0.263	2.063	0.162	2.481	0.00108	6516	6.886	1.75	42.45
2	1.50	0.0245	0.290	2.067	0.170	1.506	0.200	6602	7.286	1.60	24.46
3	1.52	0.0236	0.280	2.092	0.166	1.561	0.180	6608	7.485	1.80	29.74
4	1.52	0.0240	0.280	2.096	0.165	1.584	0.177	6578	7.382	1.80	30.99

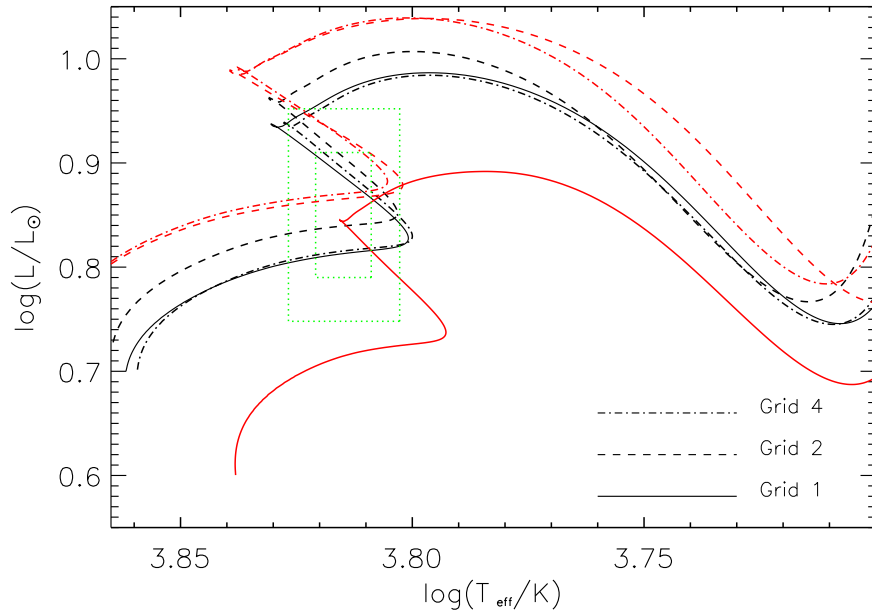


Figure 4.4: HR diagram for the selected models from three runs given in Table 4.3. The black curves represent the models for scenario A, while the red curves the scenario B with the same line styles as shown for the black curves. 1- σ and 2- σ error boxes are shown in green.

frequency (ν_{ac} , panel (a))(above this frequency the waves are interpreted as propagating outwards through the atmosphere). Fig. 4.6 also shows the location of the base of the convection zone in panel (b). We see that the upper turning point of the observed waves with frequencies roughly between 350 and 1300 μHz is between ~ 0.988 and $\sim 0.999 R$,

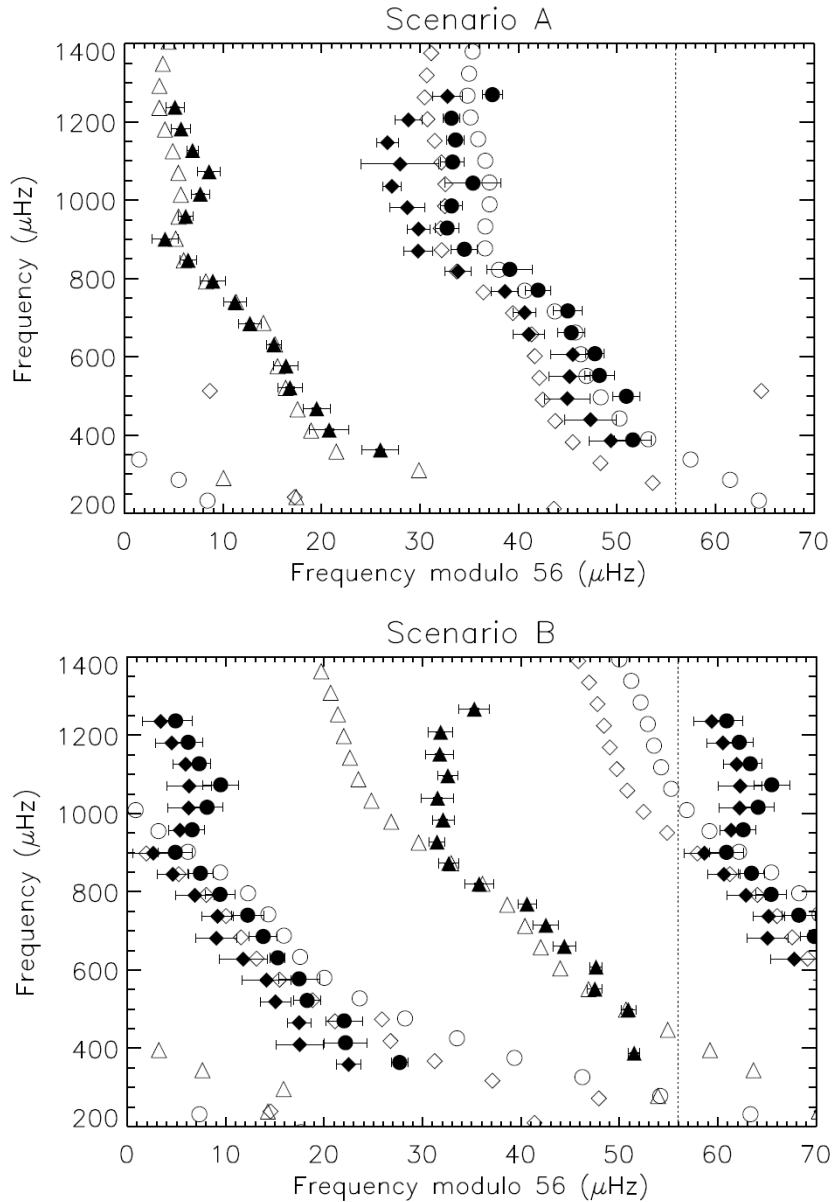


Figure 4.5: Échelle diagrams of models for scenario A (top) and scenario B (bottom). Open (filled) symbols are the model (observed) frequencies. Circles, triangles, and diamonds are used for the modes with $l = 0$, $l = 1$, and $l = 2$, respectively. Model in the top panel is from grid 4, and the model in the bottom panel is from grid 2 with their properties given in Table 4.3. Figure from Doğan et al. (2010a) (Appendix E).

where R is the surface radius of the star. This is well within the convection zone, the base of which is shown to be at $0.936R$, from where on the Schwarzschild criterion for convection, as $\nabla_{\text{rad}} > \nabla_{\text{ad}}$ is satisfied. This shows that the near-surface correction must

still affect the observed frequencies. The lack of a large difference between the observed and calculated (high) frequencies might be explained by the cancellation of the unknown effects of other mechanisms like turbulent convection, nonadiabaticity, etc. If this is the case, Procyon is rather different from the Sun. Regarding scenario B, neither high nor low frequencies have been reproduced by the models yet, but I note that this is a work in progress, and we will try to explore the parameter space to search for the possible mixed mode in the scenario B presented by Bedding et al. (2010).

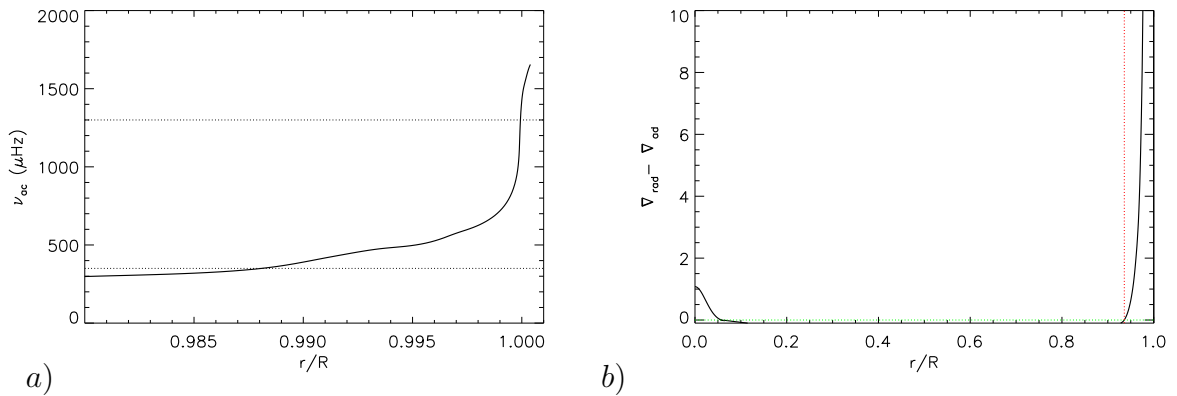


Figure 4.6: a) ν_{ac} , b) $\nabla_{rad} - \nabla_{ad}$ for a model with $M = 1.52 M_{\odot}$, $X = 0.7031$, $Z = 0.0169$. (b) is truncated at top to make visible the convective instability in the core.

Consequently, none of the identification scenarios is strongly favoured. We conclude from the preliminary interpretation that scenario A results in a better fit than scenario B. On the other hand, the preliminary models for the scenario A indicate the absence of near-surface effects, which are expected to be seen in solar-like stars. Whatever the correct scenario is, what we see in Procyon will guide us to improve our understanding of these types of stars that are different from the Sun.

4.3 Kepler stars

Kepler solar-like oscillators are being analysed within the coordinated efforts of Working Group 1 (WG1) within the Kepler Asteroseismic Science Consortium (KASC). To speed up the analysis and to ensure collaboration between members of the group, there have been work packages assigned to several topics and targets, with a lead responsible for the progress in the work and liaisons responsible for coordination within the subgroups. I am involved in several work packages. In the next subsections, I present the results from one of the earliest work packages, and prospects from another work package in progress.

4.3.1 KIC 11026764

I have made major contribution to the coordinated work of KASC WG1 on modelling the evolved solar-like star, KIC 11026764. The solar-like spectrum of this star was presented among the first results on solar-like oscillators observed by *Kepler* (Chaplin et al. 2010, Appendix F). It is the first solar-like star in the *Kepler* field that has been modelled in detail within a large collaboration (see Appendix G for a preliminary analysis, and Appendix H for the detailed results). Using the individual frequencies that were extracted by the frequency analysts in the WG1, and atmospheric parameters derived by the members of the ground-based follow-up group, different teams in the modelling subgroups employed a variety of codes, different input physics, and different fitting methods in order to determine the global properties of this star.

I have employed the Aarhus codes for stellar evolution and pulsation calculations. With the guidance of range of parameters resulting from the pipeline analysis, given in Chaplin et al. (2010), I computed grids of evolutionary tracks mainly varying stellar mass, and the metallicity. I fixed the mixing length parameter α_{MLT} to 1.7 and searched the parameter space for mass, M , from 1.0 to 1.35 M_{\odot} , for mass fraction of heavy elements, Z , from 0.009 to 0.025, and the initial mass fraction of hydrogen, X , from 0.68 to 0.76. These Z and X cover a range of $Z/X=[0.012, 0.037]$, converted to $[\text{Fe}/\text{H}]=[-0.317, 0.177]$, where the Z/X values are those at the stellar surface.

The atmospheric parameters, $[\text{Fe}/\text{H}]$, T_{eff} , and $\log g$ of the star were derived through spectroscopic observations. There were several groups who derived different parameters. As initial nonseismic constraints we used a range covering most of these results: $T_{\text{eff}} = 5635 \pm 185 \text{ K}$, $\log g = 3.95 \pm 0.25 \text{ dex}$, and $[\text{Fe}/\text{H}] = -0.06 \pm 0.25 \text{ dex}$. To investigate the effect of nonseismic constraints on the resulting models, I searched up to a range of $2\text{-}\sigma$ around the given estimates for atmospheric parameters.

As discussed in Chapter 3, my fitting method involves spotting the models having the desired values for the classical observables in the computed tracks and minimizing the differences between the calculated frequencies of those models and the observed oscillation frequencies, in the form of χ^2 -minimization.

As a result of my analysis I obtained two families of solutions, and this was confirmed by the combined results of the analysis done by several teams. The resulting best models constrain the global stellar properties to a certain extent, constituting two groups of parameters; one group being slightly more massive ($M \sim 1.23 M_{\odot}$) than the other group ($M \sim 1.13 M_{\odot}$). The more massive models have a lower He abundance. Although the stellar properties are different, the frequencies in the observed range are very similar. Hence without knowing the He abundance in the star, or having an updated list of frequencies, we would have no way of favouring one set of model parameters over the other. With the help of upcoming seismic observations, we might have additional frequencies and this issue might be resolved. I present a more detailed comparison of the two representative models from each family in the following subsection. I keep their labels as in Metcalfe et al. (2010) (Appendix H) for the sake of compatibility.

The best models I found were in the $1\text{-}\sigma$ uncertainty range of the initial values given for

the atmospheric parameters. This is because the initially selected range was large enough to host almost all the possible models (see Fig 4.7).

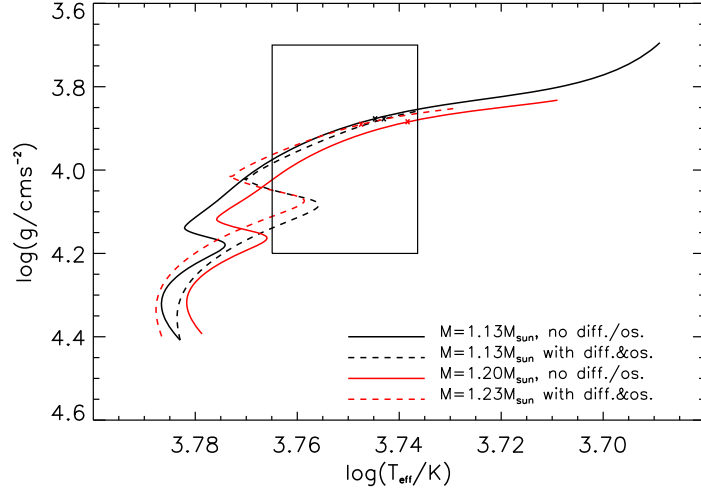


Figure 4.7: $\log g - T_{\text{eff}}$ diagram of some representative models of KIC 11026764. Error box shows the initially adopted constraints. Black solid, black dashed, red solid, and red-dashed lines correspond to models AA, AA', AB', and AB, respectively, presented in Table 4.4

In the second round of analysis, we received a more constrained set of atmospheric parameters, however this did not alter much the resulting models. Once we are in the vicinity of accurate values for the atmospheric parameters, the seismic constraints, such as the individual frequencies, become much more important in selecting the best representative models. This was also shown using the Singular Value Decomposition (SVD) analysis by Metcalfe et al. (2010, Fig. 4). The most constraining seismic input is shown to be the presence of mixed modes. I note the importance of the frequency of a mixed mode as well as its presence, since it partly lifts the degeneracy in the parameter space, including the age and the global parameters, as discussed below. For instance, I found models with higher mass ($M \sim 1.35 M_{\odot}$) having compatible χ^2 values to those of the best models before refining the solution, however, without successful reproduction of the mixed mode at the observed frequency, hence, those solutions were dropped as the analysis got more mature.

How do the mixed modes constrain the stellar age?

As discussed in Chapter 2 the frequencies of the g modes increase as the star evolves. Therefore, a g mode will interact with the p modes at higher frequencies along the evolution due to the simultaneous decrease in the p-mode frequencies (see Fig. 4.8). Once enough time has elapsed, the next g mode will catch up with the p modes around a frequency close to where a given p mode has already been perturbed by the previous g mode. This

is illustrated in Fig. 4.8 with the track of the avoided crossings followed by the labels G_1 and G_2 . Given the frequency of the mixed mode, this allows us to constrain the age of the model to a small range, due to the fact that the avoided crossings jump from one radial order to the next very quickly when compared to the time scale of stellar evolution. As seen in Fig. 4.8 for a sequence of models with $M = 1.13M_{\odot}$, the given frequency of a mixed mode constrains the age up to ~ 0.03 Gyr.

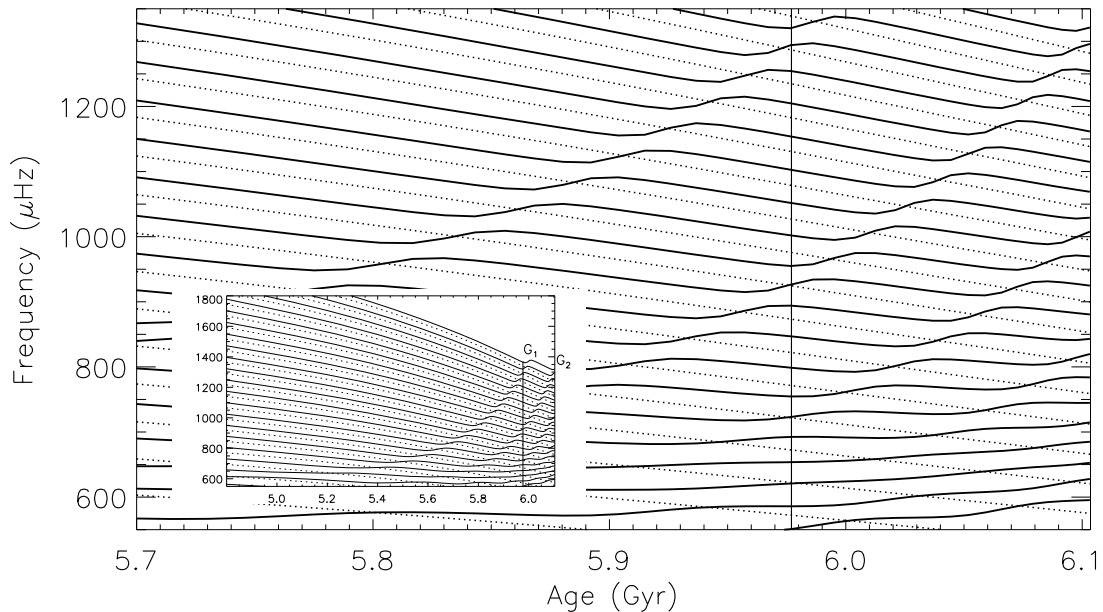


Figure 4.8: Evolution of frequencies with $l = 1$ & $n = 5 - 25$ (solid lines), and $l = 0$ & $n = 9 - 26$ (dotted lines) for model AA in Appendix H (Metcalf et al. 2010)

It should be noted that in most cases the avoided crossings do not involve only one p mode, but a number of modes around the most distorted mode, depending on the strength of the coupling between g- and p-mode cavities. This was demonstrated in detail by Deheuvels & Michel (2010) in relation to the modelling of the solar-like COROT target HD 49385. In the case of KIC 11026764, the strong distortion in $l = 1$ frequencies around $\nu = 900 \mu\text{Hz}$ is clearly seen in the échelle diagram (Fig. 4.13).

Fig. 4.9 shows the normalized mode inertia (E_{nl}) for $l = 1$ modes. The normalization of the mode inertia, E_{nl} (E (equation 2.13) for the mode with degree l , and radial order n), is done with respect to the displacement at the stellar surface; i.e. if the mode inertia is high, the displacement in the interior is larger than that at the surface, so the amplitude of the mode may not be high enough at the surface to be observed. As seen in Fig. 4.9, E_{nl} is higher for the modes with lower frequencies corresponding to g modes and low order p modes. Fig. 4.10 shows the normalized mode inertia ratio (Q_{nl}) corresponding to the frequencies of model AA with degree $l = 1$. When $Q_{nl}(= \frac{E_{nl}}{E_0(\nu_{nl})})$ is unity, it means that

the normalized inertia of the mode in question is equal to the normalized inertia of the radial mode with frequency interpolated to ν_{nl} for each set of (n, l) , and the mode is expected to be observed as long as the corresponding radial mode is also observable. However, this ratio is larger than unity when there is a mixed mode involved. The asterisks in Fig. 4.10 correspond to modes with $n = 1 - 26$. All those modes seen in Fig. 4.10 having Q_{nl} larger than unity have some g-mode character in the central regions of the star, and p-mode character at the surface. The modes at the peaks will have the strongest g-mode character, while some neighbouring modes are also slightly or substantially affected. Eigenfunctions of selected p, g, and mixed modes are shown in Fig. 4.11. It can be interpreted as the amplitude of a p mode is large at the surface, whereas that of a g mode is large in the core. A mixed mode, however, behaves like a g mode in the centre and a p mode at the surface.

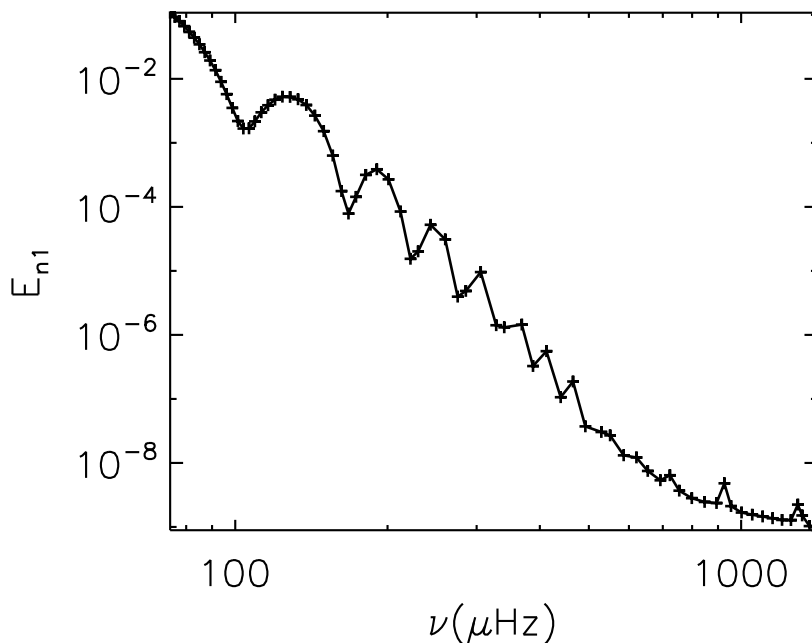


Figure 4.9: Dimensionless mode inertia E_{nl} for (p and g) modes with degree $l = 1$, and order $n = -46 - 26$ for model AA in Appendix H (Metcalf et al. 2010)

How do the mixed modes constrain the global properties?

Mixed modes do not only constrain the stellar age in a sequence of given, say, mass. Two different models being evolved enough to have mixed modes may differ in other parameters, which can further be constrained by the frequency of the mixed mode.

Fig. 4.12 shows échelle diagrams of two models that have different global properties, but similar large frequency separations. This is one of the examples to why we need individual

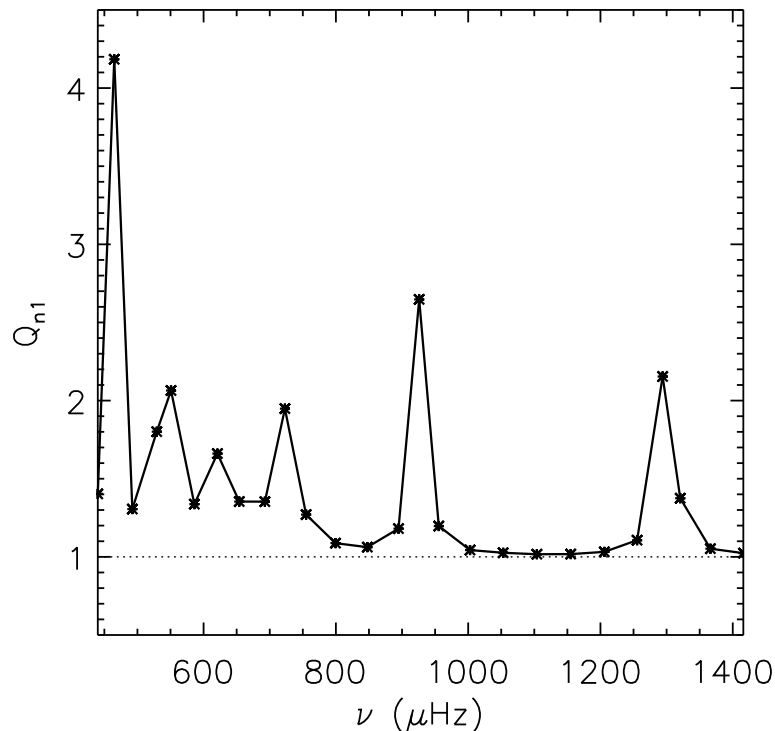


Figure 4.10: Normalized mode inertia ratio for modes with degree $l = 1$, and $n = 1 - 26$ for model AA in Appendix H (Metcalf et al. 2010). Q_{nl} is the ratio of dimensionless mode inertia of a mode with degree l and radial order n to that of a mode with degree 0, and frequency interpolated to the frequency of the $l = 1$ mode for each n .

frequencies to put stronger constraints on the models. The model with $M = 1.35 M_{\odot}$ and the one with $M = 1.15 M_{\odot}$ have similar $\Delta\nu$, with similar $l = 0$ and $l = 2$ frequencies. However, the frequencies at which the avoided crossings occur are different, and only one of the models reproduces the frequency of the observed mixed mode. So, given we have individual frequencies, the most constraining information comes from the $l = 1$ mixed modes as discussed (mixed modes with higher degrees would also be very useful, however, they are less likely to be observed). This illustrates one of the strengths of comparing the individual frequencies rather than the average quantities. Pipeline analyses which use the average seismic parameters for modelling are very fast and useful; however, their results should be handled with care, as the use of average seismic parameters can be misleading. They do, however, provide a good starting point for a detailed search of an overall representative model.

Nevertheless, mixed modes cannot lift all the degeneracy in the model parameters. Without additional information, we can only go so far, which was demonstrated by Metcalfe

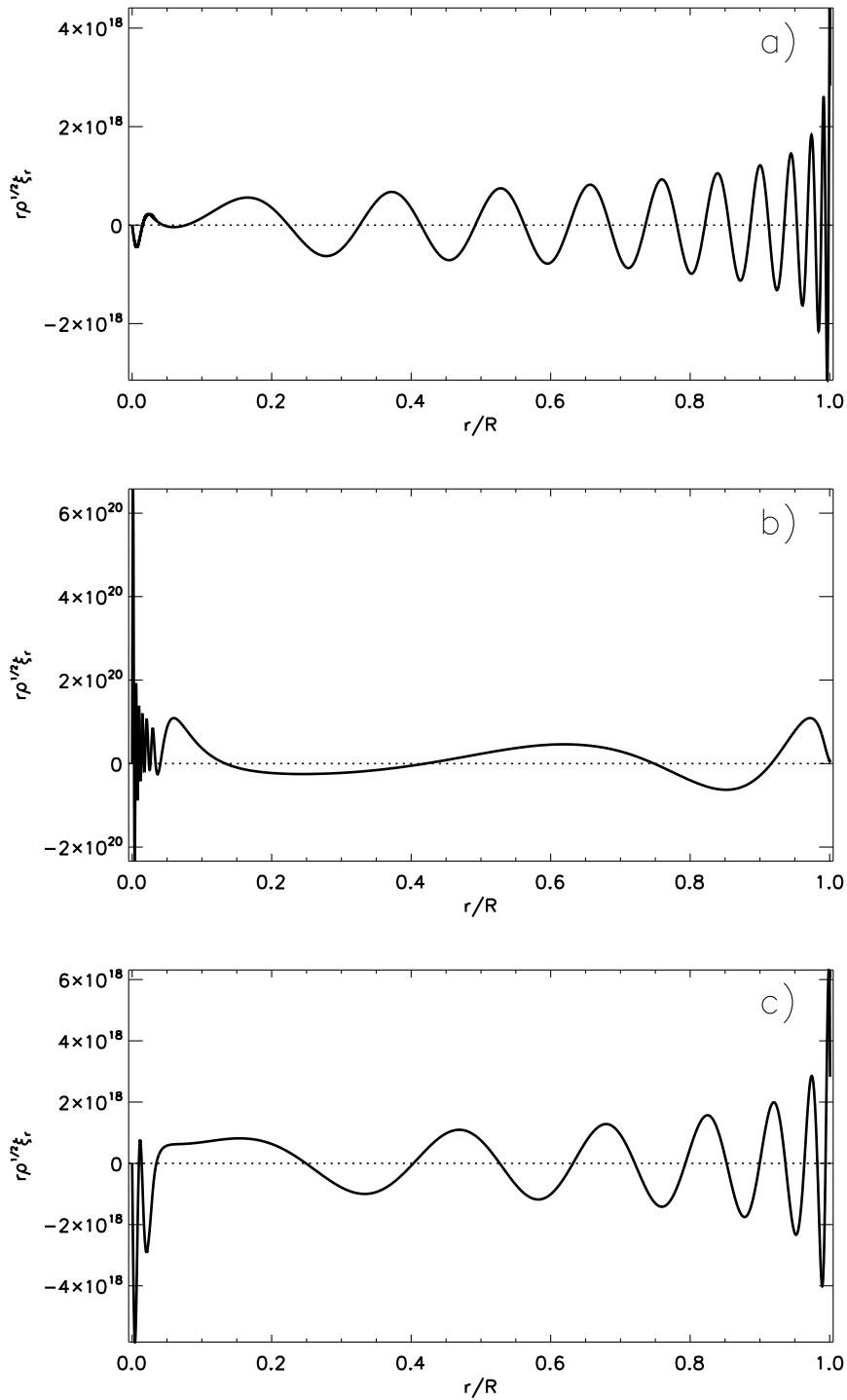


Figure 4.11: Displacement eigenfunctions for the $l = 1$ modes with radial order a) $n = 20$, b) $n = -5$, and c) $n = 10$ (mixed mode)

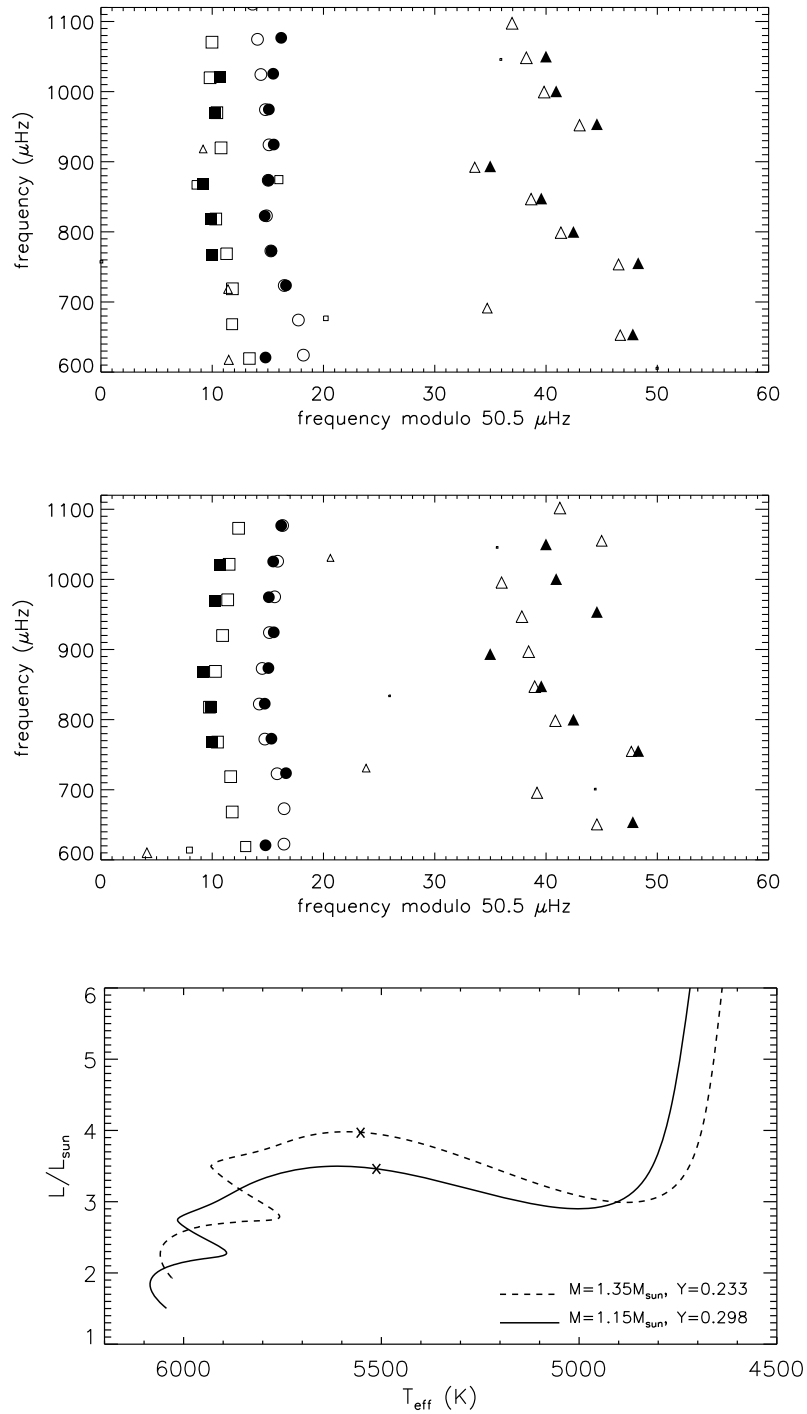


Figure 4.12: Échelle diagrams for a model with $M = 1.15 M_{\odot}$, $Z=0.0225$, $X=0.68$, $\Delta\nu = 50.12 \mu\text{Hz}$ (top panel) and a model with $M = 1.35 M_{\odot}$, $Z=0.0275$, $X=0.74$, $\Delta\nu = 50.52 \mu\text{Hz}$ (middle panel). Bottom panel: HR diagram showing the evolutionary tracks of the models shown in the top and middle panels, marked with crosses.

et al. (2010). In what follows, I present a comparison of two models representing the results of the coordinated analysis.

Models AA & AB

For the sake of completeness, the over-plotted échelle diagrams of the two representative models, models AA and AB, are shown in Fig. 4.13, while the corresponding parameters are given in Table 4.4. I proceed with comparing the inner structures of the two models.

Table 4.4: Final model fitting results for KIC 11026764. See Appendix H for all the models that are not discussed in the text here.

Model	M/M_{\odot}	Z_s	Y_s	α	t (Gyr)	L/L_{\odot}	R/R_{\odot}	$T_{\text{eff}}(\text{K})$	$\log g$	[Fe/H]	χ^2
FA...	1.13	0.017	0.305	1.64	5.268	4.141	2.036	5778	3.872	+0.009	3.69
AA...	1.13	0.019	0.291	1.70	5.977	3.520	2.029	5556	3.877	+0.051	6.11
AA'...	1.13	0.019	0.291	1.70	5.935	3.454	2.026	5534	3.877	+0.031	7.40
GA...	1.10	0.017	0.296	1.88	6.100	3.420	2.010	5539	3.870	+0.004	78.05
CA...	1.13	0.019	0.291	1.70	6.204	3.493	2.030	5546	3.876	+0.050	152.91
EA...	1.12	0.019	0.291	1.70	6.683	3.202	2.029	5424	3.870	+0.050	230.58
AB...	1.23	0.018	0.242	1.80	5.869	3.804	2.083	5591	3.890	-0.010	6.97
AB'...	1.20	0.024	0.276	1.80	5.994	3.460	2.072	5475	3.884	+0.146	7.26
BB...	1.22	0.021	0.270	1.80	5.153	4.190	2.061	5758	3.896	+0.072	7.57
FB...	1.24	0.021	0.280	1.79	4.993	4.438	2.092	5800	3.890	+0.091	8.52
EB...	1.22	0.013	0.232	1.80	4.785	4.651	2.079	5882	3.890	-0.130	18.54
CB...	1.24	0.015	0.250	1.80	5.064	4.696	2.089	5887	3.892	-0.080	45.84
J'....	1.27	0.021	0.270	1.52	4.260	4.011	2.105	5634	3.892	+0.080	...
\pm error	0.09	0.003	0.024	0.74	1.220	0.371	0.064	81	0.020	\pm 0.060	...
K'...	1.20	0.022	0.278	1.80	5.980	3.700	2.026	5619	3.900	+0.070	...
\pm error	0.04	0.003	0.003	...	0.610	0.300	0.027	79	0.006	\pm 0.060	...

The most obvious differences are in the H and He abundances (Fig. 4.14), while density, temperature, pressure and hence the sound speed profiles are very similar, except for the small scale variations, which might not be useful in the interpretation of the observed frequencies in hand. The effect of including diffusion and gravitational settling of He is seen as a slight decrease in He abundance and a slight increase in H abundance close to the surface of the model with diffusion and settling (model AB), and eventually as a decrease in [Fe/H] in Table 4.4.

The higher mass is compensated by slightly higher radius, hence the density within two models are almost same, and the frequencies remain similar. If we knew the He abundance, we would be able to distinguish between the models; however, He abundance cannot be measured directly.

As seen in Fig. 4.15, the other internal properties of these two models are also very similar. The base of the convection zone (BCZ) is at $\sim 0.67 R$ (seen as the radius where $\nabla_{\text{rad}} - \nabla_{\text{ad}} > 0$ in panels (a) and (b)), and the second helium ionization zone is located at $\sim 0.97 R$ (seen as the local minimum near the surface in panels (e) and (f)) in both models, where R is radius at the stellar surface. If we had observed modes that cross the

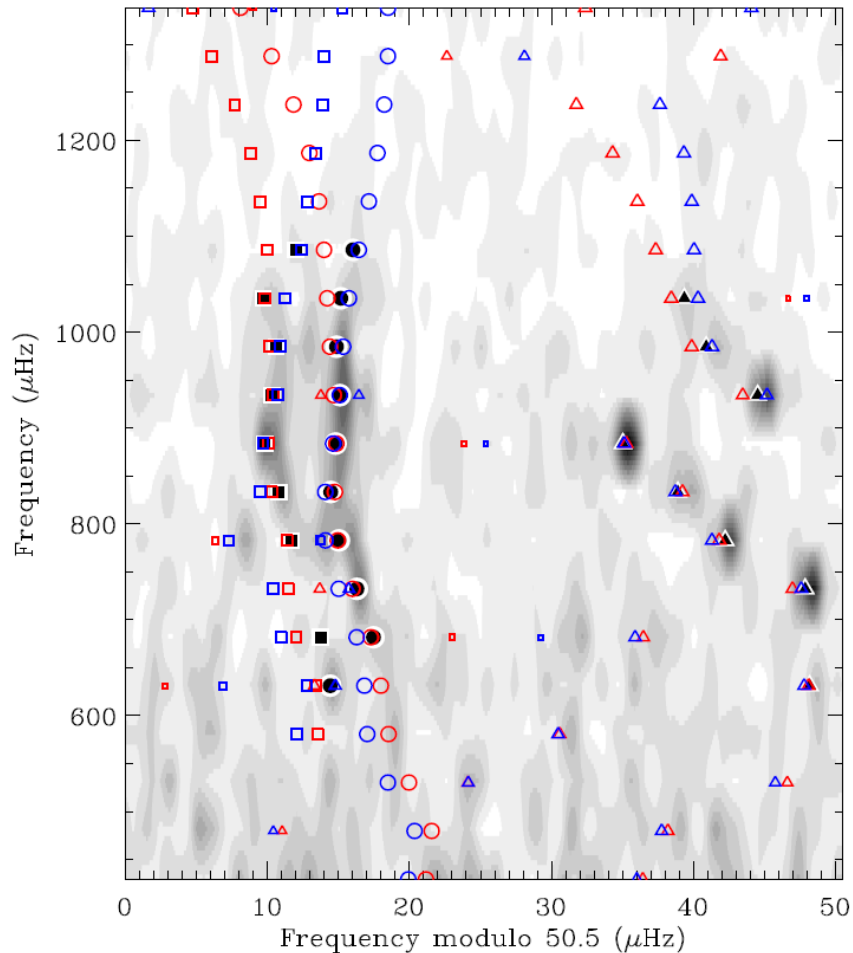


Figure 4.13: Échelle diagrams of model AA (blue) and model AB (red) (Metcalf et al. 2010).

second helium ionization zone, but not the BCZ, we might have been able to isolate the effects of different helium abundances on frequencies (Monteiro & Thompson (2005) for a method proposed for the Sun). However, this would mean that observed modes with very high l would be needed to study the oscillations trapped in such a region. S_l (equation 2.5) determines the lower turning point of a wave. Panel (f) in Fig. 4.15 shows S_l for $l=1, 2$, and 100. The modes with $l=1$ and 2, have their turning points in the deeper regions, while a high frequency mode with $l=100$ would have its lower turning point between 0.67 and 0.97 R . Nevertheless, it is not possible to observe such high l modes for stars with unresolved discs, i.e.; stars other than the Sun. Nevertheless, there is another method proposed by Houdek & Gough (2007) which employs the so-called second frequency differences through isolating the effects of sharp features inside the star, like the helium second-ionization zone, BCZ, etc., on these differences. This is expected to lead eventually to the seismic

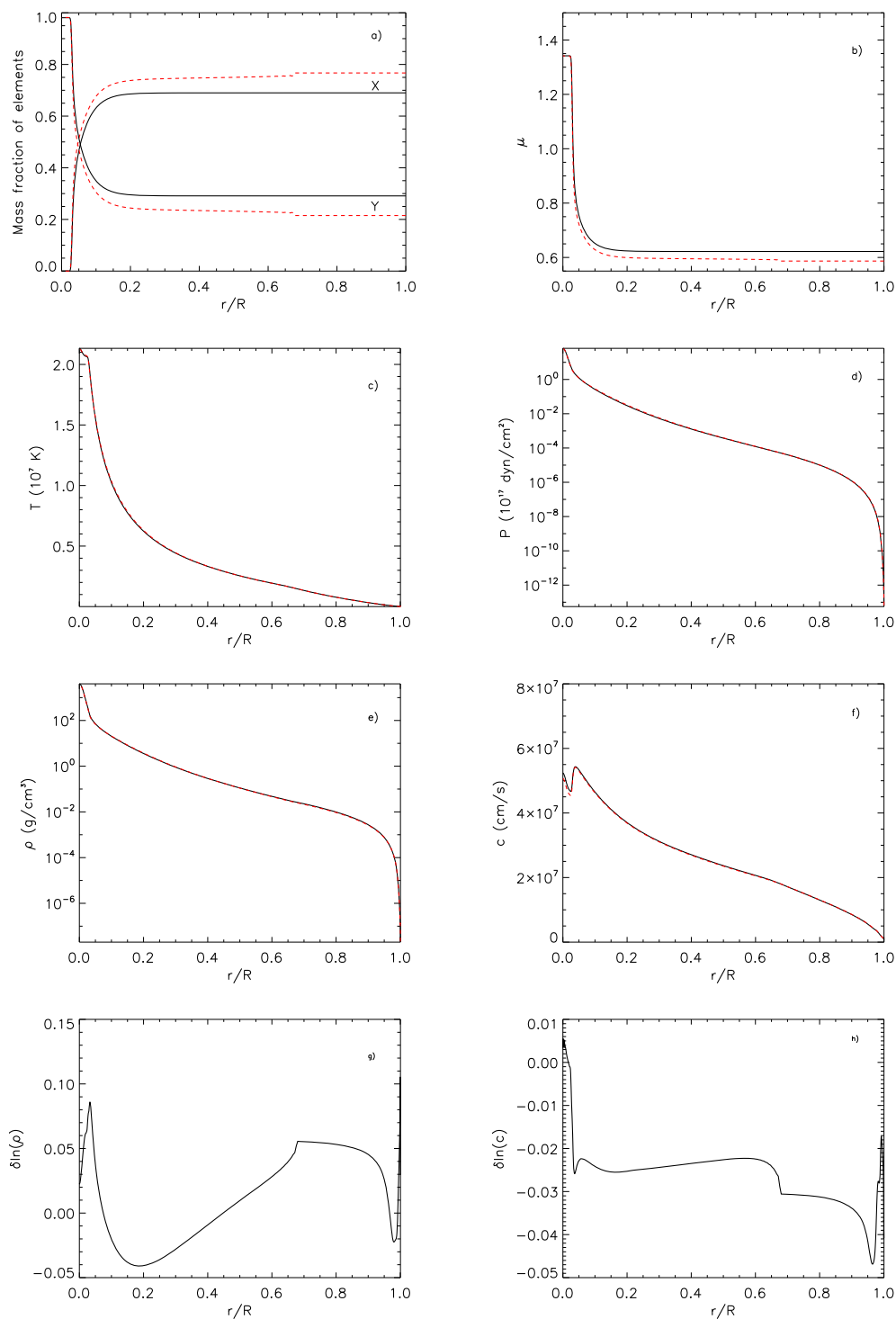


Figure 4.14: a) Fractional mass of H (X) and He (Y) throughout models AA (black solid) and AB (red dashed); b) mean molecular weight (μ), c) temperature, d) pressure, e) density (ρ), f) sound speed c , g) relative density difference, and h) relative sound speed difference from the centre to the surface

determination of the He abundance in the stellar envelopes. For this purpose, we need high-precision frequency data with many consecutive modes. Recently, Miglio et al. (2010) have successfully applied this method on the COROT data for the red giant HR7349.

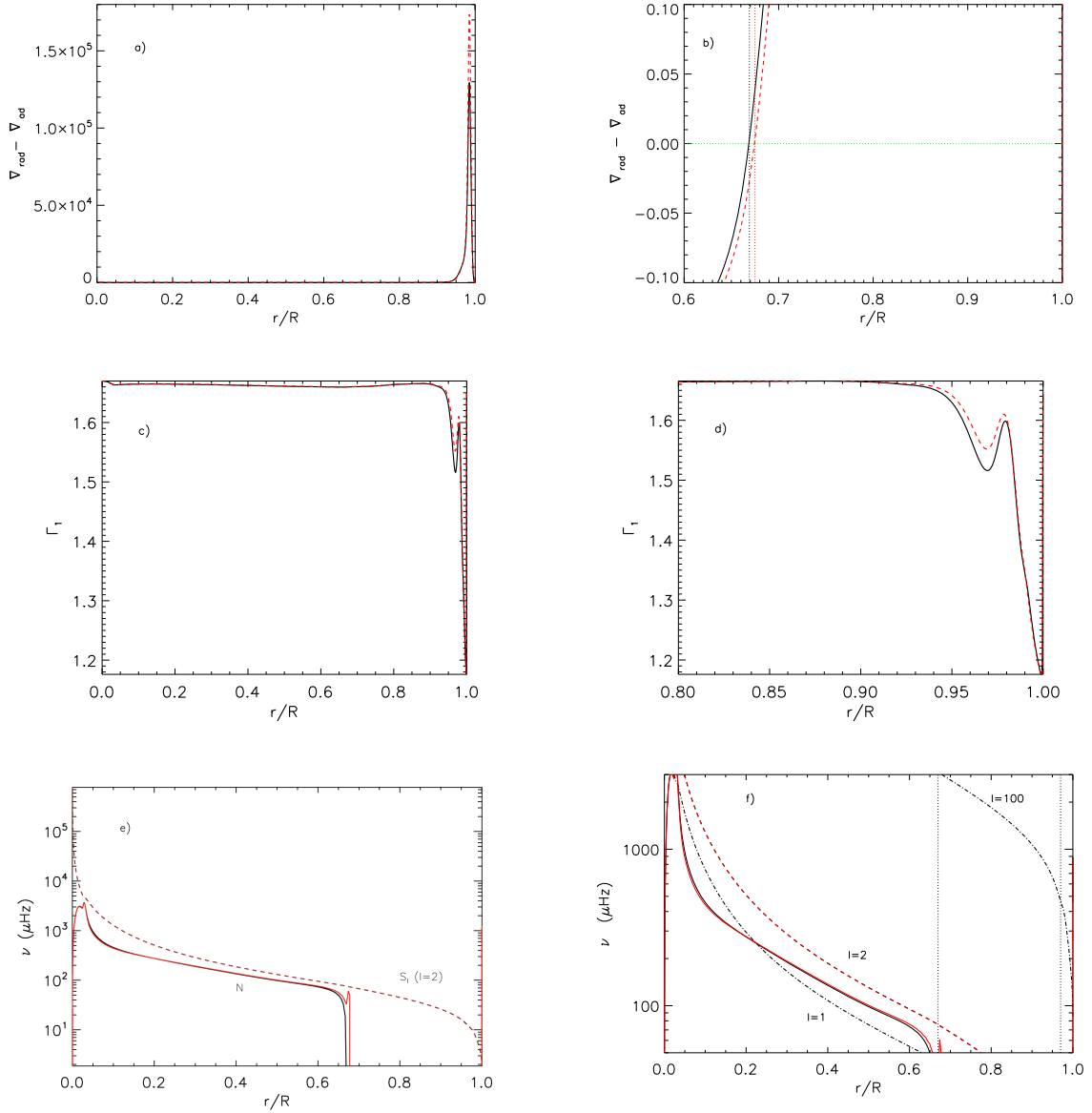


Figure 4.15: a) Difference between radiative and adiabatic gradients, b) Same as (a) zoomed around the BCZ, c) Adiabatic exponent from the centre to the surface d) Adiabatic exponent zoomed in at the He II ionization zone for models AA (black solid) and AB (red dashed), e) Characteristic frequencies: Brunt-Väisälä frequency (N), and Lamb frequency (S_l)), f) N and S_l for $l = 1, 2 \& 100$

KIC 11026764 is scheduled to be observed more months in the coming phases of the

Kepler mission. With the new observations, some other mixed modes might be detected, and this might help us to distinguish between the two models.

4.3.2 A special group of solar-like stars

Five targets have been selected for in-detail analysis due to the fact that they are among the longest observed *Kepler* solar-like targets that show clear solar-like oscillations. These five stars are KIC 11395018, KIC 10920273, KIC 10273246, KIC 10339342, and KIC 11234888.

I am currently one of the co-leaders of a coordinated work of modelling this group of stars. We have divided the work into 2 stages, and planned for three publications. The first one, led by O. L. Creevey, is to compare the atmospheric parameters determined using different methods, discuss these within the context of the different stellar parameters they lead to after being used as constraints in modelling pipelines. I will be leading the second paper which will include the detailed comparison of the stellar properties and interiors of two supposed-subgiants, KIC 11395018 and KIC 10920273. And the third paper will be on the detailed modelling of the relatively more massive star KIC 10273246, using the seismic diagnostics related to the convective core, and will be led by I. M. Brandão.

The first 7 months of the 11 months of available data have been analysed by the subgroup working on extraction of mode parameters. They have very recently provided us with the lists of individual frequencies to be used in detailed modelling of these stars. For the purpose of detailed modelling, we also need more accurate atmospheric parameters (T_{eff} , $\log g$, and the metallicity [Fe/H]) than given in the *Kepler* Input Catalogue (KIC). For that matter, I, as the PI, together with other leads as CoIs, applied for observing time with the FIES instrument at the Nordic Optical Telescope (NOT) through the Fast Track Programme (see Appendix I for the proposal). We were awarded 4 hours of spectroscopic observing time, which was divided between the 4 targets. One of them, KIC 11234888, was left for later analysis due to the poor signal-to-noise (S/N) in the seismic data. The spectroscopic data were obtained in the medium-resolution mode, and ended up having a S/N of around 80. The spectroscopic analysis to determine the atmospheric parameters is about to be completed, and we are now in the process of deciding about the method to combine different values and uncertainties from several teams, so that we can kick-start the detailed modelling work. We will most likely make use of the preliminary results of the Paper I regarding the ranges of global stellar parameters determined using the modelling pipelines which involves the atmospheric parameters and the average seismic parameters. We aim at increasing the precision and accuracy of the global parameters and analysing the stellar interiors in detail.

KIC 11395018 (*Kepler* magnitude ~ 10.8) and KIC 10920273 (*Kepler* magnitude ~ 11.9) are stars that are fainter than KIC 11026764 (*Kepler* magnitude ~ 9.3), however their data cover, at the time of writing, 11 months. Hence, it is exciting to see what we can get out even for faint stars. So far, KIC 11395018 seems very similar to KIC 11026764, presented in the previous subsection. It will be very interesting to make a detailed comparison between these subgiants, and find out the limits of what we can learn from comparative asteroseismology, which refers to analysing an ensemble of similar stars having subtle differences,

and evaluate these differences in the context of stellar structure and evolution.

Chapter 5

Summary and Outlook

In this dissertation I have shown examples to what kind of information we can obtain through asteroseismology. Specifically, I have demonstrated that using asteroseismic data we have the opportunity to determine the global properties of the stars with high precision, and more importantly, uncover their interiors, which we have no possibility to observe directly. I have presented results regarding some individual solar-like stars, and mainly have focussed on those more evolved than the Sun. These subgiants are particularly interesting, as they provide us with specific features, the so-called mixed modes. I have shown that these modes not only constrain the stellar age, but also affect the results regarding other global properties.

I have investigated the methods for modelling that would make use of the asteroseismic data to a large extent. I have shown that the precision and accuracy of a stellar model to represent an observed star increases with the inclusion of individual mode parameters. However, pipeline approach towards stellar modelling provides a very good starting point for a more detailed model search. Also, in the cases where the individual parameters are not available, the pipelines making use of the average seismic parameters still increases the precision of the stellar parameters over the modelling performed using only the classical atmospheric parameters.

I have also presented the practical use of some modifications in relation to the frequency calculations to ease the comparison between the model and observed frequencies, one having been formulated using observational data, namely the near-surface corrections, and the other being a result of a theoretical work on dipolar mode identification.

In the light of what has been presented in the preceding chapters, it is certain that there is a great deal of information to be uncovered through asteroseismology. The quality of the existing observational data has brought new challenges both for the data analysis and the modelling aspects. This is exactly what has been desired in order to develop a better understanding of the stellar interiors, and asteroseismology is currently the most powerful tool for this purpose.

As briefly discussed in Chapter 4, the sharp features in the stellar interiors, like the location of H and He ionization zones, boundaries of the outer convection zone and inner convective core can be investigated in more detail with the help of high quality asteroseismic

data. The techniques for doing so need to be improved.

One of the important problems in stellar evolution and pulsation that is left out of this thesis is rotation. So far, it has been a common practice to neglect rotation in slowly rotating solar-like stars. The reason is the difficulty of clearly detecting the rotational splitting of nonradial modes. However, with longer data on these stars, it may become possible to detect these splittings unambiguously. When that is the case, we will be urged to include rotation into the calculations, and hence test the liability of the existing treatments.

As mentioned throughout the text, one of our main goals is to test the existing theories of stellar structure, evolution, and pulsation. In this respect, seismic observations coupled with classical stellar data show that the existing models serve very well in mimicking the stars regarding the general aspects, as expected. However, neglecting the complications that are difficult to model has already shown potential to keep us from going further. Fortunately, there are ongoing theoretical efforts to develop better representative models with respect to these complexities such as the turbulent convection and nonadiabaticity. Once these processes are represented better by the stellar models, asteroseismology will also play a role in improving the current understanding related the other crucial aspects of the stellar structure, like the equation of state, opacity, and nuclear reaction rates. With the acquisition of more data we will be able to test many more aspects than those discussed here.

Bibliography

- Adelberger, E. G., Austin, S. M., Bahcall, J. N., et al. 1998, *Reviews of Modern Physics*, 70, 1265
- Aerts, C., Christensen-Dalsgaard, J., & Kurtz, D. W. 2010, *Asteroseismology*, Springer, Heidelberg
- Aizenman, M., Smeyers, P., & Weigert, A. 1977, *A&A*, 58, 41
- Angulo, C., Arnould, M., Rayet, M., et al. 1999, *Nuclear Physics A*, 656, 3
- Arentoft, T., Kjeldsen, H., Bedding, T. R., et al. 2008, *ApJ*, 687, 1180
- Asplund, M., Grevesse, N., & Sauval, A. J. 2005, in *Astronomical Society of the Pacific Conference Series*, Vol. 336, *Cosmic Abundances as Records of Stellar Evolution and Nucleosynthesis*, ed. T. G. Barnes III & F. N. Bash, 25
- Asplund, M., Grevesse, N., Sauval, A. J., & Scott, P. 2009, *ARA&A*, 47, 481
- Baglin, A., Auvergne, M., Barge, P., et al. 2002, in *ESA Special Publication*, Vol. 485, *Stellar Structure and Habitable Planet Finding*, ed. B. Battrock, F. Favata, I. W. Roxburgh, & D. Galadi, 17–24
- Bahcall, J. N., Pinsonneault, M. H., & Wasserburg, G. J. 1995, *Reviews of Modern Physics*, 67, 781
- Bazot, M., Bourguignon, S., & Christensen-Dalsgaard, J. 2008, *Mem. Soc. Astron. Italiana*, 79, 660
- Bedding, T. R., Butler, R. P., Kjeldsen, H., et al. 2001, *ApJ*, 549, L105
- Bedding, T. R. & Kjeldsen, H. 2003, *PASA*, 20, 203
- Bedding, T. R., Kjeldsen, H., Arentoft, T., et al. 2007, *ApJ*, 663, 1315
- Bedding, T. R., Kjeldsen, H., Campante, T. L., et al. 2010, *ApJ*, 713, 935
- Böhm-Vitense, E. 1958, *Zeitschrift für Astrophysik*, 46, 108

BIBLIOGRAPHY

- Bonanno, A., Schlattl, H., & Paternò, L. 2002, *A&A*, 390, 1115
- Brandão, I. M., Doğan, G., Christensen-Dalsgaard, J., et al. 2010, *A&A*, in revision
- Brickhill, A. J. 1991, *MNRAS*, 251, 673
- Brown, T. M., Gilliland, R. L., Noyes, R. W., & Ramsey, L. W. 1991, *ApJ*, 368, 599
- Bruntt, H., Bedding, T. R., Quirion, P., et al. 2010, *MNRAS*, 746
- Chaplin, W. J., Appourchaux, T., Elsworth, Y., et al. 2010, *ApJ*, 713, L169
- Chaplin, W. J., Elsworth, Y., Isaak, G. R., Miller, B. A., & New, R. 1999, *MNRAS*, 308, 424
- Christensen-Dalsgaard, J. 1976, *MNRAS*, 174, 87
- Christensen-Dalsgaard, J. 1988, in *IAU Symposium*, Vol. 123, *Advances in Helio- and Asteroseismology*, ed. J. Christensen-Dalsgaard & S. Frandsen, 295
- Christensen-Dalsgaard, J. 1993, in *Astronomical Society of the Pacific Conference Series*, Vol. 42, *GONG 1992. Seismic Investigation of the Sun and Stars*, ed. T. M. Brown, 347
- Christensen-Dalsgaard, J. 2002, *Reviews of Modern Physics*, 74, 1073
- Christensen-Dalsgaard, J. 2008a, *Ap&SS*, 316, 13
- Christensen-Dalsgaard, J. 2008b, *Ap&SS*, 316, 113
- Christensen-Dalsgaard, J. 2009, in *IAU Symposium*, Vol. 258, *IAU Symposium*, ed. E. E. Mamajek, D. R. Soderblom, & R. F. G. Wyse, 431–442
- Christensen-Dalsgaard, J. & Däppen, W. 1992, *A&A Rev.*, 4, 267
- Christensen-Dalsgaard, J., Dappen, W., Ajukov, S. V., et al. 1996, *Science*, 272, 1286
- Christensen-Dalsgaard, J., di Mauro, M. P., Houdek, G., & Pijpers, F. 2009, *A&A*, 494, 205
- Christensen-Dalsgaard, J. & Gough, D. O. 2001, *MNRAS*, 326, 1115
- Christensen-Dalsgaard, J. & Houdek, G. 2010, *Ap&SS*, 328, 51
- Christensen-Dalsgaard, J., Proffitt, C. R., & Thompson, M. J. 1993, *ApJ*, 403, L75
- Claverie, A., Isaak, G. R., McLeod, C. P., van der Raay, H. B., & Cortes, T. R. 1979, *Nature*, 282, 591
- De Ridder, J., Barban, C., Baudin, F., et al. 2009, *Nature*, 459, 398

- Deheuvels, S. & Michel, E. 2010, *Ap&SS*, 328, 259
- Di Mauro, M. P., Christensen-Dalsgaard, J., & Paternò, L. 2003, *Ap&SS*, 284, 229
- Domingo, V., Fleck, B., & Poland, A. I. 1995, *Sol. Phys.*, 162, 1
- Doğan, G., Bonanno, A., Bedding, T. R., et al. 2010a, *ArXiv* 1006.5912
- Doğan, G., Bonanno, A., & Christensen-Dalsgaard, J. 2010b, *ArXiv* 1004.2215
- Doğan, G., Brandão, I. M., Bedding, T. R., et al. 2010c, *Ap&SS*, 328, 101
- Doğan, G., Christensen-Dalsgaard, J., & Takata, M. 2008, *Communications in Asteroseismology*, 157, 301
- Dziembowski, W. A., Fiorentini, G., Ricci, B., & Sienkiewicz, R. 1999, *A&A*, 343, 990
- Elsworth, Y., Howe, R., Isaak, G. R., et al. 1995, in *Astronomical Society of the Pacific Conference Series*, Vol. 76, *GONG 1994. Helio- and Astro-Seismology from the Earth and Space*, ed. R. K. Ulrich, E. J. Rhodes Jr., & W. Dappen, 392
- Fernandes, J. & Monteiro, M. J. P. F. G. 2003, *A&A*, 399, 243
- Gautschy, A. 1997, *Vistas in Astronomy*, 41, 95
- Grec, G., Fossat, E., & Pomerantz, M. A. 1983, *Sol. Phys.*, 82, 55
- Grevesse, N. & Noels, A. 1993, in *Origin and Evolution of the Elements*, ed. N. Prantzos, E. Vangioni-Flam, & M. Casse, 15–25
- Grundahl, F., Christensen-Dalsgaard, J., Arentoft, T., et al. 2008, *Communications in Asteroseismology*, 157, 273
- Harvey, J. W., Hill, F., Hubbard, R. P., et al. 1996, *Science*, 272, 1284
- Houdek, G. 2006, in *ESA Special Publication*, Vol. 624, *Proceedings of SOHO 18/GONG 2006/HELAS I, Beyond the spherical Sun*
- Houdek, G., Balmforth, N. J., Christensen-Dalsgaard, J., & Gough, D. O. 1999, *A&A*, 351, 582
- Houdek, G. & Gough, D. O. 2007, *MNRAS*, 375, 861
- Kjeldsen, H. & Bedding, T. R. 1995, *A&A*, 293, 87
- Kjeldsen, H., Bedding, T. R., & Christensen-Dalsgaard, J. 2008, *ApJ*, 683, L175
- Kjeldsen, H., Bedding, T. R., Viskum, M., & Frandsen, S. 1995, *AJ*, 109, 1313
- Koch, D. G., Borucki, W. J., Basri, G., et al. 2010, *ApJ*, 713, L79

BIBLIOGRAPHY

- Lazrek, M., Baudin, F., Bertello, L., et al. 1997, *Sol. Phys.*, 175, 227
- Lee, U. 1985, *PASJ*, 37, 279
- Leighton, R. B., Noyes, R. W., & Simon, G. W. 1962, *ApJ*, 135, 474
- Metcalfe, T., Monteiro, M. J. P. F. G., Thompson, M. J., et al. 2010, *ApJ*, in print
- Metcalfe, T. S., Creevey, O. L., & Christensen-Dalsgaard, J. 2009, *ApJ*, 699, 373
- Michaud, G. & Proffitt, C. R. 1993, in *Astronomical Society of the Pacific Conference Series*, Vol. 40, IAU Colloq. 137: Inside the Stars, ed. W. W. Weiss & A. Baglin, 246–259
- Miglio, A., Montalbán, J., Carrier, F., et al. 2010, *ArXiv* 1009.1024
- Monteiro, M. J. P. F. G. & Thompson, M. J. 2005, *MNRAS*, 361, 1187
- Osaki, J. 1975, *PASJ*, 27, 237
- Parker, P. D. M. 1986, in *Physics of the Sun. Volume 1*, ed. P. A. Sturrock, T. E. Holzer, D. M. Mihalas, & R. K. Ulrich, Vol. 1, 15–32
- Pesnell, W. D. 1987, *ApJ*, 314, 598
- Rogers, F. J. & Nayfonov, A. 2002, *ApJ*, 576, 1064
- Roxburgh, I. W. & Vorontsov, S. V. 2003, *A&A*, 411, 215
- Saio, H. 1993, *Ap&SS*, 210, 61
- Samadi, R., Goupil, M., & Houdek, G. 2002, *A&A*, 395, 563
- Scuflaire, R. 1974, *A&A*, 36, 107
- Stello, D., Chaplin, W. J., Bruntt, H., et al. 2009, *ApJ*, 700, 1589
- Takata, M. 2005, *PASJ*, 57, 375
- Takata, M. 2006, *PASJ*, 58, 893
- Tassoul, M. 1980, *ApJS*, 43, 469
- Trampedach, R. 2010, *Ap&SS*, 328, 213
- Tripathy, S. C. & Christensen-Dalsgaard, J. 1998, *A&A*, 337, 579
- Unno, W., Osaki, Y., Ando, H., Saio, H., & Shibahashi, H. 1989, *Nonradial oscillations of stars*, ed. Unno, W., Osaki, Y., Ando, H., Saio, H., & Shibahashi, H.
- Weiss, A. & Schlattl, H. 2008, *Ap&SS*, 316, 99

Part II

Relevant publications and related work

List of Publications

Refereed papers

Asteroseismic modelling of the solar-type subgiant star β Hydri, I. M. Brandão, **G. Doğan**, J. Christensen-Dalsgaard, M. S. Cunha, T. R. Bedding, T. S. Metcalfe, H. Kjeldsen, H. Bruntt, T. Arentoft, A&A, in revision by the authors for minor changes

A precise asteroseismic age and radius for the evolved sun-like star KIC 11026764, T. S. Metcalfe and 57 coauthors including **G. Doğan**, ApJ, accepted

The asteroseismic potential of Kepler : First results for solar-type stars, W. J. Chaplin and 108 coauthors including **G. Doğan**, 2010, ApJ Letters 713, L169

SPB stars in the open SMC cluster NGC 371, C. Karoff, T. Arentoft, L. Glowienka, C. Coutures, T. B. Nielsen, **G. Doğan**, F. Grundahl and H. Kjeldsen, 2008, MNRAS, 386, 1085

Peer-reviewed conference proceedings

Asteroseismology of solar-type stars with Kepler II: Stellar Modeling, T. S. Metcalfe, M.J.P.F.G. Monteiro, M.J. Thompson, W.J. Chaplin, S. Basu, A. Bonanno, M.P. Di Mauro, **G. Doğan**, P. Eggenberger, C. Karoff, D. Stello, and KASC WG1 members), AN, accepted

Asteroseismic modelling of Procyon A: Preliminary results, **G. Doğan**, A. Bonanno, T. R. Bedding, T. L. Campante, J. Christensen-Dalsgaard, and H. Kjeldsen, AN, accepted

Asteroseismic modelling of the solar-like star β Hydri, **G. Doğan**, I. M. Brandão, T. R. Bedding, J. Christensen-Dalsgaard, M. S. Cunha, H. Kjeldsen, 2010, ApSS 328, 101

Massive B-type pulsators in low-metallicity environments, C. Karoff, T. Arentoft, L. Glowienka, C. Coutures, T. B. Nielsen, **G. Doğan**, F. Grundahl and H. Kjeldsen, 2009, CoAst 158, 174K

Dipole modes of stellar oscillations, **G. Doğan**, J. Christensen-Dalsgaard, and M. Takata, 2008, CoAst 157, 301D

Conference proceedings without referee

Near-surface effects and solar-age determination, **G. Doğan**, A. Bonanno, and J. Christensen-Dalsgaard, AN

Appendix A

Dipole modes of stellar oscillations

Comm. in Asteroseismology
 Vol. 157, 2008, Wrocław HELAS Workshop 2008
 M. Breger, W. Dziembowski, & M. Thompson, eds.

Dipole modes of stellar oscillations

G. Dogan¹, J. Christensen-Dalsgaard¹, and M. Takata²

¹ Department of Physics and Astronomy, University of Aarhus,
 Ny Munkegade, Building 1520, DK-8000 Aarhus C, Denmark

² Department of Astronomy, School of Science, University of Tokyo,
 Bunkyo-ku, Tokyo 113-0033, Japan

Abstract

We focus on dipole mode stellar oscillations (with $l=1$) which have been a challenge in identifying the modes. We make use of a new mode identification scheme specific to these oscillations.

Introduction

Nonradial stellar oscillations are governed by a fourth-order system of differential equations which is difficult to treat analytically. Nevertheless, there has been a specific treatment suggested only for dipole-mode oscillations (Takata 2005), which decreases the system of equations from fourth to second order. We apply this new treatment to realistic stellar models and check its validity.

Classification of modes

Stellar oscillation modes are investigated, in a broad sense, under two categories: the acoustic modes (p modes), and the gravity modes (g modes), with the restoring force being pressure and buoyancy, respectively. In most cases, but not for dipolar oscillations, there is also an intermediate fundamental mode, the so-called f mode, which has no radial node (for a detailed discussion; see Christensen-Dalsgaard & Gough 2001). Conventional mode identification is made by analyzing the movement of the phase point on the phase diagram plotted using two variables (y_1, y_2), where $y_1 = \xi_r/r$, and $y_2 = \sqrt{l(l+1)} \frac{\xi_h}{R}$, with ξ_r and ξ_h being the radial and horizontal displacements, respectively. The nodes of ξ_r are used to determine the label of the mode together with the direction of the phase point while going around the origin of the phase diagram at the node: it is called a g node (or p node) if the movement is clockwise (or counterclockwise): see Takata (2006) for details. The number of p and g nodes (n_p and n_g) are counted and then a mode is labelled according to the sign of radial order n , where $n = n_p - n_g$. If $n > 0$, the mode is labelled as a p mode, while it is labelled as a g mode if $n < 0$. However, this classification fails to be valid for dipolar modes. Low-order dipolar modes, labelled according to the phase diagram based on the radial and horizontal displacements, change their order as the star evolves, while a proper labelling should be invariant under the evolution. This failure comes from the fact that we can justify the conventional scheme only when we neglect the gravitational potential perturbation (ϕ'), which is not small in the condensed core of the evolved stars. Based on the identity derived by Takata (2005), which takes into account the contribution from ϕ' , Takata (2006)

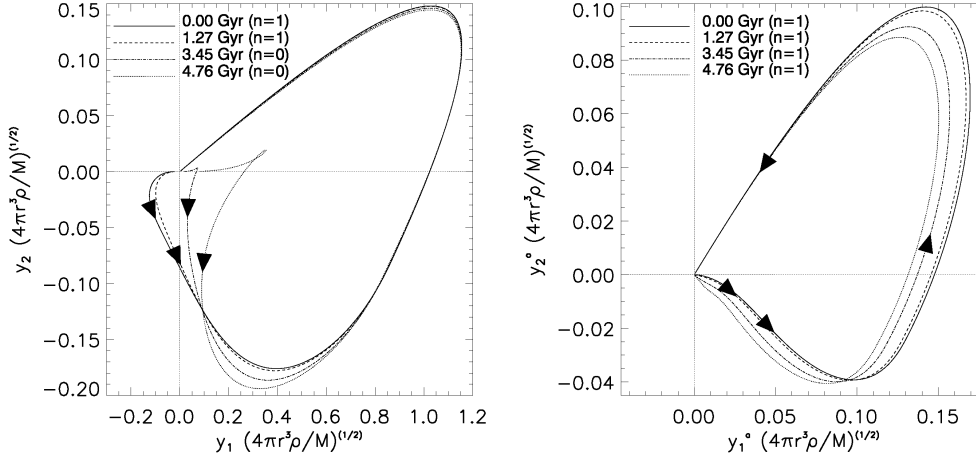


Figure 1: Evolution of an $l = 1$ mode for a model with $M = 1M_{\odot}$, and metallicity $Z=0.02$. Starting from the origin, phase points move in the direction of the arrows.

showed that an invariant labelling can be based on the pair of variables (y_1^a, y_2^a) , where $y_1^a = \frac{J\xi_r}{r} + \frac{1}{3g}(\frac{\phi'}{r} - \frac{d\phi'}{dr})$, and $y_2^a = \frac{Jp'}{\rho gr} + \frac{1}{3g}(\frac{\phi'}{r} - \frac{d\phi'}{dr})$, with $J = 1 - \frac{4\pi\rho r^3}{3M_r}$. Using these new variables; $n = n_p - n_g$ if $n_p < n_g$, while $n = n_p - n_g + 1$ if $n_p \geq n_g$. The dependence of labelling (as p or g mode) on n is as described before. Fig. 1 shows the phase diagrams plotted using the old (left panel) and the new variables (right panel).

The new definition appears to be a solution to the problem of dipolar mode labelling, at least for stars from the main sequence through the subgiant branch.

References

- Christensen-Dalsgaard, J., & Gough, D. O. 2001, MNRAS, 326, 1115
 Takata, M. 2005, PASJ, 57, 375
 Takata, M. 2006, PASJ, 58, 893

Appendix B

Near-surface effects and solar-age determination

Near-surface effects and solar-age determination

G. Doğan^{1,*}, A. Bonanno² and J. Christensen-Dalsgaard¹

¹ Department of Physics and Astronomy, Aarhus University, Ny Munkegade, DK-8000, Aarhus C, Denmark

² Catania Astrophysical Observatory, Via S.Sofia 78, 95123, Catania, Italy

Received April 2010, accepted —

Published online later

Key words Solar age – near-surface effects

The dominant part of the difference between the observed and model frequencies of the Sun can be approximated by a power law. We show that when this empirical law is employed to correct the model frequencies and then the small frequency separations, $\delta\nu_{02}(n)$, are used for solar age determination, the results are consistent with the meteoritic age ($4.563 \text{ Gyr} < t < 4.576 \text{ Gyr}$). We present the results and compare with those obtained by using the ratios, $r_{02}(n)$, of small to large frequency separations.

© 0000 WILEY-VCH Verlag GmbH & Co. KGaA, Weinheim

1 Introduction

It is known that there is a systematic offset between the observed and model frequencies of the Sun. This offset increases with increasing frequency and is shown (Kjeldsen et al. 2008) to be fitted well with a power law as

$$\nu_{\text{obs}}(n) - \nu_{\text{best}}(n) = a \left[\frac{\nu_{\text{obs}}(n)}{\nu_0} \right]^b, \quad (1)$$

where the power b is determined to be 4.90 for the Sun. Here $\nu_{\text{obs}}(n)$, and $\nu_{\text{best}}(n)$, represent the observed, and the best model, frequencies with spherical degree $l=0$, and radial order n ; ν_0 is a constant frequency (chosen to be $3100 \mu\text{Hz}$ for the Sun), which corresponds to the frequency for peak power in the spectrum. This difference between the observed and calculated frequencies exists due to improper modelling of the outer turbulent convective layers of the Sun. The outer layers affect the high frequencies most, as the upper turning point of the high-frequency waves are closer to the surface. Since all stellar models are calibrated with respect to the Sun, and since, thanks to the recent developments, we are at a stage to have observations of individual frequencies of stars other than the Sun, it is important to understand the effects of near-surface stellar layers on the oscillation frequencies. These effects also influence the small frequency separations, $\delta\nu_{l+2}(n) = \nu_{nl} - \nu_{n-1, l+2}$, and hence, for instance, inferences of stellar ages. Here ν_{nl} is the frequency of a mode with spherical degree l and radial order n . The use of $\delta\nu_{l+2}(n)$ for the purpose of solar-age determination has been presented in earlier works (e.g. Dziembowski et al. 1999; Bonanno et al. 2002). It has also been shown by several authors (e.g. Roxburgh & Vorontsov 2003; Oti Floranes et al. 2005; Christensen-Dalsgaard 2009) that the frequency separation

ratios, $r_{l+2}(n) = (\nu_{nl} - \nu_{n-1, l+2}) / (\nu_{nl} - \nu_{n-1, l})$, are not as sensitive to the near-surface layers. Christensen-Dalsgaard (2009) provides a comparison between the use of $\delta\nu_{l+2}(n)$ and $r_{l+2}(n)$. Here, we present our preliminary results on comparing different ways of using the seismic data for determination of the solar age, including the application of near-surface correction.

2 Tools and methods

We computed a series of standard solar models, using the stellar evolution codes, ASTEC (Christensen-Dalsgaard 2008a) and GARSTEC (Weiss & Schlattl 2008), with different ages while keeping the luminosity, and the surface value of Z/X fixed to $3.846 \times 10^{33} \text{ erg s}^{-1}$, and 0.0245 (Grevesse & Noels 1993), respectively. Here Z is the mass fraction of the elements heavier than helium, and X is that of the hydrogen. Models were computed with the OPAL equation of state (Rogers & Nayfonov 2002), OPAL opacities (Iglesias & Rogers 1996) together with the low-temperature opacities from Alexander & Ferguson 1994, and using the Adelberger et al. (1998) or NACRE (Angulo et al. 1999) nuclear reaction rates. We considered both the commonly used value $R_1 = 6.9599 \times 10^{10} \text{ cm}$ (Auwers 1891) of the solar radius, and the value $R_2 = 6.9551 \times 10^{10} \text{ cm}$ found by Brown & Christensen-Dalsgaard (1998). Models were computed both starting at the zero age main sequence (ZAMS) and including pre-main-sequence (PMS) evolution. We calculated the frequencies of our models using ADIPLS (Christensen-Dalsgaard 2008b), and compared the small frequency separation, $\delta\nu_{02}(n)$, and $r_{02}(n)$ of the models with those of the Sun (BISON, Chaplin et al. 2007). We selected the best model minimizing the following χ^2 , adapted for the separation ratios, $r_{02}(n)$, when relevant:

* e-mail: gulnur@phys.au.dk

Table 1 Ages of the best models

Evolution code + Nuc. reaction rates:	Seismic property used in χ^2	$R_1 = 6.9599 \times 10^{10}$ cm		$R_2 = 6.9551 \times 10^{10}$ cm	
		Age* (before correction)(Gyr)	Age* (after correction)(Gyr)	Age* (before correction)(Gyr)	Age* (after correction)(Gyr)
ASTEC + Angulo et al. (1999)	$\delta\nu_{02}(n)$	4.58 ± 0.05	4.56 ± 0.05	4.60 ± 0.06	4.57 ± 0.06
	$r_{02}(n)$	4.55 ± 0.04	4.55 ± 0.04	4.55 ± 0.05	4.55 ± 0.05
ASTEC + Adelberger et al. (1998)	$\delta\nu_{02}(n)$	4.57 ± 0.05	4.55 ± 0.05	4.59 ± 0.05	4.56 ± 0.06
	$r_{02}(n)$	4.54 ± 0.05	4.54 ± 0.05	4.54 ± 0.05	4.54 ± 0.05
GARSTEC + Angulo et al. (1999)	$\delta\nu_{02}(n)$	4.60 ± 0.08	4.56 ± 0.08	4.61 ± 0.08 (PMS: 4.67 ± 0.08)	4.56 ± 0.08 (PMS: 4.62 ± 0.08)
	$r_{02}(n)$	4.57 ± 0.08	4.57 ± 0.08	4.57 ± 0.08 (PMS: 4.62 ± 0.08)	4.57 ± 0.08 (PMS: 4.62 ± 0.08)

* Evolution starts with ZAMS (Zero Age Main Sequence) unless otherwise stated.

$$\chi^2(\delta\nu_{02}) = \frac{1}{N-1} \sum_n \frac{[\delta\nu_{02}^{\text{obs}}(n) - \delta\nu_{02}^{\text{model}}(n)]^2}{\sigma[\delta\nu_{02}(n)]^2},$$

where N is the number of modes, $\delta\nu_{02}^{\text{obs}}(n)$, and $\delta\nu_{02}^{\text{model}}(n)$ are the small frequency separations from the observations and the models; $\sigma[\delta\nu_{02}(n)]$ represents the uncertainty in the observed $\delta\nu_{02}(n)$. We repeated this comparison for $\delta\nu_{02}(n)$ and $r_{02}(n)$ of the surface-corrected frequencies (cf. Eq. 1).

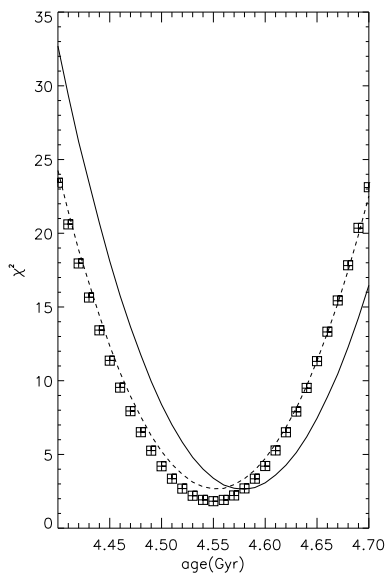


Fig. 1 The results with R_1 , using NACRE (Angulo et al. 1999). We present the χ^2 obtained using $\delta\nu_{02}(n)$ of the uncorrected model frequencies (solid line), $\delta\nu_{02}(n)$ of the corrected model frequencies (dashed line), $r_{02}(n)$ of the uncorrected model frequencies (squares), and $r_{02}(n)$ of the corrected model frequencies (crosses).

3 Results and discussion

The results of the age determinations using different input, as described in Section 2, are summarized in Table 1, and one of the cases is illustrated in Fig. 1.

The ages of our best models found using the two different evolution codes are consistent within the error limits, differing by 0.7% at most, and they are also compatible with the values in the literature obtained by employing small frequency separations: 4.57 ± 0.11 Gyr (Bonanno et al. 2002), and 4.66 ± 0.11 Gyr (Dziembowski et al. 1999). Moreover, our two sets of results agree with the meteoritic age, 4.563 Gyr $< t < 4.576$ Gyr (Wasserburg, in Bahcall & Pinsonneault 1995), within the uncertainty limits.

In principle we can determine the duration of the PMS evolution, up to the ZAMS, by calibrating the models using PMS evolution to get the meteoritic age of the Sun (see, e.g. Morel et al. 2000, for a discussion on the definition of ZAMS). Our preliminary analysis suggests that the PMS evolution for the Sun is 0.05 ± 0.11 Gyr in order to be consistent with the meteoritic age. A more precise and detailed analysis is obviously needed for defining ZAMS.

The results obtained using separation ratios are consistent with those obtained using the small frequency separation of the corrected frequencies. However, since the application of the surface correction has no significant effect on the age determined by the separation ratios, using these ratios yields a more robust age determination.

Acknowledgements. This work was supported by the European Helio- and Asteroseismology Network (HELAS), a major international collaboration funded by the European Commission's Sixth Framework Programme. GD and JC-D acknowledge financial support from the Danish Natural Science Research Council.

References

- Adelberger, E. G., Austin, S. M., Bahcall, J. N. et al.: 1998, Rev. Mod. Phys. 70, 1265
Alexander, D. R. & Ferguson, J. W.: 1994, ApJ 437, 879
Angulo, C., Arnould, M., Rayet, M. et al.: 1999, Nucl. Phys. A 656, 3

- Auwers, A.: 1891, AN 128, 361
Bahcall, J. N. & Pinsonneault, M. H. (with an appendix by G. J. Wasserburg): 1995, Rev. Mod. Phys. 67, 781
Bonanno, A., Schlattl, H. & Paternò, L.: 2002, A&A 390, 1115
Brown, T. M. & Christensen-Dalsgaard, J.: 1998, ApJ 500, L195
Chaplin, W. J., Serenelli, A. M., Basu, S., Elsworth, Y., New, R. & Verner, G. A.: 2007, ApJ 670, 872
Christensen-Dalsgaard, J.: 2008a, Ap&SS 316, 13
Christensen-Dalsgaard, J.: 2008b, Ap&SS 316, 113
Christensen-Dalsgaard, J.: 2009, IAUS 258, 431C
Dziembowski, W.A., Fiorentini, G., Ricci, B. & Sienkiewicz, R.: 1999, A&A 343, 990
Grevesse, N. & Noels, A.: 1993, in *Origin and Evolution of the Elements*, edited by N. Prantzos, E. Vangioni-Flam & M. Cassé, (Cambridge: Cambridge Univ. Press), p. 15
Iglesias, C. A. & Rogers, F. J.: 1996, ApJ 464, 943
Kjeldsen, H., Bedding, T. R. & Christensen-Dalsgaard, J.: 2008, ApJ 683, L175
Morel, P., Provost, J. & Berthomieu, G.: 2000, A&A 353, 771
Oti Floranes, H., Christensen-Dalsgaard, J. & Thompson, M. J.: 2005, MNRAS 356, 671
Rogers, F. J. & Nayfonov, A.: 2002, ApJ 576, 1064
Roxburgh, I. W. & Vorontsov, S. V.: 2003, A&A 411, 215
Weiss, A. & Schlattl, H.: 2008, Ap&SS 316, 99

Appendix C

Asteroseismic modelling of
the solar-like star β Hydri

Asteroseismic modelling of the solar-like star β Hydri

G. Doğan · I.M. Brandão · T.R. Bedding ·
J. Christensen-Dalsgaard · M.S. Cunha · H. Kjeldsen

Received: 14 September 2009 / Accepted: 20 November 2009 / Published online: 11 December 2009
© Springer Science+Business Media B.V. 2009

Abstract We present the results of modelling the subgiant star β Hydri using seismic observational constraints. We have computed several grids of stellar evolutionary tracks using the Aarhus STellar Evolution Code (ASTEC, Christensen-Dalsgaard in *Astrophys. Space Sci.* 316:13, 2008a), with and without helium diffusion and settling. For those models on each track that are located at the observationally determined position of β Hydri in the Hertzsprung-Russell (HR) diagram, we have calculated the oscillation frequencies using the Aarhus adiabatic pulsation package (ADIPLS, Christensen-Dalsgaard in *Astrophys. Space Sci.* 316:113, 2008b). Applying the near-surface corrections to the calculated frequencies using the empirical law presented by Kjeldsen et al. (*Astrophys. J.* 683:L175, 2008), we have compared the corrected model frequencies with the observed frequencies of the star. We show that after correcting the frequencies for the near-surface effects, we have a fairly good fit for both $l = 0$ and $l = 2$ frequencies. We also have good agreement between the observed and calculated $l = 1$ mode frequencies, although there is room for improvement in order to fit all the observed mixed modes simultaneously.

Keywords Beta Hydri · Solar-like oscillations

G. Doğan (✉) · J. Christensen-Dalsgaard · H. Kjeldsen
Department of Physics and Astronomy, Aarhus University, Århus,
Denmark
e-mail: gulnur@phys.au.dk

I.M. Brandão
Centro de Astrofísica da Universidade do Porto, Porto, Portugal

I.M. Brandão · M.S. Cunha
Faculdade de Ciências, Universidade do Porto, Porto, Portugal

T.R. Bedding
School of Physics A29, University of Sydney, Sydney, Australia

1 Introduction

β Hydri is a G2-type subgiant star exhibiting solar-like oscillations. It is often referred to as the future of the Sun because it has parameters (Table 1) close to those of the Sun, in addition to being at a later evolutionary stage than the Sun. Being rather evolved, β Hydri exhibits mixed modes in its observed spectrum. This makes the star particularly interesting for asteroseismic studies, as mixed modes carry more information about the core than do the regular p-mode frequencies.

An extensive analysis of this star was done by Fernandes and Monteiro (2003), who emphasized the possibility of employing seismic constraints to remove partially the parameter degeneracy that exists when only the non-seismic observational constraints (such as T_{eff} and luminosity) are used. Those constraints alone are not enough, as one can obtain the same location of a stellar model in the Hertzsprung-Russell (HR) diagram using different stellar parameters (such as mass, X , Y , Z , etc.). Fernandes and Monteiro (2003) used the large frequency separation, $\Delta\nu_0$, obtained by Bedding et al. (2001), to show how to constrain the mass independently and also noted the need for individual frequencies to further constrain the age of the star using the characteristics of the frequency spectrum that are related to the stellar core, such as mixed modes.

The first preliminary comparison of the individual observed frequencies and model frequencies was done by Di Mauro et al. (2003). They presented a model with large and small frequency separations that are within the limits derived from the observations (Bedding et al. 2001). They showed that the match between the model and observed frequencies is satisfactory except for the $l = 1$ modes, some of which are affected by avoided crossings. This emphasizes again the importance of accurate asteroseismic observations and detailed analysis to evaluate the stellar interiors.

Here, we use the latest asteroseismic observational constraints (Bedding et al. 2007) consisting of individual frequencies including some modes which are identified to be possible mixed modes. We present the methods to search for a best model and the resulting best fits within the parameter space of our survey.

2 Methods

We started calculating the grids of evolutionary tracks with a wide range of parameters and large steps of increment. Analyzing the first grid, we have selected the best models, around which we have computed denser grids. The initial parameters of the grids are given in Table 2. Diffusion and gravitational settling of helium are added in the third grid, in which not all the tracks have been successfully completed. We have carried on our analysis with the tracks that did not have convergence problems.

On each track in the grids, we have selected the models having parameters within the observational uncertainty limits. We have calculated the oscillation frequencies of those models and compared them with the observations. For comparison we used the frequencies resulting from dual-site radial velocity observations with HARPS and UCLES spectrographs (Bedding et al. 2007).

Before comparing the calculated frequencies with the observed ones, we have applied near-surface corrections to the

calculated frequencies. The correction is needed due to the fact that existing stellar models fail to represent properly the near-surface layers of the solar-like stars, where the turbulent convection takes place. This affects the high frequencies most; thus the correction should be applied in a way so that low frequencies are much less affected.

The situation is the same for the Sun, and the difference between observed and calculated frequencies is shown to be well approximated by the empirical power law given by Kjeldsen et al. (2008) as

$$\nu_{\text{obs}}(n) - \nu_{\text{best}}(n) = a \left[\frac{\nu_{\text{obs}}(n)}{\nu_0} \right]^b, \quad (1)$$

where ν_{obs} are the observed $l = 0$ frequencies with radial order n , ν_{best} are the corresponding calculated frequencies of the best model, and ν_0 is a constant frequency chosen to be the frequency corresponding to the peak power in the spectrum, which is taken as 1000 μHz for β Hydri. Kjeldsen et al. (2008) used the solar data and models to calibrate the exponent b , which is calculated as 4.90 for the Sun. Using this solar b value, and calculating a for each model, we have applied the near-surface corrections to the model frequencies. The corrections for mixed modes are probably less than for pure p modes, as discussed by Kjeldsen et al. (2008), and so we have set them to zero. We have then selected the best models performing a chi-square minimization test for the goodness of the fit as

$$\chi^2 = \frac{1}{N} \sum_{n,l} \left(\frac{\nu_l^{\text{model}}(n) - \nu_l^{\text{obs}}(n)}{\sigma(\nu_l^{\text{obs}}(n))} \right)^2, \quad (2)$$

where N is the total number of modes included, $\nu_l^{\text{obs}}(n)$, and $\nu_l^{\text{model}}(n)$ are the observed frequencies, and the corrected model frequencies, respectively, for each spherical degree l and the radial order n , and σ represents the uncertainty in the observed frequencies.

3 Results

The properties of our best models are given in Table 3, with the corresponding so-called échelle diagrams in Figs. 1 and

Table 1 Parameters of β Hydri as given in the literature. The radius was derived from the interferometric angular diameter (North et al. 2007) and the revised Hipparcos parallax (van Leeuwen 2007). The mass was then derived from the mean density from asteroseismology

Parameter	Value	Reference
M/M_{\odot}	1.085 ± 0.028	Kjeldsen et al. 2008
R/R_{\odot}	1.809 ± 0.015	Kjeldsen et al. 2008
L/L_{\odot}	3.494 ± 0.087	Current work
T_{eff} (K)	5872 ± 44	North et al. 2007
[Fe/H]	-0.08 ± 0.04	Santos et al. 2005
$\Delta\nu_0$ (μHz)	57.24 ± 0.16	Bedding et al. 2007

Table 2 Parameters used to compute the evolutionary tracks

Parameter	Grid 1	Grid 2	Grid 3
M/M_{\odot}	1.04–1.10 (with steps of 0.01)	1.076–1.084 (with steps of 0.002)	1.076–1.084 (with steps of 0.002)
Z/X	0.018–0.022 (with steps of 0.001)	0.018–0.022 (with steps of 0.001)	0.018–0.022 (with steps of 0.001)
Y	0.23, 0.27, 0.28, 0.30	0.276–0.284 (with steps of 0.002)	0.276–0.284 (with steps of 0.002)
Mixing length parameter (α)	1.4–1.8 (with steps of 0.2)	1.75–1.85 (with steps of 0.025)	1.75–1.85 (with steps of 0.025)
Diffusion & gravitational settling	None	None	He

Table 3 Parameters of the best models

Parameter	From grid 2	From grid 3
M/M_{\odot}	1.082	1.082
Z	0.01346	0.01266
Y	0.278	0.284
α	1.825	1.775
Age (Gyr)	6.447	5.712
R/R_{\odot}	1.814	1.806
L/L_{\odot}	3.444	3.473
T_{eff} (K)	5844	5869
a	-2.76	-3.76
χ^2	7.71	11.93

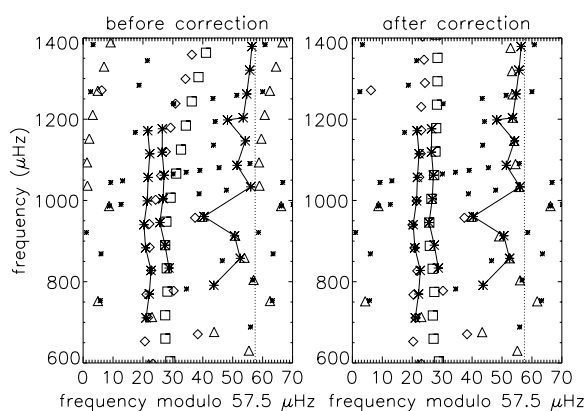


Fig. 1 Échelle diagram of the best model without gravitational settling or diffusion. *Left (right) panel* shows the case before (after) applying near-surface corrections. Stars denote the observations, squares correspond to the model frequencies with $l = 0$, triangles to the model frequencies with $l = 1$, and diamonds to the model frequencies with $l = 2$. Dashed vertical lines indicate the value of the large frequency separation, $\Delta\nu_0$

2 (see Christensen-Dalsgaard (2004) and references therein for the explanation of an échelle diagram). The increase in the systematic difference between the observed and model frequencies with increasing frequency can be seen in the left panels of the échelle diagrams.

The échelle diagrams include all the observed frequencies, while those having identified modes are connected by a solid line for clarity. The observed frequencies which are not connected by a line and shown with smaller symbols are the ones that are not assigned a mode by the observers (Bedding et al. 2007); however, they note that those frequencies will include some genuine modes although some of them might be sidelobes or noise peaks. The sizes of the largest symbols cover approximately $1.5\text{-}\sigma$ uncertainty to both sides on the horizontal axis. Three of the identified $l = 1$ frequencies that fall to the left side of the $l = 1$ ridge are identified as mixed modes by the observers (Bedding et al. 2007).

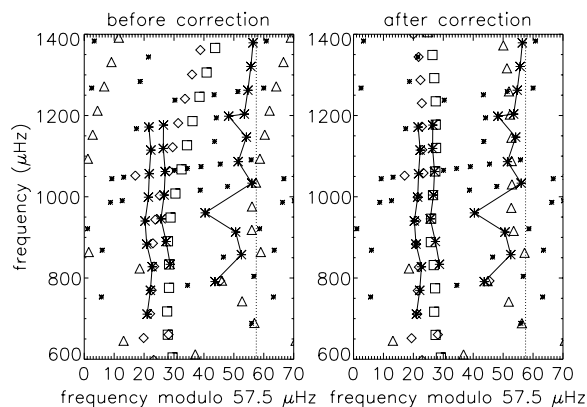


Fig. 2 Échelle diagram of the best model with He settling and diffusion. The symbols are used in the same way as in Fig. 1

The model without He settling or diffusion reproduces the observed frequencies very well except for the lowest mixed mode. It is seen from Fig. 1 that some of the unidentified observed frequencies also match the model frequencies quite well. When the diffusion and settling of helium is added, the agreement between the model and the observations is less strong than in the previous case. Although the lowest mixed mode is reproduced in this model, the mixed mode having the sharpest character (largest departure from the $l = 1$ ridge) is not. The highest mixed mode has not been reproduced by any model frequency with $l = 1$, suggesting that $l = 3$ frequencies might be investigated to search for a match to that frequency. The positions of both models on the subgiant branch are shown in Fig. 3. The model with diffusion is younger due to having completed the main sequence phase faster, as the hydrogen mass fraction decreases faster owing to diffusion and settling bringing helium to the core. Furthermore, the hook shape in the evolutionary track with diffusion is due to the fact that the star had grown a convective core up to an extent where it contained almost 4% of the stellar mass.

4 Conclusions

Our results justify that the empirical power law representing the effect of near-surface layers in the Sun works for β Hydri as well. Our best models with and without He settling and diffusion reproduce the observed $l = 0$ and $l = 2$ modes well; however, the fit at $l = 1$ modes is relatively poor due to the mixed modes, but still satisfactory. It is important to investigate the possibility of any of the observed modes being an $l = 3$ mode.

Furthermore, our results are in agreement with the findings of Fernandes and Monteiro (2003), who derived, through HR diagram analysis, the mass to be $1.10^{+0.04}_{-0.07} M_{\odot}$,

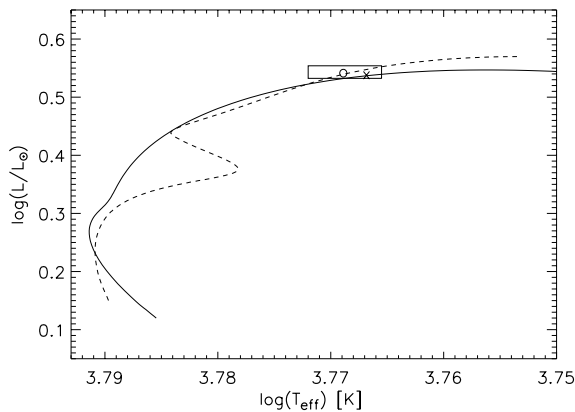


Fig. 3 Evolutionary tracks with He settling and diffusion (*dashed curve*, the best model marked with a *circle*) and without (*solid curve*, the best model marked with a *cross*)

the helium abundance to be between 0.25 and 0.30, and the stellar age to be between 6.4 and 7.1 Gyr. We, however, note that the age of our model with helium diffusion is less than the lower limit of the cited result. Employing $\Delta\nu_0$, they found the mass to be $1.09 \pm 0.22 M_{\odot}$, noting that the large uncertainty is to be improved with the improved accuracy of the observations. Further analysis may be carried out to investigate the effect of convective core overshooting, as our

models had convective cores at some earlier stage in their evolution.

Acknowledgements GD would like to thank Travis S. Metcalfe for helpful discussions regarding the analysis. This research has been partially supported by the Danish Natural Science Research Council. IMB acknowledges the support by the grant SFRH/BD/41213/2007 from FCT/MCTES, Portugal.

References

- Bedding, T.R., Butler, R.P., Kjeldsen, H., et al.: *Astrophys. J.* **549**, L105 (2001)
- Bedding, T.R., Kjeldsen, H., Arentoft, T., et al.: *Astrophys. J.* **663**, 1315 (2007)
- Christensen-Dalsgaard, J.: *Sol. Phys.* **220**, 137 (2004)
- Christensen-Dalsgaard, J.: *Astrophys. Space Sci.* **316**, 13 (2008a)
- Christensen-Dalsgaard, J.: *Astrophys. Space Sci.* **316**, 113 (2008b)
- Di Mauro, M.P., Christensen-Dalsgaard, J., Paternò, L.: *Astrophys. Space Sci.* **284**, 229 (2003)
- Fernandes, J., Monteiro, M.J.P.F.G.: *Astron. Astrophys.* **399**, 243 (2003)
- Kjeldsen, H., Bedding, T.R., Christensen-Dalsgaard, J.: *Astrophys. J.* **683**, L175 (2008)
- North, J.R., Davis, J., Bedding, T.R., et al.: *Mon. Not. R. Astron. Soc.* **380**, L80 (2007)
- Santos, N.C., Israelian, G., Mayor, M., et al.: *Astron. Astrophys.* **437**, 1127 (2005)
- van Leeuwen, F.: *Hipparcos, the New Reduction of the Raw Data*, *Astrophys. Space Sci. Library*, vol. 350 (2007)

Appendix D

Asteroseismic modelling of the
solar-type subgiant star β Hydri

Asteroseismic modelling of the solar-type subgiant star β Hydri

I. M. Brandão^{*1,2}, G. Doğan^{*3}, J. Christensen-Dalsgaard³, M. S. Cunha¹, T. R. Bedding⁴, T. S. Metcalfe⁵, H. Kjeldsen³,
H. Bruntt^{3,6}, T. Arentoft³

¹ Centro de Astrofísica da Universidade do Porto, Rua das Estrelas, 4150-762 Porto, Portugal
e-mail: isa@astro.up.pt

² Departamento de Física e Astronomia, Faculdade de Ciências da Universidade do Porto, Portugal

³ Department of Physics and Astronomy, Aarhus University, DK-8000 Aarhus C, Denmark

⁴ Sydney Institute for Astronomy (SIFA), School of Physics, University of Sydney, Australia

⁵ High Altitude Observatory and Technology Development Division, NCAR, Boulder, Colorado, USA

⁶ Observatoire de Paris, LESIA, 5 place Jules Janssen, 92195 Meudon Cedex, France

Received ; accepted

ABSTRACT

Context. The comparison between models and data of pulsating stars is a powerful way to understand the stellar structure better. Moreover, such comparisons are necessary to make improvements to the physics of the stellar models, since they do not yet perfectly represent either the interior or especially the surface layers of stars. β Hydri is an evolved solar-type pulsator with mixed modes in its frequency spectrum, hence very interesting for asteroseismic studies.

Aims. The goal of the present work is to search for a representative model of the solar-type star β Hydri, based on up-to-date non-seismic and seismic data.

Methods. We ran several grids of evolutionary models with different input parameters and different physics, using the stellar evolutionary code ASTEC. For the models that are inside the observed error box of β Hydri we computed their frequencies with the pulsation code ADIPLS. We used two approaches to find the model that best reproduces the observed frequencies of β Hydri: (i) we assume the best model is the one that best reproduces the star's interior based on the radial oscillation frequencies alone; (ii) we assume the best model is the one that produces the lowest value of the χ^2 when comparing the model and observed frequencies, after the model frequencies are corrected for near-surface effects.

Results. We show that after applying a correction for near-surface effects on the frequencies of the best models, we can reproduce well the observed modes, including those which have mixed mode character. The model that gives the lowest value of the χ^2 is a post-main-sequence model with a mass of $1.04 M_{\odot}$ and a metallicity slightly lower than that of the Sun. Our results underscore the importance of having individual frequencies to constrain the properties of the stellar model.

Key words. Asteroseismology - Stars: solar-type - Stars: individual: β Hydri

1. Introduction

β Hydri (β Hyi, HD 2151, HR 98, HIP 2021) is a single, bright subgiant star ($m_V=2.80$) and is clearly visible to the naked eye about 12° from the South pole. It is the closest subgiant star, with spectral and luminosity type between G2 IV (Hoffleit & Warren 1995; Evans et al. 1957) and G0 V (Gray et al. 2006) and it is one of the oldest stars in the solar Galactic neighbourhood. It is frequently regarded as the future of the Sun (Dravins et al. 1993c,b,a), making it a particularly interesting object of study.

Improvements on the fundamental parameters of β Hyi have been presented in a number of recent papers. Recent interferometric measurements of β Hyi have yielded an accurate (0.8%) angular diameter for this star (North et al. 2007). Also, the *Hipparcos* parallax of β Hyi has been improved from an uncertainty of 0.4% (Perryman & ESA 1997) to 0.08% (van Leeuwen 2007). The combination of these two values gives a direct measure of β Hyi's radius with a high accuracy. Moreover, since the bolometric flux of this star is known (Blackwell & Lynas-Gray 1998), its position in the Hertzsprung-Russel (HR) diagram is, in principle, well-constrained.

Frandsen (1987) and Edmonds & Cram (1995) made unsuccessful attempts to detect stellar oscillations in β Hyi, placing upper limits on the p-mode amplitudes. Bedding et al. (2001) and Carrier et al. (2001) finally confirmed the presence of solar-like oscillations in β Hyi and estimated the large frequency separation $\delta\nu$ to be about $55 \mu\text{Hz}$, but were unable to identify individual mode frequencies. Subsequently, Bedding et al. (2007) observed β Hyi during more than a week with the high-precision spectrographs HARPS and UCLES. Besides confirming the oscillations detected in their previous observations in 2000, they were able to identify 28 oscillation modes, some of which were identified as $l = 1$ mixed modes. Mixed modes occur in stars that have left the main-sequence stage of their evolution (e.g. Osaki 1975; Aizenman et al. 1977), and they provide useful information about the core. The presence of mixed modes, together with the availability of very precise non-seismic and seismic data for β Hyi, places the star in a privileged position for asteroseismic studies (e.g. Cunha et al. 2007).

Theoretical models of β Hyi based on its seismic and non-seismic data have been published by Fernandes & Monteiro (2003), Di Mauro et al. (2003), and Doğan et al. (2009). Fernandes & Monteiro (2003) examined the position of β Hyi in the HR diagram by first considering the non-seismic data of the star. In order to estimate the mass of β Hyi, they used available

* I. M. Brandão and G. Doğan contributed equally to this work.

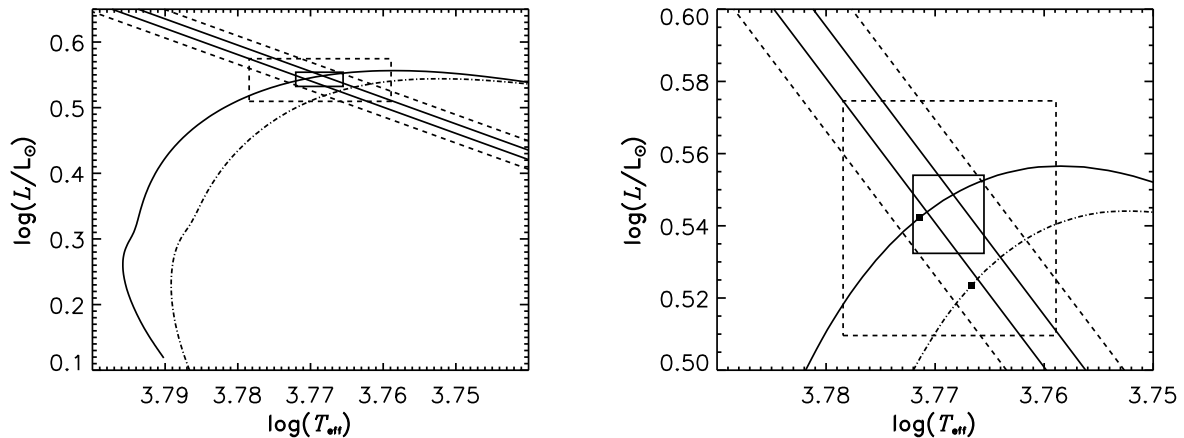


Fig. 1. Left panel: The position of β Hydr in the HR diagram. The constraints on the fundamental parameters (T_{eff} , L/L_{\odot}) are indicated by the 1σ error box (solid) and on the radius by diagonal solid lines. We also show the corresponding $3\text{-}\sigma$ uncertainties by dashed lines. Two evolutionary tracks for the best models found by method 2 (cf. Table 5) are plotted with dash-dotted and solid curves, representing the models with and without gravitational settling and diffusion, respectively. Right panel: the same as in the left panel but zoomed in. The best models are marked by filled squares.

seismic data, namely the large frequency separation, to remove partially the helium-content vs mass degeneracy that exists when only non-seismic observational constraints are used. They also emphasized the usefulness of individual frequencies to constrain the age of β Hydr due to the presence of mixed modes in its observed oscillation spectrum. Di Mauro et al. (2003) computed models of β Hydr, also based on its global parameters. They used the oscillation frequencies of β Hydr to compare with the model frequencies. Their theoretical models reproduced well the observed oscillation spectrum of β Hydr, as well as the observed large and small frequency separations, after they applied an ad-hoc shift to the computed frequencies. In fact, when comparing the computed and the observed frequencies, one should bear in mind that there may be an offset between them. This offset is well known from helioseismology and is also present when comparing the observed and computed frequencies for other stars. It arises from improper modelling of the surface layers of stars. Kjeldsen et al. (2008) used solar data to derive an empirical correction for the near-surface offset which can be applied to stars other than the Sun. In our work, we apply this empirical correction to the model frequencies of β Hydr before comparing to the observed ones. We extend the analysis of Doğan et al. (2009), and also present a detailed discussion on the application of the near-surface correction.

2. Observational constraints

2.1. Non-seismic data

The most recent determination of the radius of β Hydr is given by Kjeldsen et al. (2008). The radius was obtained by combining the interferometric angular diameter of the star, $\theta = 2.257 \pm 0.019$ mas (North et al. 2007), with the revised *Hipparcos* parallax, $\pi_p = 134.07 \pm 0.11$ mas (van Leeuwen 2007).

The luminosity, L , of a star can be obtained through the relation,

$$L = 4\pi F_{\text{bol}} C^2 / \pi_p^2, \quad (1)$$

where F_{bol} is the bolometric flux and C is the conversion factor from parsecs to metres. To compute the luminosity of β Hydr we used the same value for the bolometric flux as North et al. (2007), $F_{\text{bol}} = (2.019 \pm 0.05) \times 10^9 \text{ W m}^{-2}$ (Blackwell & Lynas-Gray 1998, the uncertainty on F_{bol} is from di Benedetto 1998) and the revised *Hipparcos* parallax (van Leeuwen 2007). Adopting $L_{\odot} = 3.842 \times 10^{26} \text{ W}$ with an uncertainty of 0.4% (Bahcall et al. 2001), we found $L = 3.494 \pm 0.087 L_{\odot}$ for β Hydr.

A number of determinations of the effective temperature (T_{eff}) of β Hydr can be found in the literature (e.g. Favata et al. 1997; Blackwell & Lynas-Gray 1998; di Benedetto 1998; Santos et al. 2005; da Silva et al. 2006; Biazzo et al. 2007; Bruntt et al. 2010). We adopted the value of North et al. (2007), which is derived from the direct measurement of the angular diameter.

The most recent value for the metallicity of β Hydr is given by Bruntt et al. (2010), $[\text{Fe}/\text{H}] = -0.10 \pm 0.07$. This value is in agreement with the one found by Santos et al. (2005), $[\text{Fe}/\text{H}] = -0.08 \pm 0.04$ and with the one adopted by Fernandes & Monteiro (2003), $[\text{Fe}/\text{H}] = -0.12 \pm 0.047$. In our analysis we adopted the metallicity from Bruntt et al. (2010).

We calculated the mass fraction of metals, Z , from the metallicity using the following approximation, valid for Population I stars which do not present the α -elements enrichment seen in metal deficient stars (Wheeler et al. 1989):

$$\begin{aligned} [\text{Fe}/\text{H}]_s &\equiv \log\left(\frac{Z_{\text{Fe}}}{Z}\right)_s + \log\left(\frac{Z}{X}\right)_s - \log\left(\frac{Z_{\text{Fe}}}{Z}\right)_{\odot} - \log\left(\frac{Z}{X}\right)_{\odot} \\ &= \log\left(\frac{Z}{X}\right)_s - \log\left(\frac{Z}{X}\right)_{\odot}, \end{aligned} \quad (2)$$

where $[\text{Fe}/\text{H}]_s$ is the star's metallicity; Z_{Fe} and X are the iron and hydrogen mass fractions, respectively; and $(Z/X)_{\odot}$ is the ratio for the solar mixture. We used $(Z/X)_{\odot} = 0.0245$ (Grevesse & Noels 1993). This gives $(Z/X) = 0.019 \pm 0.003$ for β Hydr.

From spectral analysis, Dravins & Nordlund (1990) found $v \sin i = 2 \pm 1 \text{ km s}^{-1}$ for β Hydr. More recently, Bruntt et al. (2010) found $v \sin i = 2.7 \pm 0.6 \text{ km s}^{-1}$, and Hekker & Aerts (2010)

Table 1. Stellar properties of β Hyi. The luminosity, L , and radius, R , are expressed in solar units. θ stands for the angular diameter, π_p for the *Hipparcos* parallax, T_{eff} for the effective temperature, $[\text{Fe}/\text{H}]$ is the metallicity, and Z/X is the mass ratio of heavy elements to hydrogen.

	Value	Reference
θ (mas)	2.257 ± 0.019	North et al. (2007)
π_p (mas)	134.07 ± 0.11	van Leeuwen (2007)
R/R_\odot	1.809 ± 0.015	Kjeldsen et al. (2008)
L/L_\odot	3.494 ± 0.087	Current work
T_{eff} (K)	5872 ± 44	North et al. (2007)
$[\text{Fe}/\text{H}]$	-0.10 ± 0.07	Bruntt et al. (2010)
Z/X	0.019 ± 0.003	Current work

from spectroscopic line-profile analysis, found $\nu \sin i = 4.3 \text{ km s}^{-1}$. From their analysis, Hekker & Aerts (2010) attempted to determine the inclination angle, i , of β Hyi, suggesting a value of $55 \pm 17^\circ$ for this star. Thus the effect of rotation on the modelling of the structure of the star can be neglected. Similarly, since the resulting rotational splitting is comparable with the error in the observed frequencies (see below), in the present analysis we neglect the effects of rotation on the frequencies.

The position of β Hyi in the HR diagram is shown in Fig. 1 and the fundamental parameters we adopted are given in Table 1.

2.2. Seismic data

Asteroseismic observations of β Hyi have been reported by Bedding et al. (2007). They found an excess power centred around 1 mHz with a peak amplitude of $\sim 50 \text{ cm s}^{-1}$, and the oscillation frequencies show a comb-like structure typical of solar-like oscillations with a large frequency separation of the $l = 0$ modes, $\Delta\nu_0$, of $57.24 \pm 0.16 \mu\text{Hz}$. They also identified 28 mode frequencies in the range $0.7 < \nu < 1.4 \text{ mHz}$ with the angular degrees $l = 0, 1$, and 2, three of which were identified as $l = 1$ mixed modes. In this work, we used the updated list of observed frequencies given in Table 2. To produce these, we reanalysed the 2005 dual-site observations (Bedding et al. 2007) using revised weights that were adjusted using a new method that minimizes the sidelobes (H. Kjeldsen et al., in preparation). This method is described by Bedding et al. (2010), who applied it to multi-site observations of Procyon (see also Arentoft et al. 2009). In the same way as for Procyon, we extracted oscillation frequencies from the time series of β Hyi using the standard procedure of iterative sine-wave fitting. The finite mode lifetime causes many modes to be split into two or more peaks which, coupled with the presence of mode bumping, meant that deciding on a final list of mode frequencies with correct l identifications is somewhat subjective. We followed the same approach as Bedding et al. (2010), which involved using the ridge centroids as a guide and averaging multiple peaks into a single value. The remaining unidentified peaks in the power spectrum are listed in Table 3.

3. Modelling β Hyi

3.1. Input physics to the models

To compute the evolutionary models we used the ‘Aarhus Stellar Evolution Code’, ASTEC (Christensen-Dalsgaard 2008a). The following assumptions were made: spherical symmetry, no rotation, no magnetic field and no mass loss. In the computation we used the OPAL 2005 equation of state tables (see Rogers & Nayfonov 2002), OPAL opacities (Iglesias & Rogers 1996) com-

Table 2. Oscillation frequencies in β Hyi (in μHz) resulting from the revised analysis, listed in ascending échelle order.

$l = 0$	$l = 1$	$l = 2$	$l = 3$
660.74 ± 2.43
716.68 ± 3.00	...	711.24 ± 2.13	...
774.79 ± 2.20	802.74 ± 1.69	769.97 ± 0.99	791.66 ± 1.35
831.86 ± 2.43	857.32 ± 0.86	825.86 ± 1.18	...
889.15 ± 1.23	912.91 ± 0.86	883.35 ± 0.89	...
946.11 ± 0.91	959.98 ± 0.89	939.97 ± 0.97	...
...	987.08 ± 0.87
1004.32 ± 0.86	1032.99 ± 0.86	999.40 ± 0.91	...
1061.66 ± 0.95	1089.87 ± 0.88	1057.00 ± 0.86	...
1118.67 ± 0.88	1147.35 ± 0.91	1115.20 ± 1.06	...
1177.76 ± 0.97	1203.54 ± 1.01	1172.98 ± 0.86	1198.16 ± 1.23
1235.31 ± 1.09
...	1320.42 ± 0.94
...	1378.92 ± 1.39

Table 3. Unidentified peaks with $S/N \geq 3.5$.

ν (μHz)		
753.12 ± 1.57	1013.42 ± 1.50	1130.36 ± 1.30
828.70 ± 1.83	1025.80 ± 1.68	1134.32 ± 1.63
845.02 ± 1.61	1037.90 ± 1.63	1167.62 ± 1.10
868.60 ± 1.13	1065.12 ± 1.59	1256.78 ± 1.60
911.88 ± 1.76	1070.00 ± 1.43	1383.20 ± 1.75
1010.20 ± 1.91	1084.20 ± 1.57	1462.62 ± 1.92

plemented by low-temperature opacities from Ferguson et al. (2005), the solar mixture from Grevesse & Noels (1993), and the NACRE nuclear reaction rates (Angulo et al. 1999). We considered an atmospheric temperature versus optical depth relation which is a fit to the quiet-sun relation of Vernazza et al. (1976).

Convection was treated according to the standard mixing-length theory (MLT) from Böhm-Vitense (1958), where the characteristic length of turbulence, l_{mix} , scales directly with the local pressure scale height, H_p , as $l_{\text{mix}} = \alpha H_p$, leaving the scaling factor α as a free parameter. MLT makes use of another free parameter associated with the amount of the core overshooting, α_{ov} . Both Di Mauro et al. (2003) and Fernandes & Monteiro (2003) found that models at the position of β Hyi in the HR diagram are not affected by convective overshooting, so we decided, for this work, not to consider it in our models.

Diffusion and settling were treated in the approximations proposed by Michaud & Proffitt (1993). We refer to Christensen-Dalsgaard (2008a) for a detailed explanation.

3.2. Grids of models

We calculated two grids of evolutionary tracks, Grids I and II, with the input parameters shown in Table 4. In Grid II we included diffusion and gravitational settling of helium.

For each grid, we took those models whose parameters were within the $3\text{-}\sigma$ uncertainties derived from the observations of β Hyi, and computed the corresponding oscillation frequencies using the Aarhus adiabatic oscillation code ADIPLS (Christensen-Dalsgaard 2008b). The theoretical frequencies were then compared with the observed ones in order to find the best model.

4. Near-surface corrections

It is well known from helioseismology that there is a systematic offset between the observed and the computed oscillation

APPENDIX D. ASTEROSEISMIC MODELLING OF THE SOLAR-TYPE SUBGIANT STAR β HYDRI

4

I. M. Brandão, G. Doğan et al.: Asteroseismic modelling of the solar-type subgiant star β Hydri

Table 4. Parameters used to compute the evolutionary tracks. M/M_{\odot} is the mass in solar units, Z/X is the initial ratio of heavy elements to hydrogen abundances, and Y the helium abundance.

Parameter	Grid I	Grid II
M/M_{\odot}	1.00 - 1.18 (with steps of 0.02)	1.00 - 1.18 (with steps of 0.02)
Z/X	0.010 - 0.030 (with steps of 0.004)	0.010 - 0.030 (with steps of 0.004)
Y	0.24 - 0.30 (with steps of 0.02)	0.24 - 0.30 (with steps of 0.02)
Mixing length parameter (α)	1.4 - 2.0 (with steps of 0.2)	1.4 - 2.0 (with steps of 0.2)
Diffusion & gravitational settling	None	He

frequencies of the Sun. This offset, which is nearly independent of the angular degree, l , of the mode and affects the highest frequencies the most (Christensen-Dalsgaard & Thompson 1997), arises from the improper modelling of the surface layers. Therefore, the offset is also expected to be present when comparing the observed and computed frequencies for other stars. Kjeldsen et al. (2008) used the solar data to derive an empirical correction for the near-surface offset, which can be, in principle, applied to other stars.

For the Sun, the difference between the observed, ν_{obs} , and computed frequencies of the best model, ν_{best} , was shown by Kjeldsen et al. (2008) to be well approximated by a power law fit given as

$$\nu_{\text{obs}}(n) - \nu_{\text{best}}(n) = a \left[\frac{\nu_{\text{obs}}(n)}{\nu_0} \right]^b, \quad (3)$$

where n is the radial order, and ν_0 is a reference frequency that is chosen to be the frequency at maximum power. Since the offset is independent of l , the authors considered only radial ($l = 0$) modes. Note that the ‘best model’ is the one that best represents the interior but still fails to model the near-surface layers. They also argued that the frequencies of a reference model, ν_{ref} , which is close to the best one, can be scaled from ν_{best} by a factor r , i.e.,

$$\nu_{\text{best}}(n) = r\nu_{\text{ref}}(n). \quad (4)$$

Then Eq. (3) becomes

$$\nu_{\text{obs}}(n) - r\nu_{\text{ref}}(n) = a \left[\frac{\nu_{\text{obs}}(n)}{\nu_0} \right]^b. \quad (5)$$

Kjeldsen et al. (2008), using the data and models for the Sun, found $b = 4.90$. Using this value for b it is possible to determine r and a from Eqs (6) and (10) in Kjeldsen et al. (2008). Assuming that a similar offset occurs for other solar-like stars, they showed how to use the solar b to determine r and a from the observed frequencies of $l = 0$ modes, and, consequently, use Eq. (5) to calculate the correction that must be applied to the frequencies computed for all l for a given stellar model. They noted that the correction applied to the mixed modes should be less than that for the pure p modes (see the next section).

5. Selecting the best model

We considered two methods to find the model that best reproduces the observed non-seismic and seismic data of β Hyi. For all models whose parameters were within the $3\text{-}\sigma$ uncertainties derived from the non-seismic observations of β Hyi, we calculated the r and a values, following Kjeldsen et al. (2008), using $b = 4.90$ and $\nu_0 = 1000 \mu\text{Hz}$.

In the first method we followed closely the work of Kjeldsen et al. (2008) and considered the best model to be the one having the value of r closest to 1, which means, from Eq. (4),

$$\nu_{\text{ref}}(n) \approx \nu_{\text{best}}(n). \quad (6)$$

Using the values of r and a found for this model, we then computed the correction factor to be applied to the model frequencies and compared them to those observed. Note, however, that in this method r is calculated using only the observed radial modes together with the corresponding model radial modes. If we assume that the best model is the one which has r closest to 1 then we are assuming the model that best reproduces the observed $l = 0$ modes also best reproduces the observed $l = 1$, and 2 modes, which may not be true.

In the second method we performed a statistical analysis, using the χ^2 test. Our goal was to find the reference model that, after applying the surface corrections, had the individual frequencies closest to the observed ones, for all l , i.e. we found the minimum of the χ^2 ,

$$\chi^2 = \frac{1}{N} \sum_{n,l} \left(\frac{\nu_{\text{ref,corr}}(n,l) - \nu_{\text{obs}}(n,l)}{\sigma(\nu_{\text{obs}}(n,l))} \right)^2, \quad (7)$$

where N is the total number of modes considered, $\nu_{\text{ref,corr}}(n,l)$ are the frequencies of modes with radial order n and degree l of a reference model, corrected for the surface effects, and σ represents the uncertainty in the observed frequencies.

The correction term, as shown in the right-hand side of Eq. (3) can only be applied to the frequencies of the best model. In order to compute the correction term, since we have a set of reference models and we do not know which one is the best model, we assume that the corrected best $\nu_{\text{best,corr}}$ and reference model $\nu_{\text{ref,corr}}$ frequencies also scale as

$$\nu_{\text{best,corr}}(n,0) = r\nu_{\text{ref,corr}}(n,0). \quad (8)$$

We note that this is a good approximation because the surface corrections to the frequencies are much smaller than the frequencies themselves. Moreover, since $\nu_{\text{best,corr}} = \nu_{\text{obs}}$ we have

$$\nu_{\text{ref,corr}}(n,0) = \nu_{\text{ref}}(n,0) + \left(\frac{a}{r} \right) \left[\frac{\nu_{\text{obs}}(n,0)}{\nu_0} \right]^b. \quad (9)$$

Thus, Eq. (7) becomes

$$\chi^2 = \frac{1}{N} \sum_{n,l} \left(\frac{\nu_{\text{ref}}(n,l) + \left(\frac{a}{r} \right) \left[\frac{\nu_{\text{ref}}(n,l)}{\nu_0} \right]^b - \nu_{\text{obs}}(n,l)}{\sigma(\nu_{\text{obs}}(n,l))} \right)^2. \quad (10)$$

Note that, in practice, the term $(a/r)[\nu_{\text{obs}}(n,0)/\nu_0]^b$ in the right-hand side of Eq. (9) was replaced by $(a/r)[\nu_{\text{ref}}(n,l)/\nu_0]^b$. The

reason is to enable us to correct all the reference model frequencies, instead of only the frequencies having the same radial order as those observed.

To compute the χ^2 we used all the observed and computed $l = 0, 1$, and 2 frequencies. However, as already mentioned, some of the observed $l = 1$ modes are mixed modes and the scaling is not valid for them. Mixed modes should not be affected by the surface layers as much as the p modes (Kjeldsen et al. 2008), so the correction term should be small for the mixed modes. Specifically, at a given frequency we expect the near-surface effects to scale inversely with the mode inertia, which is much higher for the mixed modes than for the p modes; thus we scaled the correction term by the inverse of the ratio Q_{nl} between the inertia of the mode and the inertia of a radial mode of the same frequency (Aerts et al. 2010). Taking that into account, Eq. (10) becomes

$$\chi^2 = \frac{1}{N} \sum_{n,l} \left(\frac{v_{\text{ref}}(n, l) + \left(\frac{1}{Q_{nl}}\right) \left(\frac{r}{r_0}\right) \left[\frac{v_{\text{ref}}(n, l)}{v_0}\right]^b - v_{\text{obs}}(n, l)}{\sigma(v_{\text{obs}}(n, l))} \right)^2. \quad (11)$$

In this method, our best model is the one that minimizes Eq. (11).

Contrary to the first method, the χ^2 test takes into account all the individual frequencies, including mixed modes. This test also includes the uncertainties in the observations. Thus, it is possible that the model with the lowest χ^2 does not have the r that is closest to 1.

6. Results and Discussion

The parameters of the best models found for Grids I and II, using the two methods described in Sec. 5, are shown in Table 5. Figures 2 and 3 show the échelle diagrams for β Hyi. An échelle diagram shows the frequency spectrum divided into segments equally spaced by the large frequency separation, after these segments are stacked in the vertical direction (Grec et al. 1983). In these figures the observed frequencies of β Hyi are compared with the theoretical frequencies of the best models from Grid I (upper panel) and from Grid II (lower panel), both before (left plot) and after (right plot), applying the near-surface corrections. The model frequencies are represented by open symbols and the observed frequencies (cf. Table 2) by solid symbols, while the asterisks represent the unidentified peaks (cf. Table 3), which may correspond to genuine modes, sidelobes, or noise peaks. The relative sizes of the open symbols reflect the expected mode amplitudes (Christensen-Dalsgaard et al. 1995). The so-called mixed modes reveal themselves in the échelle diagrams, breaking the regularity of the ridges. The models predict mixed modes with all nonradial degrees, however mostly with too small amplitudes to be observed. On the other hand, some of the observed modes match well the mixed modes with $l = 1$ (see, e.g., the right panels of Fig. 3). If we inspect Figs. 2 and 3, it is clear that the agreement between the observed and model frequencies is much better when method 2 is used (Fig. 3). This is due to the fact that in this method all the available seismic constraints were involved in selecting the best model.

It is seen from Table 5 that the model that has the r value closest to unity does not produce the lowest χ^2 value. The model with the lowest χ^2 still has an r satisfactorily close to unity. So, in addition to finding a model that represents the stellar interior reasonably, method 2 makes sure that all the available seismic constraints are simultaneously reproduced and so the fit, hence the accuracy of the model, is improved substantially. This shows the importance of the individual modes in constraining the range

of models to represent the observed star. Mixed modes, in particular, put strong constraints on the model properties, especially on the evolutionary stage. For instance, we can see from the right panels of Fig. 2 that two models resulting from method 1 have the two highest χ^2 values due to failing to match particularly the observed $l = 1$ mixed modes. In the upper right panel, the model is too massive and it matches the rest of the seismic constraints before it is evolved enough to have mixed modes, whereas the model in the lower right panel is evolved enough to have mixed modes, however, the predicted mixed modes do not match the observed ones.

In general, we found that the empirical surface corrections proposed by Kjeldsen et al. (2008) work very well for β Hyi as seen from Figs. 2 and 3, although there is room for improvement for high-frequency modes of $l = 1$. The reason for the suboptimal agreement for those modes is that the correction term is determined using only the $l = 0$ observed modes, whose frequencies span a smaller range than those of the $l = 1$ modes. Thus, radial modes with higher frequencies need to be detected in order to improve the agreement for the higher frequency $l = 1$ modes. Note that the change in the large frequency separation of the models after applying the near-surface correction is around $0.8 \mu\text{Hz}$, which is larger than the given uncertainty of the observed large separation. This should be taken into account when modelling through a pipeline analysis that uses the large separation as input. It is encouraging to see that we can observe $l = 3$ modes, and that some of the unidentified modes are also close to the model frequencies, namely $753.1 \mu\text{Hz}$ ($l = 1$?) and $1462.6 \mu\text{Hz}$ ($l = 0$?).

Even though the best model seems to be the one without diffusion, we do expect that within a star diffusion occurs. The two best models, the ones with and without diffusion, resulting from the method 2 are in fact compatible and both could be further fine-tuned.

7. Summary and Conclusions

We computed two grids of evolutionary models, using the ASTEC code, in order to find the model that best reproduces the seismic and non-seismic data of β Hyi. The parameters used for each grid are given in Table 1. We computed the oscillation frequencies for the models that lay inside the $3\text{-}\sigma$ error box of the star's position in the HR diagram with the ADIPLS code, and compared them to the observed frequencies. There is an offset regarding this comparison, due to improper modelling of the near-surface layers of the stars. We used the approach proposed by Kjeldsen et al. (2008) to correct the computed frequencies of β Hyi from this offset. We used two methods in order to find the model that best reproduces the observed oscillation frequencies of β Hyi.

In our analysis, we argue that the method involving the χ^2 test, method 2, is the most robust way to find the best model, since it takes into account all the individual frequencies, the mixed modes, and also the uncertainties on the observed frequencies. Analysing the échelle diagrams of the best models found with method 2 (cf. Sect. 6), we see that the surface correction works very well for $l = 0$ modes, and for $l = 1$ and 2 modes with frequencies lying in the frequency range of the observed radial modes. This was expected since the correction term was computed using only those radial modes. Observed $l = 0$ modes with higher frequencies are thus needed in order to improve the surface correction.

Our best models give $M=1.04 M_{\odot}$ and an age of $6.1 - 7.3$ Gyr for β Hyi, depending on the inclusion of gravitational set-

APPENDIX D. ASTEROSEISMIC MODELLING OF THE SOLAR-TYPE SUBGIANT STAR β HYDRI

6

I. M. Brandão, G. Doğan et al.: Asteroseismic modelling of the solar-type subgiant star β Hydri

Table 5. The parameters of the best models found for Grid I (no diffusion) and II (He settling and diffusion), for each of the two methods. See text for details on the methods. The mass, M , luminosity, L , and radius, R , are expressed in solar units. T_{eff} is the effective temperature, Y and Z are the initial helium and heavy element abundances, $[\text{Fe}/\text{H}]$ is the metallicity at the surface, and α is the mixing length parameter. r and a are factors used to compute the correction term, $\Delta\nu_{0b}$ and $\Delta\nu_{0a}$ are, respectively, the large frequency separation before and after applying the surface correction to the model $l = 0$ modes. χ^2 values are those calculated after correcting the frequencies for the near-surface effects.

Parameter	Grid I		Grid II	
	Method 1	Method 2	Method 1	Method 2
M/M_{\odot}	1.16	1.04	1.04	1.04
R/R_{\odot}	1.832	1.785	1.790	1.786
L/L_{\odot}	3.433	3.485	3.432	3.338
T_{eff} (K)	5810	5908	5877	5843
Age (Gyr)	4.705	6.114	7.390	7.297
Z	0.0204	0.0124	0.0075	0.0075
Y	0.30	0.30	0.24	0.24
$[\text{Fe}/\text{H}]$	0.088	-0.133	-0.416	-0.424
α	1.4	1.8	2.0	1.8
r	1.0000	0.9995	1.0000	1.0009
a (μHz)	-4.80	-3.14	-2.43	-3.11
$\Delta\nu_{0b}$ (μHz)	58.977	58.488	58.243	58.400
$\Delta\nu_{0a}$ (μHz)	57.678	57.652	57.600	57.577
χ^2	19.086	1.183	26.226	2.642

ting and diffusion of helium. In either case, the radius is found to be $R \sim 1.785 R_{\odot}$, which is in good agreement with the one determined by interferometry, $R = 1.809 \pm 0.015 R_{\odot}$. However, there are other models fitting the data similarly well. We used the parameters of those models (with $\chi^2 < 10$) to determine the internal error regarding our analysis. We calculated the mean value, and the uncertainties were taken as the standard deviation. We found $M = 1.08 \pm 0.03 M_{\odot}$, age = 6.40 ± 0.56 Gyr, and $R = 1.811 \pm 0.020 R_{\odot}$. These results are also consistent with the results of Fernandes & Monteiro (2003), who derived, $M = 1.10^{+0.04}_{-0.07} M_{\odot}$ and $M = 1.09 \pm 0.22 M_{\odot}$, through the HR diagram analysis and $\Delta\nu_0$, respectively, and a stellar age between 6.4 and 7.1 Gyr.

Acknowledgements. This work was partially supported by the project PTDC/CTE-AST/098754/2008 and the grant SFRH / BD / 41213 /2007 funded by FCT /MCTES, Portugal. MC is supported by a Ciência 2007 contract, funded by FCT/MCTES (Portugal) and POPH/FSE (EC). GD, JCD, and HK are grateful for the financial support from the Danish Natural Science Research Council. TRB is supported by Australian Research Council. NCAR is supported by the U.S. National Science Foundation.

References

Aerts, C., Christensen-Dalsgaard, J., & Kurtz, D. W. 2010, *Asteroseismology*, ed. Aerts, C., Christensen-Dalsgaard, J., & Kurtz, D. W.

Aizenman, M., Smeyers, P., & Weigert, A. 1977, *A&A*, 58, 41

Angulo, C., Arnould, M., Rayet, M., et al. 1999, *Nuclear Physics A*, 656, 3

Arentoft, T., Kjeldsen, H., & Bedding, T. R. 2009, in *Astronomical Society of the Pacific Conference Series*, Vol. 416, *Astronomical Society of the Pacific Conference Series*, ed. M. Dikpati, T. Arentoft, I. González Hernández, C. Lindsey, & F. Hill, 347–+

Bahcall, J. N., Pinsonneault, M. H., & Basu, S. 2001, *ApJ*, 555, 990

Bedding, T. R., Butler, R. P., Kjeldsen, H., et al. 2001, *ApJ*, 549, L105

Bedding, T. R., Kjeldsen, H., Arentoft, T., et al. 2007, *ApJ*, 663, 1315

Bedding, T. R., Kjeldsen, H., Campante, T. L., et al. 2010, *ApJ*, 713, 935

Biazzo, K., Pasquini, L., Girardi, L., et al. 2007, *A&A*, 475, 981

Blackwell, D. E. & Lynas-Gray, A. E. 1998, *A&AS*, 129, 505

Böhm-Vitense, E. 1958, *Zeitschrift für Astrophysik*, 46, 108

Bruntt, H., Bedding, T. R., Quirion, P., et al. 2010, *MNRAS*, 406, 142

Carrier, F., Bouchy, F., Kienziele, F., et al. 2001, *A&A*, 378, 142

Christensen-Dalsgaard, J. 2008a, *Ap&SS*, 316, 13

Christensen-Dalsgaard, J. 2008b, *Ap&SS*, 316, 113

Christensen-Dalsgaard, J., Bedding, T. R., & Kjeldsen, H. 1995, *ApJ*, 443, L29

Christensen-Dalsgaard, J. & Thompson, M. J. 1997, *MNRAS*, 284, 527

Cunha, M. S., Aerts, C., Christensen-Dalsgaard, J., et al. 2007, *A&AR*, 14, 217

da Silva, L., Girardi, L., Pasquini, L., et al. 2006, *A&A*, 458, 609

di Benedetto, G. P. 1998, *A&A*, 339, 858

Di Mauro, M. P., Christensen-Dalsgaard, J., & Paternò, L. 2003, *Ap&SS*, 284, 229

Doğan, G., Brandão, I. M., Bedding, T. R., et al. 2009, *Ap&SS*, 251

Dravins, D., Linde, P., Ayres, T. R., et al. 1993a, *ApJ*, 403, 412

Dravins, D., Linde, P., Fredga, K., & Gahm, G. F. 1993b, *ApJ*, 403, 396

Dravins, D., Lindegren, L., Nordlund, A., & Vandenberg, D. A. 1993c, *ApJ*, 403, 385

Dravins, D. & Nordlund, A. 1990, *A&A*, 228, 203

Edmonds, P. D. & Cram, L. E. 1995, *MNRAS*, 276, 1295

Evans, D. S., Menzies, A., & Stoy, R. H. 1957, *MNRAS*, 117, 534

Favata, F., Micela, G., & Sciortino, S. 1997, *A&A*, 323, 809

Ferguson, J. W., Alexander, D. R., Allard, F., et al. 2005, *ApJ*, 623, 585

Fernandes, J. & Monteiro, M. J. P. F. G. 2003, *A&A*, 399, 243

Frandsen, S. 1987, *A&A*, 181, 289

Gray, R. O., Corbally, C. J., Garrison, R. F., et al. 2006, *AJ*, 132, 161

Grec, G., Fossat, E., & Pomerantz, M. A. 1983, *Sol. Phys.*, 82, 55

Grevesse, N. & Noels, A. 1993, in *Origin and Evolution of the Elements*, ed. S. Kubono & T. Kajino, 14–+

Hekker, S. & Aerts, C. 2010, *A&A*, 515, A43+

Hoffleit, D. & Warren, Jr., W. H. 1995, *VizieR Online Data Catalog: V/50, SIMBAD*

Iglesias, C. A. & Rogers, F. J. 1996, *ApJ*, 464, 943

Kjeldsen, H., Bedding, T. R., & Christensen-Dalsgaard, J. 2008, *ApJ*, 683, L175

Michaud, G. & Proffitt, C. R. 1993, in *Astronomical Society of the Pacific Conference Series*, Vol. 40, *IAU Colloq. 137: Inside the Stars*, ed. W. W. Weiss & A. Baglin, 246–259

North, J. R., Davis, J., Bedding, T. R., et al. 2007, *MNRAS*, 380, L80

Osaki, J. 1975, *PASJ*, 27, 237

Perryman, M. A. C. & ESA, eds. 1997, *ESA Special Publication*, Vol. 1200, *The HIPPARCOS and TYCHO catalogues. Astrometric and photometric star catalogues derived from the ESA HIPPARCOS Space Astrometry Mission*

Rogers, F. J. & Nayfonov, A. 2002, *ApJ*, 576, 1064

Santos, N. C., Israelian, G., Mayor, M., et al. 2005, *A&A*, 437, 1127

van Leeuwen, F. 2007, *A&A*, 474, 653

Vernazza, J. E., Avrett, E. H., & Loeser, R. 1976, *ApJS*, 30, 1

Wheeler, J. C., Sneden, C., & Truran, Jr., J. W. 1989, *ARA&A*, 27, 279

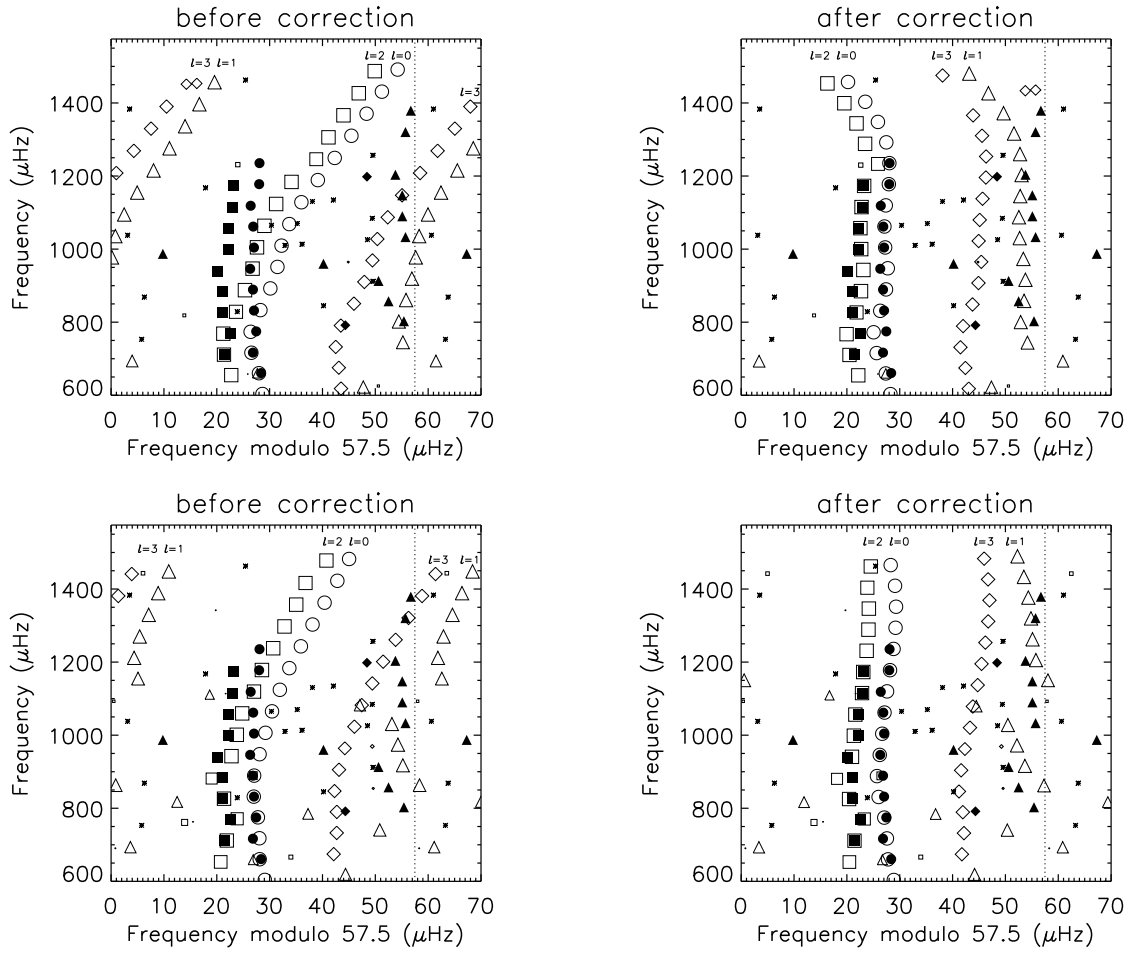


Fig. 2. Échelle diagrams for β Hyi, with a frequency separation of $\Delta\nu = 57.5 \mu\text{Hz}$, before (left plot) and after (right plot) application of the near-surface corrections to the model frequencies. Shown are the frequencies of the best models using method 1, when including no diffusion (upper panel) and diffusion (lower panel). In method 1, the best model was selected using the radial ($l = 0$) modes alone (see the text for details). The solid symbols show observed frequencies (Table 2), asterisks the unidentified peaks (Table 3), and the open symbols the model frequencies. Circles are used for $l = 0$ modes, triangles for $l = 1$, squares for $l = 2$ and diamonds for $l = 3$. Open symbols are scaled to represent the relative amplitudes of the modes as predicted by the models.

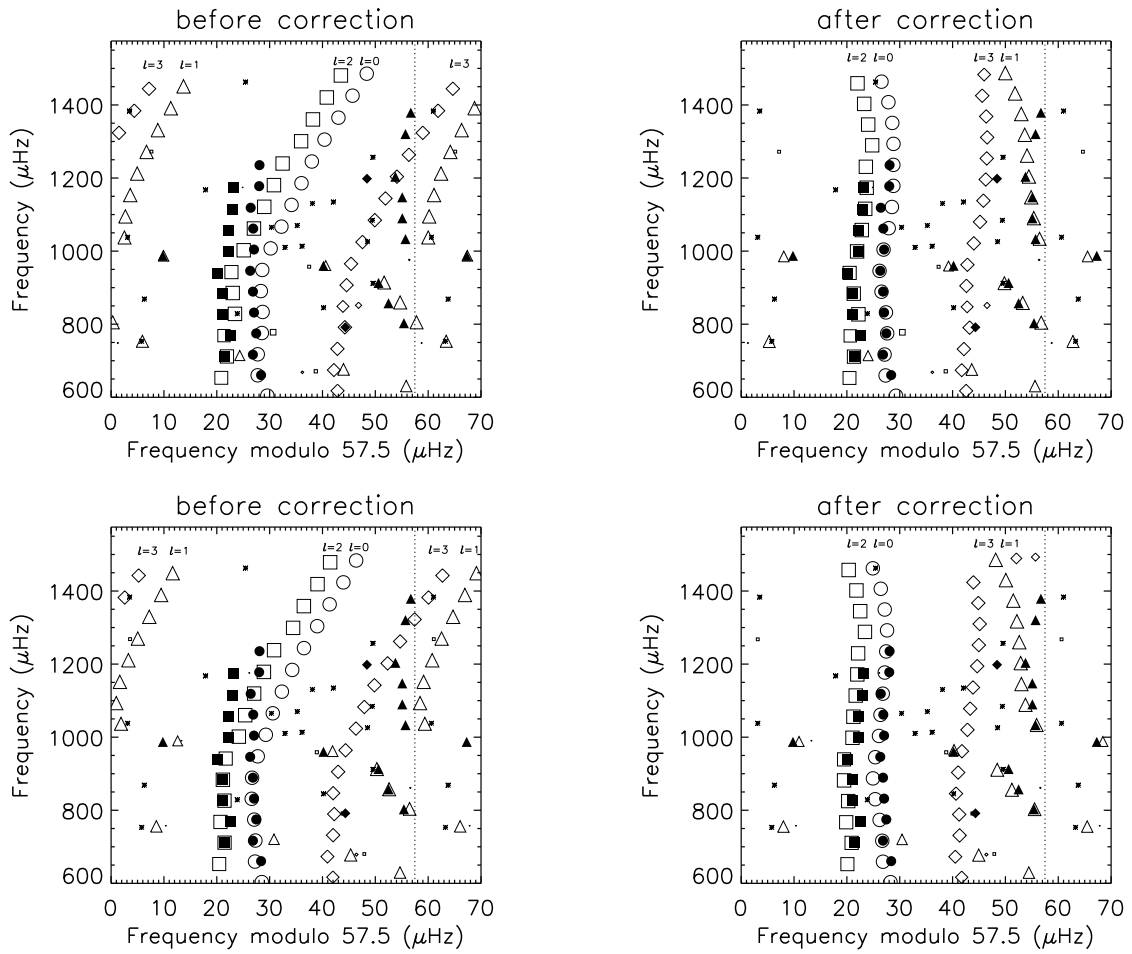


Fig. 3. The same as Fig. 2 but for the best models without (upper panel) and with (lower panel) diffusion, found using method 2. In method 2, the best model was selected using the observed and identified modes with all degrees available.

Appendix E

Asteroseismic modelling of Procyon A: Preliminary results

Asteroseismic modelling of Procyon A: Preliminary results

G. Doğan^{1,*} A. Bonanno² T. R. Bedding³ T. L. Campante^{1,4} J. Christensen-Dalsgaard¹
 and H. Kjeldsen¹

¹ Department of Physics and Astronomy, Aarhus University, Ny Munkegade, DK-8000, Aarhus C, Denmark

² Catania Astrophysical Observatory, Via S.Sofia 78, 95123, Catania, Italy

³ School of Physics A29, University of Sydney, NSW 2006, Sydney, Australia

⁴ Centro de Astrofísica da Universidade do Porto, Rua das Estrelas, 4150-762 Porto, Portugal

Received XX, accepted XX

Key words stars: individual (Procyon A) – stars: oscillations – stars: evolution

We present our preliminary results of the modelling of the F5 star Procyon A. The frequencies predicted by our models are compared with the frequencies extracted through a global fit to the power spectrum obtained by the latest ground-based observations, which provides two different mode identification scenarios.

© 2010 WILEY-VCH Verlag GmbH & Co. KGaA, Weinheim

1 Introduction

Procyon A is a member of a binary system with a white dwarf companion, Procyon B. It is one of the very bright stars to the naked eye, and hence it has been very attractive for the observers. The observational constraints which we adopted are summarized in Section 2. It has also been of asteroseismic interest for a long while (see Arentoft et al. 2008, for a summary), with a solar-like power excess in its spectrum first reported by Brown et al. (1991). However, there has been no agreement on the individual oscillation frequencies. Several authors have investigated the structure and evolution of Procyon A through an asteroseismic approach (e.g., Guenther & Demarque 1993; Barban et al. 1999; Chaboyer et al. 1999; Di Mauro & Christensen-Dalsgaard 2001; Eggenberger et al. 2005; Provost et al. 2006; Bonanno et al. 2007), but there has been a need for more accurate frequencies. Recently, the star was observed through a multi-site campaign by eleven telescopes for more than three weeks (Arentoft et al. 2008). The frequency analysis is described by Bedding et al. (2010). They presented results from different approaches of frequency extraction: Iterative sine-wave fitting and global fitting to the power spectrum. In the former method, a sine wave is fitted to each mode one after the other while the corresponding sinusoid is subtracted from the time series at each step. This is repeated until the signal to noise ratio of the remaining power is lower than a given threshold. This method was used for frequency extraction of ground-based radial velocity data before (see, e.g., the analysis on solar-like star β Hyi by Bedding et al. (2007)). In the latter method, the goal is to find an overall fit to the power spectrum for all the frequencies, mode heights, and linewidths simultaneously, using some prior knowledge of oscillation

properties as constraints. A similar implementation of this method was previously applied to space-based data (see, e.g., frequency analysis of CoRoT star HD 49933 by Benomar et al. (2009)). In this work, we adopted this Bayesian approach which provided us with two mode identification scenarios, referred to as Scenario A and B, with different posterior odds (for a detailed discussion, see Bedding et al. 2010). We chose the output of this analysis in order to test both scenarios. Note that Scenario B was favoured by Bedding et al. (2010; see that paper for a discussion), but here we test both scenarios.

2 Methods and Tools

We have adopted the following properties for the position of the star in the H-R Diagram: $T_{\text{eff}} = 6530 \pm 90$ K (Fuhrmann et al. 1997) and $\log(L/L_{\odot}) = 0.85 \pm 0.06$ (Steffen 1985). We note that there are several revised values for luminosity in the literature, such as $\log(L/L_{\odot}) = 0.840 \pm 0.018$ derived by Jerzykiewicz & Molenda-Żakowicz (2000) using the Hipparcos parallax and total absolute flux; however, we chose to scan a wider range, which largely covers most of the revised values. A similar argument applies also to the choice of the effective temperature. We have not put an additional constraint on the radius for the time being, although we do compare the stellar mean density inferred from the analysis with the value $0.172 \pm 0.005 \rho_{\odot}$, obtained from the measured radius using the angular diameter 5.404 ± 0.031 mas (Aufdenberg et al. 2005) and the revised Hipparcos parallax (284.56 ± 1.26 mas⁻¹, van Leeuwen 2007), together with the adopted mass $1.463 \pm 0.033 M_{\odot}$, which is the mean of the two different astrometric determinations (Girard et al. 2000,

¹ Note that there is an error in Bedding et al. 2010 (Section 9); the value they give for the revised parallax is actually the original one. We also note that the uncertainty on the revised parallax is larger than the original but is presumably more reliable.

* e-mail: gulfur@phys.au.dk

Gatewood and Han 2006). For the metallicity of the star, we allowed a wide range covering the 0.05 dex iron deficiency suggested by Allende Prieto et al. (2002), and we used the solar mixture from Grevesse & Noels (1993).

We have computed stellar models with two different evolutionary codes: ASTEC (Aarhus STellar Evolution Code) (Christensen-Dalsgaard 2008a) and GARSTEC (Garching Stellar Evolution Code) (Weiss & Schlattl 2008). The method we used is to compute several grids of standard models scanning through a parameter space formed by varying the mass, the initial metallicity at the stellar surface, Z_i/X_i , and the mixing-length parameter, α , where the mixing length is defined as $\ell = \alpha H_p$, H_p being the pressure scale height. So far, we have searched within the following ranges: $M = 1.42 - 1.52 M_\odot$, $Z_i/X_i = 0.0204 - 0.0245$, $Y_i = 0.26 - 0.31$, and $\alpha = 1.6 - 1.9$. Here X_i , Y_i , and Z_i are the initial mass fractions of hydrogen, helium, and the elements heavier than helium, respectively. We have computed the models without taking into account diffusion, convective overshooting, or rotation.

The Aarhus adiabatic pulsation package (ADIPLS) (Christensen-Dalsgaard 2008b) has been used to calculate the frequencies of the models having properties that are in agreement with the observations. We have then compared the model frequencies with the observed frequencies. We selected the models that minimize the following χ^2 :

$$\chi^2 = \sum_{n,l} \left(\frac{\nu_l^{\text{obs}}(n) - \nu_l^{\text{model}}(n)}{\sigma(\nu_l^{\text{obs}}(n))} \right)^2,$$

where $\nu_l^{\text{obs}}(n)$, and $\nu_l^{\text{model}}(n)$ are the model, and the observed, frequencies with spherical degree l and radial order n , and $\sigma(\nu_l^{\text{obs}}(n))$ represents the uncertainties in the observed frequencies.

3 Results

The results from the two different stellar evolution codes are similar; hence we present some of the selected models computed with ASTEC. The so-called échelle diagrams of the best models for both of the scenarios, chosen without applying any near-surface corrections are shown in Figs 1 and 2, with their parameters summarized in Table 1. One plots the échelle diagrams using the frequency modulo the large frequency separation, $\Delta\nu$, in the horizontal axis. In order to allow easy comparison with the diagrams shown by Bedding et al. (2010), we use the same value, $\Delta\nu = 56 \mu\text{Hz}$, in our diagrams.

The behaviour of the frequency differences between the models and the observations (shown in Figs 3 and 4) are quite different from that in the Sun. Kjeldsen et al. (2008) showed that the difference between observed and model frequencies of the Sun can be fitted by a power law, which can also be employed to correct the model frequencies for near-surface effects in other solar-like stars, such as β Hyi and

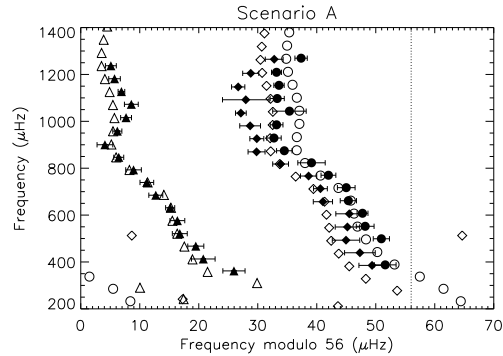


Fig. 1 Échelle diagram of the selected model for Scenario A. Open symbols represent the model frequencies, while the filled symbols with the uncertainties correspond to the frequencies extracted from the observations. Circles, triangles, and diamonds are used for the modes with spherical degree $l=0, 1$, and 2 , respectively. The vertical dot-dashed line corresponds to the value of $\Delta\nu$.

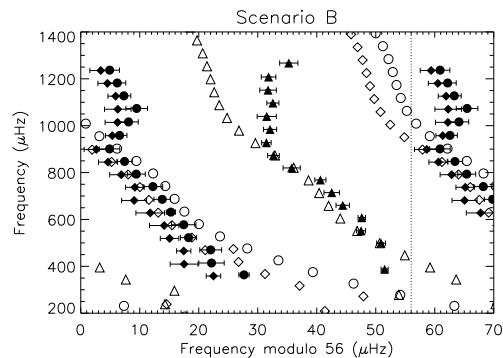


Fig. 2 Échelle diagram of the selected model for Scenario B. Symbols are used in the same way as in Fig. 1.

α Cen A. However, in Procyon, we cannot justify the application of such a surface correction to yield a significant improvement in the fit, since the frequency differences do not follow the power-law behaviour (see also Figs 16 and 17 of Bedding et al. 2010).

4 Discussion and Conclusion

We can argue, if Scenario A is the correct one, that the predictions of the stellar evolutionary models match the observations quite well; however, a surface correction for the model frequencies seems not to be needed, unlike in the solar case. Therefore, the effects of different near-surface properties on the high frequencies might be cancelling out in Procyon; this deserves further investigation.

If, on the other hand, Scenario B is correct, there seems to be no good agreement between the models and the ob-

Table 1 Parameters of the best models

Parameter	Scenario A	Scenario B
M/M_{\odot}	1.50	1.50
Z_i/X_i	0.0235	0.0245
Y_i	0.266	0.290
Age (Gyr)	1.83	1.51
R/R_{\odot}	2.058	2.067
ρ/ρ_{\odot}	0.1721	0.1698
L/L_{\odot}	6.565	7.286
$T_{\text{eff}}(\text{K})$	6446	6603
α	1.8	1.6
X_c^*	0.1585	0.1995
χ^2	3.79	24.46

* Mass fraction of hydrogen remaining in the centre of the star

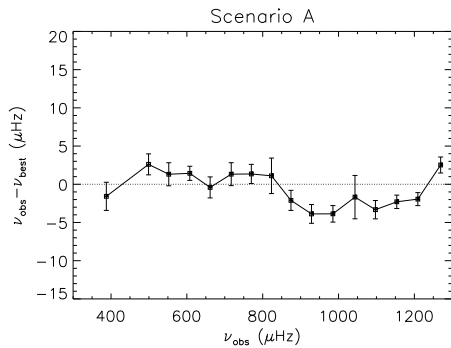


Fig. 3 The difference between the radial ($l = 0$) frequencies from the observations and the selected model for Scenario A. The indicated uncertainties are those from the data analysis.

servations, even in the low-frequency region, which means that there is something incompatible in the structure of the models.

We have presented preliminary results from our ongoing work. To come to a conclusion we need to extend our analysis. Effects of inclusion of overshooting and use of different treatments of convection should be analysed. In addition, the suspected mixed mode reported by Bedding et al. (2010) could help us distinguish between the two scenarios, and put further constraints on the age, and the chemical composition.

Although from the point of view of modelling, Scenario A seems to be less problematic, we cannot yet strongly favour either of the scenarios; therefore, it is difficult to set accurate constraints on the stellar properties. Nevertheless, either of the cases suggests that Procyon is quite different from the Sun, which provides a very good opportunity to test our understanding of stellar structure and evolution.

Acknowledgements. This work was supported by the European Helio- and Asteroseismology Network (HELAS), a major international collaboration funded by the European Commission's Sixth Framework Programme. GD, JC-D, and HK acknowledge financial support from the Danish Natural Science Research Council.

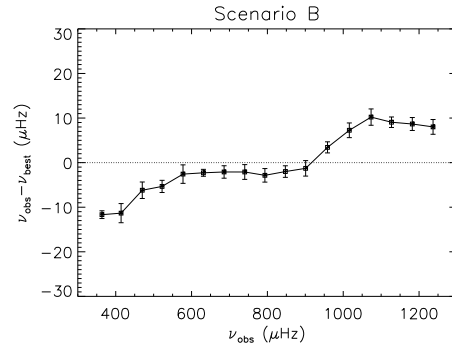


Fig. 4 Same as Fig. 3, but for Scenario B

GD would like to thank Pierre-Olivier Quirion for providing a parallel-programming code for faster evolution computation.

References

- Allende Prieto, C., Asplund, M., López, R. J. G. & Lambert, D. L.: 2002, *ApJ* 567, 544
- Arentoft, T., Kjeldsen, H., Bedding, T. R. et al.: 2008, *ApJ* 687, 1180
- Aufdenberg, J.P., Ludwig, H.-G. & Kervella, P.: 2005, *ApJ* 633, 424
- Barban, C., Michel, E., Martić, M. et al.: 1999, *A&A* 350, 617
- Bedding, T. R., Kjeldsen, H., Arentoft, T. et al.: 2007, *ApJ* 663, 1315
- Bedding, T. R., Kjeldsen, H., Campante, T. L. et al.: 2010, *ApJ* 713, 935
- Benomar, O., Appourchaux, T. & Baudin, F.: 2009, *A&A* 506, 15
- Bonanno, A., Küker, M. & Paternò, L.: 2007, *A&A* 462, 1031
- Brown, T. M., Gilliland, R. L., Noyes, R. W. & Ramsey, L. W.: 1991, *ApJ* 368, 599
- Chaboyer, B., Demarque, P. & Guenther, D. B.: 1999, *ApJ* 525, L41
- Christensen-Dalsgaard, J.: 2008a, *Ap&SS* 316, 13
- Christensen-Dalsgaard, J.: 2008b, *Ap&SS* 316, 113
- Di Mauro, M. P. & Christensen-Dalsgaard, J.: 2001, *IAUS* 203, 94
- Eggenberger, P., Carrier, F. & Bouchy, F.: 2005, *New Astron.* 10, 195
- Fuhrmann, K., Pfeiffer, M., Franck, C. et al.: 1997, *A&A* 323, 909
- Gatewood, G. & Han, I.: 2006, *AJ* 131, 1015
- Girard, T. M. et al.: 2000, *AJ* 119, 2428
- Grevesse, N. & Noels, A.: 1993, in *Origin and Evolution of the Elements*, edited by N. Prantzos, E. Vangioni-Flam & M. Cassé, (Cambridge: Cambridge Univ. Press), p. 15
- Guenther, D. B. & Demarque, P.: 1993, *ApJ* 405, 298
- Jerzykiewicz, M. & Molenda-Zakowicz, J.: 2000, *Acta Astronomica* 50, 369
- Kjeldsen, H., Bedding, T. R. & Christensen-Dalsgaard, J.: 2008, *ApJ* 683, L175
- Provost, J., Berthomieu, G., Martić, M. & Morel, P.: 2006, *A&A* 460, 759
- Steffen, M.: 1985, *A&AS* 59, 403
- van Leeuwen, F.: 2007, *Hipparcos, the New Reduction of the Raw Data*, *Astrophys. Space Sci. Library*, 350
- Weiss, A. & Schlattl, H.: 2008, *Ap&SS* 316, 99

Appendix F

The asteroseismic potential of

Kepler:

First results for solar-type stars

APPENDIX F. THE ASTEROSEISMIC POTENTIAL OF KEPLER: FIRST RESULTS FOR SOLAR-TYPE STARS

THE ASTROPHYSICAL JOURNAL LETTERS, 713:L169–L175, 2010 April 20
© 2010. The American Astronomical Society. All rights reserved. Printed in the U.S.A.

doi:10.1088/2041-8205/713/2/L169

THE ASTEROSEISMIC POTENTIAL OF *KEPLER*: FIRST RESULTS FOR SOLAR-TYPE STARS

W. J. CHAPLIN¹, T. APPOURCHAUX², Y. ELSWORTH¹, R. A. GARCÍA³, G. HOUDEK⁴, C. KAROFF¹, T. S. METCALFE⁵,
J. MOLEND-ŻAKOWICZ⁶, M. J. P. F. G. MONTEIRO⁷, M. J. THOMPSON⁸, T. M. BROWN⁹, J. CHRISTENSEN-DALSGAARD¹⁰,
R. L. GILLILAND¹¹, H. KJELDSSEN¹⁰, W. J. BORUCKI¹², D. KOCH¹², J. M. JENKINS¹³, J. BALLOT¹⁴, S. BASU¹⁵, M. BAZOT⁷,
T. R. BEDDING¹⁶, O. BENOMAR², A. BONANNO¹⁷, I. M. BRANDÃO⁷, H. BRUNTT¹⁸, T. L. CAMPANTE^{7,10}, O. L. CREEVEY^{19,20},
M. P. DI MAURO²¹, G. DOĞAN¹⁰, S. DREIZLER²², P. EGGENBERGER²³, L. ESCH¹⁵, S. T. FLETCHER²⁴, S. FRANDSEN¹⁰, N. GAI^{15,25},
P. GAULME², R. HANDBERG¹⁰, S. HEKKER¹, R. HOWE²⁶, D. HUBER¹⁶, S. G. KORZENNIK²⁷, J. C. LEBRUN²⁸, S. LECCIA²⁹,
M. MARTIC²⁸, S. MATHUR³⁰, B. MOSSER³¹, R. NEW²⁴, P.-O. QUIRION^{10,32}, C. RÉGULO^{19,20}, I. W. ROXBURGH³³, D. SALABERT^{19,20},
J. SCHOU³⁴, S. G. SOUSA⁷, D. STELLO¹⁶, G. A. VERNER³³, T. ARENTOFT¹⁰, C. BARBAN³¹, K. BELKACEM³⁵, S. BENATTI³⁶,
K. BIAZZO³⁷, P. BOUMIER², P. A. BRADLEY³⁸, A.-M. BROOMHALL¹, D. L. BUZASI³⁹, R. U. CLAUDI⁴⁰, M. S. CUNHA⁷,
F. D'ANTONA⁴¹, S. DEHEUVELS³¹, A. DEREKAS^{42,16}, A. GARCÍA HERNÁNDEZ⁴³, M. S. GIAMPAPA²⁶, M. J. GOUPIL¹⁸,
M. GRUBERBAUER⁴⁴, J. A. GUZIK³⁸, S. J. HALE¹, M. J. IRELAND¹⁶, L. L. KISS^{42,16}, I. N. KITASHVILI⁴⁵, K. KOLENBERG⁴,
H. KORHONEN⁴⁶, A. G. KOSOVICHEV³⁴, F. KUPKA⁴⁷, Y. LEBRETON⁴⁸, B. LEROY³¹, H.-G. LUDWIG⁴⁸, S. MATHIS³, E. MICHEL³¹,
A. MIGLIO³⁵, J. MONTALBÁN³⁵, A. MOYA⁴⁹, A. NOELS³⁵, R. W. NOYES²⁷, P. L. PALLÉ²⁰, L. PIAU³, H. L. PRESTON^{39,50},
T. ROCA CORTÉS^{19,20}, M. ROTH⁵¹, K. H. SATO³, J. SCHMITT⁵², A. M. SERENELLI⁵³, V. SILVA AGUIRRE⁵³, I. R. STEVENS¹,
J. C. SUÁREZ⁴³, M. D. SURAN⁵⁴, R. TRAMPEDACH⁵⁵, S. TURCK-CHIÈZE³, K. UYTTERHOEVEN³, R. VENTURA¹⁷, AND
P. A. WILSON^{56,57}

¹ School of Physics and Astronomy, University of Birmingham, Edgbaston, Birmingham, B15 2TT, UK

² Institut d'Astrophysique Spatiale, Université Paris XI–CNRS (UMR8617), Batiment 121, 91405 Orsay Cedex, France

³ Laboratoire AIM, CEA/DSM–CNRS–Université Paris Diderot–IRFU/SAP, 91191 Gif-sur-Yvette Cedex, France

⁴ Institute of Astronomy, University of Vienna, A-1180 Vienna, Austria

⁵ High Altitude Observatory and Scientific Computing Division, National Center for Atmospheric Research, Boulder, CO 80307, USA

⁶ Astronomical Institute, University of Wrocław, ul. Kopernika, 11, 51-622 Wrocław, Poland

⁷ Centro de Astrofísica, Universidade do Porto, Rua das Estrelas, 4150-762, Portugal

⁸ School of Mathematics and Statistics, University of Sheffield, Hounsfield Road, Sheffield S3 7RH, UK

⁹ Las Cumbres Observatory Global Telescope, Goleta, CA 93117, USA

¹⁰ Department of Physics and Astronomy, Aarhus University, DK-8000 Aarhus C, Denmark

¹¹ Space Telescope Science Institute, Baltimore, MD 21218, USA

¹² NASA Ames Research Center, MS 244-30, Moffett Field, CA 94035, USA

¹³ SETI Institute/NASA Ames Research Center, MS 244-30, Moffett Field, CA 94035, USA

¹⁴ Laboratoire d'Astrophysique de Toulouse-Tarbes, Université de Toulouse, CNRS, 14 av E. Belin, 31400 Toulouse, France

¹⁵ Department of Astronomy, Yale University, P.O. Box 208101, New Haven, CT 06520-8101, USA

¹⁶ Sydney Institute for Astronomy (SfA), School of Physics, University of Sydney, NSW 2006, Australia

¹⁷ INAF Osservatorio Astrofisico di Catania, Via S. Sofia 78, 95123, Catania, Italy

¹⁸ Observatoire de Paris, 5 place Jules Janssen, 92190 Meudon Principal Cedex, France

¹⁹ Departamento de Astrofísica, Universidad de La Laguna, E-28207 La Laguna, Tenerife, Spain

²⁰ Instituto de Astrofísica de Canarias, E-38200 La Laguna, Tenerife, Spain

²¹ INAF-IASF Roma, Istituto di Astrofísica Spaziale e Fisica Cosmica, via del Fosso del Cavaliere 100, 00133 Roma, Italy

²² Georg-August Universität, Institut für Astrophysik, Friedrich-Hund-Platz 1, D-37077 Göttingen, Germany

²³ Geneva Observatory, University of Geneva, Maillettes 51, 1290 Sauverny, Switzerland

²⁴ Materials Engineering Research Institute, Faculty of Arts, Computing, Engineering and Sciences, Sheffield Hallam University, Sheffield, S1 1WB, UK

²⁵ Beijing Normal University, Beijing 100875, China

²⁶ National Solar Observatory, 950 N. Cherry Ave., P.O. Box 26732, Tucson, AZ 85726-6732, USA

²⁷ Harvard-Smithsonian Center for Astrophysics, 60 Garden Street, Cambridge, MA 02138, USA

²⁸ LATMOS, University of Versailles St Quentin, CNRS, BP 3, 91371 Verrières le Buisson Cedex, France

²⁹ INAF-OAC, Salita Moiariello, 16 80131 Napoli, Italy

³⁰ Indian Institute of Astrophysics, Koramangala, Bangalore 560034, India

³¹ LESIA, CNRS, Université Pierre et Marie Curie, Université, Denis Diderot, Observatoire de Paris, 92195 Meudon Cedex, France

³² Canadian Space Agency, 6767 Boulevard de l'Aéroport, Saint-Hubert, QC, J3Y 8Y9, Canada

³³ Astronomy Unit, Queen Mary, University of London, Mile End Road, London, E1 4NS, UK

³⁴ HEPL, Stanford University, Stanford, CA 94305-4085, USA

³⁵ Département d'Astrophysique, Géophysique et Océanographie (AGO), Université de Liège, Allée du 6 Août 17 4000 Liège 1, Belgium

³⁶ CISAS (Centre of Studies and Activities for Space), University of Padova, Via Venezia 15, 35131 Padova, Italy

³⁷ Arcetri Astrophysical Observatory, Largo Enrico Fermi 5, 50125 Firenze, Italy

³⁸ Los Alamos National Laboratory, Los Alamos, NM 87545-2345, USA

³⁹ Eureka Scientific, 2452 Delmer Street Suite 100, Oakland, CA 94602-3017, USA

⁴⁰ INAF Astronomical Observatory of Padova, vicolo Osservatorio 5, 35122 Padova, Italy

⁴¹ INAF Osservatorio di Roma, via di Frascati 33, I-00040 Monte Porzio, Italy

⁴² Konkoly Observatory of the Hungarian Academy of Sciences, Budapest, Hungary

⁴³ Instituto de Astrofísica de Andalucía (CSIC), CP3004, Granada, Spain

⁴⁴ Department of Astronomy and Physics, Saint Mary's University, Halifax, NS B3H 3C3, Canada

⁴⁵ Center for Turbulence Research, Stanford University, 488 Escondido Mall, Stanford, CA 94305, USA

⁴⁶ European Southern Observatory, Karl-Schwarzschild-Str. 2, D-85748 Garching bei München, Germany

⁴⁷ Faculty of Mathematics, University of Vienna, Nordbergstraße 15, A-1090 Wien, Austria

⁴⁸ GEPI, Observatoire de Paris, CNRS, Université Paris Diderot, 5 Place Jules Janssen, 92195 Meudon, France

⁴⁹ Laboratorio de Astrofísica Estelar y Exoplanetas, LAEX-CAB (INTA-CSIC), Villanueva de la Cañada, Madrid, P.O. Box 78, 28691, Spain

⁵⁰ Department of Mathematical Sciences, University of South Africa, Box 392, UNISA 0003, South Africa

⁵¹ Kiepenheuer-Institut für Sonnenphysik, Schöneckstr. 6, 79104 Freiburg, Germany

- ⁵² Observatoire de Haute-Provence, F-04870, St. Michel l'Observatoire, France
⁵³ Max Planck Institute for Astrophysics, Karl Schwarzschild Str. 1, Garching, D-85741, Germany
⁵⁴ Astronomical Institute of the Romanian Academy, Str. Cutitul de Argint, 5, RO 40557, Bucharest, Romania
⁵⁵ JILA, University of Colorado, 440 UCB, Boulder, CO 80309-0440, USA
⁵⁶ Nordic Optical Telescope, Apartado 474, E-38700 Santa Cruz de la Palma, Santa Cruz de Tenerife, Spain
⁵⁷ Institute of Theoretical Astrophysics, University of Oslo, P.O. Box 1029, Blindern, N-0315 Oslo, Norway
 Received 2009 November 13; accepted 2010 January 14; published 2010 March 31

ABSTRACT

We present preliminary asteroseismic results from *Kepler* on three G-type stars. The observations, made at one-minute cadence during the first 33.5 days of science operations, reveal high signal-to-noise solar-like oscillation spectra in all three stars: about 20 modes of oscillation may be clearly distinguished in each star. We discuss the appearance of the oscillation spectra, use the frequencies and frequency separations to provide first results on the radii, masses, and ages of the stars, and comment in the light of these results on prospects for inference on other solar-type stars that *Kepler* will observe.

Key words: stars: interiors – stars: late-type – stars: oscillations

Online-only material: color figure

1. INTRODUCTION

The *Kepler Mission* (Koch et al. 2010) will realize significant advances in our understanding of stars, thanks to its asteroseismology program, particularly for cool (solar-type) main-sequence and subgiant stars that show solar-like oscillations, i.e., small-amplitude oscillations intrinsically damped and stochastically excited by the near-surface convection (e.g., Christensen-Dalsgaard 2004). Solar-like oscillation spectra have many modes excited to observable amplitudes. The rich information content of these seismic signatures means that the fundamental stellar properties (e.g., mass, radius, and age) may be measured and the internal structures constrained to levels that would not otherwise be possible (e.g., see Gough 1987; Cunha et al. 2007).

High-precision results are presently available on a selection of bright solar-type stars (e.g., see Aerts et al. 2010, and references therein). Recent examples include studies of *CoRoT* satellite data (e.g., Michel et al. 2008; Appourchaux et al. 2008) and data collected by episodic ground-based campaigns (e.g., Arentoft et al. 2008). However, the *Kepler* spacecraft will increase by more than 2 orders of magnitude the number of stars for which high-quality observations will be available, and will also provide unprecedented multi-year observations of a selection of these stars.

During the initial 10 months of science operations, *Kepler* will survey photometrically more than 1500 solar-type targets selected for study by the Kepler Asteroseismic Science Consortium (KASC; Gilliland et al. 2010a). Observations will be one month long for each star. In order to aid preparations for analyses of these stars, *Kepler* data on three bright solar-type targets—KIC 6603624, KIC 3656476, and KIC 11026764—have been made available in a preliminary release to KASC (see Table 1 for the 2MASS ID of each star). The stars are at the bright end of the *Kepler* target range, having apparent magnitudes of 9.1, 9.5, and 9.3 mag, respectively. The Kepler Input Catalog (KIC; Latham et al. 2005), from which all KASC targets were selected, categorizes them as G-type stars. In this Letter, we present initial results on these stars.

2. THE FREQUENCY–POWER SPECTRA OF THE STARS

The stars were observed for the first 33.5 days of science operations (2009 May 12 to June 14). Detection of oscillations of cool main-sequence and subgiant stars demands use of the

58.85 s, high-cadence observations since the dominant periods in some solar-type stars can be as short as 2 minutes. Time-series data were then prepared from the raw observations in the manner described by Gilliland et al. (2010b). Figure 1 shows the frequency–power spectra on a log–log scale (gray). Heavily smoothed spectra (Gaussian filter) are over-plotted as continuous black lines. The quality of these data for asteroseismology is excellent, with each spectrum showing a clear excess of power due to solar-like oscillations. The excess is in each case imposed upon a background that rises slowly toward lower frequencies.

2.1. Power Spectral Density of the Background

The average power spectral density at high frequencies provides a good measure of the power due to photon shot noise. The high-frequency power is in all cases close to pre-launch estimates, given the apparent magnitudes of the targets, suggesting that the data are close to being shot-noise limited (e.g., see Gilliland et al. 2010b). This result lends further confidence to our expectations—from hare-and-hounds exercises with simulated data—that we will be able to conduct asteroseismology of solar-like KASC survey targets down to apparent magnitudes of 11 and fainter (e.g., see Stello et al. 2009).

There are also background components of stellar origin, and we describe these components by power laws in frequency. Kinks in the observed backgrounds of KIC 6603624 and KIC 3656476 (kinks in solid black curves, indicated by arrows on Figure 1) suggest the presence of two stellar components in the plotted frequency range. One component (dotted lines) is possibly the signature of bright faculae. A similar signature, due to faculae, is seen clearly in frequency–power spectra of Sun-as-a-star data collected by the *VIRGO/SPM* photometers on *SOHO* (e.g., Aigrain et al. 2004). We do not see a kink in the background of KIC 11026764, and it may be that the characteristic “knee” of the facular component coincides in frequency with the oscillation envelope, making it hard to discriminate from the other components. The other stellar component, which is shown by all three stars (dashed lines), carries the signature of stellar granulation.

2.2. The Oscillation Spectra

Figure 2 shows in more detail the oscillation spectra of the three stars. The high signal-to-noise ratios observed in the mode

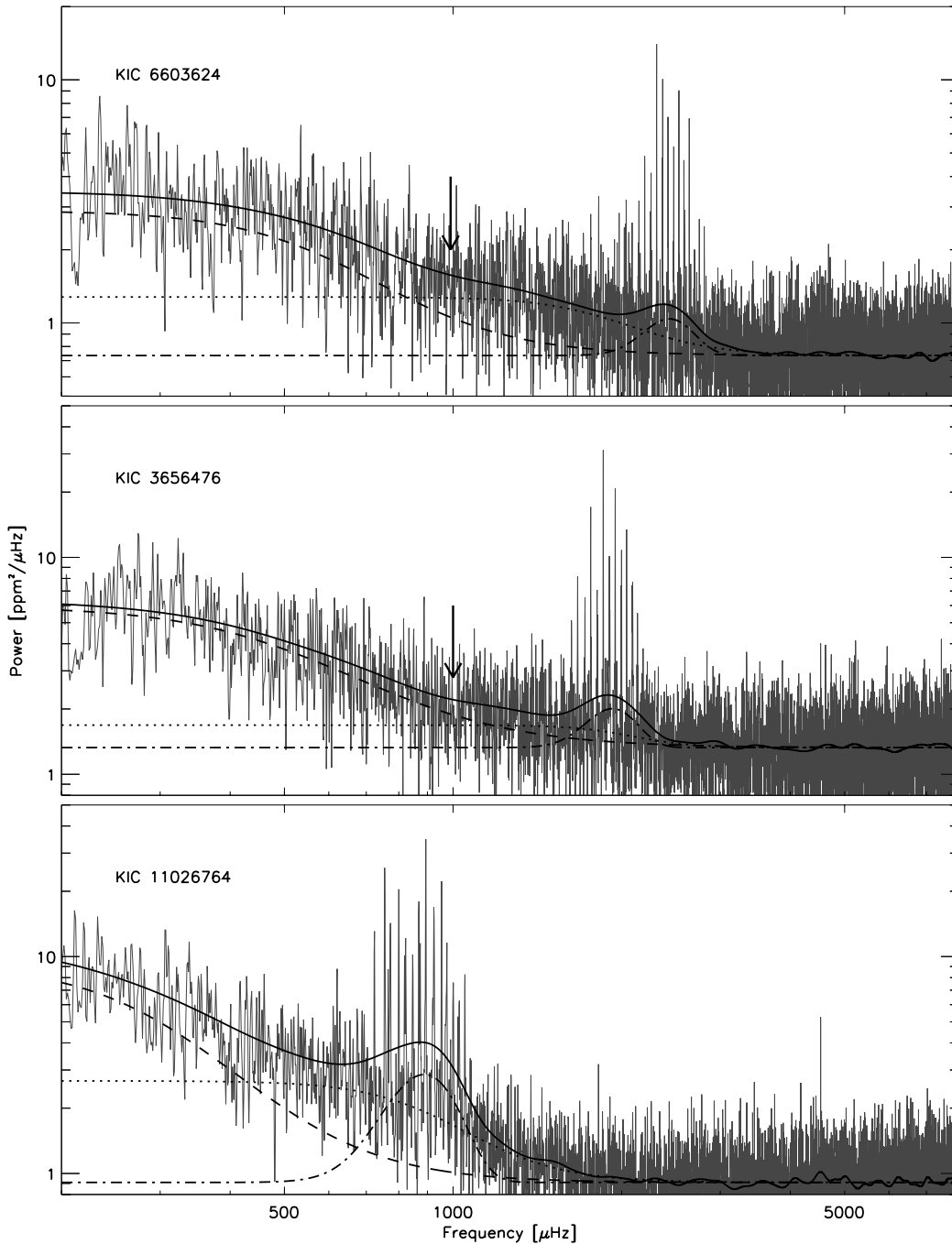


Figure 1. Frequency–power spectra of the three stars, smoothed over $1 \mu\text{Hz}$, plotted on a log–log scale (gray). The continuous black lines show heavily smoothed spectra (Gaussian filter). The other lines show best-fitting estimates of different components: the power envelope due to oscillations, added to the offset from shot noise (dot-dashed), faculae (dotted), and granulation (dashed). The arrows indicate kinks in the rising background (see the text).

peaks allow about 20 individual modes to be identified very clearly in each star.

Stars KIC 6603624 and KIC 3656476 present patterns of peaks that all show nearly regular spacings in frequency. These peaks are due to acoustic (pressure, or p) modes of high radial order, n , with frequencies approximately proportional to $\sqrt{\bar{\rho}}$, $\bar{\rho} \propto M/R^3$ being the mean density of the star, with

mass M and surface radius R . The most obvious spacings are the “large frequency separations,” $\Delta\nu$, between consecutive overtones of the same spherical angular degree, l . These large separations are related to the acoustic radii of the stars. The “small frequency separations” are the spacings between modes adjacent in frequency that have the same parity angular degree. Here, we see clearly the small separations $\delta\nu_{02}$ between modes

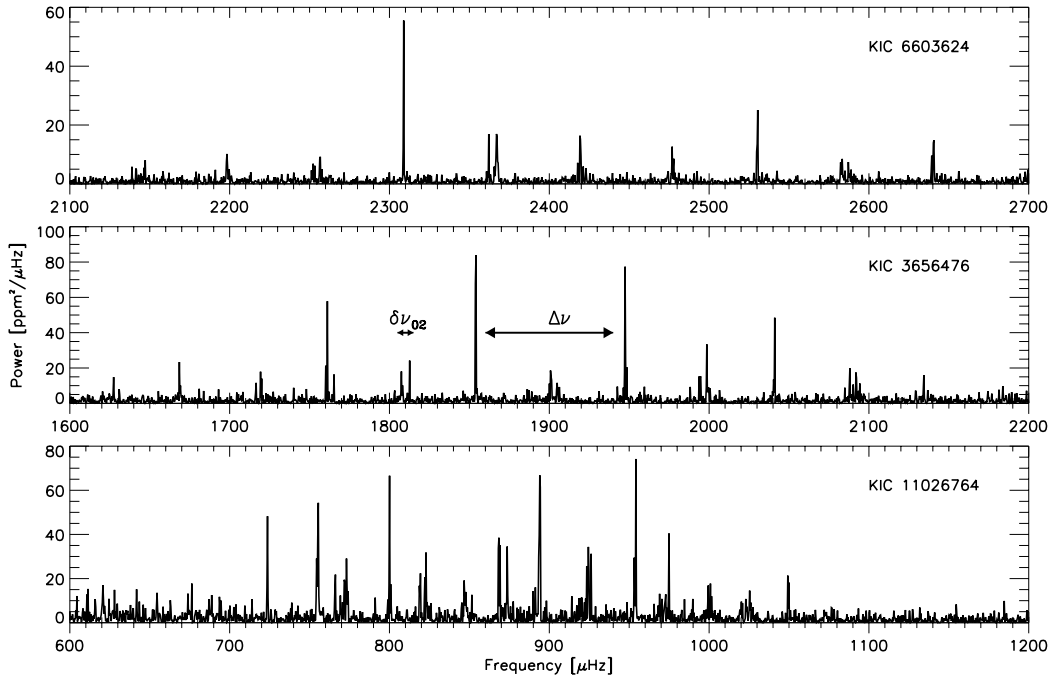


Figure 2. Frequency–power spectra of the three stars, plotted on a linear scale over the frequency ranges where the mode amplitudes are most prominent. Examples of the characteristic large ($\Delta\nu$) and small ($\delta\nu_{02}$) frequency separations are also marked on the spectrum of KIC 3656476.

Table 1
Non-seismic and Seismic Parameters, and Preliminary Stellar Properties^a

Star	2MASS ID	T_{eff} (K)	$\log g$ (dex)	[Fe/H] (dex)	$\Delta\nu$ (μHz)	$\delta\nu_{02}$ (μHz)	R (R_{\odot})	M (M_{\odot})
KIC 6603624 ^b	19241119+4203097	5790 ± 100	4.56 ± 0.10	0.38 ± 0.09	110.2 ± 0.6	4.7 ± 0.2	1.18 ± 0.02	1.05 ± 0.06
KIC 3656476 ^c	19364879+3842568	5666 ± 100	4.32 ± 0.06	0.22 ± 0.04	94.1 ± 0.6	4.4 ± 0.2	1.31 ± 0.02	1.04 ± 0.06
KIC 11026764 ^b	19212465+4830532	5640 ± 80	3.84 ± 0.10	0.02 ± 0.06	50.8 ± 0.3	4.3 ± 0.5	2.10 ± 0.10	1.10 ± 0.12

Notes.

^a Non-seismic parameters are T_{eff} , $\log g$, and [Fe/H]; seismic parameters are $\Delta\nu$ and $\delta\nu_{02}$; and the stellar properties inferred from the non-seismic and seismic data are M and R .

^b Non-seismic parameters for KIC 6603624 and KIC 11026764 from observations made with FIES at the Nordic Optical Telescope (NOT); data reduced in the manner of Bruntt et al. (2004, 2008).

^c Non-seismic parameters for KIC 3656476 from observations made with SOPHIE at Observatoire de Haute-Provence; data reduced in the manner of Santos et al. (2004).

of $l = 0$ and $l = 2$ (photometric observations have low sensitivity to $l = 3$ modes, and so they cannot be seen clearly in these frequency–power spectra). The small separations are very sensitive to the gradient of the sound speed in the stellar cores and hence the evolutionary state of the stars.

The near regularity of the frequency separations of KIC 6603624 and KIC 3656476 is displayed in the échelle diagrams in Figure 3. Here, we have plotted estimates of the mode frequencies of the stars (see Section 3) against those frequencies modulo the average large frequency separations. In a simple asymptotic description of high-order p -modes (e.g., Tassoul 1980), the various separations do not change with frequency. Stars that obeyed this description would show vertical, straight ridges in the échelle diagram (assuming use of the correct $\Delta\nu$). Solar-type stars do in practice show departures of varying degrees from this simple description. These variations with frequency carry signatures of, for example, regions of abrupt structural change in the stellar interiors, e.g., the near-surface

ionization zones and the bases of the convective envelopes (Houdek & Gough 2007).

While the variations are clearly modest in KIC 6603624 and KIC 3656476, KIC 11026764 presents a somewhat different picture. Its $l = 1$ ridge is noticeably disrupted, and shows clear evidence of so-called avoided crossings (Osaki 1975; Aizenman et al. 1977), where modes resonating in different cavities exist at virtually the same frequency.

These avoided crossings are a tell-tale indicator that the star has evolved significantly. In young solar-type stars, there is a clear distinction between the frequency ranges that will support p -modes and buoyancy (gravity, or g) modes. As stars evolve, the maximum buoyancy (Brunt-Väisälä) frequency increases. After exhaustion of the central hydrogen, the buoyancy frequency in the deep stellar interior may increase to such an extent that it extends into the frequency range of the high-order acoustic modes. Interactions between acoustic modes and buoyancy modes may then lead to a series of avoided crossings, which

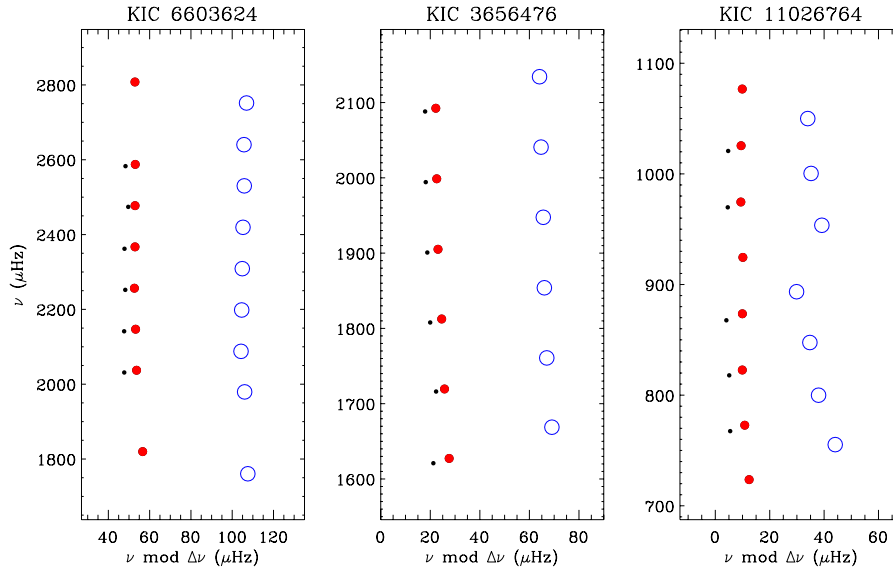


Figure 3. Échelle diagrams of the observed frequencies in each star, showing the $l = 0$ (filled red symbols), $l = 1$ (open blue symbols), and $l = 2$ (small black symbols) ridges.

(A color version of this figure is available in the online journal.)

affect (or “bump”) the frequencies and also change the intrinsic properties of the modes, with some taking on mixed p and g characteristics. The jagged appearance of the $l = 1$ ridge of KIC 11026764 illustrates these effects, which are strikingly similar to those seen in ground-based asteroseismic data on the bright stars η Boo (Christensen-Dalsgaard et al. 1995; Kjeldsen et al. 1995) and β Hyi (Bedding et al. 2007). Deheuvels & Michel (2009) and Deheuvels et al. (2009) have also reported evidence for avoided crossings in *CoRoT* observations of the oscillation spectrum of the star HD49385.

Next, we consider the peaks of individual modes. The observed oscillation modes in solar-type stars are intrinsically stable (e.g., Balmforth 1992a; Houdek et al. 1999) but driven stochastically by the vigorous turbulence in the superficial stellar layers (e.g., Goldreich & Keeley 1977; Balmforth 1992b; Samadi & Goupil 2001). Solar-like mode peaks have an underlying form that follows, to a reasonable approximation, a Lorentzian. The widths of the Lorentzians provide a measure of the linear damping rates, while the amplitudes are determined by the delicate balance between the excitation and damping. Measurement of these parameters therefore provides the means to infer various important properties of the still poorly understood near-surface convection.

The observed maximum mode amplitudes are all higher than solar. This is in line with predictions from simple scaling relations (Kjeldsen & Bedding 1995; Samadi et al. 2007), which use the inferred fundamental stellar properties (see Section 3) as input. Data from a larger selection of survey stars are required before we can say anything more definitive about the relations.

It is clear even from simple visual inspection of the spectra that the intrinsic line widths of the most prominent modes are comparable in size in all three stars to the line widths shown by the most prominent solar p -modes ($\approx 1 \mu\text{Hz}$). It would not otherwise be possible to distinguish the $l = 0$ and $l = 2$ modes so easily. The intrinsic frequency resolution of these short survey spectra ($\sim 0.35 \mu\text{Hz}$) makes it difficult to provide more definitive widths. However, the appearance of the modes in these stars is

consistent with the suggestion of Chaplin et al. (2009) that the line widths are a strong function of effective temperature. The three stars here all have effective temperatures that are similar to, or slightly cooler than, solar; while the F-type main-sequence stars observed by *CoRoT*—which have effective temperatures a few hundred degrees hotter than the Sun—exhibit line widths that are several times larger than solar (e.g., see Appourchaux et al. 2008; Barban et al. 2009; García et al. 2009). We add that *CoRoT* sees line widths in the G-type star HD49385 (Deheuvels et al. 2009) that are also narrower than those observed in F-type stars.

Given the inference on the line widths of the stars, we are able to state with renewed confidence that it should be possible to extract accurate and precise frequencies of $l = 0$, 1, and 2 modes in many of the brighter solar-type KASC targets observed by *Kepler*, because the peaks will be clearly distinguishable. The prospects on cool stars selected for long-term observations are particularly good. Here, the combination of improved resolution in frequency and modest (i.e., solar-like) line widths will in principle allow for robust estimation of frequency splittings of modes. These splittings have contributions from the internal stellar rotation and magnetic fields. We add that longer-term observations of the three survey stars reported in this Letter will be needed to show indisputable evidence of frequency splitting.

3. INFERENCE ON THE STELLAR PROPERTIES

An estimate of the average separations $\Delta\nu$ and $\delta\nu_{02}$ provides a complementary set of seismic data well suited to constraining the stellar properties (Christensen-Dalsgaard 1993). In faint KASC survey targets—where lower signal-to-noise ratios will make it difficult to extract robust estimates of individual frequencies—the average separations will be the primary seismic input data. The signatures of these separations are quite amenable to extraction, owing to their near-regularity.

Different teams extracted estimates of the average separations of the three stars, with analysis methods based largely on use

of the autocorrelation of either the timeseries or the power spectrum (e.g., see Huber et al. 2009; Mosser & Appourchaux 2009; Roxburgh 2009; Hekker et al. 2010; Mathur et al. 2010). We found good agreement between the different estimates (i.e., at the level of precision of the quoted parameter uncertainties). Representative estimates of the separations are given in Table 1. The teams also used peak-fitting techniques (like those applied to *CoRoT* data; see, for example, Appourchaux et al. 2008) to make available to the modeling teams initial estimates of the individual mode frequencies. The échelle diagrams plotted in Figure 3 show representative sets of these frequencies.

Several modeling teams then applied codes to estimate the stellar properties using the frequency separations, and other non-seismic data (see below), as input; the results from these analyses were then used as the starting points for further modeling, involving comparisons of the observed frequencies with frequencies calculated from evolutionary models. Use of individual frequencies increases the information content provided by the seismic data (e.g., see Monteiro et al. 2000; Roxburgh & Vorontsov 2003; Mazumdar et al. 2006; Cunha & Metcalfe 2007). For a general discussion of the modeling methods, see Cunha et al. (2007); Stello et al. (2009); Aerts et al. (2010); and references therein. Further detailed presentations of the modeling techniques applied here will appear in future papers.

The frequencies and the frequency separations depend to some extent on the detailed physics assumed in the stellar models (Monteiro et al. 2002). Consequently, a more secure determination of the stellar properties is possible when other complementary information—such as effective temperature T_{eff} , luminosity (or $\log g$), and metallicity—is known to sufficiently high accuracy and precision. The potential to test the input physics of models of field stars (e.g., convective energy transport, diffusion, opacities, etc.) requires non-seismic data for the seismic diagnostics to be effective (e.g., see Creevey et al. 2007). The modeling analyses therefore also incorporated non-seismic constraints, using T_{eff} , metallicity ([Fe/H]), and $\log g$ from complementary ground-based spectroscopic observations (see Table 1). The uncertainties in these spectroscopically estimated parameters are significantly lower than those given by the KIC parameters. Preliminary results given by different groups on the same ground-based spectra of these stars do however suggest that the true, external errors are higher than the quoted errors. Follow-up spectroscopic and photometric observations, and further comparative analyses, are now being carried out for other bright solar-type KASC targets by more than 20 members of KASC (e.g., Molenda-Žakowicz et al. 2008).

Our initial estimates of the stellar radii and masses are presented in Table 1. Given the close relation between the global properties of the stars and their oscillation frequencies, these seismically inferred properties are more precise, and more accurate, than properties inferred without the seismic inputs. The radii of KIC 6603624 and KIC 3656476 have been determined to better than 2%, and the masses to better than 6%. The modeling suggests both stars may be near the end of their main-sequence lifetimes.

The precision achieved for KIC 11026764 is not quite as good (about 5% in the radius and about 10% in the mass). This star has evolved off the main sequence, and is harder to model. KIC 11026764 demonstrates that when mixed modes are observed, individual frequencies can provide more stringent tests of the modeling than the average separations can. Initial results from modeling individual frequencies show it is possible to reproduce the disrupted $l = 1$ frequency ridge (Figure 3), indicating an age

in the range 6 and 7 Gyr. The modeling also suggests that some of the $l = 2$ modes may have mixed character.

Initial modeling results may also help to interpret the observed seismic spectra, allowing further mode frequencies to be identified securely. A possible example for KIC 11026764 concerns the prominent mode at $\sim 723 \mu\text{Hz}$. The peak lies on the $l = 0$ ridge, yet its appearance—a narrow peak, indicating a lightly damped mode having mixed characteristics—suggests a possible alternative explanation: the modeling points strongly to the observed power being predominantly from an $l = 1$ mode that has been shifted so far in frequency that it lies on top of an $l = 0$ mode.

In summary, all three stars are clearly excellent candidates for long-term observations by *Kepler*. With up to 1 yr of data we would, for example, expect to measure the depths of the near-surface convection zones and the signatures of near-surface ionization of He. It should also be possible to constrain the rotational frequency splittings. With 2 yr of data and more, we would also hope to begin to constrain any long-term changes to the frequencies and other mode parameters due to stellar-cycle effects (Karoff et al. 2009). More detailed modeling will also allow us to characterize the functional form of any required near-surface corrections to the model frequencies (see Kjeldsen et al. 2008).

Funding for this Discovery mission is provided by NASA's Science Mission Directorate. The authors wish to thank the entire *Kepler* team, without whom these results would not be possible. We also thank all funding councils and agencies that have supported the activities of KASC Working Group 1, and the International Space Science Institute (ISSI). The analyses reported in this Letter also used observations made with FIES at the Nordic Optical Telescope, and with SOPHIE at Observatoire de Haute-Provence.

Facilities: Kepler

REFERENCES

- Aerts, C., Christensen-Dalsgaard, J., & Kurtz, D. W. 2010, *Asteroseismology* (Heidelberg: Springer)
- Aigrain, S., Favata, G., & Gilmore, G. 2004, *A&A*, **414**, 1139
- Aizenman, M., Smeyers, P., & Weigert, A. 1977, *A&A*, **58**, 41
- Appourchaux, T., et al. 2008, *A&A*, **488**, 705
- Arentoft, T., et al. 2008, *ApJ*, **687**, 1180
- Balmforth, N. J. 1992a, *MNRAS*, **255**, 603
- Balmforth, N. J. 1992b, *MNRAS*, **255**, 639
- Barban, C., et al. 2009, *A&A*, **506**, 51
- Bedding, T. R., et al. 2007, *ApJ*, **663**, 1315
- Bruntt, H., De Cat, P., & Aerts, C. 2008, *A&A*, **478**, 487
- Bruntt, H., et al. 2004, *A&A*, **425**, 683
- Chaplin, W. J., Houdek, G., Karoff, K., Elsworth, Y., & New, R. 2009, *A&A*, **500**, 21L
- Christensen-Dalsgaard, J. 1993, in ASP Conf. Ser. 42, Proc. GONG 1992: Seismic Investigation of the Sun and Stars, ed. T. M. Brown (San Francisco, CA: ASP), 347
- Christensen-Dalsgaard, J. 2004, *Sol. Phys.*, **220**, 137
- Christensen-Dalsgaard, J., Bedding, T. R., & Kjeldsen, H. 1995, *ApJ*, **443**, L29
- Creevey, O. L., Monteiro, M. J. P. F. G., Metcalfe, T. S., Brown, T. M., Jiménez-Reyes, S. J., & Belmonte, J. A. 2007, *ApJ*, **659**, 616
- Cunha, M. S., & Metcalfe, T. S. 2007, *ApJ*, **666**, 413
- Cunha, M. S., et al. 2007, *A&AR*, **14**, 217
- Deheuvels, S., & Michel, E. 2009, *Ap&SS*, in press (tmp.241D)
- Deheuvels, S., et al. 2009, *A&A*, submitted
- García, R. A., et al. 2009, *A&A*, **506**, 41
- Gilliland, R. L., et al. 2010a, *PASP*, in press
- Gilliland, R. L., et al. 2010b, *ApJ*
- Goldreich, P., & Keeley, D. A. 1977, *ApJ*, **212**, 243
- Gough, D. O. 1987, *Nature*, **326**, 257

APPENDIX F. THE ASTEROSEISMIC POTENTIAL OF KEPLER:
FIRST RESULTS FOR SOLAR-TYPE STARS

No. 2, 2010

THE ASTEROSEISMIC POTENTIAL OF *KEPLER*

L175

- Hekker, S., et al. 2010, MNRAS, in press (arXiv:0911.2612)
- Houdek, G., Balmforth, N. J., Christensen-Dalsgaard, J., & Gough, D. O. 1999, A&A, 351, 582
- Houdek, G., & Gough, D. O. 2007, MNRAS, 375, 861
- Huber, D., et al. 2009, Commun. Asteroseismol., 160, 74
- Karoff, C., Metcalfe, T. S., Chaplin, W. J., Elsworth, Y., Kjeldsen, H., Arentoft, T., & Buzasi, D. 2009, MNRAS, 399, 914
- Kjeldsen, H., & Bedding, T. R. 1995, A&A, 293, 87
- Kjeldsen, H., Bedding, T. R., & Christensen-Dalsgaard, J. 2008, ApJ, 683, L175
- Kjeldsen, H., Bedding, T. R., Viskum, M., & Frandsen, S. 1995, AJ, 109, 1313
- Koch, D., et al. 2010, ApJ, 713, L79
- Latham, D. W., Brown, T. M., Monet, D. G., Everett, M., Esquerdo, G. A., & Hergenrother, C. W. 2005, BAAS, 37, 1340
- Mathur, S., et al. 2010, A&A, in press (arXiv:0912.3367)
- Mazumdar, A., Basu, S., Collier, B. L., & Demarque, P. 2006, MNRAS, 372, 949
- Michel, E., et al. 2008, Science, 322, 558
- Molenda-Żakowicz, J., Frasca, A., & Latham, D. 2008, Acta Astron., 58, 419
- Monteiro, M. J. P. F. G., Christensen-Dalsgaard, J., & Thompson, M. J. 2000, MNRAS, 365, 165
- Monteiro, M. J. P. F. G., Christensen-Dalsgaard, J., & Thompson, M. J. 2002, in Proc. First Eddington Workshop on Stellar Structure and Habitable Planet Finding, Córdoba, Spain, ed. B. Battrick (scientific editors: F. Favata, I. W. Roxburgh, & D. Galadi) (ESASP 485; Noordwijk: ESA), 291
- Mosser, B., & Appourchaux, T. 2009, A&A, 508, 877
- Osaki, Y. 1975, PASJ, 27, 237
- Roxburgh, I. W. 2009, A&A, 506, 435
- Roxburgh, I. W., & Vorontsov, S. V. 2003, A&A, 411, 215
- Samadi, R., & Goupil, M.-J. 2001, A&A, 370, 136
- Samadi, R., et al. 2007, A&A, 463, 297
- Santos, N. C., Israelian, G., & Mayor, M. 2004, A&A, 415, 1153
- Stello, D., et al. 2009, ApJ, 700, 1589
- Tassoul, M. 1980, ApJS, 43, 469

Appendix G

Asteroseismology of Solar-type stars with Kepler II: Stellar Modeling

Asteroseismology of Solar-type stars with Kepler II: Stellar Modeling

T.S. Metcalfe¹, M.J.P.F.G. Monteiro², M.J. Thompson³, W.J. Chaplin⁴, S. Basu⁵, A. Bonanno⁶, M.P. Di Mauro⁷, G. Doğan⁸, P. Eggenberger⁹, C. Karoff^{4,8}, D. Stello¹⁰, and KASC WG1*

¹ High Altitude Observatory, National Center for Atmospheric Research, P.O. Box 3000, Boulder Colorado 80307 USA

² Centro de Astrofísica and DFA-Faculdade de Ciências, Universidade do Porto, Portugal

³ School of Mathematics and Statistics, University of Sheffield, Hounsfield Road, Sheffield S3 7RH, UK

⁴ School of Physics and Astronomy, University of Birmingham, Edgbaston, Birmingham, B15 2TT, UK

⁵ Department of Astronomy, Yale University, P.O. Box 208101, New Haven, CT 06520-8101, USA

⁶ INAF Osservatorio Astrofisico di Catania, Via S.Sofia 78, 95123, Catania, Italy

⁷ INAF-IASF, Istituto di Astrofisica Spaziale e Fisica Cosmica, via del Fosso del Cavaliere 100, 00133 Roma, Italy

⁸ Department of Physics and Astronomy, Aarhus University, DK-8000 Aarhus C, Denmark

⁹ Geneva Observatory, University of Geneva, Maillettes 51, 1290, Sauverny, Switzerland

¹⁰ Sydney Institute for Astronomy (SIfA), School of Physics, University of Sydney, NSW 2006, Australia

Received 15 April 2010, accepted 30 June 2010

Key words stars: oscillations—stars: individual (KIC 11026764)—stars: interiors—stars:late-type

Observations from the Kepler satellite were recently published for three bright G-type stars, which were monitored during the first 33.5 d of science operations. One of these stars, KIC 11026764, exhibits a characteristic pattern of oscillation frequencies suggesting that the star has evolved significantly. We have derived initial estimates of the properties of KIC 11026764 from the oscillation frequencies observed by Kepler, combined with ground-based spectroscopic data. We present preliminary results from detailed modeling of this star, employing a variety of independent codes and analyses that attempt to match the asteroseismic and spectroscopic constraints simultaneously.

© 2010 WILEY-VCH Verlag GmbH & Co. KGaA, Weinheim

1 Introduction

In March 2009, NASA launched the *Kepler* satellite—a mission designed to find habitable Earth-like planets around distant Sun-like stars. The satellite consists of a 0.95-m telescope with an array of digital cameras that will monitor the brightness of more than 150,000 solar-type stars with a few parts-per-million precision for between 4–6 years (Borucki et al. 2010). Some of these stars are expected to have planetary systems, and some of the planets will have orbits such that they periodically pass in front of the host star, causing a

brief decrease in the amount of light recorded by the satellite. The depth of such a *transit* contains information about the size of the planet relative to the size of the host star.

Since we do not generally know the precise size of the host star, the mission design includes a revolving selection of 512 stars monitored with the higher cadence that is necessary to detect solar-like oscillations, allowing us to apply the techniques of asteroseismology (Aerts et al. 2010; Christensen-Dalsgaard et al. 2007). Even a relatively crude analysis of such measurements can lead to reliable determinations of stellar radii to help characterize the planetary systems discovered by the satellite, and stellar ages to reveal how such systems evolve over time. For the asteroseismic targets that do not contain planetary companions, these data will allow a uniform determination of the physical properties of hundreds of solar-type stars, providing a new window on stellar structure and evolution.

Initial results from the Kepler Asteroseismic Investigation were presented in Gilliland et al. (2010), while a more detailed analysis of the solar-like oscillations detected in several early targets was published by Chaplin et al. (2010). The latter paper includes observations of three bright ($V \sim 9$) G IV–V stars, which were monitored during the first 33.5 d of science operations. One of these stars, KIC 11026764 (\equiv 2MASS J19212465+4830532 \equiv BD+48 2882), exhibits a characteristic pattern of oscillation frequencies suggesting that the star has evolved significantly.

* The Kepler Asteroseismic Science Consortium Working Group 1 also includes: Appourchaux, T., Elsworth, Y., Garcia, R.A., Houdek, G., Molenda-Żakowicz, J., Brown, T.M., Christensen-Dalsgaard, J., Gilliland, R.L., Kjeldsen, H., Borucki, W.J., Koch, D., Jenkins, J.M., Ballot, J., Bazot, M., Bedding, T.R., Benomar, O., Brandao, I.M., Bruntt, H., Campante, T.L., Creevey, O.L., Drexler, S., Esch, L., Fletcher, S. T., Frandsen, S., Gai, N., Gaulme, P., Handberg, R., Hekker, S., Howe, R., Huber, D., Korzennik, S.G., Lebrun, J.C., Leccia, S., Martic, M., Mathur, S., Mosser, B., New, R., Quirion, P.-O., Regulo, C., Roxburgh, I.W., Salabert, D., Schou, J., Sousa, S.G., Verner, G.A., Arentoft, T., Barban, C., Belkacem, K., Benatti, S., Biazzo, K., Boumier, P., Bradley, P.A., Broomhall, A.-M., Buzasi, D.L., Claudi, R.U., Cunha, M.S., D’Antona, F., Deheuvels, S., Derekas, A., Garcia Hernandez, A., Giampapa, M.S., Goupil, M.J., Gruberbauer, M., Guzik, J.A., Hale, S.J., Ireland, M.J., Kiss, L.L., Kitiashvili, I.N., Kolenberg, K., Korhonen, H., Kosovichev, A.G., Kupka, F., Lebreton, Y., Leroy, B., Ludwig, H.-G., Mathis, S., Michel, E., Miglio, A., Montalbán, J., Moya, A., Noels, A., Noyes, R.W., Palte, P. L., Piau, L., Preston, H.L., Roca Cortes, T., Roth, M., Sato, K.H., Schmitt, J., Serenelli, A.M., Silva Aguirre, V., Stevens, I.R., Suarez, J. C., Suran, M.D., Trampedach, R., Turck-Chieze, S., Uytterhoeven, K., Ventura, R. & Wilson, P.A.

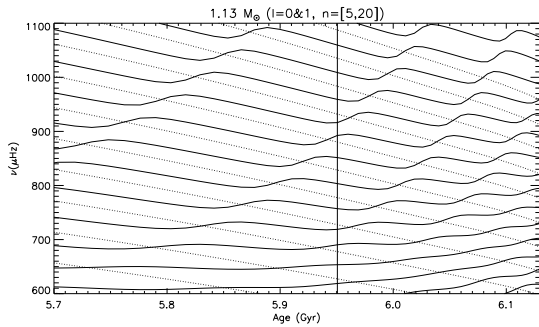


Fig. 1 Evolution of the $l = 0$ (dotted) and $l = 1$ (solid) oscillation frequencies as a function of age for a representative stellar model of KIC 11026764.

In unevolved stars, the high radial order (n) acoustic oscillation modes (p -modes) with a given spherical degree (l) are almost evenly spaced in frequency. As the star evolves and the envelope expands and cools, the p -mode frequencies gradually decrease. Meanwhile, as the star becomes more centrally condensed, the buoyancy-driven (g -mode) oscillations in the core shift to higher frequencies. This eventually leads to a range of frequencies where the oscillation modes can take on a mixed character, behaving like g -modes in the core and p -modes in the envelope (“mixed modes”), with their frequencies shifted as they undergo so-called *avoided crossings*. This behavior changes very quickly with stellar age, and propagates from one radial order to the next as the star continues to evolve (see Figure 1). Consequently, the particular modes that deviate significantly from uniform frequency spacing yield a strong (though model-dependent) constraint on the age of the star (see Christensen-Dalsgaard 2004). As noted by Gilliland et al. (2010) and Chaplin et al. (2010), the dipole ($l = 1$) modes observed in KIC 11026764 show the signature of an avoided crossing—raising the exciting possibility that detailed modeling of this star will ultimately provide a very precise determination of its age.

In this paper we derive initial estimates of the stellar properties of KIC 11026764 by matching the observed oscillation frequencies from *Kepler* data and the spectroscopic constraints from ground-based observations. The extraction and identification of the oscillation frequencies is described by Karoff et al. (this volume), and the analysis of ground-based observations to derive spectroscopic constraints is described by Molenda-Żakowicz et al. (this volume). We focus on the initial results from detailed modeling of this star employing a variety of independent codes and analyses, all attempting to match the asteroseismic and spectroscopic constraints simultaneously.

2 Stellar Modeling

Traditional stellar modeling in the absence of asteroseismic information involves matching, as closely as possible, the non-seismic constraints in a classical Hertzsprung-Russell

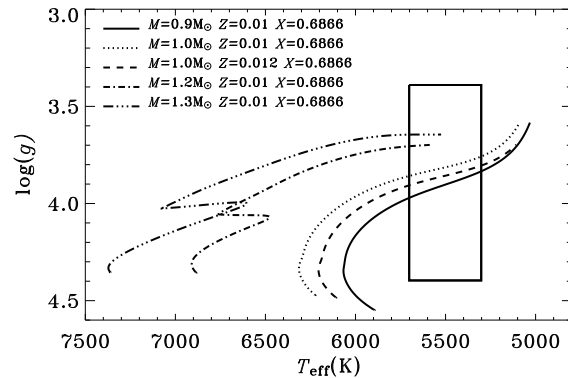


Fig. 2 The observational error box for KIC 11026764 from the Kepler Input Catalog (rectangle) along with several stellar evolution tracks, showing that the non-seismic constraints imply either a slightly evolved star with a mass comparable to the Sun, or a higher mass star in a more advanced stage of evolution.

(H-R) diagram. A spectroscopic determination of $[\text{Fe}/\text{H}]$ can be used to fix the composition of the stellar models, and evolution tracks are then typically compared to the available constraints on T_{eff} and $\log(g)$ from photometry and spectroscopy. The ambiguity of such a comparison is illustrated in Figure 2, which shows the observational error box for KIC 11026764 from the Kepler Input Catalog (KIC) along with several stellar evolution tracks. Evidently, the non-seismic constraints imply either a slightly evolved star with a mass comparable to the Sun, or a higher mass star in a more advanced stage of evolution.

For stars that exhibit solar-like oscillations, an estimate of the average large and small frequency spacing provides a complementary set of data well suited to constraining the stellar properties (Christensen-Dalsgaard 1993; Monteiro et al. 2000). In faint KASC survey targets—where lower signal-to-noise ratios make it difficult to extract robust estimates of individual frequencies—the average spacings will be the primary seismic data. The signatures of these spacings are quite amenable to extraction, owing to their near-regularity. When the data are sufficient to allow a robust estimation of individual frequencies—as is the case for KIC 11026764—use of those frequencies increases the information content provided by the seismic data (e.g., see Cunha & Metcalfe 2007; Mazumdar et al. 2006; Roxburgh & Vorontsov 2003).

Different teams extracted estimates of the average separations of KIC 11026764, with analysis methods based on autocorrelation of either the time series or the power spectrum (e.g., see Campante et al. 2010; Hekker et al. 2010; Huber et al. 2009; Karoff et al. 2010; Mathur et al. 2010; Mosser & Appourchaux 2009; Roxburgh 2009). We found good agreement between the different estimates (i.e., at the level of precision of the quoted parameter uncertainties). The teams also used peak-fitting techniques (like those applied to CoRoT data; see, for example, Appourchaux et al.

2008) to provide initial estimates of the individual mode frequencies to the modeling teams. Complete details of this analysis can be found in Karoff et al. (this volume).

Several modeling teams then applied codes to estimate the stellar properties of KIC 11026764 using the frequency separations and other non-seismic data as input. The results of these initial analyses were used as starting points for further modeling, involving comparisons of the observed frequencies with those calculated from evolutionary models. The frequencies and the frequency separations depend to some extent on the detailed physics assumed in the stellar models (Metcalf et al. 2009; Monteiro et al. 2002). Consequently, a more secure determination of the stellar properties is possible when complementary data are known with sufficiently high accuracy and precision. Indeed, the potential to test the input physics of models of field stars (e.g., convective energy transport, diffusion, opacities, etc.) actually requires non-seismic data for the seismic diagnostics to be effective (e.g., see Creevey et al. 2007).

The modeling analyses therefore also incorporated non-seismic constraints, using T_{eff} , $\log(g)$ and $[\text{Fe}/\text{H}]$ from complementary ground-based spectroscopic observations. For KIC 11026764 only the KIC estimates were initially available, with large uncertainties of about 200 K in T_{eff} , and up to 0.5 dex in $\log(g)$ and $[\text{Fe}/\text{H}]$. We performed several cross-checks of the T_{eff} for KIC 11026764 using different suggested temperature calibrations of the available 2MASS (Cutri et al. 2003) $VJHK$ magnitudes (Gallardo et al. 2005; Kinman & Castelli 2002; Masana et al. 2006). These tests yielded satisfactory agreement with the T_{eff} value from KIC at the level of the estimated uncertainties. Preliminary results given by different groups on the same ground-based spectra of these stars do however suggest that the true, external errors are higher than the quoted errors. Complete details of this analysis can be found in Molenda-Żakowicz et al. (this volume).

3 Initial Results

Our initial estimates of the properties of KIC 11026764 using several independent codes and analyses are presented in Table 1. Given the close relation between the global properties of the stars and their oscillation frequencies, these seismically inferred properties are more precise, and more accurate, than properties inferred without the seismic inputs.

The precision achieved for KIC 11026764 is about 5% in the radius, and about 10% in the mass. This star has evolved off the main sequence, and is relatively difficult to model. The analysis demonstrates that when mixed modes are observed, individual frequencies can provide more stringent tests of the modeling than the average frequency spacings alone. Initial results from modeling the individual frequencies show that it is possible to reproduce the disrupted $l = 1$ frequency ridge (see Figure 3), and indicate a stellar age near 6 Gyr.

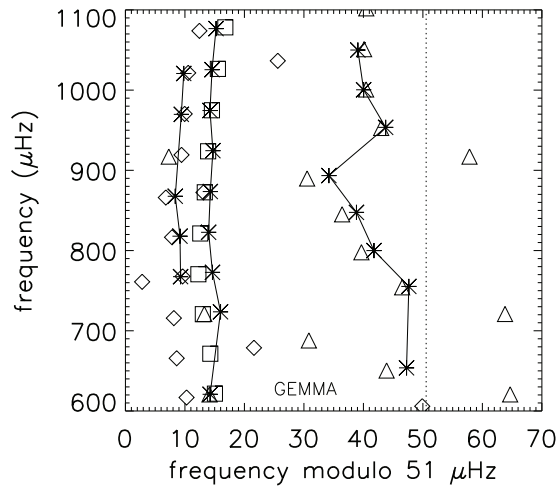


Fig. 3 An echelle diagram for the observed frequencies of KIC 11026764 (connected points), where we divide the oscillation spectrum into segments of length $\langle \Delta\nu_0 \rangle$ and plot them against the oscillation frequency, along with a representative stellar model (open points) showing the $l = 0$ (squares), $l = 1$ (triangles) and $l = 2$ modes (diamonds). Note the $l = 1$ avoided crossing near 900 μHz and the overlapping $l = 0$ and $l = 1$ modes near 620 and 720 μHz , which were common features in all analyses.

These initial results may also help us to interpret the observed seismic spectra, allowing additional mode frequencies to be identified securely. For example, the prominent mode near 720 μHz lies on the $l = 0$ ridge, yet its appearance suggests a possible alternative explanation. Mixed modes exhibit g -mode character in the core, so the mode inertia is typically much higher than regular p -modes at the same frequency (see Christensen-Dalsgaard 2004). This inertia prevents mixed modes from being as strongly damped, leading to narrower peaks in the power spectrum. The modeling points strongly to the observed power being predominantly from an $l = 1$ mode that has been shifted so far in frequency that it lies on top of an $l = 0$ mode. This was a generic feature of several independent analyses using different stellar evolution codes, lending further credibility to this interpretation.

In summary, KIC 11026764 is clearly an excellent candidate for long-term observations by *Kepler*. With up to 1 yr of data we would expect to measure the depth of the near-surface convection zone, and the signatures of near-surface ionization of He (Verner et al. 2006). It should also be possible to constrain the rotational frequency splittings. With 2 yr of data and more, we could also begin to constrain any long-term changes to the frequencies and other mode parameters due to stellar-cycle effects (Karoff et al. 2009). More detailed modeling will also allow us to characterize the functional form of any required near-surface corrections to the model frequencies (see Kjeldsen et al. 2008). Considering

Table 1 Preliminary model-fitting results for KIC 11026764 from several different codes.

Code	M/M_{\odot}	Z	X	α	t(Gyr)	$T_{\text{eff}}(\text{K})$	L/L_{\odot}	R/R_{\odot}	log g	Reference
YREC	1.20	0.0142	0.76	1.83	6.25	5500	3.53	2.07	3.88	Demarque et al. (2008)
Catania	1.10	0.0159	0.77	1.10	6.60	5357	2.97	2.00	3.87	Bonanno et al. (2002)
ASTEC-1	1.00	0.0100	0.69	1.88	6.51	5700	3.60	1.95	3.86	Christensen-Dalsgaard (2008)
ASTEC-2	1.10	0.0125	0.72	1.70	6.35	5653	3.65	2.01	3.88	Christensen-Dalsgaard (2008)
Geneva	1.15	0.0150	0.71	1.80	5.80	5581	3.73	2.07	3.86	Eggenberger et al. (2008)
SEEK	1.20	0.0197	0.71	1.15	5.50	5500	3.36	2.03	3.90	Quirion et al. (2010)
RADIUS	2.03	...	Stello et al. (2009)

that KIC 11026764 is just one of the thousands of solar-type stars that have been observed during the survey phase of *Kepler*, the future of asteroseismology looks very bright.

Acknowledgements. This work was supported in part by NASA grant NNX09AE59G. The National Center for Atmospheric Research is a federally funded research and development center sponsored by the U.S. National Science Foundation. GD and CK acknowledge financial support from the Danish Natural Science Research Council. Funding for the Kepler mission is provided by NASA's Science Mission Directorate. We thank the entire Kepler team for the development and operations of this outstanding mission.

References

- Aerts, C., Christensen-Dalsgaard, J., & Kurtz, D. W.: 2010, *Asteroseismology*, Springer, (ISBN: 978-1-4020-5178-4)
- Appourchaux, T., Michel, E., Auvergne, M., et al., 2008: *A&A* 488, 705
- Bonanno, A., Schlattl, H., Paternó L., 2002: *A&A* 390, 1115
- Borucki, W. J., et al., 2010: *Science* 327, 977
- Campante, T. L. et al., 2010: *MNRAS*, submitted
- Chaplin, W. J., et al., 2010: *ApJ* 713, L169
- Christensen-Dalsgaard, J., 1993: *ASP Conf.* 42, 347
- Christensen-Dalsgaard, J., 2004: *Sol. Phys.* 220, 137
- Christensen-Dalsgaard, J., Arentoft, T., Brown, T. M., Gilliland, R. L., Kjeldsen, H., Borucki, W. J., & Koch, D., 2007: *CoAst* 150, 350
- Christensen-Dalsgaard, J., 2008: *Ap&SS* 316, 13
- Creevey, O. L., Monteiro, M. J. P. F. G., Metcalfe, T. S., Brown, T. M., Jiménez-Reyes, S. J., Belmonte, J. A., 2007: *ApJ* 659, 616
- Cunha, M. S., Metcalfe, T. S., 2007: *ApJ* 666, 413
- Cutri, R. M., et al., 2003: *The 2MASS All-Sky Catalog of Point Sources*, University of Massachusetts and Infrared Processing and Analysis Center IPAC/California Institute of Technology
- Demarque, P., Guenther, D. B., Li, L. H., Mazumdar, A., Straka, C. W., 2008: *Ap&SS* 316, 311
- Eggenberger, P., Meynet, G., Maeder, A., et al., 2008: *Ap&SS* 316, 43
- Gallardo, J., Minniti, D., Valls-Gabaud, D., Rejkuba, M., 2005: *A&A* 431, 707
- Gilliland, R. L., et al., 2010: *PASP* 122, 131
- Hekker, S., Broomhall, A.-M., Chaplin, W. J., et al., 2010: *MNRAS* 402, 2049
- Huber, D., Stello, D., Bedding, T. R., et al., 2009: *CoAst* 160, 74
- Karoff, C., Metcalfe, T. S., Chaplin, W. J., Elsworth, Y., Kjeldsen, H., Arentoft, T., Buzasi, D., 2009: *MNRAS* 399, 914
- Karoff, C., Campante, T. L., Chaplin, W. J., 2010: AN, submitted (arXiv:1003.4167)
- Kinman, T., Castelli, F., 2002: *A&A* 391, 1039
- Kjeldsen, H., Bedding, T. R., Christensen-Dalsgaard, J., 2008: *ApJ* 683, L175
- Masana, E., Jordi, C., Ribas, I., 2006: *A&A* 450, 735
- Mathur, S., García, R. A., Régulo C., et al., 2010: *A&A* 511, 46
- Mazumdar, A., Basu, S., Collier, B. L., Demarque, P., 2006: *MNRAS* 372, 949
- Metcalfe, T. S., Creevey, O. L., Christensen-Dalsgaard, J., 2009: *ApJ* 699, 373
- Monteiro, M. J. P. F. G., Christensen-Dalsgaard, J., Thompson, M. J., 2000: *MNRAS* 316, 165
- Monteiro, M. J. P. F. G., Christensen-Dalsgaard, J., Thompson, M. J., 2002: *ESASP* 485, 291
- Mosser, B., Appourchaux, T., 2009: *A&A* 508, 877
- Quirion, P.-O., Christensen-Dalsgaard, J., Arentoft, T., 2010: in preparation
- Roxburgh, I. W., Vorontsov, S. V., 2003: *A&A* 411, 215
- Roxburgh, I. W., 2009: *A&A* 506, 435
- Stello, D., et al., 2009: *ApJ* 700, 1589
- Verner, G. A., Chaplin, W. J., & Elsworth, Y. 2006: *ApJ* 638, 440

Appendix H

A precise asteroseismic age and
radius for the evolved sun-like star
KIC 11026764

APPENDIX H. A PRECISE ASTEROSEISMIC AGE AND RADIUS FOR THE EVOLVED SUN-LIKE STAR KIC 11026764

ACCEPTED FOR PUBLICATION IN THE ASTROPHYSICAL JOURNAL
Preprint typeset using L^AT_EX style emulateapj v. 2/16/10

A PRECISE ASTEROSEISMIC AGE AND RADIUS FOR THE EVOLVED SUN-LIKE STAR KIC 11026764

T. S. METCALFE¹, M. J. P. F. G. MONTEIRO², M. J. THOMPSON^{3,1}, J. MOLEND-
A-ZAKOWICZ⁴, T. APPOURCHAUX⁵, W. J. CHAPLIN⁶,
G. DOĞAN⁷, P. EGGENBERGER⁸, T. R. BEDDING⁹, H. BRUNTT¹⁰, O. L. CREEVEY^{11,12}, P.-O. QUIRION¹³, D. STELLO⁹, A. BONANNO¹⁴,
V. SILVA AGUIRRE¹⁵, S. BAŞU¹⁶, L. ESCH¹⁶, N. GAI^{16,17}, M. P. DI MAURO¹⁸, A. G. KOSOVICHEV¹⁹, I. N. KITIASHVILI²⁰,
J. C. SUÁREZ²¹, A. MOYA²², L. PIAU²³, R. A. GARCÍA²³, J. P. MARQUES²⁴, A. FRASCA¹⁴, K. BIAZZO²⁵, S. G. SOUSA²,
S. DREIZLER²⁶, M. BAZOT², C. KAROFF⁶, S. FRANDBSEN⁷, P. A. WILSON^{27,28}, T. M. BROWN²⁹, J. CHRISTENSEN-DALSGAARD⁷,
R. L. GILLILAND³⁰, H. KJELDBSEN⁷, T. L. CAMPANTE^{2,7}, S. T. FLETCHER³¹, R. HANDBERG⁷, C. RÉGULO^{11,12}, D. SALABERT^{11,12},
J. SCHOU¹⁹, G. A. VERNER³², J. BALLOT³³, A.-M. BROOMHALL⁶, Y. ELSWORTH⁶, S. HEKKER⁶, D. HUBER⁹, S. MATHUR¹, R. NEW³¹,
I. W. ROXBURGH^{32,10}, K. H. SATO³³, T. R. WHITE⁹, W. J. BORUCKI³⁴, D. G. KOCH³⁴, J. M. JENKINS³⁵

Draft version September 9, 2010

ABSTRACT

The primary science goal of the *Kepler Mission* is to provide a census of exoplanets in the solar neighborhood, including the identification and characterization of habitable Earth-like planets. The asteroseismic capabilities of the mission are being used to determine precise radii and ages for the target stars from their solar-like oscillations. Chaplin et al. (2010) published observations of three bright G-type stars, which were monitored during the first 33.5 d of science operations. One of these stars, the subgiant KIC 11026764, exhibits a characteristic pattern of oscillation frequencies suggesting that it has evolved significantly. We have derived asteroseismic estimates of the properties of KIC 11026764 from *Kepler* photometry combined with ground-based spectroscopic data. We present the results of detailed modeling for this star, employing a variety of independent codes and analyses that attempt to match the asteroseismic and spectroscopic constraints simultaneously. We determine both the radius and the age of KIC 11026764 with a precision near 1%, and an accuracy near 2% for the radius and 15% for the age. Continued observations of this star promise to reveal additional oscillation frequencies that will further improve the determination of its fundamental properties.

Subject headings: stars: evolution—stars: individual (KIC 11026764)—stars: interiors—stars: oscillations

1. INTRODUCTION

In March 2009 NASA launched the *Kepler* satellite, a mission designed to discover habitable Earth-like planets around distant Sun-like stars. The satellite consists of a 0.95-m telescope with an array of digital cameras that will monitor the brightness of more than 150,000 solar-type stars with a precision of a few parts-per-million for 4-6 years (Borucki et al. 2007). Some of these stars are expected to have planetary systems, and some of the planets will have orbits such that they periodically pass in front of the host star, causing a brief de-

¹ High Altitude Observatory, National Center for Atmospheric Research, Boulder, CO 80307, USA

² Centro de Astrofísica and DFA-Faculdade de Ciências, Universidade do Porto, Portugal

³ School of Mathematics and Statistics, University of Sheffield, Hounsfield Road, Sheffield S3 7RH, UK

⁴ Astronomical Institute, University of Wrocław, ul. Kopernika 11, 51-622 Wrocław, Poland

⁵ Institut d'Astrophysique Spatiale, Université Paris XI – CNRS (UMR8617), Batiment 121, 91405 Orsay Cedex, France

⁶ School of Physics and Astronomy, University of Birmingham, Edgbaston, Birmingham, B15 2TT, UK

⁷ Department of Physics and Astronomy, Aarhus University, DK-8000 Aarhus C, Denmark

⁸ Geneva Observatory, University of Geneva, Maillettes 51, 1290, Sauverny, Switzerland

⁹ Sydney Institute for Astronomy (SfA), School of Physics, University of Sydney, NSW 2006, Australia

¹⁰ Observatoire de Paris, 5 place Jules Janssen, 92190 Meudon Principal Cedex, France

¹¹ Instituto de Astrofísica de Canarias, E-38200 La Laguna, Spain

¹² Departamento de Astrofísica, Universidad de La Laguna, E-38206 La Laguna, Spain

¹³ Canadian Space Agency, 6767 Boulevard de l'Aéroport, Saint-Hubert, QC, J3Y 8Y9, Canada

¹⁴ INAF – Osservatorio Astrofisico di Catania, Via S.Sofia 78, 95123 Catania, Italy

¹⁵ Max Planck Institute for Astrophysics, Karl Schwarzschild Str. 1, Garching, D-85741, Germany

¹⁶ Department of Astronomy, Yale University, P.O. Box 208101, New Haven, CT 06520-8101, USA

¹⁷ Beijing Normal University, Beijing 100875, P.R. China

¹⁸ INAF-IASF Roma, Istituto di Astrofisica Spaziale e Fisica Cosmica, via del Fosso del Cavaliere 100, 00133 Roma, Italy

¹⁹ HEPL, Stanford University, Stanford, CA 94305-4085, USA

²⁰ Center for Turbulence Research, Stanford University, 488 Escondido Mall, Stanford, CA 94305, USA

²¹ Instituto de Astrofísica de Andalucía (CSIC), CP3004, Granada, Spain

²² Laboratorio de Astrofísica, CAB (CSIC-INTA), Villanueva de la Cañada, Madrid, PO BOX 78, 28691, Spain

²³ Laboratoire AIM, CEA/DSM-CNRS, Université Paris 7 Diderot, IRFU/SAP, Centre de Saclay, 91191, Gif-sur-Yvette, France

²⁴ LESIA, CNRS UMR 8109, Observatoire de Paris, Université Paris 6, Université Paris 7, 92195 Meudon Cedex, France

²⁵ Arcetri Astrophysical Observatory, Largo Enrico Fermi 5, 50125 Firenze, Italy

²⁶ Georg-August Universität, Institut für Astrophysik, Friedrich-Hund-Platz 1, D-37077 Göttingen

²⁷ Nordic Optical Telescope, Apartado 474, E-38700 Santa Cruz de La Palma, Santa Cruz de Tenerife, Spain

²⁸ Institute of Theoretical Astrophysics, University of Oslo, P.O. Box 1029, Blindern, N-0315 Oslo, Norway

²⁹ Las Cumbres Observatory Global Telescope, Goleta, CA 93117, USA

³⁰ Space Telescope Science Institute, Baltimore, MD 21218, USA

³¹ Materials Engineering Research Institute, Sheffield Hallam University, Sheffield, S1 1WB, UK

³² Astronomy Unit, Queen Mary, University of London, Mile End Road, London, E1 4NS, UK

³³ Laboratoire d'Astrophysique de Toulouse-Tarbes, Université de Toulouse, CNRS, 14 av E. Belin, 31400 Toulouse, France

³⁴ NASA Ames Research Center, MS 244-30, Moffett Field, CA 94035, USA

³⁵ SETI Institute, NASA Ames Research Center, MS 244-30, Moffett Field, CA 94035, USA

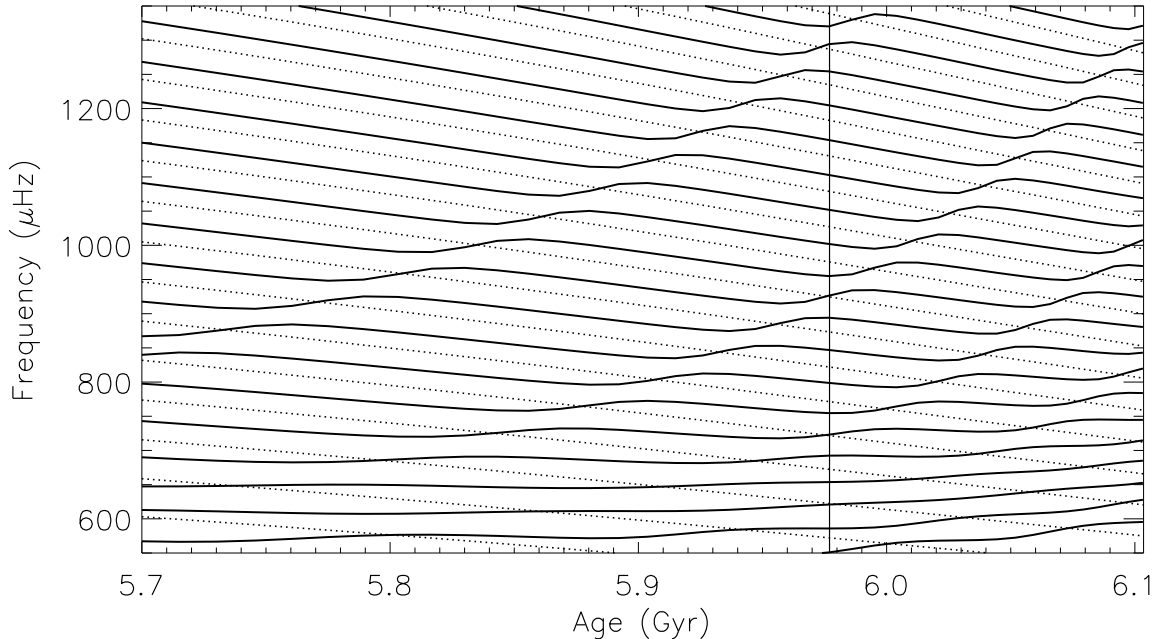


Figure 1. Evolution of the $l = 0$ (dotted) and $l = 1$ (solid) oscillation frequencies as a function of age for a representative stellar model of KIC 11026764. The frequency separation between consecutive $l = 1$ modes during an avoided crossing is a strong function of the stellar age. Note the prediction of a high-frequency avoided crossing above 1250 μHz for Model AA, indicated by the vertical line.

crease in the amount of light recorded by the satellite. The depth of such a *transit* contains information about the size of the planet relative to the size of the host star.

Since we do not generally know the precise size of the host star, the mission design includes a revolving selection of 512 stars monitored with the higher cadence that is necessary to detect short period solar-like oscillations, allowing us to apply the techniques of asteroseismology (Christensen-Dalsgaard et al. 2007; Aerts et al. 2010). Even a relatively crude analysis of such measurements can lead to reliable determinations of stellar radii to help characterize the extra-solar planetary systems discovered by the mission, and stellar ages to reveal how such systems evolve over time. For the asteroseismic targets that do not contain planetary companions, these data will allow a uniform determination of the physical properties of hundreds of solar-type stars, providing a new window on stellar structure and evolution.

Initial results from the Kepler Asteroseismic Investigation were presented by Gilliland et al. (2010a), while a more detailed analysis of the solar-like oscillations detected in several early targets was published by Chaplin et al. (2010). The latter paper includes observations of three bright ($V \sim 9$) G-type stars, which were monitored during the first 33.5 d of science operations. One of these stars, the subgiant KIC 11026764 (\equiv 2MASS J19212465+4830532 \equiv BD+48 2882 \equiv TYC 3547-12-1), exhibits a characteristic pattern of oscillation frequencies suggesting that it has evolved significantly.

In unevolved stars, the high radial order (n) acoustic oscillation modes (p-modes) with a given spherical degree (l) are almost evenly spaced in frequency. As the star evolves and the envelope expands, the p-mode frequencies gradually decrease. Meanwhile, as the star becomes more centrally condensed, the buoyancy-driven (g-mode) oscillations in the core shift to higher frequencies. This eventually leads to a range of

frequencies where the nonradial ($l > 0$) oscillation modes can take on a mixed character, behaving like g-modes in the core and p-modes in the envelope (“mixed modes”), with their frequencies shifted as they undergo so-called *avoided crossings* (Osaki 1975; Aizenman et al. 1977). This behavior changes relatively quickly with stellar age, and propagates from one radial order to the next as the star continues to evolve (see Figure 1). Consequently, those modes that deviate significantly from uniform frequency spacing yield a strong (though model-dependent) constraint on the age of the star (e.g., see Christensen-Dalsgaard 2004). Avoided crossings have been observed in the subgiant stars η Boo (Kjeldsen et al. 1995, 2003; Carrier et al. 2005) and β Hyi (Bedding et al. 2007), and possibly also in Procyon (Bedding et al. 2010) and HD 49385 (Deheuvels et al. 2010). As noted by Gilliland et al. (2010a) and Chaplin et al. (2010) the dipole ($l = 1$) modes observed in KIC 11026764 show the signature of an avoided crossing, raising the exciting possibility that detailed modeling of this star will provide a very precise determination of its age.

In this paper we derive the stellar age, radius and other characteristics of KIC 11026764 by matching both the observed oscillation frequencies from *Kepler* photometry and the best available spectroscopic constraints from ground-based observations. We describe the extraction and identification of the oscillation frequencies in §2, and the analysis of ground-based data for spectroscopic constraints in §3. In §4 we provide the details of the independent codes and analysis methods used for the fitting, and in §5 we describe our final modeling results. We summarize and discuss the broader significance of the results in §6.

2. OSCILLATION FREQUENCIES

The 58.85-second (short-cadence) photometric data on KIC 11026764 came from the first 33.5 d of science operations (2009 May 12 to June 14). Time series data were then

Table 1
The minimal and maximal sets of observed oscillation frequencies for KIC 11026764.

n^*	Minimal Frequency Set (μHz)			Maximal Frequency Set (μHz)		
	$l=0$	$l=1$	$l=2$	$l=0$	$l=1$	$l=2$
10	615.49 ± 0.45^b
11	620.79 ± 0.29^c	653.80 ± 0.23	...	620.42 ± 0.37^c	654.16 ± 0.39	670.23 ± 1.21^a
12	673.97 ± 0.71^a	699.87 ± 0.66^b	716.36 ± 0.21^b
13	723.63 ± 0.10	755.28 ± 0.26	767.46 ± 0.46	723.30 ± 0.24	754.85 ± 0.23	769.16 ± 0.71
14	772.82 ± 0.30	799.96 ± 0.40	817.91 ± 0.58	772.53 ± 0.33	799.72 ± 0.23	818.81 ± 0.30
15	822.72 ± 0.14	847.57 ± 0.30	867.66 ± 0.86	822.46 ± 0.31	846.88 ± 0.34	868.31 ± 0.24
16	873.55 ± 0.14	893.48 ± 0.33	...	873.30 ± 0.27	893.52 ± 0.20	919.31 ± 0.52^a
17	924.53 ± 0.37	953.57 ± 0.39	969.77 ± 0.36	924.10 ± 0.29	953.51 ± 0.22	970.12 ± 0.68
18	974.59 ± 0.35	1000.41 ± 0.52	1020.72 ± 1.33	974.36 ± 0.26	1000.38 ± 0.41	1019.72 ± 0.44
19	1025.48 ± 0.63	1049.99 ± 0.35	...	1025.16 ± 0.37	1049.34 ± 0.29	1072.49 ± 0.62^a
20	1076.70 ± 0.29	1076.52 ± 0.51

* Reference value of n , not used for model-fitting. ^a Observed mode adopted for refined model-fitting.
^b Mode not present in any of the optimal models. ^c Models suggest an alternate mode identification (see §6).

prepared from the raw observations in the manner described by Gilliland et al. (2010b). The power spectrum is shown in Figures 1 and 2 of Chaplin et al. (2010). Eight teams extracted estimates of the mode frequencies of the star. The teams used slightly different strategies to extract those estimates, but the main idea was to maximize the likelihood (Anderson et al. 1990) of a multi-parameter model designed to describe the frequency-power spectrum of the time series. The model included Lorentzian peaks to describe the p-modes, with flat and power-law terms in frequency (e.g., Harvey 1985) to describe instrumental and stellar background noise.

The fitting strategies followed well-established recipes. Some teams performed a global fit—optimizing simultaneously every free parameter needed to describe the observed spectrum (e.g., see Appourchaux et al. 2008)—while others fit the spectrum a few modes at a time, an approach traditionally adopted for Sun-as-a-star data (e.g., see Chaplin et al. 1999). Some teams also incorporated a Bayesian approach, with the inclusion of priors in the optimization and Markov Chain Monte Carlo (MCMC) analysis to map the posterior distributions of the estimated frequencies (e.g., see Benomar et al. 2009; Campante et al. 2010).

We then implemented a procedure to select two of the eight sets of frequencies, which would subsequently be passed to the modeling teams. Use of individual sets—as opposed to some average frequency set—meant that the modeling could rely on an easily reproducible set of input frequencies, which would not be the case for an average set. We selected a *minimal frequency* set to represent the modes that all teams agreed upon within the errors, and a *maximal frequency* set, which included all possible frequencies identified by at least two of the teams, as explained below.

From the sets of frequencies $\nu_{nl,i}$ provided by the eight teams, we calculated a list of average frequencies $\bar{\nu}_{nl}$. For each mode $\{n, l\}$, we computed the number of teams returning frequencies that satisfied

$$|\nu_{nl,i} - \bar{\nu}_{nl}| \leq \sigma_{nl,i}, \quad (1)$$

with $\sigma_{nl,i}$ representing the frequency uncertainties returned by each team. We then compiled a *minimal* list of modes. For each $\{n, l\}$ we counted the total number of teams with iden-

tified frequencies, as well as the number of those frequencies that satisfied Eq.(1). Modes for which *all* identifications satisfied the inequality were added to the minimal list. We also compiled a *maximal* list of modes, subject to the much more relaxed criterion that the $\{n, l\}$ satisfying Eq.(1) should be identified by at least two teams.

In the final stage of the procedure, we computed for each of the eight frequency sets the normalized root-mean-square (*rms*) deviations with respect to the $\bar{\nu}_{nl}$ of the minimal and maximal lists of modes. The frequency set with the smallest *rms* deviation with respect to the minimal list was chosen to be the *minimal frequency* set, while the set with the smallest *rms* deviation with respect to the maximal list was chosen to be the *maximal frequency* set. The minimal frequency set was also used by Chaplin et al. (2010), and provided the initial constraints for the modeling teams (see Table 1). The maximal frequency set was used later for additional validation, as explained in §5. Note that the same modes have slightly different frequencies in these two sets, since they come from individual analyses. The true radial order (n) of the modes can only be determined from a stellar model, so we provide arbitrary reference values for convenience.

3. GROUND-BASED DATA

KIC 11026764 ($\alpha_{2000} = 19^{\text{h}}21^{\text{m}}24^{\text{s}}.65$, $\delta_{2000} = +48^{\circ}30'53''.2$) has a magnitude of $V = 9.55$. The atmospheric parameters given in the Kepler Input Catalog³⁶ (KIC; Latham et al. 2005) as derived from photometric observations acquired in the Sloan filters are $T_{\text{eff}} = 5502$ K, $\log g = 3.896$ dex, and $[\text{Fe}/\text{H}] = -0.255$ dex. The quoted uncertainties on these values are 200 K in T_{eff} and 0.5 dex in $\log g$ and $[\text{Fe}/\text{H}]$. Since this level of precision is minimally useful for asteroseismic modeling, we acquired a high-resolution spectrum of the star to derive more accurate values of its effective temperature, surface gravity, and metallicity.

3.1. Observations and Data Reduction

The spectrum was acquired with the Fibre-fed Echelle Spectrograph (FIES) at the 2.56-m Nordic Optical Telescope

³⁶ http://archive.stsci.edu/kepler/kepler_fov/search.php

(NOT) on 2009 November 9 (HJD 2455145.3428). The 1800 s exposure covers the wavelength range 3730–7360 Å at a resolution $R \sim 67000$ and signal-to-noise ratio $S/N = 80$ at 4400 Å. The Th-Ar reference spectrum was acquired immediately after the stellar spectrum. The reduction was performed with the FIESTOOL software, which was developed specifically for the FIES instrument and performs all of the conventional steps of echelle data reduction³⁷. This includes the subtraction of bias frames, modeling and subtraction of scattered light, flat-field correction, extraction of the orders, normalization of the spectra (including fringe correction), and wavelength calibration.

3.2. Atmospheric Parameters

We derived the atmospheric parameters of KIC 11026764 using several methods to provide an estimate of the external errors on T_{eff} , $\log g$, and $[\text{Fe}/\text{H}]$, which would be used in the asteroseismic modeling. The five independent reductions included: the VWA³⁸ software package (Bruntt et al. 2004, 2010a), the MOOG³⁹ code (Snedden 1973), the ARES⁴⁰ code (Sousa et al. 2007), the SYNPEC method (Hubeny 1988; Hubeny & Lanz 1995), and the ROTFIT code (Frasca et al. 2003, 2006). The principal characteristics of the methods employed by each of these codes are described below, and the individual results are listed in Table 2.

For the VWA method, the T_{eff} , $\log g$ and microturbulence of the adopted MARCS atmospheric models (Gustafsson et al. 2008) are adjusted to minimize the correlations of Fe I with line strength and excitation potential. The atmospheric parameters are then adjusted to ensure agreement between the mean abundances of Fe I and Fe II. Additional constraints on the surface gravity come from the two wide Ca lines at 6122 and 6162 Å, and from the Mg-1b lines (Bruntt et al. 2010b). The final value of $\log g$ is the weighted mean of the results obtained from these methods. The mean metallicity is calculated only from those elements (Si, Ti, Fe and Ni) exhibiting at least 10 lines in the observed spectrum. The uncertainties in the derived atmospheric parameters are determined by perturbing the computed models, as described in Bruntt et al. (2008). Having computed the mean atmospheric parameters for the star, VWA finally determines abundances for all of the elements contained in the spectrum (see Figure 2). No trace of Li I 6707.8 absorption is seen in the spectrum of KIC 11026764. We estimate an upper limit for the equivalent width $EW \leq 5 \text{ m}\text{\AA}$.

The 2002 version of the MOOG code determines the iron abundance under the assumption of local thermodynamic equilibrium (LTE), using a grid of 1D model atmospheres by Kurucz (1993). The LTE iron abundance was derived from the equivalent widths of 65 Fe I and 10 Fe II lines in the 4830–6810 Å range, measured with a Gaussian fitting procedure in the IRAF⁴¹ task *splot*. For the analysis, we followed the prescription of Randich et al. (2006), using the same list of lines as Biazzo et al. (2010). The effective temperature and microturbulent velocity were determined by requiring that the

³⁷ <http://www.not.iac.es/instruments/fies/fiestool/FIESTool.html>

³⁸ <http://www.hans.bruntt.dk/vwa/>

³⁹ <http://verdi.as.utexas.edu/>

⁴⁰ <http://www.astro.up.pt/~sousasag/ares/>

⁴¹ IRAF is distributed by the National Optical Astronomy Observatories, which are operated by the Association of Universities for Research in Astronomy, Inc., under cooperative agreement with the National Science Foundation.

Table 2
Atmospheric parameter estimates for KIC 11026764.

T_{eff}	$\log g$	$[\text{Fe}/\text{H}]$	Method
5640 ± 80	3.84 ± 0.10	$+0.02 \pm 0.06$	VWA
5750 ± 50	4.10 ± 0.10	$+0.11 \pm 0.06$	MOOG
5774 ± 39	4.01 ± 0.07	$+0.09 \pm 0.03$	ARES ^a
5793 ± 26	4.06 ± 0.04	$+0.10 \pm 0.02$	ARES ^b
5630 ± 70	3.79 ± 0.17	$+0.10 \pm 0.07$	SYNSPEC
5777 ± 77	4.19 ± 0.16	$+0.07 \pm 0.08$	ROTFIT

^a 40 Fe I and 12 Fe II lines from Sousa et al. (2006).

^b 247 Fe I and 34 Fe II lines from Sousa et al. (2008).

iron abundance be independent of the excitation potentials and the equivalent widths of Fe I lines. The surface gravity was determined by requiring ionization equilibrium between Fe I and Fe II. The initial values for the effective temperature, surface gravity, and microturbulence were chosen to be solar ($T_{\text{eff}} = 5770 \text{ K}$, $\log g = 4.44 \text{ dex}$, and $\xi = 1.1 \text{ km s}^{-1}$).

ARES provides an automated measurement of the equivalent widths of absorption lines in stellar spectra: the LTE abundance is determined differentially relative to the Sun with the help of MOOG and a grid of ATLAS-9 plane-parallel model atmospheres (Kurucz 1993). We used ARES with two different lists of iron lines: a ‘short’ one composed of isolated iron lines (Sousa et al. 2006), and a ‘long’ one composed of iron lines suitable for automatic measurements (Sousa et al. 2008). Our computations resulted in two consistent sets of atmospheric parameters for KIC 11026764.

SYNSPEC provides synthetic spectra based on model atmospheres, either calculated by TLUSTY or taken from the literature. We used the new grid of ATLAS-9 models (Kurucz 1993; Castelli & Kurucz 2003) to calculate synthetic spectra, which were then compared to the observed spectrum. Based on the list of iron lines from Sousa et al. (2008), we derived the stellar parameters in two ways to estimate the uncertainty due to the normalization of the observed spectrum. For the first approach we determined the minimum χ^2 of the deviation between the synthetic iron lines and the observed spectrum for a fixed set of stellar parameters. For the second approach, we determined the best fitting effective temperature and surface gravity for each iron line from the list, and adopted stellar parameters from the mean. The primary uncertainty in the final parameters arises from the correlation between the effective temperature and surface gravity: a reduction of the effective temperature can be compensated by a reduction of the gravity. While the χ^2 method results in lower values for both parameters ($T_{\text{eff}} = 5560 \text{ K}$, $\log g = 3.62 \text{ dex}$), the averaging approach yields higher values ($T_{\text{eff}} = 5701 \text{ K}$, $\log g = 3.95 \text{ dex}$). The differences between the two results exceed the formal errors of each method. We therefore adopt the mean, and assume half of the difference for the uncertainty. The metallicity is determined by minimizing the scatter in the parameters derived from individual lines.

ROTFIT performs a simultaneous and fast determination of T_{eff} , $\log g$, and $[\text{Fe}/\text{H}]$ for a star—as well as its projected rotational velocity $v \sin i$ —by comparing the observed spectrum with a library of spectra for reference stars (see Katz et al. 1998; Soubiran et al. 1998). The adopted estimates for the stellar parameters come from a weighted mean of the pa-

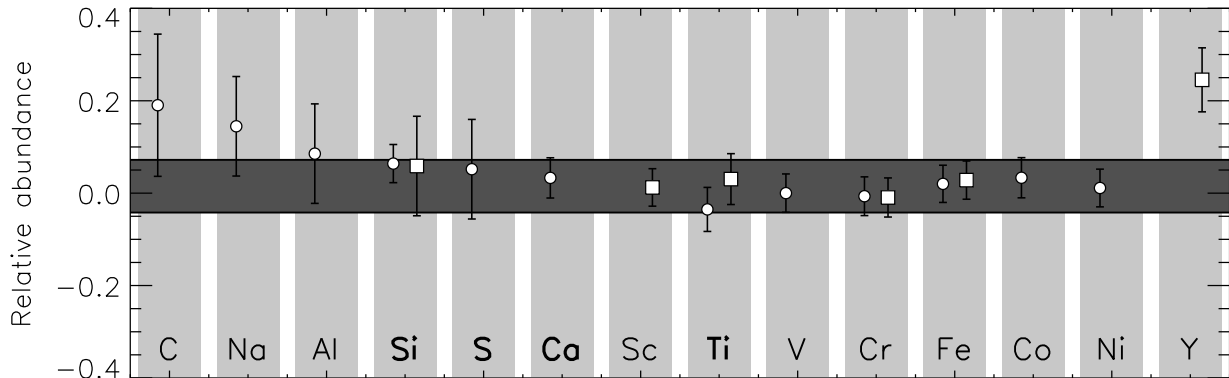


Figure 2. The mean abundances of the elements in the spectrum of KIC 11026764 as derived with the VWA software, including neutral lines (circles) and singly ionized lines (squares). The species labeled in bold are alpha elements. The horizontal bar indicates the mean metallicity of the star and the 1σ uncertainty range of the determination. The abundances are given relative to solar (Grevesse et al. 2007).

rameters for the 10 reference stars that most closely resemble the target spectrum, which is quantified by a χ^2 measure. We applied the ROTFIT code to all echelle orders between 21-69, which cover the range 4320-6770 Å in the observed spectrum. We also derived a projected rotational velocity for KIC 11026764 of 2.8 ± 1.6 km s⁻¹.

3.3. Adopted Spectroscopic Constraints

The effective temperature of KIC 11026764 derived from the five methods outlined above generally have overlapping 1σ errors. They all point to a star that is hotter than the KIC estimate by 100-300 K. We find reasonable agreement between the derived values for surface gravity and the KIC estimate. Most of the applied methods result in $\log g$ above 4.0 dex, again slightly higher than in the KIC. Only VWA and SYNPEC yield slightly lower values, which is not surprising considering the correlation between T_{eff} and $\log g$. Finally, all of the methods agree that the star is slightly metal-rich compared to the Sun, in contrast to the photometric estimate of $[\text{Fe}/\text{H}] = -0.255$ dex from the KIC. The initial set of spectroscopic constraints provided to the modeling teams (see §4) came from a mean of the preliminary results from the analyses discussed above, with uncertainties large enough to cover the full range for each parameter: $T_{\text{eff}} = 5635 \pm 185$ K, $\log g = 3.95 \pm 0.25$ dex, and $[\text{Fe}/\text{H}] = -0.06 \pm 0.25$ dex.

For the final estimate of the atmospheric parameters (see §5) we adopted the results from the VWA method, since it has been carefully tested against direct methods for 10 nearby solar-type stars. Specifically, Bruntt et al. (2010a) used VWA to determine T_{eff} from high-quality spectra and these values were compared to a direct method (nearly independent of model atmospheres) using the measured angular diameters from interferometry and bolometric flux measurements. A comparison of the direct (interferometric) and indirect (VWA) methods showed only a slight offset of -40 ± 20 K, and this offset has been removed for KIC 11026764. Similarly, Bruntt et al. (2010a) determined the spectroscopic $\log g$ parameter, which agrees very well for the three binary stars in their sample where the absolute masses and radii (and hence $\log g$) have been measured. Based on these comparisons of direct and indirect methods, Bruntt et al. (2010a) also discuss the issue of realistic uncertainties on spectroscopic parameters, and their estimates of the systematic uncertainties have been incorporated into the adopted values from VWA listed in Table 2.

4. STELLAR MODEL SEARCH

Starting with the minimal frequency set described in §2 and the initial set of spectroscopic constraints from §3, eleven teams of modelers performed a “meta-search” of the parameter space. Each modeler had complete freedom to decide on the input physics and fitting strategy to optimize the match to the observations. The results of the individual fits were evaluated in a uniform manner and ranked according to the total χ^2 between the observed and calculated values of the individual oscillation frequencies and the spectroscopic properties. These individual fits are listed in Table 3, and the details of the codes and fitting strategies employed by each team of modelers are described in the following subsections.

4.1. Model A

We employed the Aarhus stellar evolution code (ASTEC; Christensen-Dalsgaard 2008a) for stellar evolution computations, and the adiabatic pulsation package (ADIPLS; Christensen-Dalsgaard 2008b) for frequency calculations. The input physics for the evolution calculations included the OPAL 2005 equation of state (Rogers & Nayfonov 2002), OPAL opacity tables (Iglesias & Rogers 1996) with low-temperature opacities from Ferguson et al. (2005), and the NACRE nuclear reaction rates (Angulo et al. 1999). Convection was treated according to the mixing-length theory of Böhm-Vitense (1958). We did not include diffusion or convective overshoot in the models.

We computed several grids of evolutionary tracks spanning the parameter space around the values given by Chaplin et al. (2010). We primarily adjusted the stellar mass and metallicity in our grids, while fixing the mixing-length parameter α to 1.7. We scanned the parameter space in mass M from 1.00 to 1.35 M_{\odot} ; initial heavy-element mass fraction Z_i from 0.009 to 0.025; and initial hydrogen mass fraction X_i from 0.68 to 0.76. These values of Z_i and X_i cover a range of $(Z/X)_i = 0.012$ -0.037, or $[\text{Fe}/\text{H}] = -0.317$ to $+0.177$ dex using $[\text{Fe}/\text{H}] = \log(Z/X) - \log(Z/X)_{\odot}$, where (Z/X) is the ratio at the stellar surface and $(Z/X)_{\odot} = 0.0245$ (Grevesse & Noels 1993). This range of $[\text{Fe}/\text{H}]$ is compatible with the initial spectroscopic constraints. However, we later extended our grids to determine whether there was a better model with lower or higher metallicity. For all of the models on our tracks, we calculated the oscillation frequencies when the values of T_{eff} and $\log g$ were within 2σ of the derived values (see

Table 3
Initial model-fitting search for KIC 11026764.

Model	M/M_{\odot}	Z_s	Y_s	α	t (Gyr)	L/L_{\odot}	R/R_{\odot}	T_{eff} (K)	$\log g$	[Fe/H]	χ^2
A	1.13	0.019	0.291	1.70	5.967	3.523	2.026	5562	3.878	+0.051	9.8
B	1.23	0.015	0.250	1.80	4.861	4.730	2.097	5885	3.885	-0.068	12.4
C	1.24	0.021	0.275	1.79	5.231	4.293	2.093	5750	3.890	+0.120	22.5
D	1.31	0.044	0.241	1.42	7.775	2.598	2.139	5016	3.895	+0.400	49.7
E	1.22	0.013	0.233	1.83	4.745	4.710	2.080	5899	3.888	-0.100	55.8
F	1.10	0.014	0.269	1.85	5.839	3.850	2.015	5706	3.870	-0.102	60.6
G	1.20	0.022	0.291	1.88	5.100	3.960	2.160	5663	3.880	+0.116	66.8
H	1.10	0.010	0.250	1.75	6.752	3.776	2.012	5677	3.872	-0.250	284.3
I	1.27	0.021	0.280	0.50	3.206	3.202	1.792	4854	4.034	+0.080	637.3
J	1.12	0.016	0.276	1.90	6.505	3.644	2.026	5593	3.870	-0.139	...
\pm error	0.14	0.007	0.030	0.78	1.961	0.678	0.091	188	0.023	± 0.166	...
K	1.13	0.017	0.283	1.80	6.450	3.610	1.988	5634	3.890	-0.044	...
\pm error	0.13	0.009	0.009	...	1.930	0.770	0.080	161	0.018	± 0.250	...

§3.3). We then assigned a goodness of fit to the frequency set of each model by calculating χ^2 :

$$\chi^2 = \frac{1}{N} \sum_{n,l} \left(\frac{\nu_l^{\text{obs}}(n) - \nu_l^{\text{model}}(n)}{\sigma(\nu_l^{\text{obs}}(n))} \right)^2, \quad (2)$$

where N is the total number of modes included, $\nu_l^{\text{obs}}(n)$ and $\nu_l^{\text{model}}(n)$ are the observed and model frequencies for a given spherical degree l and radial order n , while $\sigma(\nu_l^{\text{obs}}(n))$ represents the uncertainties on the observed frequencies. We calculated χ^2 after correcting the frequencies for surface effects, following Kjeldsen et al. (2008):

$$\nu_{\text{obs}}(n) - \nu_{\text{best}}(n) = a \left[\frac{\nu_{\text{obs}}(n)}{\nu_0} \right]^b, \quad (3)$$

where $\nu_{\text{obs}}(n)$ and $\nu_{\text{best}}(n)$ are the observed and best model frequencies with spherical degree $l = 0$ and radial order n , and ν_0 is the frequency of maximum power in the oscillation spectrum, which is $857 \mu\text{Hz}$ for KIC 11026764. We fixed the exponent b to the value derived for the Sun ($b = 4.90$) by Kjeldsen et al. (2008), and a was calculated for each model. We computed smaller and more finely sampled grids around the models with the lowest χ^2 to refine the fit. The properties of the best model are listed in Table 3. Although we found models with higher or lower $\log g$ that had large separations quite close to the observed value, the individual frequencies were not close to the observations, and the larger range of metallicity did not yield improved results. We also found more massive models (around $1.3 M_{\odot}$) with a total χ^2 value comparable to our best fit, but they did not include the mixed modes. Model A is the best match from the family of solutions (also including Models F, H, J and K) with masses near $1.1 M_{\odot}$.

4.2. Model B

We used the Geneva stellar evolution code including rotation (Eggenberger et al. 2008) for all computations. This code includes the OPAL equation of state (Rogers & Nayfonov 2002), the OPAL opacities (Iglesias & Rogers 1996) complemented at low temperatures with the molecular opacities of Alexander & Ferguson (1994), the NACRE nuclear

reaction rates (Angulo et al. 1999) and the standard mixing-length formalism for convection (Böhm-Vitense 1958). Overshooting from the convective core into the surrounding radiatively stable layers by a distance $d_{\text{ov}} \equiv \alpha_{\text{ov}} \min[H_p, r_{\text{core}}]$ (Maeder & Meynet 1989) is included with an overshoot parameter $\alpha_{\text{ov}} = 0.1$.

In the Geneva code, rotational effects are computed in the framework of shellular rotation. The transport of angular momentum then obeys an advection-diffusion equation (Zahn 1992; Maeder & Zahn 1998), while the vertical transport of chemicals through the combined action of vertical advection and strong horizontal diffusion can be described as a purely diffusive process (Chaboyer & Zahn 1992). Since the modeling of these rotational effects has been described in previous papers (e.g. Eggenberger et al. 2010), we simply note that the Geneva code includes a comprehensive treatment of shellular rotation and that meridional circulation is treated as a truly advective process. For a detailed analysis of the effect of centrifugal force on the oscillation frequencies, see Appendix A. In addition to rotation, atomic diffusion of helium and heavy elements is included with diffusion coefficients calculated according to the prescription of Paquette et al. (1986).

The properties of a stellar model including rotation depend on six parameters: the mass M , the age t , the mixing-length parameter $\alpha \equiv l/H_p$ for convection, the initial rotation velocity on the ZAMS and two parameters describing the initial chemical composition of the star. For these two parameters, we chose the initial helium abundance Y_i and the initial ratio between the mass fraction of heavy elements and hydrogen $(Z/X)_i$. This ratio can be related to the metallicity $[\text{Fe}/\text{H}]$ assuming that $\log(Z/X) \cong [\text{Fe}/\text{H}] + \log(Z/X)_{\odot}$; we adopt the solar value $(Z/X)_{\odot} = 0.0245$ given by Grevesse & Noels (1993). For these computations, the mixing-length parameter was fixed to a solar calibrated value ($\alpha_{\odot} = 1.7998$) and the initial rotation velocity on the ZAMS was 50 km s^{-1} . The braking law of Kawaler (1988) was used to reproduce the magnetic braking experienced by low-mass stars during main-sequence evolution.

With the above assumptions, the characteristics of a stellar model depend on only four parameters: M , t , Y_i and $(Z/X)_i$. The determination of the parameters that best reproduce the observational constraints was then performed in two

steps as described in Eggenberger & Carrier (2006). First, a grid of models with global properties in reasonable agreement (within 2σ) with the adopted spectroscopic constraints was constructed. Theoretical frequencies of $l \leq 2$ modes in the observed range of 590-1100 μHz were computed using the adiabatic pulsation code (Christensen-Dalsgaard 2008b) along with the characteristic frequency separations. The mean large separation was determined by considering only radial modes. The effects of incomplete modeling of the external layers on computed frequencies were taken into account using the empirical power law given by Kjeldsen et al. (2008). This correction was applied to theoretical frequencies using the solar calibrated value of the exponent ($b = 4.90$) and calculating the coefficient a for each stellar model.

Using spectroscopic measurements of $[\text{Fe}/\text{H}]$, T_{eff} and $\log g$ together with the observed frequencies, a χ^2 minimization was performed to determine the set of model parameters that resulted in the best agreement with all observational constraints. The properties of the best model are listed in Table 3. This model correctly reproduces the spectroscopic measurements of the surface metallicity and $\log g$, but exhibits a slightly higher effective temperature. It is in good agreement with the asteroseismic data and in particular with the observed deviation of the $l = 1$ modes from asymptotic behavior. Model B is the best match from the family of solutions (also including Models C, E and G) with masses near $1.2 M_{\odot}$.

4.3. Model C

The Garching Stellar Evolution Code (GARSTEC; Weiss & Schlattl 2008) is a one-dimensional hydrostatic code which does not include the effects of rotation. For the model calculations we used the OPAL equation of state (Rogers et al. 1996) complemented with the MHD equation of state at low temperatures (Hummer & Mihalas 1988), OPAL opacities for high temperatures (Iglesias & Rogers 1996) and Ferguson’s opacities for low temperatures (Ferguson et al. 2005), the Grevesse & Sauval (1998) solar mixture, and the NACRE compilation of thermonuclear reaction rates (Angulo et al. 1999). Mixing is performed diffusively in convective regions using the mixing-length theory for convection in the formulation from Kippenhahn & Weigert (1990), and convective overshooting can optionally be implemented as a diffusive process with an exponential decay of the convective velocities in the radiative zone. The amount of mixing for overshooting depends on an efficiency parameter A calibrated with open clusters (typically $A = 0.016$). Atomic diffusion can be applied following the prescription of Thoul et al. (1994), and we use a plane-parallel Eddington grey atmosphere.

We started all of our calculations from the pre-main sequence phase. The value of the mixing-length parameter for convection was fixed ($\alpha = 1.791$ from our solar calibration), the Schwarzschild criterion for definition of convective boundaries was used, and we did not consider convective overshooting or atomic diffusion. We constructed a grid of models in the mass range between $1.0 M_{\odot}$ and $1.3 M_{\odot}$ (in steps of 0.01) for several $[\text{Fe}/\text{H}]$ values from the spectroscopic analysis: 0.06, 0.09, 0.12, and 0.15. To convert the observed values into total metallicity, we applied a chemical enrichment law of $\Delta Y/\Delta Z = 2$ and used the primordial abundances from our solar calibration. We did not explore variations in either the hydrogen or helium abundances.

Once all of the tracks were computed, we restricted our analysis to those models contained within the spectroscopic uncertainties. For these cases, we calculated the oscillation

frequencies using the adiabatic pulsation package (ADIPLS; Christensen-Dalsgaard 2008b) and looked for the model which best reproduced the large frequency separation (no surface correction was applied to the calculated frequencies). Several models were found to fulfill these requirements for each metallicity grid, and among those best fit models to the large frequency separation we then performed a χ^2 test to obtain the global best fit to the individual frequencies and the spectroscopic constraints. Our global best fit model came from the grid with $[\text{Fe}/\text{H}] = 0.12$, and the properties are listed in Table 3. This model reproduces well the observed mixed modes.

4.4. Model D

The Asteroseismic Modeling Portal (AMP) is a web-based tool tied to TeraGrid computing resources that uses the Aarhus stellar evolution code (ASTECS; Christensen-Dalsgaard 2008a) and adiabatic pulsation code (ADIPLS; Christensen-Dalsgaard 2008b) in conjunction with a parallel genetic algorithm (Metcalf & Charbonneau 2003) to optimize the match to observational data (see Metcalfe et al. 2009). The models use the OPAL 2005 equation of state (see Rogers & Nayfonov 2002) and the most recent OPAL opacities (see Iglesias & Rogers 1996), supplemented by Kurucz opacities at low temperatures. The nuclear reaction rates come from Bahcall & Pinsonneault (1995), convection is described by the mixing-length theory of Böhm-Vitense (1958), and we can optionally include the effects of helium settling as described by Michaud & Proffitt (1993).

Each model evaluation involves the computation of a stellar evolution track from the zero-age main sequence (ZAMS) through a mass-dependent number of internal time steps, terminating prior to the beginning of the red giant stage. Rather than calculate the pulsation frequencies for each of the 200-300 models along the track, we exploit the fact that the average frequency separation of consecutive radial orders $\langle \Delta \nu_0 \rangle$ in most cases is a monotonically decreasing function of age (Christensen-Dalsgaard 1993). Once the evolution track is complete, we start with a pulsation analysis of the model at the middle time step and then use a binary decision tree—comparing the observed and calculated values of $\langle \Delta \nu_0 \rangle$ —to select older or younger models along the track. This allows us to interpolate the age between the two nearest time steps by running the pulsation code on just 8 models from each stellar evolution track. The frequencies of each model are then corrected for surface effects following the prescription of Kjeldsen et al. (2008).

The genetic algorithm (GA) optimizes four adjustable model parameters, including the stellar mass (M) from 0.75 to $1.75 M_{\odot}$, the metallicity (Z) from 0.002 to 0.05 (equally spaced in $\log Z$), the initial helium mass fraction (Y_i) from 0.22 to 0.32, and the mixing-length parameter (α) from 1 to 3. The stellar age (t) is optimized internally during each model evaluation by matching the observed value of $\langle \Delta \nu_0 \rangle$ (see above). The GA uses two-digit decimal encoding, such that there are 100 possible values for each parameter within the specified ranges. Each run of the GA evolves a population of 128 models through 200 generations to find the optimal set of parameters, and we execute 4 independent runs with different random initialization to ensure that the best model identified is truly the global solution. The resulting properties of the optimal model are listed in Table 3.

The extreme values in this global fit arose from treating each spectroscopic constraint as equivalent to a single fre-

quency. Since the adopted spectroscopic errors are large, they provide much more flexibility for the models compared to the individual frequencies with relatively small errors. Consequently, the fitting algorithm found it advantageous to shift the effective temperature and metallicity by several σ from their target values to achieve significantly better agreement with the 22 oscillation frequencies. The improvement in the frequency match outweighed the degradation in the spectroscopic fit for the calculation of χ^2 . The solution to this problem may be to calculate a separate value of χ^2 for the asteroseismic and spectroscopic constraints, and then average them to provide more equal weight to the two types of constraints. This is an important lesson for future automated searches, and explains why Model D does not align with either of the two major families of solutions.

4.5. Model E

We used the Yale Stellar Evolution Code (YREC; Demarque et al. 2008) in its non-rotating configuration to model KIC 11026764. All models were constructed with the OPAL equation of state (Rogers & Nayfonov 2002). We used OPAL high temperature opacities (Iglesias & Rogers 1996) supplemented with low temperature opacities from Ferguson et al. (2005). The NACRE nuclear reaction rates (Angulo et al. 1999) were used. We assumed that the current solar metallicity is that given by Grevesse & Sauval (1998). We have not explored the consequences of using the lower metallicity measurements of Asplund et al. (2005) or the intermediate metallicity measurements of Ludwig et al. (2009). We searched for the best fit within a fixed grid of models. There were eight separate grids defined by different combinations of the mixing-length parameter ($\alpha = 1.83$ or $\alpha = 2.14$), the initial helium abundance (either $Y_i = 0.27$ or Y_i calculated assuming a $\Delta Y/\Delta Z = 2$, with Y_i for $[\text{Fe}/\text{H}] = 0$ being the current solar CZ helium abundance), and the amount of overshoot ($0H_p$ or $0.2H_p$). All models included gravitational settling of helium and heavy elements using the formulation of Thoul et al. (1994).

Our fitting method included two steps. In the first step, we calculated the average large frequency separation for the models and selected all of those that fit the observed separation within 3σ errors. We adopted the observed value of $\Delta\nu = 50.8 \pm 0.3 \mu\text{Hz}$ from Chaplin et al. (2010). A second cut was made using the effective temperature: all models within $\pm 2\sigma$ of the observed value were chosen. A third cut was made using the frequencies of the three lowest-frequency $l = 0$ modes. Given the small variation in mass, this process was effectively a radius cut. The selected models had radii around $2R_\odot$. Note that the Yale-Birmingham radius pipeline (Basu et al. 2010) finds a radius of $2.18^{+0.04}_{-0.05} R_\odot$ for this star using the adopted values of $\Delta\nu$, T_{eff} , $\log g$ and $[\text{Fe}/\text{H}]$. In the second step of the process, we made a finer grid in mass and age around the selected values and then compared the models with the observed set of frequencies. The properties of our best fit model are listed in Table 3. This model was constructed with $Y_i = 0.27$, $Z_i = 0.0147$ and core overshoot of $0.2H_p$. We were unable to find a good model without core overshoot.

4.6. Model F

We modeled KIC 11026764 with the Catania Astrophysical Observatory version of the GARSTEC code (Bonanno et al. 2002) using a grid-based approach. The input physics of this stellar evolution code included the OPAL 2005 equation

of state (Rogers & Nayfonov 2002) and the OPAL opacities (Iglesias & Rogers 1996) complemented in the low temperature regime with the tables of Alexander & Ferguson (1994). The nuclear reaction rates were taken from the NACRE collaboration (Angulo et al. 1999) and the standard mixing-length formalism for convection was used (Kippenhahn & Weigert 1990). Microscopic diffusion of hydrogen, helium and all of the major metals can optionally be taken into account. The outer boundary conditions were determined by assuming an Eddington grey atmosphere.

A grid of evolutionary models was computed to span the 1σ uncertainties in the spectroscopic constraints obtained from ground based observations. When a given evolutionary track was in the error box, a maximum time step of 20 Myr was chosen and the frequencies were computed with the ADIPLS code. A non-uniform grid of mass in the range 1.0 - $1.24 M_\odot$, helium abundance in the range $Y_i = 0.26$ - 0.31 , mixing-length parameter $\alpha = 1.6$ - 1.9 and initial surface heavy-element abundances $(Z/X)_i = 0.022$ - 0.029 was scanned. A global optimization strategy was implemented by minimizing the χ^2 for all of the $l = 0$, $l = 1$ and $l = 2$ modes. The empirical surface effect, as discussed by Kjeldsen et al. (2008), was used to correct all theoretical frequencies. The properties of the best model with heavy-element diffusion and surface corrected frequencies are listed in Table 3.

4.7. Model G

We used a version of the Aarhus stellar evolution code (ASTEC; Christensen-Dalsgaard 2008a) which includes the OPAL 2001 equation of state (Rogers et al. 1996), OPAL opacities (Iglesias & Rogers 1996), Bahcall & Pinsonneault (1995) nuclear cross sections and the mixing-length formalism (Böhmer-Vitense 1958) for convection. We computed several grids of models by varying all of the input parameters within the range of the observed errors (Chaplin et al. 2010). In particular we calculated evolutionary tracks by varying the input mass in the range $M = 0.9$ - $1.2 M_\odot$, the metallicity in the range $Z = 0.009$ - 0.03 , and the hydrogen abundance in the range $X = 0.67$ - 0.7 . We also adopted different values of the mixing-length parameter in the range $\alpha = 1.67$ - 1.88 . We calculated additional evolutionary models using the Canuto & Mazzitelli (1992) convection formulation. The mixing-length parameter α of the CM formulation was chosen in the range $\alpha = \alpha_{\text{CM}} = 0.9$ - 1.0 . To obtain the deviation from asymptotic behavior observed in the $l = 1$ modes (the mixed modes) we did not include overshooting in the calculation, following the conclusion of Di Mauro et al. (2003). These models are distinct from the grid used to produce Model A, not only because they employ a slightly older EOS and nuclear reaction rates, but also because the grid search included α and calculated fewer models within the specified range of parameter values. We used the adiabatic oscillation code (ADIPLS; Christensen-Dalsgaard 2008b) to calculate the p-mode eigenfrequencies with harmonic degree $l = 0$ - 2 . The characteristics of the model which best fits the observations are listed in Table 3.

4.8. Model H

For the evolution calculations we used the publicly available Dartmouth stellar evolution code (DSEP; Chaboyer et al. 2001; Guenther et al. 1992; Dotter et al. 2007), which is based on the code developed by Pierre Demarque and his students (Larson & Demarque 1964; Demarque & Mengel 1971). The

input physics includes high temperature opacities from OPAL (Iglesias & Rogers 1996), low temperature opacities from Ferguson et al. (2005), the nuclear reaction rates of Bahcall & Pinsonneault (1992), helium and heavy-element settling and diffusion (Michaud & Proffitt 1993), and Debye-Hückel corrections to the equation of state (Guenther et al. 1992). The models employ the standard mixing-length theory. Convective core overshoot is calculated assuming that the extent is proportional to the pressure scale height at the boundary (Demarque et al. 2004). The models used the standard conversion from $[\text{Fe}/\text{H}]$ and $\Delta Y/\Delta Z$ to Z and Y (Chaboyer et al. 1999). The oscillation frequencies were computed using the adiabatic oscillation codes of Kosovichev (1999) and Christensen-Dalsgaard (2008b). No surface corrections were applied.

The strategy to find a model matching the observed spectroscopic constraints involved calculating a series of evolutionary tracks in the $\log g$ - T_{eff} plane for a mass range of 1.0-1.3 M_{\odot} , heavy-element abundance $Z = 0.01$ -0.03, initial helium abundance $Y_i = 0.25$ -0.30, and mixing-length parameter $\alpha = 1.70$ -1.75. We then selected the models closest to the target values within half of the specified uncertainties. All models for the search were calculated assuming an overshoot parameter $\alpha_{\text{ov}} = 0.2$, and included element diffusion. For comparison, the corresponding models without diffusion and convective overshoot were also calculated. The oscillation spectra were matched to the observed frequencies, first by comparing the frequencies of radial ($l = 0$) modes with the corresponding observed frequencies, and then selecting a model with the closest frequency values for the $l = 1$ and $l = 2$ modes. The properties of the final model are listed in Table 3. This model matches the observed frequencies quite well except for the first two $l = 1$ modes, which deviate by about 12-13 μHz . Our search demonstrated that the behavior of the mixed mode frequencies is sensitive to element diffusion and convective overshoot. This requires further investigation.

4.9. Model I

To characterize KIC 11026764 we constructed a grid of stellar models with the CESAM code (Morel 1997), and computed their oscillation frequencies with the adiabatic oscillation code FILOU (Suárez 2002; Suárez & Goupil 2008). Opacity tables were taken from the OPAL package (Iglesias & Rogers 1996), complemented at low temperatures ($T \leq 10^4 \text{ K}$) with the tables provided by Alexander & Ferguson (1994). The atmosphere was constructed from a Eddington T - τ relation and was assumed to be grey. The stellar metallicity (Z/X) was derived from the $[\text{Fe}/\text{H}]$ value assuming $(Z/X)_{\odot} = 0.0245$ (Grevesse & Noels 1993), $Y_{\text{pr}} = 0.235$ and $Z_{\text{pr}} = 0$ for the primordial helium and heavy-element abundances, and a value $\Delta Y/\Delta Z = 2$ for the enrichment ratio. No microscopic diffusion of elements was considered.

The main strategy was to search for representative equilibrium models of the star in a database of 5×10^5 equilibrium models, querying for those matching the global properties of the star, including the effective temperature, gravity and metallicity. Using this set of models, we then applied the asteroseismic constraints, including the individual frequencies and large separations. The global fitting method involved a χ^2 minimization, taking into account all of the observational constraints simultaneously. No correction for surface effects was applied, and no *a priori* information on mode identification was assumed when fitting the individual frequencies. The properties of the best model we found is listed in Table 3, and

includes overshooting with $\alpha_{\text{ov}} = 0.3$. Note that the analysis did not adopt the identifications of spherical degree (l) from §2, and it included $l = 3$ modes to perform the match. As a consequence, the final result is much different than any of the others and it does not fall into either of the two major families of solutions.

4.10. Model J

The SEEK procedure makes use of a large grid of stellar models computed with the Aarhus stellar evolution code (ASTEC; Christensen-Dalsgaard 2008a). It compares the observations with every model in the grid and makes a probabilistic assessment, with the help of Bayesian statistics, about the global properties of the star. The model grid includes 7,300 evolution tracks containing 5,842,619 individual models. Each track begins at the ZAMS and continues to the red giant branch or a maximum age of $t = 15$ Gyr. The tracks are separated into 100 subsets with different combinations of metallicity Z , initial hydrogen content X_i and mixing-length parameter α . These combinations are separated into two regularly spaced and interlaced subgrids. The first subgrid comprises tracks with $Z = [0.005, 0.01, 0.015, 0.02, 0.025, 0.03]$, $X_i = [0.68, 0.70, 0.72, 0.74]$, and $\alpha = [0.8, 1.8, 2.8]$ while the second subset has $Z = [0.0075, 0.0125, 0.0175, 0.0225, 0.0275]$, $X_i = [0.69, 0.71, 0.73]$, $\alpha = [1.3, 2.3]$. Every subset is composed of 73 tracks with masses between 0.6 and 3.0 M_{\odot} . The spacing in mass between the tracks is 0.02 M_{\odot} from 0.6 to 1.8 M_{\odot} and 0.1 from 1.8 to 3.0 M_{\odot} . A relatively high value of $Y_{\odot} = 0.2713$ and $Z_{\odot} = 0.0196$ for the Sun has been used for the standard definition of $[\text{Fe}/\text{H}]$ in SEEK. This value is used to calibrate solar models from ASTEC to the correct luminosity (Christensen-Dalsgaard 1998). The input physics include the OPAL equation of state, opacity tables from OPAL (Iglesias & Rogers 1996) and Alexander & Ferguson (1994), and the metallic mixture of Grevesse & Sauval (1998). Convection is treated according to the mixing-length theory of Böhm-Vitense (1958) with the convective efficiency characterized by the mixing-length to pressure height scale ratio α , which varies across the grid of models. Diffusion and overshooting were not included.

The grid allows us to map the physical input parameters of the model $\mathbf{p} \equiv \{M, t, Z, X_i, \alpha\}$ into the grid of observable quantities $\mathbf{q}^{\text{g}} \equiv \{\Delta\nu, \delta\nu, T_{\text{eff}}, \log g, [\text{Fe}/\text{H}], \dots\}$, defining the transformation

$$\mathbf{q}^{\text{g}} = \mathcal{K}(\mathbf{p}). \quad (4)$$

We compare these quantities to the observed values \mathbf{q}^{obs} with the help of a likelihood function \mathcal{L} ,

$$\mathcal{L} = \left(\prod_{i=0}^n \frac{1}{\sqrt{2\pi}\sigma_i} \right) \exp(-\chi^2/2), \quad (5)$$

and the usual χ^2 definition

$$\chi^2 = \frac{1}{N} \sum_{i=0}^N \left(\frac{q_i^{\text{obs}} - q_i^{\text{g}}}{\sigma_i} \right)^2 \quad (6)$$

where σ_i is the estimated error for each observation q_i^{obs} , and N is the number of observables. The maximum likelihood is then combined with the prior probability of the grid f_0 to yield the posterior, or the resulting probability density

$$f(\mathbf{p}) \propto f_0(\mathbf{p})\mathcal{L}(\mathcal{K}(\mathbf{p})). \quad (7)$$

Table 4
Final model-fitting results for KIC 11026764.

Model	M/M_{\odot}	Z_{s}	Y_{s}	α	t (Gyr)	L/L_{\odot}	R/R_{\odot}	T_{eff} (K)	$\log g$	[Fe/H]	χ^2
FA...	1.13	0.017	0.305	1.64	5.268	4.141	2.036	5778	3.872	+0.009	3.69
AA..	1.13	0.019	0.291	1.70	5.977	3.520	2.029	5556	3.877	+0.051	6.11
AA'..	1.13	0.019	0.291	1.70	5.935	3.454	2.026	5534	3.877	+0.031	7.40
GA..	1.10	0.017	0.296	1.88	6.100	3.420	2.010	5539	3.870	+0.004	78.05
CA...	1.13	0.019	0.291	1.70	6.204	3.493	2.030	5546	3.876	+0.050	152.91
EA...	1.12	0.019	0.291	1.70	6.683	3.202	2.029	5424	3.870	+0.050	230.58
AB...	1.23	0.018	0.242	1.80	5.869	3.804	2.083	5591	3.890	-0.010	6.97
AB'..	1.20	0.024	0.276	1.80	5.994	3.460	2.072	5475	3.884	+0.146	7.26
BB...	1.22	0.021	0.270	1.80	5.153	4.190	2.061	5758	3.896	+0.072	7.57
FB...	1.24	0.021	0.280	1.79	4.993	4.438	2.092	5800	3.890	+0.091	8.52
EB...	1.22	0.013	0.232	1.80	4.785	4.651	2.079	5882	3.890	-0.130	18.54
CB...	1.24	0.015	0.250	1.80	5.064	4.696	2.089	5887	3.892	-0.080	45.84
J'...	1.27	0.021	0.270	1.52	4.260	4.011	2.105	5634	3.892	+0.080	...
\pm error	0.09	0.003	0.024	0.74	1.220	0.371	0.064	81	0.020	± 0.060	...
K'...	1.20	0.022	0.278	1.80	5.980	3.700	2.026	5619	3.900	+0.070	...
\pm error	0.04	0.003	0.003	...	0.610	0.300	0.027	79	0.006	± 0.060	...

This probability density can be integrated to obtain the value and uncertainty for each of the parameters, as listed in Tables 3 and 4. It can also be projected onto any plane to get the correlation between two parameters, as shown in Appendix B. The details of the SEEK procedure, including the choice of priors, and an introduction to Bayesian statistics can be found in Quirion, Christensen-Dalsgaard & Arentoft (2010).

SEEK uses the large and small separations and the median frequency of the observed modes as asteroseismic inputs. Values of $\Delta\nu_0 = 50.68 \pm 1.30$ (computed with $l = 0$ modes only) and $\delta\nu_{0,2} = 4.28 \pm 0.73$ (computed from $l = 0, 2$ modes) were derived from *Kepler* data around a central value $900 \mu\text{Hz}$. Each separation is the mean of the individual observed separations, while the error is the standard deviation of the individual values from the mean. These values differ slightly from those given in Chaplin et al. (2010) because they are calculated from the individual frequencies rather than derived from the power spectrum. Using these asteroseismic inputs along with the initial spectroscopic constraints, we obtained the parameters listed in Table 3. For a SEEK analysis of the importance of the asteroseismic constraints, see Appendix B.

4.11. Model K

To investigate how well we can find an appropriate model without comparing individual oscillation frequencies, we used the RADIUS pipeline (Stello et al. 2009a), which takes T_{eff} , $\log g$, [Fe/H], and $\Delta\nu$ as the only inputs to find the best fitting model. The value of $\Delta\nu = 50.8 \pm 0.3 \mu\text{Hz}$ from Chaplin et al. (2010) was adopted. The pipeline is based on a large grid of ASTEC models (Christensen-Dalsgaard 2008a) using the EFF equation of state (Eggleton et al. 1973). We use the opacity tables of Rogers & Iglesias (1995) and Kurucz (1991) for $T < 10^4$ K with the solar mixture of Grevesse & Noels (1993). Rotation, overshooting and diffusion were not included. The grid was created with fixed values of the mixing-length parameter ($\alpha = 1.8$) and the initial hydrogen abundance ($X_{\text{H}} = 0.7$). The resolution in $\log Z$ was 0.1 dex between $0.001 < Z < 0.055$, and the resolution in mass was $0.01 M_{\odot}$ from 0.5 to $4.0 M_{\odot}$. The evolution begins at the ZAMS

and continues to the tip of the red giant branch. To convert between the model values of Z and the observed [Fe/H], we used $Z_{\odot} = 0.0188$ (Cox 2000).

We made slight modifications to the RADIUS approach described by Stello et al. (2009a). First, the large frequency separation was derived by scaling the solar value (Kjeldsen & Bedding 1995) instead of calculating it directly from the model frequencies. Although there is a known systematic difference between these two ways of deriving $\Delta\nu$, the effect is probably below the 1% level (Stello et al. 2009b; Basu et al. 2010). Second, we pinpointed a single best-fitting model based on a χ^2 formalism that was applied to all models within $\pm 3\sigma$ of the observed properties. The properties of the best fitting model are listed in Table 3. This model shows a frequency pattern in the échelle diagram that looks very similar to the observations if we allow a small tweaking of the adopted frequency separation ($52.1 \mu\text{Hz}$) used to generate the échelle. This basically means that we found a model that homologously represents the observations quite well. In particular, we see relative positions of the $l = 1$ mode frequencies that are very similar to those observed.

5. MODEL-FITTING RESULTS

Based on the value of χ^2 from the initial search in §4, we adopted two reference models (Models A and B in Table 3) each constructed with a very different set of input physics, but almost equally capable of providing a good match to the observations. Note that Model A does not include overshoot or diffusion, while Model B includes overshoot, diffusion and a full treatment of rotation. These two models differ significantly in the optimal values of the mass, effective temperature, metallicity and luminosity, but they both agree with the observational constraints at approximately the same level ($\chi^2 \sim 10$). With the exceptions of Models D and I (see subsections above), the other independent analyses generally fall into the two broad families of solutions defined by Models A and B. The lower mass family includes Models A, F, H, J and K, while the higher mass family includes Models B, C, E and

G. We identified several additional asteroseismic constraints from the maximal frequency set (see §2) and we adopted revised spectroscopic constraints from VWA (see §3) to refine our analysis of Models A and B using several different codes.

5.1. Refining the Best Models

Comparing the theoretical frequencies of Models A and B with the maximal frequency set from §2, we identified four of the seven additional oscillation modes that could be used for refined model-fitting (see Table 1). Recall that the maximal frequency set comes from the *individual analysis* with the smallest *rms* deviation with respect to the maximal list, so the frequencies of the modes from the minimal set are slightly different in the maximal set. Without any additional fitting, these subtle frequency differences improve the χ^2 of Models A and B when comparing them to those modes from the maximal set that are also present in the minimal set. There is one additional $l = 0$ mode ($n = 12$) and three additional $l = 2$ modes ($n = 11, 16, 19$) in the maximal set that are within 3σ of frequencies in both Models A and B. Considering the very different input physics of these two models, we took this agreement as evidence of the reliability of these four additional frequencies and we incorporated them as constraints for our refined model-fitting. Two of the remaining frequencies in the maximal set ($n = 12, l = 1$ and 2) were not present in either Models A or B, while one ($n = 10, l = 2$) had a close match in Model B but not in Model A. We excluded these three modes from the refined model-fitting. Given that the $l = 1$ modes provide the strongest constraints on the models (see §5.2), the additional $l = 0$ and $l = 2$ modes are expected to perturb the final fit only slightly.

In addition to the 26 oscillation frequencies from the maximal set, we also included stronger spectroscopic constraints in the refined model-fitting by adopting the results of the VWA analysis instead of using the mean atmospheric parameters from the preliminary analyses (see §3.3). Although the uncertainties on all three parameters are considerably smaller from the VWA analysis, the actual values only differ slightly from the initial spectroscopic constraints. These were just three of the 25 constraints used to calculate the χ^2 and rank the initial search results in Table 3. Since the 22 frequencies from the minimal set were orders of magnitude more precise, they dominated the χ^2 determination. Although the spectroscopic constraints from VWA are more precise than the initial atmospheric parameters, they are still much less precise than the frequencies and should only perturb the χ^2 ranking slightly. Consequently, we do not need to perform a new global search after adopting the additional and updated observational constraints.

Several modeling teams used the updated asteroseismic and spectroscopic constraints for refined model-fitting with a variety of codes. Each team started with the parameters of Models A and B from Table 3, and then performed a local optimization to produce the best match to the observations within each family of solutions. The results of this analysis are shown in Table 4, where the refined Models A and B are ranked separately by their final χ^2 value. Each model is labeled with a letter from Table 3 to identify the modeling team, followed by either A or B to identify the family of solutions. The two pipeline approaches labeled J' and K' simply adopted the revised constraints to evaluate any shift in the optimal parameter estimates and errors. Note that both the SEEK and RADIUS pipelines identified parameters in the high-mass family

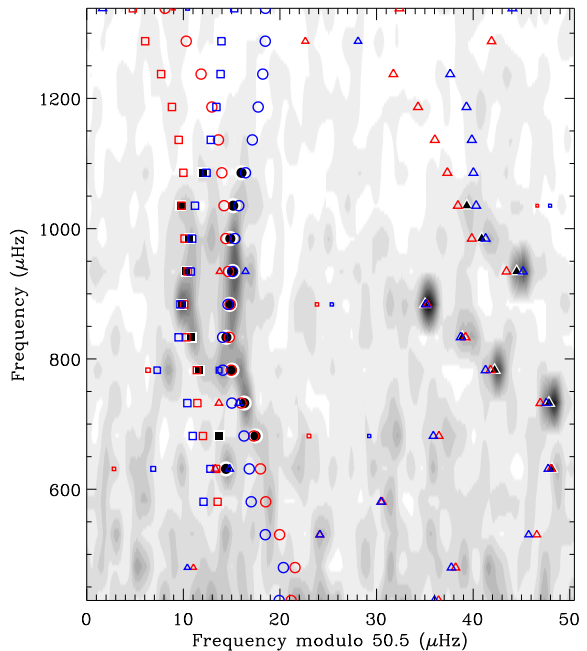


Figure 3. An échelle diagram showing the 26 frequencies from the maximal set that were used as constraints (solid points) with the frequencies of Models AA (blue) and AB (red) for comparison. The star exhibits modes with $l = 0$ (circles), $l = 1$ (triangles), and $l = 2$ (squares). A grayscale map showing the power spectrum (smoothed to $1 \mu\text{Hz}$ resolution) is included in the background for reference.

of solutions when using the revised constraints, but the low-mass family was only marginally suboptimal. The apparent bifurcation of results in Table 4 into two values of α arises from the decision of most modelers to fix this parameter in each case to the original value from Table 3. For each family of solutions, the modeling teams adopted the appropriate input physics: neglecting overshoot and diffusion for the refined Models A, while including both ingredients for the refined Models B. One team produced two additional models (labeled AA' and AB') to isolate the effect of input physics on the final results. Model AA' started from the parameters of Model A but included overshoot and helium settling, while Model AB' searched in the region of Model B but neglected overshoot and diffusion.

5.2. Stellar Properties & Error Analysis

An inspection of the results in Table 4 reveals that models in either family of solutions can provide a comparable match to the observational constraints. This ambiguity cannot be attributed to the input physics, since the models that sample all four combinations of the input physics and family of solutions (AA, AA', AB, AB') have comparable χ^2 values. The individual frequencies of these models all provide a good fit to the data, including the $l = 1$ mixed modes. The observations are compared to two representative models in Figure 3 using an échelle diagram, where we divide the frequency spectrum into segments of length $\langle \Delta\nu \rangle$ and plot them against the oscillation frequency. This representation of the data aligns modes with the same spherical degree into roughly vertical columns, with $l = 0$ modes shown as circles, $l = 1$ modes shown as triangles, and $l = 2$ modes shown as squares. The 26 modes from the maximal frequency set that were included

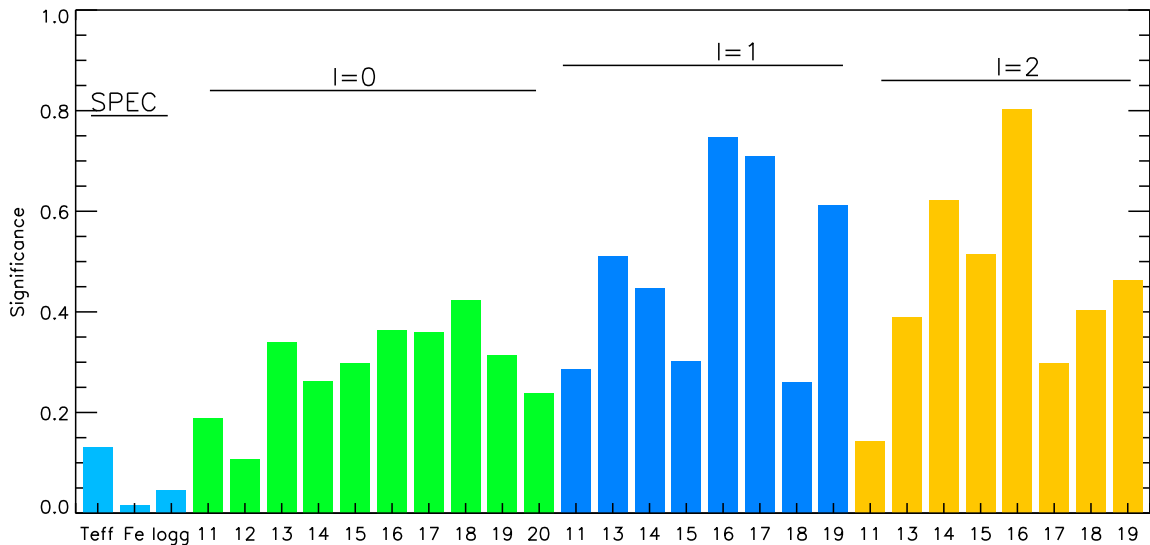


Figure 4. The significance S_i of each observational constraint in determining the parameters of Model AA. Each oscillation frequency is labeled with the reference radial order from Table 1, and the degrees $l = 0, 1$ and 2 are shown sequentially in different shades from left to right.

in the final fit are indicated with solid points. Open points indicate the model frequencies, with Model AA shown in blue and Model AB shown in red. A greyscale map of the power spectrum (smoothed to $1 \mu\text{Hz}$ resolution) is included in the background for reference. The different models appear to be sampling comparable local minima in a correlated parameter space. Without additional constraints, we have no way of selecting one of these models over the other.

We can understand the two families of models by considering the general properties of subgiant stars, where a wide range of masses can have the same stellar luminosity with minor adjustments to the input physics and other model parameters—in particular the helium mass fraction. This degeneracy between mass and helium abundance has been discussed in the modeling of specific subgiant stars (e.g. Fernandes & Monteiro 2003; Pinheiro & Fernandes 2010; Yang & Meng 2010), and it adds a large uncertainty to the already difficult problem of determining the helium abundance in main-sequence stars (e.g. Vauclair et al. 2008; Soriano & Vauclair 2010). The luminosity of stellar models on the subgiant branch is mainly determined by the amount of energy produced at the edge of the helium core established during the main-sequence phase. The rate of energy production depends on the temperature and the hydrogen abundance in that layer. As a consequence it is possible to find models at the same luminosity with quite different values of total mass, by adjusting the other parameters to yield the required temperature at the edge of the helium core. Fortunately, for subgiant stars the presence of mixed modes can provide additional constraints on the size of the helium core. For KIC 11026764 this mixed mode constraint significantly reduces the range of possible masses to two specific intervals, where the combination of stellar mass and core size are compatible with the atmospheric parameters and the frequencies of the mixed modes.

Regardless of which family of solutions is a better representation of KIC 11026764, the parameter values in Table 4 already yield precise determinations of some of the most interesting stellar properties—in particular, the asteroseismic age and radius. If we consider only the four models that were

produced by the same modeling team with an identical fitting method (the ASTEC models: AA, AA', AB, AB'), we can calculate the mean value and an internal (statistical) uncertainty in isolation from external (systematic) errors arising from differences between the various codes and methods. The asteroseismic ages of the two families of solutions range from 5.87 to 5.99 Gyr, with a mean value of $t = 5.94 \pm 0.05$ Gyr. The stellar radii of the two families range from 2.03 to $2.08 R_\odot$, with a mean value of $R = 2.05 \pm 0.03 R_\odot$. The luminosity ranges from 3.45 to $3.80 L_\odot$, with a mean value of $L = 3.56 \pm 0.14 L_\odot$. These are unprecedented levels of precision for an isolated star, despite the fact that the stellar mass is still ambiguous at the 10% level. Of course, *precision* does not necessarily translate into *accuracy*, but we can evaluate the possible systematic errors on these determinations by looking at the distribution of parameter values for the entire sample of modeling results, not just those from ASTEC.

Considering the full range of the best models ($\chi^2 < 10$) in Table 4, there is broad agreement on the value of the stellar radius. The low value of $2.03 R_\odot$ is from one of the ASTEC models considered above, while the high value of $2.09 R_\odot$ is from the Catania-GARSTEC code, leading to a systematic offset of $^{+0.04}_{-0.02} R_\odot$ compared to the mean ASTEC value. There is a slightly higher dispersion in the values of the asteroseismic age. Again considering only the best models, we find a full range for the age as low as 4.99 Gyr from Catania-GARSTEC up to 5.99 Gyr from ASTEC, for a systematic offset of $^{+0.05}_{-0.95}$ Gyr relative to the ASTEC models. The best models exhibit the highest dispersion in the values of the luminosity, with a low estimate of $3.45 L_\odot$ from ASTEC and a high value of $4.44 L_\odot$ from Catania-GARSTEC. These models establish a systematic offset of $^{+0.88}_{-0.11} L_\odot$ compared to the ASTEC results.

To evaluate the relative contribution of each observational constraint to the final parameter determinations, we can study the significance S_i using singular value decomposition (SVD; see Brown et al. 1994). An observable with a low value of S_i has little influence on the solution, while a high value of S_i indicates an observable with greater impact. The

significance of each observable in determining the parameters of KIC 11026764 for Model AA is shown in Figure 4. From left to right we show the spectroscopic constraints followed by the $l = 0, 1$ and 2 frequencies labeled with the reference radial order from Table 1, and each group of constraints is shown in a different shade. It is immediately clear that the $l = 1$ and $l = 2$ frequencies have more weight in determining the parameters. If we examine how the significance of each spectroscopic constraint changes when we combine them with modes of a given spherical degree, we can quantify the impact of each set of frequencies because the information content of the spectroscopic data does not change. The spectroscopic constraints contribute more than 25% of the total significance when combined with the $l = 0$ modes (13% from the effective temperature alone), indicating that these two sets of constraints contain redundant information. By contrast, the total significance of the spectroscopic constraints drops to 4% for the $l = 2$ modes, and 7% when combined with the $l = 1$ modes—confirming that these frequencies contain more independent information than the $l = 0$ modes, as expected from the short evolutionary timescale for mixed modes. Although the significance of the atmospheric parameters on the final solution appears to be small, we emphasize that accurate spectroscopic constraints are essential for narrowing down the initial parameter space.

6. SUMMARY & DISCUSSION

We have determined a precise asteroseismic age and radius for KIC 11026764. Although no planets have yet been detected around this star, similar techniques can be applied to exoplanet host stars to convert the relative planetary radius determined from transit photometry into an accurate absolute radius—and the precise age measurements for field stars can provide important constraints on the evolution of exoplanetary systems. By matching stellar models to the individual oscillation frequencies, and in particular the $l = 1$ mixed mode pattern, we determined an asteroseismic age and radius of $t = 5.94 \pm 0.05(\text{stat})_{-0.95}^{+0.05}(\text{sys})$ Gyr and $R = 2.05 \pm 0.03(\text{stat})_{-0.02}^{+0.04}(\text{sys}) R_{\odot}$. This represents an order of magnitude improvement in the age precision over pipeline results—which fit only the mean frequency separations—while achieving comparable or slightly better precision on the radius (cf. Models J' and K' in Table 4). The systematic uncertainties on the radius are almost negligible, while the model-dependence of the asteroseismic age yields impressive accuracy compared to other age indicators for field stars (see Soderblom 2010). Whatever the limitations on absolute asteroseismic ages, studies utilizing a single stellar evolution code can precisely determine the *chronology* of stellar and planetary systems.

The $l = 1$ mixed modes in KIC 11026764, shifted from regularity by avoided crossings, play a central role in constraining the models. Bedding et al. (in prep.) have pointed out the utility of considering the frequencies of the avoided crossings themselves, since they reflect the g-mode component of the eigenfunction that is trapped in the core (Aizenman et al. 1977). The avoided crossing frequencies are revealed by the distortions in the $l = 1$ modes, which are visible as rising branches in Figure 1. For Model AA, marked by the vertical line, we see that the frequencies of the first four avoided crossings are $G_1 \approx 1270 \mu\text{Hz}$, $G_2 \approx 920 \mu\text{Hz}$, $G_3 \approx 710 \mu\text{Hz}$ and $G_4 \approx 600 \mu\text{Hz}$. Each of these avoided crossings produces a characteristic feature in the échelle diagram that can be matched to the observations. Indeed, the observed power

spectrum of KIC 11026764 (greyscale in Figure 3) shows a clear feature that matches G_2 and another, slightly less clear, that matches G_3 . The avoided crossing at G_1 that is predicted by the models lies outside the region of detected modes, but it is possible that additional data expected from the *Kepler Mission* will confirm its existence. We also note a peak in the observed power spectrum at $586 \mu\text{Hz}$ (greyscale in Figure 3) that lies close to an $l = 1$ mixed mode in the models, and also at $766 \mu\text{Hz}$ near an $l = 2$ mixed mode. Again, additional data are needed for confirmation.

It is interesting to ask whether all of the models discussed in this paper have the same avoided crossing identification. For example, are there any models that fit the observed frequencies but for which the avoided crossing at $920 \mu\text{Hz}$ corresponds to G_1 instead of G_2 ? This would imply a different local minimum in parameter space, and a different location in the p-g diagram introduced by Bedding et al. Although this may be the case for some of the models in Table 3 from the initial search, all of the models listed in Table 4 have the avoided crossing identification described above.

The observed structure of the $l = 1$ ridge suggests relatively strong coupling between the oscillation modes. At frequencies above the observed range, the best models suggest that the unperturbed $l = 1$ ridge would align vertically near $40 \mu\text{Hz}$ in the échelle diagram (see Figure 3). It is evident from Figure 1 that at a given age the frequencies of numerous p-modes are affected by the rising g-mode frequency, and this manifests itself in the échelle diagram with several modes deviating from the location of the unperturbed ridge on either side of the avoided crossing (Deheuvels & Michel 2009). Stronger coupling suggests a smaller evanescent zone between the g-mode cavity in the core and the p-mode cavity in the envelope. Although the evanescent zone will be larger for $l = 2$ modes, the strength of the coupling for the $l = 1$ modes raises the possibility that weakly mixed $l = 2$ modes—like those near $766 \mu\text{Hz}$ in Model AA—may be observable in longer time series data from continued observations by *Kepler*.

It is encouraging that with so many oscillation frequencies observed, the impact of an incorrect mode identification appears to be minimal. For example, the models suggest that the lowest frequency $l = 0$ mode in Table 1 may actually be on the $l = 2$ ridge—or it could even be an $l = 1$ mixed mode produced by the G_4 avoided crossing. However, the influence of the other observational constraints is sufficient to prevent any serious bias in the resulting models. Even so, adopting either of these alternate identifications for the lowest frequency $l = 0$ mode would cut the χ^2 of Model AB nearly in half.

Despite a 10% ambiguity in the stellar mass, we have determined a luminosity for KIC 11026764 of $L = 3.56 \pm 0.14(\text{stat})_{-0.11}^{+0.88}(\text{sys}) L_{\odot}$. With the radius so well determined from asteroseismology, differences of 200–300 K in the effective temperatures of the models are largely responsible for the uncertainties in the luminosity. These differences are generally correlated with the composition—hotter models at a given mass tend to have a higher helium mass fraction and lower metallicity, while cooler models tend to be relatively metal-rich. The adopted spectroscopic constraints fall in the middle of the range of temperatures and metallicities for the two families of models, and leave little room for substantial improvement. Perhaps the best chance for resolving the mass ambiguity, aside from additional asteroseismic constraints, is a direct measurement of the luminosity. Although *Kepler* was not optimized for astrometry, it will eventually provide high-

quality parallaxes (Monet et al. 2010). The resulting luminosity error is expected to be dominated by uncertainties in the bolometric correction (~ 0.02 mag) and the amount of interstellar reddening (~ 0.01 mag), although saturation from this bright target may present additional difficulties. This should lead to a luminosity precision near 3%, which would be sufficient to distinguish between our two families of solutions for KIC 11026764.

Funding for the *Kepler Mission* is provided by NASA's Science Mission Directorate. This work was supported in part by NASA grant NNX09AE59G. Computer time was provided by TeraGrid allocation TG-AST090107. The National Center for Atmospheric Research is sponsored by the U.S. National Science Foundation. Observations were made with the Nordic Optical Telescope, operated on the island of La Palma jointly by Denmark, Finland, Iceland, Norway, and Sweden, in the Spanish Observatorio del Roque de los Muchachos of the Instituto de Astrofísica de Canarias. TA gratefully acknowledges support from the Programme National de Physique Stellaire of INSU/CNRS. GD, P-OQ, CK, JC-D and HK are grateful for financial support from the Danish Natural Science Research Council. J.M-Ž acknowledges MNiSW grant N203 014 31/2650. MJPFM acknowledges financial support from project TDC/CTE-AST/098754/2008 from FCT & FEDER, Portugal. TRB and DS acknowledge financial support from the Australian Research Council. WJC, YE, A-MB, STF, SH and RN acknowledge the support of the UK Science and Facilities Technology Council. OLC and P-OQ acknowledge support from HELAS, a major international collaboration funded by the European Commission's Sixth framework program. SGS acknowledges support from the FCT (Portugal) through grants SFRH/BPD/47611/2008 and PTDC/CTE-AST/66181/2006. The authors wish to thank the Kepler Science Team and everyone who helped make the *Kepler Mission* possible.

REFERENCES

Aerts, C., Christensen-Dalsgaard, J., & Kurtz, D. W. 2010, *Asteroseismology*, Springer, (ISBN: 978-1-4020-5178-4)
 Aizenman, M., Smeyers, P., & Weigert, A. 1977, *A&A*, 58, 41
 Alexander, D. R. & Ferguson, J. W. 1994, *ApJ*, 437, 879
 Anderson, E. R., Duvall, T. L. Jr., Jefferies, S. M., 1990, *ApJ*, 364, 699
 Angulo, C., Arnould, M., Rayet, M., et al. 1999, *Nucl. Phys. A.*, 656, 3
 Appourchaux, T., Michel, E., Auvergne, M., et al., 2008, *A&A*, 488, 705
 Asplund, M., Grevesse, N., & Sauval, A. J. 2005, *ASP Conf.*, 336, 25
 Bahcall, J. N., & Pinsonneault, M. H. 1992, *Rev. Mod. Phys.*, 64, 885
 Bahcall J. N., Pinsonneault M. H., 1995, *Rev. Mod. Phys.*, 67, 781
 Basu, S., Chaplin, W. J., Elsworth, Y. 2010, *ApJ*, 710, 1596
 Bedding, T. R., et al. 2007, *ApJ*, 663, 1315
 Bedding, T. R., et al. 2010, *ApJ*, 713, 935
 Benomar, O., Appourchaux, T., Baudin, F., 2009, *A&A*, 506, 15
 Biazzo, K., Randich, S., Palla, F. 2010, *A&A*, in preparation
 Böhm-Vitense, E. 1958, *Zeitschrift für Astrophysik*, 46, 108
 Bonanno, A., Schlattl, H., Paternó L., 2002, *A&A*, 390, 1115
 Borucki, W. J., et al. 2007, *ASP. Conf.* 366, 309
 Brown, T. M., et al. 1994, *ApJ*, 427, 1013
 Bruntt H., et al. 2004, *A&A*, 425, 683
 Bruntt H., De Cat P., Aerts, C. 2008, *A&A*, 478, 487
 Bruntt H., et al. 2010a, *MNRAS*, accepted (arXiv:1002.4268)
 Bruntt, H., et al. 2010b, *A&A*, accepted (arXiv:1005.3208)
 Campante, T. L., et al. 2010, *MNRAS*, submitted
 Canuto, V. M. & Mazzitelli, I. 1992, *ApJ*, 389, 724
 Carrier, F., Eggenberger, P., & Bouchy, F. 2005, *A&A*, 434, 1085
 Castelli, F., & Kurucz, R. L. 2003, *IAU Symp.*, 210, 20
 Chaboyer, B., & Zahn, J.-P. 1992, *A&A*, 253, 173
 Chaboyer, B., Green, E. M., & Liebert, J. 1999, *AJ*, 117, 1360

Chaboyer, B., Fenton, W. H., Nelan, J. E., Patnaude, D. J., & Simon, F. E. 2001, *ApJ*, 562, 521 (<http://andes.dartmouth.edu/StellarEvol/>)
 Chaplin, W. J., et al. 1999, *MNRAS*, 308, 424
 Chaplin, W. J., et al. 2010, *ApJ*, 713, L169
 Christensen-Dalsgaard, J. 1993, *ASP Conf.*, 42, 347
 Christensen-Dalsgaard, J. 1998, *Space Sci. Rev.*, 85, 19
 Christensen-Dalsgaard, J. 2004, *Sol. Phys.*, 220, 137
 Christensen-Dalsgaard, J., et al. 2007, *Communications in Asteroseismology*, 150, 350
 Christensen-Dalsgaard, J. 2008a, *Ap&SS*, 316, 13
 Christensen-Dalsgaard, J. 2008b, *Ap&SS*, 316, 113
 Cox, A. N. 2000, *Allen's astrophysical quantities*, 4th ed. (New York: Springer)
 Deheuvels, S., & Michel, E. 2009, *Ap&SS*, 241, in press
 Deheuvels, S., et al. 2010, a, accepted (arXiv:1003.4368)
 Demarque, P., & Mengel, J. G. 1971, *ApJ*, 164, 317
 Demarque, P., et al. 2004, *ApJS*, 155, 667
 Demarque, P., et al. 2008, *Ap&SS*, 316, 311
 Di Mauro, M. P., et al. 2003, *A&A*, 404, 341
 Dotter, A., et al. 2007, *AJ*, 134, 376
 Eggenberger, P. & Carrier, F. 2006, *A&A*, 449, 293
 Eggenberger, P., Meynet, G., Maeder, A., et al. 2008, *Ap&SS*, 316, 43
 Eggenberger, P., Miglio, A., Montalbán, J., et al. 2010, *A&A*, 509, 72
 Eggleton, P. P., Faulkner, J., & Flannery, B. P. 1973, *A&A*, 23, 325
 Ferguson, J. W., et al. 2005, *ApJ*, 623, 585
 Fernandes, J., & Monteiro, M.J.P.F.G. 2003, *A&A*, 399, 243
 Frasca, A., et al. 2003, *A&A*, 405, 149
 Frasca, A., et al. 2006, *A&A*, 454, 301
 Gilliland, R. L., et al. 2010a, *PASP*, 122, 131
 Gilliland, R. L., et al. 2010b, *ApJ*, 713, L160
 Grevesse, N., & Noels, A. 1993, in *Origin and Evolution of the Elements*, ed. S. Kubono & T. Kajino, 14
 Grevesse, N. & Sauval, A. J. 1998, *Space Sci. Rev.*, 85, 161
 Grevesse, N., Asplund, M., Sauval, A. J., 2007 *Space Sci. Rev.*, 130, 105
 Guenther, D. B., et al. 1992, *ApJ*, 387, 372
 Gustafsson, et al. 2008, *A&A*, 486, 951
 Harvey, J., 1985, *ESA SP-235*, 199
 Hubeny, I. 1988, *Comput. Phys. Comm.*, 52, 103
 Hubeny I., Lanz T., 1995, *ApJ*, 439, 875
 Hummer, D.G., & Mihalas, D. 1988, *ApJ*, 331, 794
 Iglesias, C. A., & Rogers, F. J. 1996, *ApJ*, 464, 943
 Katz, D., et al. 1998, *A&A*, 338, 151
 Kawaler, S. D. 1988, *ApJ*, 333, 236
 Kippenhahn, R., & Weigert, A. 1990, *Stellar Structure and Evolution*, (Heidelberg: Springer)
 Kjeldsen, H., & Bedding, T. R. 1995, *A&A*, 293, 87
 Kjeldsen, H., et al. 1995, *AJ*, 109, 1313
 Kjeldsen, H., et al. 2003, *AJ*, 126, 1483
 Kjeldsen, H., et al. 2008, *ApJ*, 683, L175
 Kosovichev, A. G. 1999, *J. Comput. App. Math.*, 109, 1
 Kurucz, R. L. 1991, in *NATO ASIC Proc. 341: Stellar Atmospheres - Beyond Classical Models*, 441
 Kurucz, R.L., 1993 *ATLAS9 Stellar Atmosphere Programs and 2 km s⁻¹ grid*, (Kurucz CD-ROM No. 13)
 Larson, R. B., & Demarque, P. R. 1964, *ApJ*, 140, 524
 Latham, D. W., et al. 2005, *BAAS*, 37, 1340
 Ludwig, H.-G. et al. 2009, *IAU Symp.*, 265, 201
 Maeder, A. & Meynet, G. 1989, *A&A*, 210, 155
 Maeder, A. & Zahn, J.-P. 1998, *A&A*, 334, 1000
 Metcalfe, T. S., & Charbonneau, P. 2003, *J. Computat. Phys.*, 185, 176
 Metcalfe, T. S., et al. 2009, *ApJ*, 699, 373
 Michaud, G., & Proffitt, C. R. 1993, *ASP Conf.*, 40, 246
 Monet, D. G., et al. 2010, *ApJ*, submitted (arXiv:1001.0305)
 Morel, P. 1997, *A&AS*, 124, 597
 Morel P., Lebreton Y., 2008, *Ap&SS*, 316, 61
 Moya, A. & Garrido, R. 2008, *Ap&SS*, 316, 129
 Osaki, J. 1975, *PASJ*, 27, 237
 Paquette, C., Pelletier, C., Fontaine, G., & Michaud, G. 1986, *ApJS*, 61, 177
 Pinheiro, F.J.G., & Fernandes, J.M. 2010, *Ap&SS*, 328, 73
 Quirion, P.-O., Christensen-Dalsgaard, J. & Arentoft, T. 2010, in prep.
 Randich, S., et al. 2006, *A&A*, 450, 557
 Rogers, F. J., & Iglesias, C. A. 1995, *ASP Conf.*, 78, 31
 Rogers, F.J., Swenson, F.J., & Iglesias, C.A. 1996, *ApJ*, 456, 902
 Rogers, F. J. & Nayfonov, A. 2002, *ApJ*, 576, 1064
 Senden C., 1973 <http://verdi.as.utexas.edu/>
 Soderblom, D. R. 2010, *ARA&A*, 48, in press (arXiv:1003.6074)
 Soriano, M., & Vauclair, S. 2010, *A&A*, 513, A49

- | | |
|---|--|
| <p>Soubiran, C., Katz, D., & Cayrel, R. 1998, A&AS, 133, 221
 Soufi, F., Goupil, M. J., & Dziembowski, W. A. 1998, A&A, 334, 911
 Sousa S.G., et al. 2006, A&A, 458, 873
 Sousa S.G., et al. 2007, A&A, 469, 783
 Sousa S.G., et al. 2008, A&A, 487, 373
 Stello, D., et al. 2009a, ApJ, 700, 1589
 Stello, D., et al. 2009b, MNRAS, 400, L80
 Suárez, J. C. 2002, Ph.D. Thesis, Observatoire de Paris.
 Suárez, J. C., Garrido, R., & Moya, A. 2007, A&A, 474, 961</p> | <p>Suárez, J. C., & Goupil, M. J. 2008, Ap&SS, 316, 155
 Thoul, A. A., Bahcall, J. N., & Loeb, A. 1994, ApJ, 421, 828
 Vauclair, S., et al. 2008, A&A, 482, L5
 Weiss, A., & Schlattl, H. 2008, Ap&SS, 316, 99
 Yang, W., & Meng, X. 2010, New Astronomy, 15, 367
 Zahn, J.-P. 1992, A&A, 265, 115</p> |
|---|--|

APPENDIX

A. THE INFLUENCE OF ROTATION

Rotation velocity can have a large influence on the frequencies of a given stellar model, since angular momentum transport can change the internal structure and evolution of the star. Thus, rotation velocity and angular momentum transport processes must be taken into account for accurate modeling. However, if the rotation velocity is not too large, the effect on the frequencies can be comparable to or smaller than the observational accuracy, in which case non-rotating models can be trusted. We have examined two angular momentum transport processes covering the extreme cases to quantify the influence of rotation on the modeling of KIC 11026764.

The study was performed using the CESAM code (Morel & Lebreton 2008). The first-order effects of rotation on the equilibrium models were considered by subtracting the spherically averaged contribution of the centrifugal acceleration to the gravity of the model, $g_{\text{eff}} = g - \mathcal{A}_c(r)$, where g corresponds to the local gravity, and $\mathcal{A}_c(r)$ represents the radial component of the centrifugal acceleration. This spherically averaged component of the centrifugal acceleration does not change the order of the hydrostatic equilibrium equations. Such models are referred to as *pseudo-rotating* (see Soufi et al. 1998; Suárez et al. 2007). Since we have only a weak constraint on the rotation velocity of KIC 11026764 (see §3.2), we used an initial rotation velocity that leads to solar rotation at the solar age. Standard physical inputs were used, including the EFF equation of state. The opacity tables were taken from the OPAL package (Rogers & Iglesias 1995), complemented at low temperatures ($T \leq 10^4$ K) with the tables provided by Alexander & Ferguson (1994). The outer boundary conditions were determined by assuming a plane-parallel Eddington grey atmosphere. The model metallicity (Z/X) is derived from the observed $[\text{Fe}/\text{H}]$ value assuming $(Z/X)_{\odot} = 0.0245$ (Grevesse & Noels 1993), $Y_{\text{pr}} = 0.235$ and $Z_{\text{pr}} = 0$ for the primordial helium and heavy-element abundances, and $\Delta Y/\Delta Z = 2$ for the enrichment ratio. The thermonuclear reactions incorporated the PP and CNO cycles with the NACRE coefficients. No microscopic diffusion was included in the calculation.

We studied the following angular momentum transport processes: (1) Global Conservation of the angular momentum [GC, solid rigid rotation]: $\Omega(t, r) = \Omega(t)$, and (2) Local Conservation of the angular momentum [LC, differential rotation]: $dr^2\Omega/dt = 0$. The GC and LC of angular momentum represent the two extreme cases in nature. The actual rotation profile of the star must fall between these two solutions.

The theoretical frequencies were calculated using GraCo (Moya & Garrido 2008). We found that for the rotation velocity studied here, rigid rotation yields frequencies closer to the non-rotating case, with differences in the range $[-0.01, -0.025]$ μHz . Differential rotation yields larger differences in the range $[-0.051, -0.045]$ μHz . Considering the large frequency separations, rigid rotation leads to differences relative to the non-rotating case in the range $[+0.0025, -0.0045]$ μHz while differential rotation yields differences in the range $[0, -0.004]$ μHz . All of these differences are much smaller than the observational errors, so rotation can safely be neglected in the frequency analysis of KIC 11026764. However, note that rotational mixing—which has not been considered in this study—may lead to changes in the global and internal properties of the models even for slowly rotating stars (Eggenberger et al. 2010).

B. THE IMPORTANCE OF ASTEROSEISMIC CONSTRAINTS

We compared results from SEEK with and without the asteroseismic inputs to see how the large and small separations can help reduce the uncertainty on the inferred stellar properties. We see that the uncertainty in the radius of 3% provided by SEEK is in line with what was expected from simulated data (Stello et al. 2009a). With $R = 2.10 \pm 0.06 R_{\odot}$, the precision is a factor of five better than what we could get using only the available spectroscopic input (T_{eff} , $\log g$ and $[\text{Fe}/\text{H}]$), which resulted in a 14.6% uncertainty ($R = 2.06 \pm 0.30 R_{\odot}$). This dramatic improvement was obtained using the large and small separations as the only seismic constraints, as opposed to fitting individual mode frequencies.

In Figure 5 we show 2D projections of the probability distributions provided by SEEK, which illustrate the correlations between the spectroscopic input parameters and the value of the inferred radius. To produce these figures we fixed all but one of the spectroscopic input parameters to the observed values. Hence, in Figure 5a the dark red regions are where we would most likely find the star if we did not know its temperature. The cross marks the observed value of the temperature with its measured uncertainty in the vertical direction while the horizontal direction marks the inferred value of R and its precision. We can see that changing the temperature within the error bars does not greatly affect the value of the radius. Reducing the uncertainty of the temperature would not affect the uncertainty of the radius, since the width of the correlation function is large compared to its slope. In Figure 5b we see that the value of $\log g$ is well determined without any spectroscopic measurement. The spectroscopic value of $\log g$ has no significant influence in constraining the radius. The constraints from the seismic measurements are simply much stronger than what is found from spectroscopy in this case. We found similar results for the determination of the mass. Quite apparent in Figure 5c are several local maxima due to the discrete nature of the grid. However, the resolution of the grid is sufficient to see the underlying correlation between the metallicity and the radius. From this figure we see that if the star had a

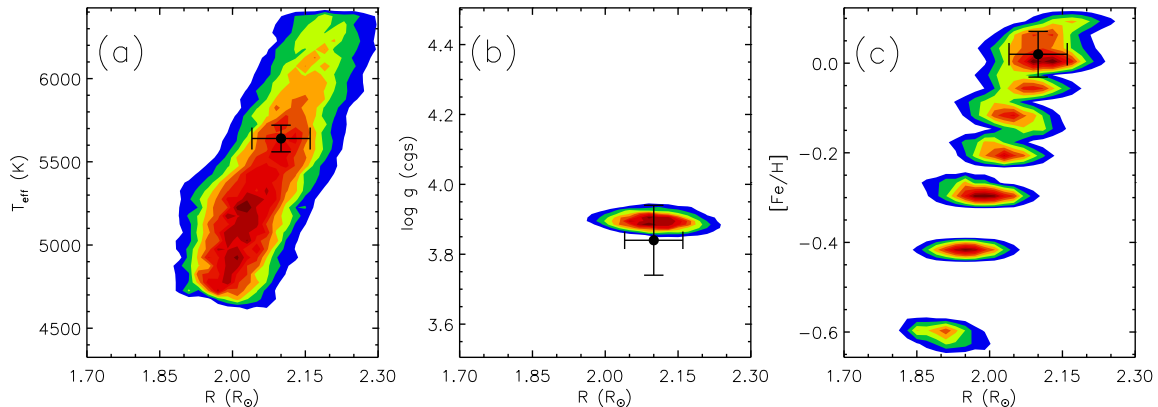


Figure 5. Normalized probability distributions, showing the correlation of the radius with several spectroscopic constraints when they are excluded from the fit, including (a) the effective temperature T_{eff} , (b) the surface gravity $\log g$ and (c) the metallicity $[\text{Fe}/\text{H}]$ relative to solar, where the gaps between the islands are caused by the discrete nature of the grid. Dark red indicates the maximum probability, which decreases linearly to white for zero probability. In each panel, the cross shows the observed values from the VWA method (see Table 2) and the final fit for $R = 2.10 \pm 0.06$. We see that $\log g$ is determined precisely before any spectroscopic knowledge of its value is included in the fit.

metallicity of $[\text{Fe}/\text{H}] \sim -0.6$ it would have a radius of $R \sim 1.91 R_{\odot}$. We remark that the uncertainty in radius is mainly caused by the unknown value of the initial helium content Y_i which has not been constrained by any of the observables (for more details on the effect of Y_i on stellar parameters, see Quirion, Christensen-Dalsgaard & Arentoft 2010).

Finally, in Figure 6 both the large and the small separations are left as free parameters. We note that the curved shape of the probability function is typical when the correlation between the large separation and the radius is plotted. In addition to showing that the large separation is the main constraint on the radius, Figure 6 illustrates that a star with a large radius, and hence smaller value of the large separation, will have a larger uncertainty on the inferred radius. The larger uncertainty is caused by the changing slope of the correlation, which tends to be flatter for larger radii. Figure 6 also shows that without the asteroseismic constraints, the uncertainty in the radius increases dramatically since the most probable region for the radius, in red, spans $1.76 \lesssim R/R_{\odot} \lesssim 2.36$.

For the mass, SEEK demonstrates that the precision is only slightly improved by including the large and small separations in the fitting process. We find $M = 1.25 \pm 0.13 M_{\odot}$ when only the spectroscopic input parameters are used and $M = 1.27 \pm 0.09 M_{\odot}$ when asteroseismic inputs are added. For the age, the results of SEEK without the asteroseismic inputs yield a relatively weak constraint of 40% with $t = 5.03 \pm 2.02$ Gyr. This uncertainty is reduced by nearly a factor of two when the large and small separations are used, which gives $t = 4.26 \pm 1.22$ Gyr. If we compare this result with Quirion, Christensen-Dalsgaard & Arentoft (2010), 30% error on the age is unusually large for a star having well measured values of $\Delta\nu$ and $\delta\nu$. It seems that $\delta\nu$ does not provide an additional constraint on the age of the star, since we were able to determine a very similar age $t = 4.21 \pm 1.25$ Gyr when $\delta\nu$ was excluded from the fit. Bedding et al. (in prep.) find this to be generally true for subgiant stars.

Finally, we stress that the mixing-length parameter α and the initial helium content Y_i are not constrained by our fit. For Y_i , the output value is simply the central value used in SEEK’s grid plus a 1σ uncertainty extending toward the edges of the grid. For α , a value smaller than 1.8 is preferred, but not decisively. Our overall conclusion from SEEK is that the asymptotic asteroseismic inputs can be used to reduce significantly the uncertainty on the radius of KIC 11026764. The age and the mass precision can also be improved, though less substantially.

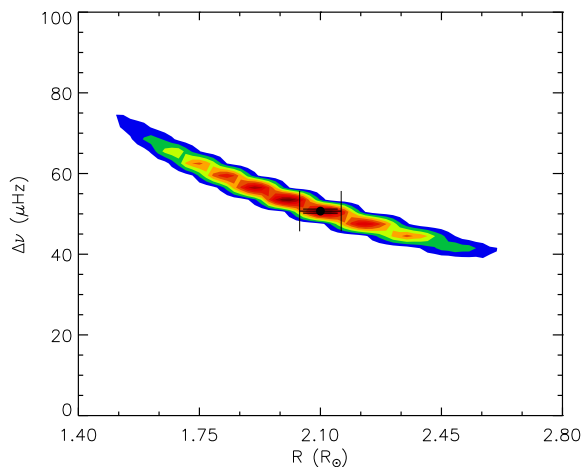


Figure 6. Similar to Figure 5, but for $\Delta\nu_0$ when the small separation is also excluded from the fit. The point with error bars indicates the result when both the large and small separations are included as constraints.

Appendix I

NOT "Fast Track" proposal
for five *Kepler* stars

*APPENDIX I. NOT "FAST TRACK" PROPOSAL
FOR FIVE KEPLER STARS*

NOT SERVICE APPLICATION

PI	Gulnur Dogan	Email	gulnur@phys.au.dk	ID	*****
Inst.	Aarhus University	Country	DK		
Cols	I.Brandao(2),T.Campante(2),R.Handberg,O.Creevey(3),S.Mathur(4),H.Bruntt,C.Karoff				
Title	Urgent spectroscopic support for Kepler photometry on 5 unique solar-like stars				

Abstract

Our purpose is to characterize 5 solar-like stars in the field of view of NASA's Kepler satellite. These are unique targets since they are the only stars that have been observed for 7 consecutive months and show solar-like oscillations in their spectra. Only together with reliable fundamental parameters obtained through spectroscopy with FIES, will we be able to perform a complete study of their structure and evolution -- including measuring the extent the convective regions and differential rotation in these stars.

Why use the NOT

FIES & NOT have a well-suited combination of aperture and resolution for our purpose. Moreover, the fast track option offered by NOT is much needed due to the urgency of our project. We (4 PhD students+2 young scientists) are given the opportunity to lead the work on data analysis and modelling of these stars among a working group comprising over 100 senior and junior scientists(*). The resulting scientific papers must be submitted by 15/9/2010.

Scientific Justification

With the Kepler satellite, we have started to obtain invaluable photometric data leading to unprecedented information about stellar structure and evolution. Kepler made it possible (together with its predecessor CoRoT satellite) to extract individual frequencies for around 30 p-mode (acoustic) oscillations for each star. Every frequency is valuable as it carries signatures from a different region inside the star. Asteroseismology, a unique tool to sound the stellar interiors, is hence in its most fruitful era. However, neither the seismic observables nor the fundamental parameters are sufficient for an in-depth analysis of the stars when they are used alone. The classical observables combined with the seismic constraints from Kepler will allow us to perform detailed and precise modelling of these stars, which is not possible otherwise. We are currently working on characterizing five exciting stars, and we have excellent seismic data including the individual frequencies. These data are unique as these targets are the only ones that have showed solar-like oscillations and have been observed for 7 consecutive months (while other data sets in hand cover ~1 month). Having observations over such a long time increases the precision of the frequencies and more oscillation modes can be measured confidently. This is very important in order to put strong constraints on the stellar models, hence to lift the degeneracy, for instance between stellar mass and He content, which exists when only the classical observables are available. For the classical observables of our targets; we now only have poor estimates from the Kepler Input Catalogue (KIC), determined by calibrating griz + Mg b filter photometry of all stars in Kepler FOV. According to the KIC estimates, these 5 stars might cover a temperature (effective) range of 600 K including the solar temperature. These constitute an interesting sample of stars in which solar-like oscillations are observed. Having reliable constraints on classical observables (temperature, metallicity ([Fe/H]), and log(g)) through spectroscopy, we will be able to uncover the interiors of these promising targets. On the other hand, this opportunity is very special only now, because the articles related to the Kepler mission can only be submitted in certain windows in time, due to the embargo on the data. The duty given to us includes submitting our results for publication in the window of 1-15 September 2010. Thus, the quality of our results will increase substantially if we can obtain the spectroscopic data now.

Technical Description

The target list we are proposing includes five northern hemisphere stars with magnitudes $V=10.8$, 10.9 , and 11.9 (3 of them). We would like the observations to be performed in the medium-resolution setting ($R = 46000$). Observing each of the two relatively bright stars in this mode twice for 20 minutes will result in spectra with signal-to-noise ratio of 80, while observing the rest for 2×22 minutes each will give signal-to-noise ratio of about 50. This will provide us with effective temperature, $\log(g)$ and $[Fe/H]$ with a certainty of about 100K, 0.10, and 0.08, respectively. The spectra will be analyzed using a specialized software, VWA (**). Our group has expertise in this kind of analysis.

We reserve 28 minutes for the overheads. Around 15 minutes of this time is for the readouts (10 readouts \times 90 sec), and 13 minutes is for the target acquisition. Once the first target is acquired (5 min.), the rest of the targets would take around 2 minutes each as they are within a few degrees.

(**) Bruntt, H., Bedding, T. R., Quirion, P.-O. et al. 2010, MNRAS tmp 746B

Instrument Configuration

{FIES}{Spectro-Echelle}{Med-Res Fiber}

Targets

KIC 11395018, RA:19 09 55.49 Dec:+49 15 04.5, $V=10.8$, 2×20 min exposures
KIC 10273246, RA:19 26 05.76 Dec:+47 21 30.1, $V=10.9$, 2×20 min exposures
KIC 10920273, RA:19 27 45.77 Dec:+48 19 45.4, $V=11.9$, 2×22 min exposures
KIC 10339342, RA:19 27 05.35 Dec:+47 24 08.2, $V=11.9$, 2×22 min exposures
KIC 11234888, RA:19 07 00.22 Dec:+48 56 07.0, $V=11.9$, 2×22 min exposures

(*) Note that this project is part of the collaborative work of Kepler Asteroseismic Science Consortium (KASC), Working Group 1, on solar-like oscillations, led by William J. Chaplin (University of Birmingham, UK).

(2) Centro de Astrofisica da Universidade do Porto, Portugal

(3) Instituto de Astrofisica de Canarias, Tenerife, Spain

(4) High Altitude Observatory, Boulder, CO, USA

Max Seeing

Weather

Moon

Total Time sec

